

Light-shift and temperature-shift studies in atomic clocks based on Coherent Population Trapping

Thèse présentée à la Faculté des Sciences pour l'obtention du grade de
docteur ès sciences par :

Danijela Miletic

acceptée le 04. 09. 2013 par les membres du jury:

Prof. assoc. Gaetano Mileti, Directeur de thèse

Dr. Christoph Affolderbach, Rapporteur

Dr. Vincent Giordano, Rapporteur

Dr. Jean-Pierre Aubry, Rapporteur

Dr. Patrick Berthoud, Examineur

IMPRIMATUR POUR THESE DE DOCTORAT

**La Faculté des sciences de l'Université de Neuchâtel
autorise l'impression de la présente thèse soutenue par**

Madame Daniela MILETIC DJORIC

Titre:

**“Light-shift and temperature-shift studies in atomic clocks
based on Coherent Population Trapping”**

sur le rapport des membres du jury:

- Prof. ass. Gaetano Mileti, Université de Neuchâtel, directeur de thèse
- Dr. Vincent Giordano, institut femto-st, Besançon, F
- Dr. Jean-Pierre Aubry, consultant, ex CEO de Oscilloquartz SA, Neuchâtel
- Dr. Christoph Affolderbach, Université de Neuchâtel
- Dr. Patrick Berthoud, Oscilloquartz SA, Neuchâtel

Neuchâtel, le 8 octobre 2013

Le Doyen, Prof. P. Kropf



Abstract

Vapor-cell atomic clocks exploit the ground-state microwave transition in an alkali atom to provide a stable frequency reference. At the heart of a conventional vapor-cell atomic clock is a cell containing the alkali atoms. A vapor-cell atomic clock can be realized using two different basic principles: Double Resonance (DR) and Coherent Population Trapping (CPT). In DR, the alkali atoms are optically pumped in order to be placed in the desired states, and the microwave resonances are excited by a microwave field resonant with the clock transition. In the CPT principle, the two ground-state atomic levels of the alkali atom are coupled to a common excited state, using two coherent electromagnetic fields (here, the microwave transition frequency is present in the frequency difference of the two coherent electromagnetic fields). The atoms are trapped in a coherent superposition of the ground states, called a dark state. The frequency of the vapor-cell atomic clocks can shift due to various residual variations such as: the properties of the light field (through the light-shift effect), the buffer gas pressure in the resonance cell, the temperature of the clock cell, and others. It is therefore critical to carefully stabilize all these parameters and to find a clock operational scheme that minimizes the sensitivity of the clock frequency towards them.

This thesis presents the studies on two laboratory atomic clocks: based on DR and CPT, using different vapor-cell content and size and different laser wavelengths. The main part of this thesis is focused on the study of the light-shift and temperature-shift phenomena in DR and CPT atomic clocks. These studies include theoretical developments and experimental measurements of these phenomena, showing a good agreement between them. Two novel approaches for the CPT vapor-cell atomic clock frequency shift suppression are proposed. The first is on the light-shift suppression as function of the miniature vapor-cell temperature. The second is on the temperature-shift suppression in the miniature single buffer gas vapor-cell. This temperature-shift suppression is obtained for the temperature that coincides with the cell temperature for suppressed intensity light-shift and it is also in the range of suitable temperatures for clock operation. DR and CPT clocks frequency stabilities are measured using both: buffer gas and wall-coated cell. A first ever wall-coated clock long-term frequency stability measurement is shown here. These results potentially provide possibilities for a number of applications like realization of novel CPT miniature atomic clocks with frequency stability of $\sim 10^{-11}$ at 10 000s, which will enable a new generation of portable instruments for positioning, navigation, smart-grid synchronization and telecommunication applications. Also, the results discussed in this thesis are used in devising the first European integrated miniature atomic clock.

Résumé

Les horloges atomiques à cellules exploitent une transition de l'état fondamental d'un atome alcalin afin d'obtenir une référence de fréquence stable. La cellule contenant ces atomes est au cœur de ce type d'horloges. Une horloge atomique à cellule peut être réalisée selon deux principes différents: La Double Résonance (DR) et le Piégeage Cohérent des Populations (CPT). Dans le cas de la DR, les atomes sont pompés optiquement dans l'état désiré, puis interrogés par un champ micro-onde résonnant avec la transition dite "horloge". Dans le cas de la CPT, les deux états fondamentaux de l'atome alcalin sont couplés à un état excité commun en utilisant deux champs électromagnétiques cohérents (ici, la fréquence de transition micro-onde est appliquée à travers la différence de fréquence entre les deux champs électromagnétiques cohérents). Les atomes sont ainsi «piégés» dans une superposition cohérente des deux états fondamentaux, appelée «état noir». La fréquence d'une horloge atomique à cellule est sensible aux variations de divers paramètres, tels que: les propriétés de la lumière utilisée pour l'excitation (à travers l'effet du «déplacement radiatif»), de la pression du gaz tampon dans la cellule, de la température de la cellule, etc. Il est donc très important de stabiliser tous ces paramètres et de trouver une configuration qui minimise la sensibilité de l'horloge aux variations de ces paramètres.

Cette thèse décrit l'étude de deux horloges atomiques de laboratoire, basées sur la DR et la CPT, utilisant des cellules de tailles et contenus différents. L'impact de la source lumineuse y est également étudié. La partie principale de cette thèse se concentre sur l'étude du déplacement radiatif et du décalage en température (temperature-shift) des deux types d'horloges atomiques. Ces études incluent un développement théorique ainsi que des mesures expérimentales de ces phénomènes, montrant une bonne correspondance entre eux. Deux nouvelles approches de suppression de ces taux de variation de fréquence sont proposées pour les horloges CPT. La première est la suppression du déplacement radiatif en fonction de la température de la cellule. La seconde est la suppression du taux de variation de fréquence en température. La suppression du taux de variation de fréquence en température est obtenue à une température coïncidant avec la température de la cellule à laquelle le déplacement radiatif d'intensité est supprimé. De plus, cette température se trouve dans une gamme favorable à l'opération de l'horloge. La stabilité en fréquence des horloges DR et CPT est mesurée avec deux types de cellules: des cellules avec gaz tampon et des cellules avec revêtement. La première mesure à long-terme de stabilité en fréquence avec une cellule à revêtement est présentée dans cette thèse. Les résultats obtenus

permettront la réalisation de nouvelles horloges atomiques miniatures basées sur le principe CPT, ayant des stabilités en fréquence de l'ordre de 10^{-11} à 10^{-10} s, ce qui permettra de produire une nouvelle génération d'instruments portables pour le positionnement, la navigation, la synchronisation des réseaux de distribution d'énergie (smart-grids) ou encore les télécommunications. De plus, les résultats discutés dans cette thèse ont été utilisés dans l'élaboration de la première horloge atomique miniature Européenne.

Acknowledgments

First I would like to thank my supervisor Prof. Gaetano Mileti for giving me the opportunity to be a part of LTF team. My professional and private life changed when I came in Neuchâtel five years ago. Not only that I had excellent work condition, well equipment laboratory, educated and experienced colleagues, but I also learn a lot about project management and project reporting. I would also like to thank him for giving me the opportunity to attend many conferences where I exchanged my knowledge with the other scientists and learn about their research. Prof. Mileti knows how to create an environment where the scientific work is on high level and often very exciting. I will always be grateful for his impact on my life, professionally and privately. I would also like to thank Dr. Christoph Affolderbach, who helped me enormously in these five years. My first laboratory steps are taken with him, teaching me about laboratory books, equipment and the experiments. I thank him for his patience, for solving the unsolved scientific problems for me, and nice scientific discussions. We share a similar sense of humor, which meant a lot for me and often made me smile.

I was lucky to have such nice colleagues. Thank you Dr. Thejesh Bandy for the discussions and patience, for being always there for me and for becoming the true friend of mine. Thank you Matthieu Pellaton, for being not so easy to convince in our discussions, for helping me with French and for being a friend. Thank you Florian Gruet for helping me with the laser characterizations, French language and nice jokes. Thank you to all my past and present colleagues: Dr. Renaud Matthey, Dr. Gianni Di Domenico, Dr. Daniel Hofstetter, Prof. Thomas Südmeyer, Dr. Stéphane Schilt, Prof. Pierre Thomann, Nikola Bucalovic, Lionel Tombez, Joab Di Francesco, Dr. Laurent Devanoges, and Dr. Vladimir Dolgovskiy. Thank you Dr. Clément Didiot, Alexander Wirthmueller and Dr. Gunnar Garnier for sharing the TPD moments with me.

I would like to thank Patrick Scherler for building physic packages in both of my experiments. Thank to Daniel Varidel for his help with computers and electronics. I would also like to thank Marc Durrenberger for building precise laser control and resonator control electronics systems and Dominique Schenker for his technical support. I also thank the machine shop crew André Cornu and Isidro Fernandez along with Christian Heche.

I would like to thank all the jury members for accepting to be the jury for this thesis, for reading this manuscript and for their suggestions. Also, I would like to thank Dr.

Hartmut Schweda for correcting the English in my thesis.

Many thanks to Muriel Vallery, for being much more for me than the secretary of LTF. She was always there for me, to talk, understand, suggest and do her job on the best possible way.

Working in MAC-TFC project made me opportunity to collaborate with many different nice people: University Franche-Comte FEMTO-ST, France (Dr. Christoph Gorecki, Dr. Vincent Giordano, Dr. Rodolphe Boudot, Dr. Madoka Hasegawa, Dr. P. Dziuban, Dr. R. K. Chutani, Dr. S. Galliou and Dr. N. Passilly), Politechnika Wroclawska, Poland (Dr. Jan Dziuban and Dr. Pawel Knapkiewicz) Ecole Polytechnique Fédérale de Lausanne-EPFL SAMLAB, Switzerland (Dr. Yves Petremand, Dr. Rahel Strassle, Dr. Danic Briand, Dr. Nico de Rooij, Dr. Pierre-André Farine, Dr. Steve Tanner and Dr. Yazhou Zhao), Universität Ulm, Germany (Dr. Rainer Michalzik, Dr. Ahmed Al-Samaneh and Dietmar Wahl), VTT Technical Research Group of Finland, Finland (Dr. M. Heikkinen, Dr. Kari Kautio, Dr. Pentti Karioja and Dr. Antti Keränen), SAES Getters SpA, Italy (Dr. Luca Mauri), Commissariat à l'Énergie Atomique et aux Energies Alternative CEA, France (Dr. Jean-Michel Lèger and Dr. Matthieu Le Prado), Oscilloquartz S.A. - Swatch Group, Switzerland, (Dr. Patric Berthoud, Dr. Luc Schneller, Dr. Jean-Pierre Aubry and Dr. Alain Michaud) and The Swatch Group Recherche et Developpment S.A, Switzerland (Dr. Alain Jornod and Dr. Francois Gueissas). I thank to all of them.

I thank FP7, FNS, ASRH and UniNE for the financial support during my PhD.

I always had a lot of love and support from my family, especially during this time. My father Tode did not live to see this day but I hope that he knows somehow. Everything what I am and who I am today is because of him. My mother Draga is always there for me, through all-bad and good moments, with the pure love only. I would like to thank my sister Jelena, for unconditional love, support and connection that is indescribable. Even though it was hard to be far away from them, I always felt their presence and their love.

On the end, I would like to thank my new family: my husband Ugljesa, for understanding, patience and love. And, to my daughter Helena, for teaching me about new love, for making me proud to be a mother and for helping me writing this thesis, being nice and quiet in my belly.

Mojim roditeljima: tati Todi i mami Dragi

To my parents Tode and Draga

Contents

Abstract	iii
Résumé	v
Acknowledgments	vii
Glossary of Acronyms	xv
Introduction	1
Chapter 1 Gas-cell atomic clocks	13
1.1 Operating principle of a gas-cell atomic clock.....	13
1.2 Cs and Rb atoms.....	19
1.3 Linear and saturated absorption in a Cs and Rb vapor cell	21
1.4 Systematic shifts in gas-cell atomic clocks	26
1.4.1 Buffer-gas pressure and temperature shift	26
1.4.2 Magnetic field shift.....	27
1.4.3 Light shift (AC-Stark shift).....	28
1.4.4 Summary of typical shifts in gas-cell atomic clocks	29
1.5 Atomic clock frequency stability	30
1.6 Summary and conclusions.....	33
Chapter 2 Coherent Population Trapping theory	37
2.1 Three-level models for CPT in Λ systems.....	37
2.2 CPT signal amplitude and linewidth.....	41
2.2.1 Time of flight.....	42
2.2.2 Spin-exchange	43
2.2.3 Doppler broadening.....	43
2.2.4 Atom-cell walls collisions (diffusion equation)	44

2.2.5	Collisions with buffer gas atoms	45
2.3	Light shift in CPT for a simple three-level model atom	47
2.4	Light shift in CPT for a four-level model atom	50
2.5	Temperature coefficient	54
2.5.1	Temperature coefficient in a buffer gas cell.....	54
2.5.2	Temperature coefficient in a wall-coated cell.....	55
2.6	Summary and conclusions.....	57
Chapter 3	Experimental methods.....	61
3.1	Laser sources.....	61
3.1.1	DFB lasers	63
3.1.2	Laser linewidth measurements	64
3.1.3	Laser noise	67
3.1.4	Laser modulation with Electro-Optical Modulator (EOM).....	69
3.2	Micro-fabricated (MEMS) and glass-blown cells	72
3.2.1	The Cs MEMS single buffer gas cell (FEMTO cell).....	73
3.2.2	The Cs MEMS single and mixture buffer gas cell (PWL cell)	75
3.2.3	The Cs MEMS cell with buffer gas mixture (SAMLAB-LTF cell).....	75
3.2.4	The glass-blown ^{87}Rb cm-scale wall-coated cell.....	76
3.3	Clock experimental setup	77
3.3.1	The CPT clock using the MEMS Cs buffer gas cell.....	78
3.3.2	The DR and/or CPT clock using the cm-scale Rb wall-coated cell... 80	
3.4	DR and CPT signal: first characterization	83
3.4.1	CPT signal obtained from the Cs MEMS cell	83
3.4.2	The DR and CPT signal obtained from the ^{87}Rb wall-coated cell.....	88
3.5	Summary and conclusions.....	92
Chapter 4	Light shift and temperature shift in CPT atomic clocks.....	97
4.1	Light shift and temperature shift in the Cs MEMS cell with buffer gas	98
4.1.1	Intensity light shift in the Cs MEMS cell with buffer gas.....	98

4.1.2	Frequency light-shift in the Cs MEMS cell with buffer gas	103
4.1.3	Comparison of the light-shift coefficients α and β	107
4.1.4	Temperature shift in the Cs MEMS cell with buffer gas.....	108
4.1.5	Summary and conclusions	112
4.2	Light shift and temperature shift in the ^{87}Rb wall-coated cm-scale cells....	113
4.2.1	Frequency light shift in the ^{87}Rb wall-coated cell	113
4.2.2	Intensity light shift in the ^{87}Rb wall-coated cell	117
4.2.3	Temperature shift in the ^{87}Rb wall-coated cell.....	125
4.2.4	Summary and conclusions	127
4.3	Comparison and discussions of the results.....	128
Chapter 5	Clock frequency stability.....	135
5.1	CPT atomic clock using the MEMS Cs buffer gas cell.....	135
5.1.1	Short-term frequency stability	135
5.1.2	Medium-term frequency stability	140
5.1.3	Long-term frequency stability	142
5.1.4	Summary and conclusions	143
5.2	CPT and DR atomic clock using the cm-scale ^{87}Rb wall-coated cell	144
5.2.1	Short-term frequency stability	144
5.2.2	Medium-term frequency stability	147
5.2.3	Long-term frequency stability	148
5.2.4	Summary and conclusions	150
5.3	Conclusions and future prospects on the clock stability measurements....	151
	Conclusions and prospects.....	155
	Publications and Conferences	159
	Curriculum Vitae	163
	APPENDIX A DR atomic clock using the cm-scale glass-blown ^{87}Rb cell with buffer gas mixture	165

APPENDIX B	Compact laser head.....	169
APPENDIX C	Relative optical transition strengths of the D1 line in Cs and ⁸⁷Rb atoms.....	171

Glossary of Acronyms

AOM	Acousto-Optical Modulator
CAD	Computer Aided Design
CPT	Coherent Population Trapping
CSAC	Chip-Scale Atomic Clock
CSAM	Chip-Scale Atomic Magnetometer
DFB	Distributed FeedBack lasers
DR	Double Resonance
ECDL	Extended-Cavity Diode Laser
EIT	Electromagnetically Induced Transparency
EOM	Electro-Optical Modulator
FFT	Fast Fourier Transform
FP	Fabry-Perot
GLONASS	Russian Global Satellite Navigation System
GNSS	Global Navigation Satellite System
GPS	Global Positioning System
LO	Local Oscillator
LS	Light Shift
LTF	Laboratoire Temps - Fréquence
MEMS	Micro-Electro-Mechanical System
MWR	MicroWaveResonator
NIST	National Institute for Standards and Technology
PD	PhotoDetector
PSD	Power Spectral Density
PWL	Politechnika WrocLawska
RIN	Relative Intensity Noise
SMSR	Side-Mode Suppression Ratio
VCSEL	Vertical-Cavity Surface-Emitting Laser

Introduction

The first idea about using an atomic transition to measure time was proposed by Lord Kelvin in 1879 [1]. It took 60 years before this idea was implemented experimentally. Rabi's pioneering work on molecular beams bred the concept of stabilizing a quartz oscillator to an atomic transition, which suppressed the instability of the quartz frequency over longer timescales [2]. This approach was advanced by Ramsey and his method of successive oscillatory fields [3], and eventually led to the first atomic frequency standards [4, 5, 6].

In more than 130 years of research, a large body of experiments triggered further developments either directly or indirectly. One of them is Zacharias Cesium (Cs) atomic beam experiment in 1954 [5]. Although unsuccessful, this experiment led to the first practical laboratory Cesium beam frequency standard [6]. In 1967, the 13th "Conférence Générale des Poids et Mesures", defined the second in the International System of Units (SI) as the duration of 9 192 631 770 periods of the radiation corresponding to the transition between the two hyperfine levels of the ground state of the Cs 133 atom. In the following 40 years, the 1.5×10^{-11} frequency accuracy obtained with the first Cs beam [7] was improved to 3×10^{-15} by the development of a Cs fountain in Laboratoire Primaire du Temps et Fréquences (LPTF) in Paris [8]. The present Cs atomic fountain clocks have reached an accuracy of 4×10^{-16} and stability at the $10^{-14} / \tau^{1/2}$ level [9].

In the 1980's clocks with ions trapped [10] and cooled in RF potentials were built [11, 12], operating at microwave frequencies. Their stability is intrinsically limited by the relatively small frequencies of the clock transition and therefore comparable with the best fountain clocks [13]. Clocks operating at optical frequencies were developed starting in the 1980's. Nowadays with the advance of frequency combs it has become possible to directly transfer frequencies from the optical to the microwave domain. Subhertz linewidth lasers are realized through stabilization to a high finesse FP cavity. The narrowband lasers can then be used to sample narrow (Hz-level) atomic lines with quality factors on the order of $Q=10^{14}$, while this optical stability can be transferred to the microwave domain using frequency combs. The combination of frequency combs and subhertz linewidth lasers is used in realization of optical clocks [14-28]. The present optical atomic clocks are considered to be the most stable atomic frequency standards in the world with stability of $10^{-15} \tau^{-1/2}$.

In 1949, Lyons built the first microwave ammonia clock [29], and in the same year, Kastler showed that optical pumping technique [30] can be effectively combined with the double resonance (DR) method [31]. A vapor-cell standard can be established by stabilizing a quartz oscillator using the ground-state transition of an alkali atom: simultaneously, the alkali atoms are optically pumped in order to create the polarization, and the microwave resonances are excited by a microwave field. Here, alkali atoms are contained in a glass-cell placed in a microwave cavity that produces the microwave field resonant with the clock frequency. This combination together with the buffer gas method for reducing Doppler shift [32] references the optically pumped gas-cell clock as secondary frequency standards since their frequency must be calibrated against a primary frequency standard. Their assets consist in simplicity, small size and relatively low cost. Large shift in frequency due to buffer gas pressure and temperature or changes in the intensity and frequency of the pump light prevent them from being primary time and frequency standards.

In most commercially available gas-cell atomic clocks, the optical pumping technique is implemented using a discharge lamp. Several experiments have shown that significantly better performances can be achieved if the discharge lamp is replaced by a laser diode. Recent advances in laser diode technology incite to exploit the advantages of laser optical pumping to develop high performance gas-cell clocks [33, 34]. In parallel to the laser optical pumping technique, the need for miniaturized gas-cell clocks was growing. As the size of the microwave cavity used for inducing the atomic resonance was considered as limiting factor, alternative technique is devised. In 1976 Alzetta observed the Coherent Population Trapping (CPT) effect in a Sodium cell by coupling two ground-state atomic levels to a common excited state, using two coherent electromagnetic fields in a so-called Λ -scheme [35]. The atoms are trapped in a coherent superposition of the ground states (the dark state) where, ideally, they stop absorbing incident photons (the difference from optical pumping where atoms are also placed in non-absorbing state is in the fact that in CPT the dark state is given by a coherent superposition of atomic states). CPT represents a mechanism to achieve electromagnetically induced transparency (EIT) [36] and slowed speed of light [37]. In 1993, Cyr suggested to use the CPT method in atomic clocks by irradiating alkali vapor with an RF modulated laser beam [38]. Since then a number of existing CPT atomic clocks have been reported [39, 40, 41, 56-58]. The idea of using CPT method in atomic clocks also led to their strong miniaturization. In 2004 the NIST group presented a first fully operational physics package of a micro-fabricated gas-cell atomic clock with a size of 9.5 mm^3 and a frequency stability of $6 \times 10^{-11} \tau^{-1/2}$ [42].

The miniature gas-cell atomic clocks based on the CPT are one of the research subjects of this thesis. This study was done in the frame of the European FP7 project MAC-TFC (MEMS Atomic Clocks for Timing, Frequency Control & Communications). The goal of this project was to develop the first European Cesium miniature atomic clock based on CPT using a micro-fabricated buffer-gas cell, with a stability on the $6 \times 10^{-11} \tau^{-1/2}$ level. This project represented a consortium of 10 partners from six different European countries: University Franche-Comte FEMTO-ST (France), Politechnika Wroclawska (Poland) and Ecole Polytechnique Fédérale de Lausanne-EPFL SAMLAB (Switzerland) developed the miniature Cs vapor cells, Universität Ulm (Germany) was in charge for developing the VCSELs emitting at 894 nm, VTT Technical Research Group of Finland (Finland) part was to do 3D LTCC packaging of the miniature clock, SAES Getters SpA (Italy) provided the getters placed in miniature vapor cells, Commissariat à l'Énergie Atomique et aux Energies Alternative CEA (France) was in charge to evaluate the possibility to use the developed subsystems and building blocks for the development of an atomic magnetometer, finally there were two industrial partners: Oscilloquartz S.A. - Swatch Group and The Swatch Group Recherche et Developpment S.A., both from Switzerland. Our part in this project was to focus on the clock characterization and optimization.

In the first part of this thesis we discuss the frequency shifts of the CPT gas-cell miniature atomic clock resonance due to instabilities of the cell temperature, the light intensity and light frequency. The effect of the cell temperature instability can be minimized if a mixture of two buffer gases with opposite temperature coefficients is used, to obtain a suppressed linear temperature coefficient at a specific inversion temperature [43-45]. This result was confirmed in the collaboration with the (FEMTO-ST group), France and (SAMLAB group) Switzerland (published in a peer-reviewed journal [46] and presented at four different conferences [69-71, 75]). Working in the same collaboration we showed that in the case of Cs, the same effect can be obtained with pure Ne as buffer gas, without need for a gas mixture [47, 64, 73], see Chapter 4.

Concerning the clock instabilities due to the light intensity and frequency, several methods are already known for light-shift reduction in commercial lamp-pumped Rb clocks [48, 49], in laboratory clocks based on laser optical pumping [50-53], and in CPT-based vapor-cell clocks [54-58]. In the case of a CPT-based clock with continuous-wave laser excitation, the light-shift can be significantly reduced by optimizing the modulation index of the RF frequency-modulated laser field used to create the CPT signal [54, 55]. In all published cases the light-shift reduction was obtained on Rb D2 line [51], Rb D1 line [54] or Cs D2 line [55-58]. There are no reported methods of a light-shift reduction for a CPT atomic clock using the Cs D1 line. This thesis proposes a

technique for the light-shift suppression using the Cs D1 line for the case of a frequency-modulated laser field, but as function of the Cs cell temperature [59, 60, 65, 72, 73], see Chapter 4.

This thesis not only provides results that will be used in devising a miniature atomic clock using a micro-fabricated buffer-gas cell but also discusses atomic clocks using a wall-coated cell (Chapter 4, section 4.3). Alkali cells whose walls are coated are of high interest to, achieve both narrow clock signal linewidths (therefore improving the clock frequency stability) and allow further clock miniaturization. Studying the light shift effect in DR and/or CPT clocks using wall-coated cells allow comparisons between the frequency shifts in two different CPT clocks: using either the Cs micro-fabricated buffer gas cell or the Rb cm-scale wall-coated cell. Furthermore, it is possible to compare the frequency shift measurements in CPT and DR cases, and thus obtain an overall picture of the observed effects [61, 66, 68, 74, 76].

This research was also supported by the Swiss National Science Foundation (FNS) and part of the research on Rb wall-coated cell benefitted from a project funded by the Association Suisse pour la Recherche Horlogère (ASRH).

The thesis is organized as follows.

In the first chapter, the operational principle of the atomic clock with detailed description of the DR and CPT method is given. The general information on Cs and Rb atoms are followed by a description of the absorption signals obtained from Cs and Rb vapor cells. Finally, the main systematic shifts in vapor-cell atomic clocks and Allan deviation, as a measure of the clock frequency stability, are introduced.

In Chapter two, the CPT theory is briefly introduced through the simple three-level model, followed by a presentation of expected line-shapes of the CPT signal. Theoretical descriptions of the light shift and temperature coefficient in a gas-cell atomic clock are given here.

Chapter three describes the experimental setups: it contains a detailed characterization of the laser and its modulation parameters, lists the vapor cells used in the experiments, describes the experimental setups and gives the characterization of the obtained DR and CPT signals.

Chapter four discusses the experimental measurements of the light shift and temperature coefficient in two different cases: using Cs MEMS buffer gas cell, and the Rb cm-scale wall-coated cell.

To conclude, in Chapter five, short-, medium- and long-term stabilities are shown for the two clocks. The influence of the light shift and temperature coefficient to the clock stability is evaluated.

The main results are summarized and next experimental steps are proposed. Appendix A describes the experimental setup used for obtaining the results shown in section 4.4. Appendix B details on the laser head used for obtaining the results discussed in section 4.3. Appendix C gives information about the relevant transition strengths of the ^{133}Cs and ^{87}Rb alkali atom.

REFERENCES:

[1] W. F. SNYDER, *Lord Kelvin on atoms as fundamental natural standards*, IEEE Trans. Instrum. Meas. IM-22 (1973), p. 99.

[2] I. I. RABI, S. MILLMAN, P. KUSCH and J. R. ZACHARIAS, *The molecular beam resonance method for measuring nuclear magnetic moments*, Phys. Rev. 55 (1939), pp. 526-535.

[3] N. F. RAMSEY, *The method of successive oscillatory fields*, Phys. Today 33 (1980), pp. 25-30.

[4] J. P. GORDON, H. J. ZEIGER and C. H. TOWNES, *The Maser – New Type of Microwave Amplifier, Frequency Standard, and Spectrometer*, Phys. Rev. 99 (1955), pp. 1264-1274.

[5] J. R. ZACHARIAS, *An atomic frequency standard*, Proc. of the Inst. of Radio-Engineers 43 (3) (1955), p. 364.

[6] L. ESSEN and J. V. L. PARRY, *Atomic standard of frequency and time interval*, Nature 176 (1955), pp. 280-282.

[7] P. FORMAN, *The first atomic clock program: NBS, 1947-1954*, in Proc. Ann. PTII Meeting (1985), pp.1-17.

[8] A. CLAIRON, S. GHEZALI, G. SANTARELLI, P. LAURENT, S. N. LEA, M. BAHOURA, E. SIMON, S. WEYERS and K. SZYMANIEC, *Preliminary accuracy evaluation of a cesium fountain frequency standard*, in Proc. 5th Symp. On Freq. Standards and Metrology, J. C. Bergquist, editor, World Scientific, London (1996), p. 49.

- [9] J. GUENA, P. ROSENBUSCH, P. LAURENT, M. ABGRALL, D. ROVERA, G. SANRATELLI, M. E. TOBAR, S. BIZE, and A. CLAIRON, *Demonstration of a dual alkali Rb/Cs fountain clock*, IEEE Trans. Ultrason. Ferroelec., Freq. Control 57 (2010), pp. 647-653.
- [10] W. PAUL, *Electromagnetic traps for charged and neutral particles*, Rev. Mod. Phys. 62 (1990), pp. 531-540.
- [11] R. DRULLINGER, D. WINELAND and J. BERGQUIST, *High-resolution optical spectra of laser cooled ions*, Appl. Phys. A-Mater. 22 (1980), pp. 365-368.
- [12] J. J. BOLLINGER, J. D. PRESTAGE, W. M. ITANO and D. J. WINELAND, *Lasercooled- atomic frequency standard*, Phys. Rev. Lett. 54 (1985), p. 1000.
- [13] P. T. H. FISK, M. J. SELLARS, M. A. LAWN, and C. COLES, *A microwave frequency standard based on trapped, buffer gas-cooled $^{171}\text{Yb}^+$ ions*, in Proc. 5th Symp. on Freq. Standards and Metrology (1995), pp. 27-32.
- [14] H. KATORI, M. TAKAMOTO, V. PAL'CHIKOV and V. D. OVSIANNIKOV, *Ultrastable Optical Clock with Neutral Atoms in an Engineered Light Shift Trap*, Phys. Rev. Lett. 91 (2003), pp. 173005-4.
- [15] J. FRIEBE, A. PAPE, M. RIEDMANN, K. MOLDENHAUER, T. MEHLSTAUBLER, N. REHBEIN, C. LISDAT, E. M. RASEL, W. ERTMER, H. SCHNATZ, B. LIPPHARDT and G. GROSCHE, *Absolute frequency measurement of the magnesium intercombination transition 1S_0 - 3P_1* , Phys. Rev. A, 78 (2008), pp. 033830-7.
- [16] C. W. CHOU, D. B. HUME, J. C. J. KOELEMENIJ, D. J. WINELAND, and T. ROSENBAND, *Frequency comparison of two high-accuracy Al^+ optical clocks*, Phys. Rev. Lett. 104 (2010), pp. 070802-4.
- [17] M. EICHENSEER, A. NEVSKY, C. SCHWEDES, J. von ZANTHIER, and H. WALTHER, *Towards an indium single-ion optical frequency standard*, J. Phys. B: At., Mol. Opt. Phys. 36 (2003), pp. 553-559.
- [18] S. A. DIDDAMS, T. UDEM, J. C. BERGQUIST, E. A. CURTIS, R. E. DRULLINGER, L. HOLBERG, W. M. ITANO, W. D. LEE, C. W. OATES, K. R. VOGEL and D. R. WINELAND, *An Optical Clock Based on a Single Trapped $^{199}\text{Hg}^+$ Ion*, Science 293 (2001), pp. 825-828.
- [19] T. SCHNEIDER, E. PEIK and C. TAMM, *Sub-Hertz Optical Frequency Comparisons between Two Trapped $^{171}\text{Yb}^+$ Ions*, Phys. Rev. Lett. 94 (2005), pp. 230801-4.

- [20] S. WEBSTER, R. GODUN, S. KING, G. HUANG, B. WALTON, V. TSATOURIAN, H. MARGOLIS, S. LEA and P. GILL, *Frequency Measurement of the $^2S_{(1/2)}-^2D_{(3/2)}$ Electric Quadrupole Transition in a Single ^{171}Yb (+) Ion*, IEEE Trans., Ultrason. Ferroelectr., Freq. Control 57 (2010), pp. 592-599.
- [21] H. S. MARGOLIS, G. P. BARWOOD, G. HUANG, H. A. KLEIN, S. N. LEA, K. SZYMANIEC and P. GILL, *Hertz-Level Measurement of the Optical Clock Frequency in a Single $^{88}\text{Sr}+$ Ion*, Science, 306 (2004), pp. 1355-1358.
- [22] M. CHWALLA, J. BENEHLM, K. KIM, G. KIRCHAIR, T. MONZ, M. RIEBE, P. SCHINDLER, A. S. VILLAR, W. HANSEL, C. F. ROOS, R. BLATT, M. ABGRALL, G. SANTARELLI, G. D. ROVERA and P. LAURENT, *Absolute Frequency Measurement of the $^{40}\text{Ca}+ 4s2S_{1/2} \rightarrow 3d2D_{5/2}$ Clock Transition*, Phys. Rev. Lett. 102 (2009), pp. 023002-4.
- [23] R. Le TARGAT, X. BAILLARD, M. FOUICHE, A. BRUSCH, O. TCHERBAKOFF, G. D. ROVERA and P. LEMONDE, *Accurate Optical Lattice Clock with ^{87}Sr Atoms*, Phys. Rev. Lett. 97 (2006), pp. 130801-4.
- [24] A. D. LUDLOW, T. ZELEVINSKY, G. K. CAMPBELL, S. BLATT, M. M. BOYD, M. H. G. de MIRANDA, M. J. MARTIN, J. W. THOMSEN, S. M. FOREMAN, J. YE, T. M. FORTIER, J. STALNAKER, S. A. DIDDAMS, Y. Le COQ, Z. W. BARBER, N. POLI, N. LEMKE, K. M. BECK and C. W. OATES, *Sr Lattice Clock at 1×10^{-16} Fractional Uncertainty by Remote Optical Evaluation with a Ca Clock*, Science, 319 (2008), pp. 1805-1808.
- [25] N. D. LEMKE, A. D. LUDLOW, Z. W. BARBER, T. M. FORTIER, S. A. DIDDAMS, Y. JIANG, S. R. JEFFERTS, T. P. HEAVNER, T. E. PARKER and C. W. OATES, *In Spin-1/2 optical lattice clock*, Phys. Rev. Lett. 103 (2009), pp. 063001-4.
- [26] S. G. PORSEV, A. DEREVIANKO and E. N. FORTSON, *Possibility of an optical clock using the $61S_0-63P_0$ transition in $^{171,173}\text{Yb}$ atoms held in an optical lattice*, Phys. Rev. A 69 (2004), pp. 021403-4.
- [27] H. HACHISU, K. MIYAGISHI, S. G. PORSEV, A. DEREVIANKO, V. D. OVSIANNIKOV, V. G. PAL'CHIKOV, M. TAKAMOTO and H. KATORI, *Trapping of neutral mercury atoms and prospects for optical lattice clocks*, Phys. Rev. Lett. 100 (2008), pp. 05300-4.
- [28] M. PETERSEN, R. CHICIREANU, S. T. DAWKINS, D. V. MAGALHES, C. MANDACHE, Y. Le COQ, A. CLAIRON and S. BIZE, *Doppler-Free Spectroscopy of the $1S_0-3P_0$ Optical Clock Transition in Laser-Cooled Fermionic Isotopes of Neutral Mercury*, Phys. Rev. Lett. 101 (2008), pp. 183004-4.

- [29] H. LYONS and N. Y. ANN, *Spectral lines as frequency standards*, Acad. Sci. 55 (1952), pp. 831-871.
- [30] F. BITTER, *The optical detection of radiofrequency resonance*, Phys. Rev. 76 (1949), pp. 833-835.
- [31] J. BROSSEL and A. KASTLER, *La détection de la résonance magnétique des niveaux excités - l'effet de depolarization des radiations de résonance optique et de fluorescence*, C. R. Acad. Sci. (Paris) 229 (1949), pp. 1213-1215.
- [32] R. H. DICKE, *The effect of collisions upon the Doppler width of spectral lines*, Phys. Rev. 76 (1953), pp. 472-473.
- [33] C. AFFOLDERBACH, F. GRUET, R. MATTHEY and G. MILETI, *A compact laser-pumped Rb clock with $5 \times 10^{-13} \tau^{-1/2}$ frequency stability*, Proc. of the Joint Meeting of the European Frequency and Time Forum (EFTF) and the IEEE International Frequency Control Symposium (FCS), San Francisco (USA), May 2-5 (2011), pp. 944-946.
- [34] T. BANDI, C. AFFOLDERBACH, C. E. CALOSSO and G. MILETI, *High-performance laser-pumped rubidium frequency standard for satellite navigation*, Electron. Lett. 47 (2011), pp. 698-699.
- [35] G. ALZETTA, A. GOZZINI, M. MOI and G. ORRIOLS, *Experimental-method for observation of r. f. transitions and laser beat resonances in oriented Na vapor*, Nuovo Cimento B 36 (1976), pp. 5-20.
- [36] S. E. HARRIS, J. E. FIELD, A. IMAMOGLU, *Nonlinear Optical Processes Using Electromagnetically Induced Transparency*, Phys. Rev. Lett. 64 (1990), pp. 1107-1110.
- [37] L. V. HAU, S. E. HARRIS, Z. DUTTON, C. H. BEHROOZI, *Light speed reduction to 17 metres per second in an ultracold atomic gas* Nature 397 (1999), pp. 594-598.
- [38] N. CYR, M. TETU and M. BRETON, *All-Optical Microwave Frequency Standard: A Proposal*, IEEE Trans. Instrum. Meas. 42 (1993), pp. 640-649.
- [39] N. CYR, M. TETU and M. BRETON, *All-Optical Microwave Frequency Standard: A Proposal*, IEEE Trans. Instrum. Meas. 42 (1993), pp. 640-649.
- [40] M. MERIMAA, T. LINDVALL, I. TITTONEN and E. IKONEN, *All-optical atomic clock based on coherent population trapping in ^{85}Rb* , JOSA B 20 (2003), pp. 273-279.

- [41] N. CASTAGNA, R. BOUDOT, S. GUERANDEL, E. DE CLERCQ, N. DIMARCO and A. CLAIRON, *Investigations on continuous and pulsed interrogation for a CPT atomic clock*, IEEE Trans Ultrason Ferroelectr Freq Control. 56(2) (2009), pp. 246-253.
- [42] S. KNAPPE, P. D. D. SCHWINDT, V. GEORGINOV, V. SHAH, L. HOLLBERG and J. KITCHING, *Microfabricated atomic clocks at NIST*, 36th Annual Precise and Time Interval (PTTI) Meeting, (2004), pp. 383-392.
- [43] R. BOUDOT, D. MILETIC, P. DZIUBAN, C. AFFOLDERBACH, P. KNAPKIEWICZ, J. DZIUBAN, G. MILETI, V. GIORDANO and C. GORECKI, *First-order cancellation of the Cs clock frequency temperature-dependence in Ne-Ar buffer gas mixture*, Opt. Express 19 (2011), pp. 3106-3114.
- [44] K. DENG, X. CHEN and Z. WANG, *Minimization of the temperature coefficient of resonance frequency shift in the coherent population trapping clock*, Opt. Lett. 36 (2011), pp. 1740-1742.
- [45] O. KOZLOVA, S. GUERANDEL and E. DE CLERCQ, *Temperature and pressure shift of the Cs clock transition in the presence of buffer gases: Ne, N₂, Ar*, Phys. Rev. A 83 (2011), pp. 062714-9.
- [46] R. BOUDOT, D. MILETIC, P. DZIUBAN, C. AFFOLDERBACH, P. KNAPKIEWICZ, J. DZIUBAN, G. MILETI, V. GIORDANO and C. GORECKI, *First-order cancellation of the Cs clock frequency temperature-dependence in Ne-Ar buffer gas mixture*, Opt. Express 19 (4) (2011), pp. 3106-3114.
- [47] D. MILETIC, P. DZIUBAN, R. BOUDOT, M. HASEGAWA, R. K. CHUTANI, G. MILETI, V. GIORDANO and C. GORECKI, *Quadratic Dependence on Temperature of the Cs 0-0 Hyperfine Resonance Frequency in a Single Ne Buffer Gas Microfabricated Vapor Cell*, Electron. Lett. 46 (2010), pp. 1069-1070.
- [48] J. VANIER and C. AUDOIN, *The Quantum Physics of Atomic Frequency Standards*, Adam Hilger, Bristol, UK, (1989).
- [49] J. C. CAMPARO, R. P. FRUEHOLZ and C. H. VOLK, *Inhomogeneous light shift in alkali-metal atoms*, Phys. Rev. A 27 (1983), pp. 1914 - 1924.
- [50] J. DENG, *Light shift compensation in a Rb gas cell frequency standard with two-laser pumping*, IEEE Trans., Ultrason. Ferroelectr., Freq. Control 48 (2001), pp. 1657-1661.

- [51] C. AFFOLDERBACH, C. ANDREEVA, S. CARTALEVA, T. KARAUANOV, G. MILETI and D. SLAVOV, *Light-shift suppression in laser optically pumped vapour-cell atomic frequency standards*, Appl. Phys. B 80 (2005), pp. 841-848.
- [52] F. LEVI, C. NOVERO, A. GODONE and G. BRIDA, *Analysis of the light shift effect in the ^{87}Rb frequency standard*, IEEE Trans. Instrum. Meas. 46 (1997), pp. 126-129.
- [53] B. H. MCGUYER, Y. -Y. JAU and W. HAPPER, *Simple method of light-shift suppression in optical pumping systems*, Appl. Phys. Lett. 94 (2009), pp. 251110-3.
- [54] F. LEVI, A. GODONE and J. VANIER, *The light shift effect in the coherent population trapping cesium maser*, IEEE Trans. Ultrason. Ferroelectr. Freq. Control 47 (2000), pp. 466-470.
- [55] M. ZHU and L. S. CUTLER, *Theoretical and experimental study of light shift in a CPT based Rb vapour cell frequency standard*, Proceedings of the 32nd Precise Time and Time Interval Systems and Applications Meeting, ed. By L.A. Breakiron (US Naval Observatory, Washington, DC, 2000) (2000), pp. 311-324.
- [56] R. BOUDOT, P. DZIUBAN, M. HASEGAWA, R. K. CHUTANI, S. GALLIOU, V. GIORDANO and C. GORECKI, *Coherent population trapping resonances in Cs-Ne vapor microcells for miniature clocks applications*, J. Appl. Phys. 109 (2011), pp. 014912-11.
- [57] V. GEORGINOV, S. KNAPPE, P. D. SCHWINDT, L. HOLLBERG and J. KITCHING, *Long-term frequency instability of atomic frequency references based on coherent population trapping and microfabricated vapor cells*, J. Opt. Soc. Am. B 23 (2006), pp. 593-597.
- [58] E. E. MIKHAILOV, T. HORROM, N. BELCHER and I. NOVIKOVA, *Performance of a prototype atomic clock based on lin//lin coherent population trapping resonances in Rb atomic vapor*, J. Opt. Soc. Am. B 27 (2010), pp. 417-422.
- [59] D. MILETIC, C. AFFOLDERBACH, G. MILETI, M. HASEGAWA and C. GORECKI, *Spectroscopy of micro-fabricated Cs vapors cells for miniature atomic clocks*, Proc. SPIE of ISQE 7747 (2011), pp. 77470F-77470F-9.
- [60] D. MILETIC, C. AFFOLDERBACH, M. HASEGAWA, C. GORECKI, R. BOUDOT and G. MILETI, *AC Stark shift in CPT-based Cs miniature atomic clocks*, Appl. Phys. B 109 (1) (2012), pp. 89-97.

- [61] D. MILETIC, T. BANDI, C. AFFOLDERBACH, and G. MILETI, *AC Stark-shift in Double Resonance and Coherent Population Trapping in Wall-Coated Cells for Compact Rb Atomic Clocks*, Phys. Scr. T149 (2012), pp. 1-3.
- [62] F. GRUET, A. AL-SAMANEH, E. KROEMER, L. BIMBOES, D. MILETIC, C. AFFOLDERBACH, D. WAHL, R. BOUDOT, G. MILETI and R. MICHALZIK, *Metrological characterization of custom-designed 894 nm VCSELs for miniature atomic Clocks*, Opt. Express 21(5) (2013), pp. 5781-5792.
- [63] F. GRUET, D. MILETIC, C. AFFOLDERBACH and G. MILETI, *Characterization of aged/non-aged 894 nm DFB for their application in Cs atomic clocks*, Proc. of the International Symposium On Reliability Of Optoelectronic For Space (ISROS), Cagliari (Italy), May 11-15 (2009), pp. 1-14.
- [64] D. MILETIC, C. AFFOLDERBACH, E. BRESCHI, C. SCHORI, G. MILETI, M. HASEGAWA, R. CHUTANI, P. DZIUBAN, R. BOUDOT, V. GIORDANO and C. GORECKI, *Fabrication and spectroscopy of Cs vapour cells with buffer gas for miniature atomic clock*, Proc. of the European Frequency and Time Forum (EFTF), Noordwijk (Netherlands), 13-16 April (2010), pp. 1-6.
- [65] D. MILETIC, C. AFFOLDERBACH, G. MILETI, M. HASEGAWA and C. GORECKI, *Light Shift in CPT Based Cs Miniature Atomic Clocks*, Proc. of the Joint Meeting of the European Frequency and Time Forum (EFTF) and the IEEE International Frequency Control Symposium (FCS), San Francisco (USA), May 2-5 (2011), pp. 200-202.
- [66] D. MILETIC, T. BANDI, C. AFFOLDERBACH and G. MILETI, *Light shift of double resonance and coherent population trapping in wall-coated cells for compact Rb clocks*, Proc. of the Joint Meeting of the European Frequency and Time Forum (EFTF) and the IEEE International Frequency Control Symposium (FCS), San Francisco (USA), May 2-5 (2011), pp. 203-205.
- [67] F. GRUET, L. BIMBOES, D. MILETIC, C. AFFOLDERBACH, G. MILETI, A. AL-SAMANEH, D. WAHL and R. MICHALZIK, *Spectral characterization of VCSELs emitting at 894.6 nm for CPT-based miniature atomic clocks*, Proc. of the European Conference on Lasers and Electro-Optics and the XIIth European Quantum Electronics Conference (CLEO/Europe-EQEC), Munich (Germany), 22-26 May (2011), pp. 1-1.
- [68] T. BANDI, M. PELLATON, D. MILETIC, C. AFFOLDERBACH, F. GRUET, R. MATTHEY and G. MILETI, *Double-resonance in alkali vapor cells for high performance and miniature atomic clocks*, Proc. of the IEEE International Frequency Control Symposium (IFCS), Baltimore (USA), May 21-24 (2012).

- [69] C. AFFOLDERBACH, F. GRUET, D. MILETIC and G. MILETI, *Optimizing a High-Stability CW Laser Pumped Rubidium Gas-Cell Frequency Standard*, Poster at the 7th Symposium on Frequency Standards and Metrology, Pacific Grove (USA), October 05-11 (2008).
- [70] D. MILETIC, C. AFFOLDERBACH, F. GRUET, M. DURRENBERGER and G. MILETI, *Progress on the optimization of a compact laser-pumped Rubidium frequency standard*, Poster at European Frequency and Time Forum & International Frequency Control Symposium (EFTF-IFCS), Besançon (France), April 20 – 24 (2009).
- [71] D. MILETIC, M. PELLATON, C. AFFOLDERBACH, E. BRESCHI, Y. PETREMAND, C. SCHORI, N. F. DE ROOIJ and G. MILETI, *CPT spectroscopy on miniature rubidium vapor cells*, Poster at the Annual Meeting of the Austrian Physical Society, Poster at Swiss Physical Society and Austrian Society of Astronomy and Astrophysics (SPS), Innsbruck (Austria) September 2-4 (2009).
- [72] D. MILETIC, C. AFFOLDERBACH and G. MILETI, *AC Stark shift and temperature shift in laser pumped Rubidium frequency standard*, Poster at the Annual Meeting of the Austrian Physical Society, Swiss Physical Society and Austrian Society of Astronomy and Astrophysics (SPS), Innsbruck (Austria) September 2-4 (2009).
- [73] D. MILETIC, C. AFFOLDERBACH and G. MILETI, *Spectroscopy of micro-fabricated Cs vapor cells for a miniature atomic clock*, Poster at Sixteenth International School on Quantum Electronics (ISQE), Nesebar (Bulgaria), September 20-24 (2010).
- [74] D. MILETIC, T. BANDI, C. AFFOLDERBACH and G. MILETI, *Double-resonance (DR) and Coherent Population Trapping (CPT) in wall-coated cells for compact Rb atomic clocks*, Poster at III International Schools and Conference on Photonics, Belgrade (Serbia), August 29 - September 2 (2011).
- [75] R. BOUDOT, D. MILETIC, P. DZIUBAN, M. HASEGAWA, P. KNAPKIEWICZ, J. DZIUBAN, C. AFFOLDERBACH, G. MILETI, V. GIORDANO and C. GORECKI, *Cs collisional frequency shift measurements in microcells filled with a Ne-Ar buffer gas mixture*, Poster at the Joint Meeting of the European Frequency and Time Forum (EFTF) and the IEEE International Frequency Control Symposium (FCS), San Francisco (USA), May 2-5 (2011).
- [76] D. MILETIC, T. BANDI, C. AFFOLDERBACH and G. MILETI, *Double-resonance (DR) and Coherent Population Trapping (CPT) in wall-coated cells for compact Rb atomic clocks*, Poster at the 43rd Congress of the European Group on Atomic Systems (EGAS), Fribourg (Switzerland), June 28 –July 2 (2011).

Chapter 1

Gas-cell atomic clocks

In this chapter the operational principle of the gas-cell atomic clock and the Double Resonance (DR) and the Coherent Population Trapping (CPT) method are described. A short summary on Cs and Rb atom is presented. The description of the laser linear and saturated absorption obtained from an evacuated and buffer gas Cs cell is given. The main systematic shifts in gas-cell atomic clocks are listed. The introduction on the Allan deviation, a measure of the clock frequency stability, concludes the chapter.

1.1 Operating principle of a gas-cell atomic clock

A quartz crystal oscillator with frequency stabilized to an atomic transition provides the timekeeping signal of a vapor-cell atomic clock. The frequency of a free-running quartz crystal oscillator is influenced by a number of environmental factors like temperature, vibration, etc. In order to stabilize this frequency, specified ground-state transitions in alkali atoms (Cs, Rb) are used to transfer the stability of the atomic structure to the quartz frequency. The selected transition is typically a transition between the two hyperfine ground-state levels in Rubidium (Rb) or Cesium (Cs). Their ground-state hyperfine frequency in the microwave region can be synthesized by frequency multiplication and mixing from available quartz oscillators in the radiofrequency domain, acting as local oscillator (LO).

Figure 1-1 shows the simplified level models in alkali atoms. The ground state of an alkali atom ($^2S_{1/2}$) is split into two hyperfine levels by magnetic-dipole interaction between the single valence electron and the nucleus. Energy levels are labeled by the total-angular momentum quantum number F equal to the sum or difference of the total nuclear angular momentum I and the total angular momentum of the outer electron $J=S+L$. In the case of the ground-state levels, the total orbital angular momentum is $L=0$, so the ground-state levels depend only on the spin angular momentum S and the total nuclear angular momentum I . When a magnetic field is applied to the alkali atom each hyperfine level is further split into Zeeman sublevels, characterized by magnetic quantum numbers m_F . The $m_F=0$ levels are unaffected in first-order by the magnetic

field, qualifying the $m_F=0$ - $m_F=0$ transition as the one to be used for the quartz oscillator stabilization. This transition is often referred to as the “clock transition”.

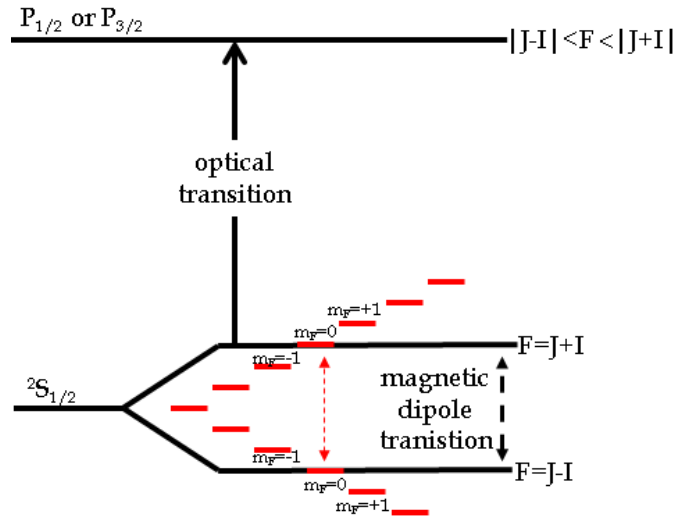


Figure 1-1: Energy level scheme of the atomic transition in alkali atoms. Black solid arrow indicates the optical D transitions. Dashed arrow indicates the magnetic dipole transitions. The Zeeman levels of the ground states are shown as red lines (for example $I=5/2$, splittings not to scale). The Zeeman splitting of the excited states are not shown. The red dashed arrow indicates the “clock transition”.

The electronic energy levels are generally represented by the notation $^{2S+1}X_{L+S}$, where X designates the total orbital angular momentum by a capital letter, where S stands for $L=0$, P for $L=1$, D for $L=2$, etc. In alkali atoms with $L=0$ the ground-state level is represented by $^2S_{1/2}$. The states with $L=1$ are represented by $^2P_{1/2}$ and $^2P_{3/2}$, split by the spin-orbit interaction and labeled by the total-angular momentum F . The transitions between ground-state levels and the electronically excited P levels are two spectral lines called $D1$ ($^2S_{1/2} \rightarrow P_{1/2}$) and $D2$ ($^2S_{1/2} \rightarrow P_{3/2}$) lines. The optical transitions are produced by electric-dipole interaction, applying a suitable light field to the atoms in the ground-state energy levels. The transitions between the hyperfine ground-state levels are realized through a magnetic-dipole interaction by applying a microwave field.

A gas-cell atomic clock, where the atoms are contained in a vapor cell, can be realized using two different preparation principles: Double Resonance (DR) or Coherent Population Trapping (CPT). The DR principle of a gas-cell atomic clock [1] is shown in Figure 1-2.

In DR two fields are applied on atoms: microwave and optical. The microwave field is resonant at the ground-state hyperfine frequency of the alkali atom causing the transfer of the atoms from one to the other ground-state level.

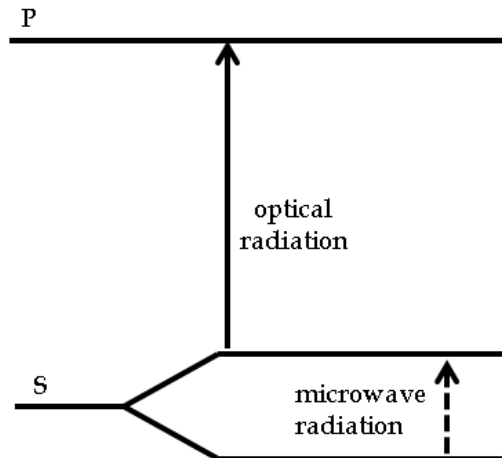


Figure 1-2: Energy level scheme of the atomic transition in an alkali atom, for the DR case. Solid and dashed arrows indicate the optical and microwave radiation, respectively. The Zeeman splitting of the ground and excited states is not shown.

Optical detection of the resonant microwaves is possible when there is a population imbalance between the two levels that allows the applied microwave field to change the population of the two ground states. At the operation temperature of atomic clocks the two ground state levels are almost equally populated and therefore no difference in optical light absorption would be detected. The imbalance between the two ground-state levels population is created by optical pumping [2], produced by using an optical light field, acting selectively on one of the ground-states level only, which creates a non-thermal population distribution among energy levels. The laser field excites the atoms from one of the ground-state levels. Decay from the excited state repopulates both ground-state levels, but the atoms are re-pumped from the selected ground-state level. After several cycles, a population imbalance is created ($\tau_{\text{decay}} \sim \text{ns}$ [3]). If the resonant laser light field and microwave radiation are applied simultaneously the transmitted laser light through the vapor cell is decreased and this decrease in the transmission (i.e. increase in the absorption) is measured. Adding the buffer gas in the cell improves the efficiency of the optical pumping by impairing the diffusion of alkali atoms to the cell walls (the interaction of alkali atoms with the cell walls leads to depolarization of the atomic state).

Figure 1-3 shows the microwave-optical DR gas-cell atomic clock scheme. The optical pumping is done by using a discharge lamp or a laser stabilized at the frequencies of the specific transition in alkali atoms (e.g. 795 and 780 nm for D1 and D2 ^{87}Rb line and 895 or 852 nm for ^{133}Cs D1 and D2 line, respectively). The DR signal is detected by a photodetector (PD) as a decrease in the pump light level transmitted through the vapor cell. This absorption signal is used to stabilize the quartz local

oscillator (LO) frequency in a feedback loop. The microwave synthesizer feeds the microwave cavity with the magnetic microwave field resonant with the clock frequency. The microwave synthesizer is referenced to the LO that oscillates usually at 5, 10 or 100 MHz providing the clock signal output.

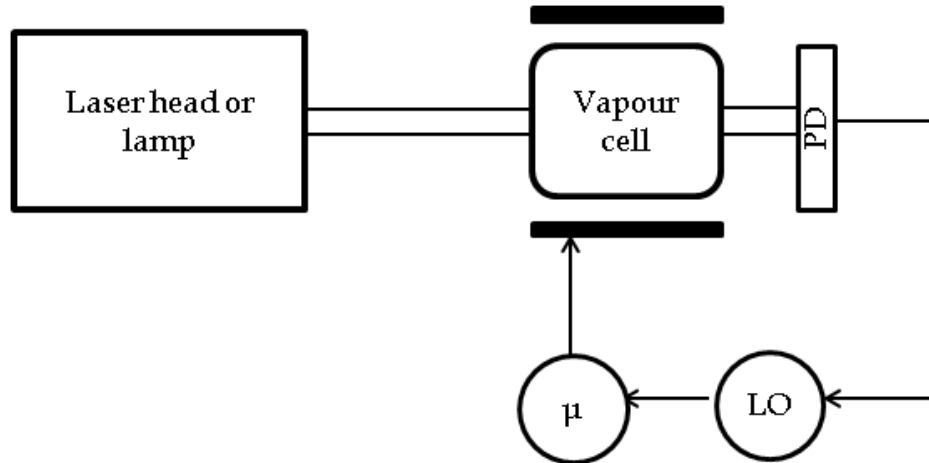


Figure 1-3: DR clock scheme. PD is the photodetector detecting the DR signal. LO is quartz local oscillator and μ is microwave source. The vapor cell is placed in the microwave resonator, represented by the two solid lines).

Today's commercially available DR Rb atomic clocks are used in radio, video and mobile communications [4, 6], satellite navigation and communication [7, 8]. The best high-performance Rb DR atomic clocks are used in the space segment of satellite navigation and positioning systems (GNSS: GPS, Galileo and GLONASS) [4, 9].

An alternative technique proposed for the replacement of the DR technique is known as the Coherent Population Trapping (CPT) technique, shown in the Figure 1-4 [10]. Here, two ground-state atomic levels are coupled to a common excited state, using two coherent electromagnetic fields in the so-called Λ -scheme. When the Raman resonance condition is satisfied (Raman detuning is zero $\delta_R = \nu_1 - \nu_2 - \nu_{hfs} = 0$), destructive quantum interference occurs and the atoms are trapped in a coherent superposition of the ground-states (the "dark state"), which is the non-absorbing state (see Chapter 2).

In the realization of a CPT experiments the two coherent electromagnetic fields can be produced from two phase-locked diode lasers [11], or by external modulation of one diode laser [12], or direct modulation of the diode laser injection current [13, 14].

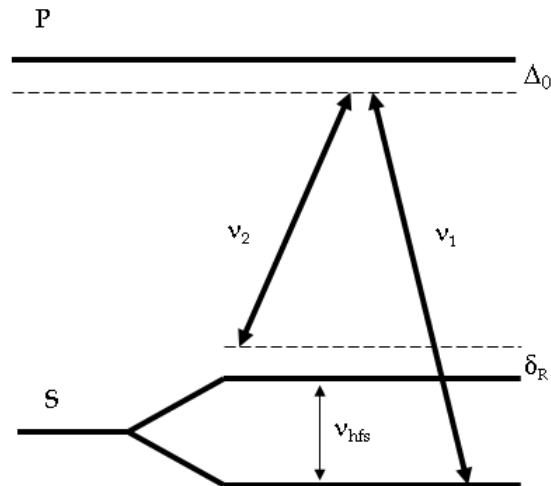


Figure 1-4: Principal interaction scheme in an alkali atom for the CPT case. Solid arrows indicate the optical light field frequencies ν_1 and ν_2 . Δ_0 is the optical detuning and δ_R is Raman detuning. The Zeeman sublevels of the ground and excited states are not shown. ν_{hfs} is the frequency of the ground-state hyperfine splitting in alkali atom.

The frequency of the laser carrier is modulated creating the optical light fields with sidebands, usually separated by the frequency equal to the ground-state hyperfine splitting frequency in alkali atom or half of this value (typically in range from 1.5 GHz to 10 GHz), see Figure 1-5. If the frequency of the laser modulation is equal to the frequency of the ground-state hyperfine splitting in the irradiated alkali atom (ν_{hfs}), the carrier and one of the first-order sideband are used to create CPT (Figure 1-5 Left). If the frequency of the modulation matches to half of the frequency of the ground-state hyperfine splitting in the alkali atom ($\nu_{\text{hfs}}/2$), CPT is created by the two first-order sidebands (Figure 1-5 right).

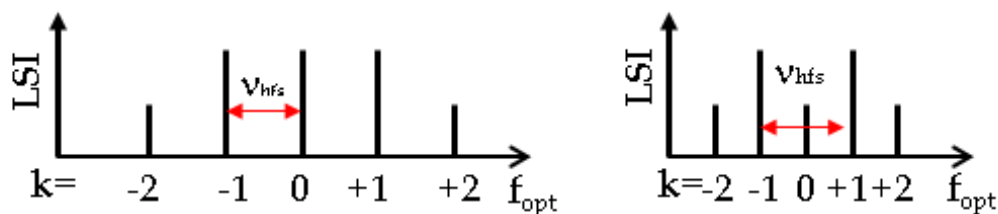


Figure 1-5: Modulated laser spectrum. LSI represents the laser sideband intensity and f_{opt} is optical frequency. k represents the laser sideband order. Red arrow represents the frequency of the ground-state hyperfine splitting in alkali atom ν_{hfs} . Left: Laser modulation frequency is equal to Δ_{hfs} . Right: Laser modulation frequency is equal to $\nu_{\text{hfs}}/2$.

In Figure 1-6 the block scheme of the CPT atomic clock with external laser modulation is shown. Here the CPT resonance is prepared using a diode laser, whose frequency is modulated using an Electro-Optical Modulator (EOM). The microwave frequency,

provided by the microwave synthesizer (marked as μ in the Figure 1-6) is referenced to a local oscillator (LO). The CPT signal is detected by a photodetector (PD) and used to stabilize the LO.¹

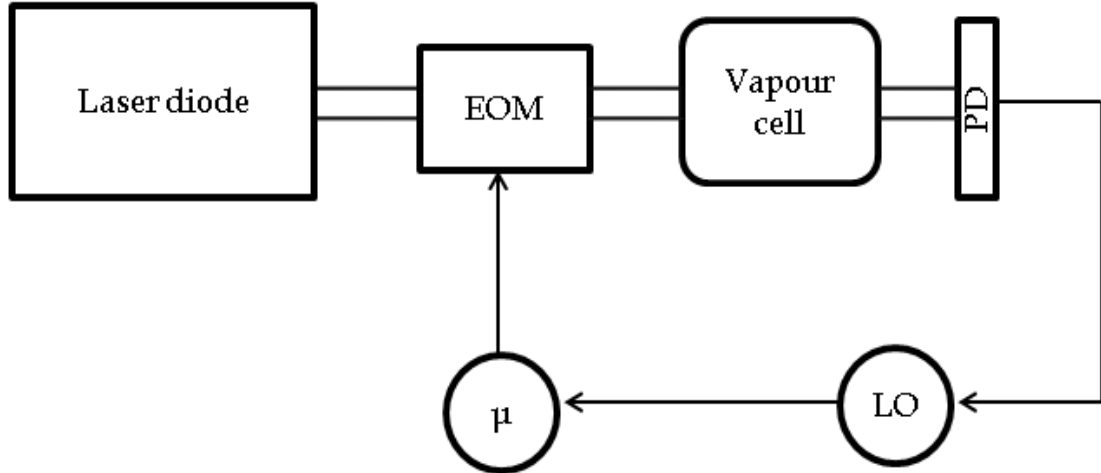


Figure 1-6: CPT clock scheme. EOM is Electro Optical Modulator used to modulate the laser frequency. PD is photodetector detecting the DR signal. LO is the quartz local oscillator and μ is the microwave source.

Reported existing CPT atomic clocks are [15-19]. NIST group realized the first miniature CPT clock prototype in 2001 [20]. Nowadays, commercial miniature CPT clocks are devised by Symmetricom (Chip Scale Atomic Clock - CSAC) [5], for use in underwater sensors for seismic research, gas and oil exploration or military systems.

In both DR and CPT cases, it is necessary to modulate the microwave frequency in order to use phase-sensitive lock-in detection. In this way, signal-to-noise ratio of the clock signal is increased and the produced error signal is used to stabilize the quartz LO frequency.

¹ In this work, the microwave frequencies refers to 6.834 GHz in the case of ⁸⁷Rb atoms and 9.192 GHz in the case of Cs atoms; LO refers to the quartz.

1.2 Cs and Rb atoms

Gas-cell atomic clocks use atomic transitions in Cs or Rb atoms to stabilize the quartz frequency. The use of these two atoms is associated with several advantages: even though their hyperfine frequency is relatively high (low GHz range) it can be synthesized from existing quartz oscillators, their temperature of operation (melting point < 313 K, allowing high density of alkali vapor for relatively low vapor cell temperatures of Tc~323 to 333 K) and available lasers diodes on these wavelengths. The widespread use of Rb clocks with fluorescent lamp excitation is due to the fact that Rb has two abundant isotopes with partly overlapping hyperfine lines that can be used to filter the lamp light in order to obtain hyperfine optical pumping. Table 1-1 lists some of the important data of these elements:

Alkali metal	Cesium (Cs)	Rubidium (Rb)	
Isotopes present in the nature	¹³³ Cs	⁸⁷ Rb	⁸⁵ Rb
Relative natural abundance (%)	100	27.83	72.17
Atomic number	55	37	37
Melting temperature (K)	301.5	312.30	312.30
Boiling temperature (K)	671	688	688
Specific heat capacity (J/g*K)	0.242	0.363	0.363
Molar heat capacity (J/mol*K)	32.210	31.060	31.060
Vapor pressure at 298 K (Torr)	1.488 (74) × 10 ⁻⁶	3.92 (20) × 10 ⁻⁷	3.92 (20) × 10 ⁻⁷
Density at 298 K (g/cm ³)	1.93	1.53	1.53
Nuclear spin	7/2	3/2	5/2

Table 1-1: Basic data of Cs and Rb atom [21].

The relevant information for the calculation of the DR and CPT signal is the number of atoms per cell cubic centimeter, at the exact cell temperature. Using the ideal gas formula the density number n of the Cs and Rb vapor as function of temperature can be calculated [25]:

$$n = \frac{P_0}{k_B T} e^{-\frac{T_0}{T}} \quad (1.1)$$

where P_0 and T_0 are the reference pressure and temperature, respectively. Figure 1-7 shows density number n of the Rb and Cs vapor as function of temperature:

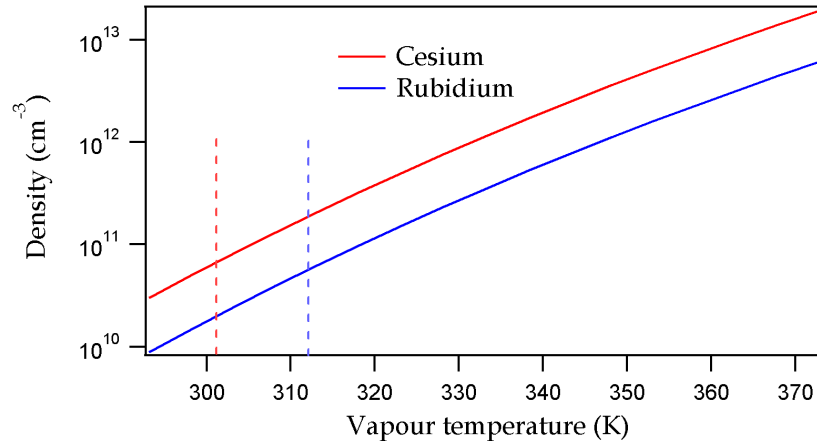


Figure 1-7: Densities of the Rb and Cs vapor as function of temperature are labeled with blue and red solid lines, respectively. Red and blue dashed lines indicate the respective melting temperatures. References for P_0 and T_0 for liquid and solid state of Cs and Rb are taken from [23].

The energy levels for the Cs and Rb atoms, D1 and D2 lines are shown in Figure 1-8 and Figure 1-9:

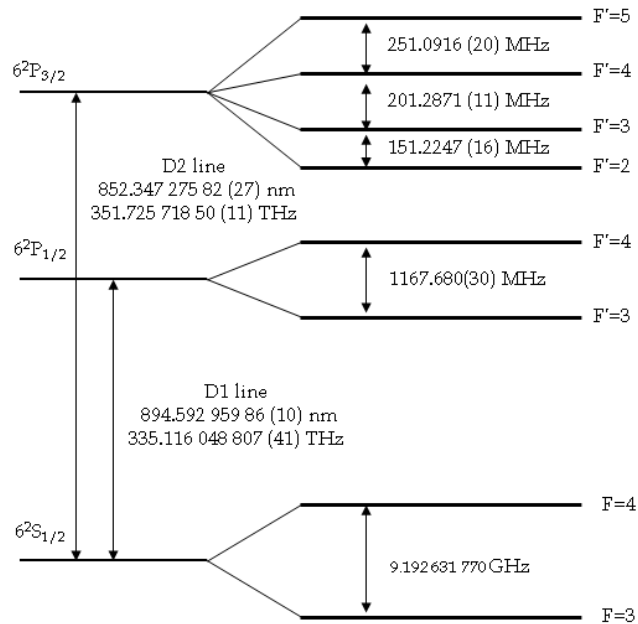


Figure 1-8: Energy levels of the ^{133}Cs atom, nuclear spin quantum number $I=7/2$, involved in the D line transitions. Energy splitting is not drawn to scale. Figure was taken from [21] and numerical values are cited according to references given in [21, 22].

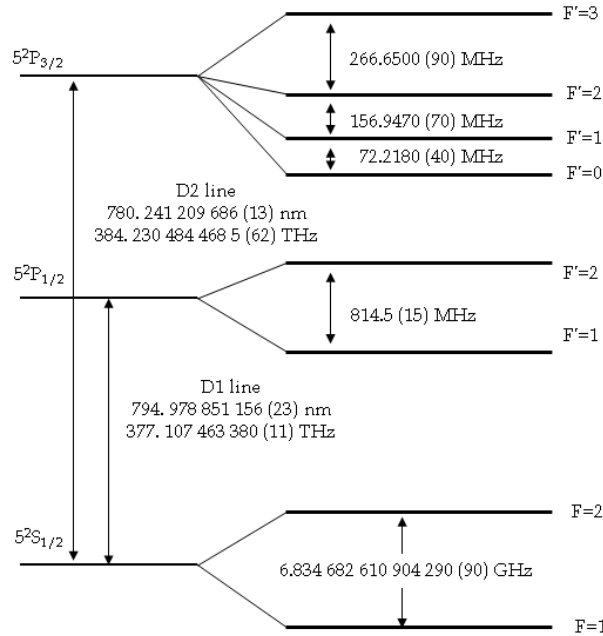


Figure 1-9: Energy levels of the ^{87}Rb atom, nuclear spin quantum number $I=3/2$, involved in the D line transitions. Energy splitting is not drawn to scale. Figure was taken from [21] and numerical values are cited according to references given in [21, 22].

1.3 Linear and saturated absorption in a Cs and Rb vapor cell

In the interaction between a laser light field and atomic vapor the atoms may absorb photons. The resulting absorption spectrum reveals the atomic energy structure of the atom and the optical density of the atoms in the sample. The relative intensity of the transmitted light varies exponentially to the vapor density and the path length of the light through the atomic vapor, which can be determined by the Beer-Lambert law. This law says that the intensity decays exponentially with the distance travelled through the sample (until optical saturation condition is reached):

$$I_1 = I_0 e^{-\alpha L} \quad (1.2)$$

I_1 and I_0 are the transmitted and incident intensities, respectively. α is the absorption coefficient, which depends on the density of atoms and the absorption cross section of the alkali atom σ , and L is the path length of the light through the atomic vapor.

The simple configuration shown in Figure 1-10 is used to measure a linear absorption spectrum. The cell contains the Cs or Rb atomic vapor and the laser frequency is scanned through the optical resonances of the atoms.

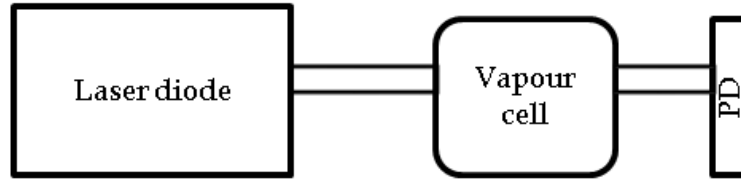


Figure 1-10: Basic setup for absorption spectroscopy.

The absorption process is described by an absorption rate γ [rad/s], giving the probability per unit time for the atom to absorb the laser photon:

$$\gamma = \int \frac{I(\nu_L)}{h\nu_L} \sigma_i(\nu) d\nu \quad (1.3)$$

In (1.3) $I(\nu_L)$ is the incident laser intensity, h is the Planck's constant, ν_L is the laser light frequency and $\sigma_i(\nu)$ is the effective absorption cross section of the alkali atom for the transition under consideration. The line shape of the absorption can be expressed with the Lorentzian function:

$$g(\nu_L) = \frac{1}{4(\nu_L - \nu_0)^2/\Gamma^2 + 1}, \quad (1.4)$$

where Γ is the natural linewidth of the transition $\Gamma = \gamma/\pi$ (Hz), also known as full width at the half maximum (FWHM), ν_L is the laser frequency and ν_0 is the resonant frequency.

Figure 1-11 shows a simple linear absorption spectrum across the Cs D1 line. The four peaks represent the transitions of the atoms from the ground states $F=3$ and $F=4$ to excited states $F'=3$ and $F'=4$. Each peak represents a Gaussian curve due to thermal motion of individual atoms in the gas. Different atom velocities result in the cumulative effect that causes absorption in a wider spectrum than just the natural width. This effect is known as Doppler broadening [24]. The Doppler widths, which depend on the cell temperature (~ 500 MHz [25], see 2.2.3) limits the resolution of optical spectroscopy, e.g. D2 line of Cs and Rb (see section 2.2.3). Table 1-2 shows the natural and Doppler widths of D1 and D2 lines of Cs and ^{87}Rb atoms.

Atom	Cs		⁸⁷ Rb	
Transition	D1	D2	D1	D2
Natural width (MHz)	$2\pi*4.575(12)$	$2\pi*5.234(13)$	$2\pi*5.7500(56)$	$2\pi*6.0666(18)$
Doppler width (MHz)	390	410	530	538

Table 1-2: Natural and Doppler widths of D1 and D2 lines of Cs and ⁸⁷Rb atoms [21]. Doppler widths are calculated for the Cs vapor cell temperature of T=353 K and Rb vapor cell temperature of T=333 K.

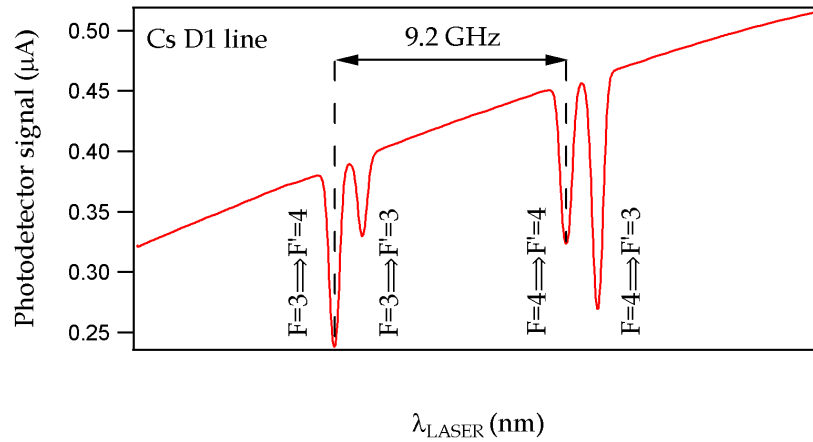


Figure 1-11: Linear absorption spectrum obtained with the light field scanned over the Cs D1 line showing an absorption in the 25 mm long and 26 mm diameter glass-blown evacuated cell at room temperature. Laser frequency is varied by the laser current variation. Sloping background is present due to the laser frequency scan obtained by injecting the laser current.

The frequency ν_0 of the absorption line of an atom moving with a velocity \vec{v} with respect to a laser beam with wave vector \vec{k} is Doppler shifted by an amount:

$$\delta\nu_D = \vec{k} \cdot \vec{v} = v \frac{\nu_0}{c} \quad (1.5)$$

Laser saturated absorption spectroscopy [26-28] allows to overcome the Doppler broadening and to observe the hyperfine splitting of the excited states even when they overlap due to the Doppler broadening, e.g. D2 line of Cs and Rb atoms. The pump and probe laser beams, having the same frequency but different intensities, are shining from opposite directions ($\vec{k}_{probe} = -\vec{k}_{pump}$) through the atomic medium in a vapor cell, interacting with different velocity classes of atoms. The probe beam will be shifted by a Doppler shift ($\vec{k}_{probe} \cdot \vec{v}$) when interacting with an atom of a given velocity \vec{v} , while the pump beam will be shifted by a Doppler shift of the same magnitude but of opposite sign ($-\vec{k}_{pump} \cdot \vec{v}$). Only for $|\vec{k}_{probe}| = |\vec{k}_{pump}|$, the two laser beams will interact with the same velocity class of atoms observing the spectral linewidth its natural width:

$$\vec{k}_{pump} \vec{v} = \vec{k}_{probe} \vec{v} = 0 \quad (1.6)$$

Figure 1-12 shows a setup used for saturated absorption spectroscopy.

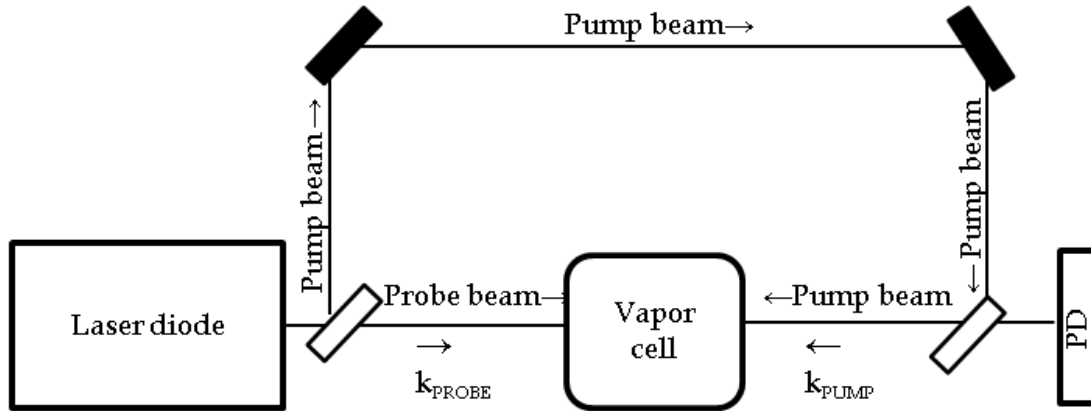


Figure 1-12: Saturated absorption spectroscopy setup.

The observed signal (using the setup described in Figure 1-12) is a Doppler-free profile, the so-called saturated absorption dip (Lamb dip). Figure 1-13 shows the saturated absorption spectrum obtained from the Cs evacuated cell (the same cell was also used in linear absorption spectroscopy setup, see Figure 1-11). The difference in the amplitude of the absorption peaks between Figure 1-11 and Figure 1-13 (a) comes from the different laser intensities used in these two cases (in the case of the Figure 1-11, the laser intensity is three times smaller than in the case of Figure 1-13 (a)). Figure 1-13 (b) gives the zoom on the two absorption peaks, representing the transitions from ground state $F=4$ to excited states $F'=3$ and $F'=4$, in order to highlight the saturated absorption dips (Lamb dips).

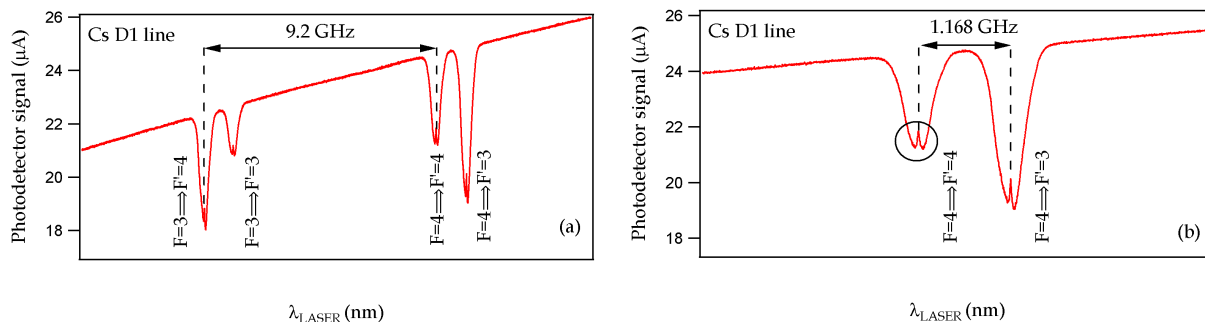


Figure 1-13: (a) Saturated absorption spectrum obtained with the light field scanned over the Cs D1 line showing the absorption in the 25 mm long and 26 mm diameter glass-blown evacuated cell at room temperature. (b) Zoom on two peaks (Lamb dips are more visible) presenting the transitions from ground state $F=4$ to excited states $F'=3$ and $F'=4$.

In order to prevent the collisions of the alkali atoms with the cell window (for DR and CPT), buffer gas atoms and/or molecules are added into a vapor cell containing alkali atoms. Usually, inert gases such as nitrogen, argon or neon are used as buffer gases, because they have small cross sections for alkali atoms ground-state decoherence which means that they affect only weakly the ground-state relaxation of alkali atoms [29]. Buffer gas atoms not only prevent collisions with the glass walls of the vapor cell but also virtually eliminate the Doppler broadening of the microwave transition. However, adding the buffer gas causes a shift and broadening of the ground-state and excited state optical transitions [30]. Optical transitions to electronically excited states are much stronger affected by the buffer gas collisions than the alkali ground state transitions. The excited P state involved in the transitions gets shifted in energy and each of its hyperfine components undergoes additional dephasing, resulting in population redistribution between the respective m_F sublevels and broadening of the optical transitions. Table 1-3 lists the broadening (γ_{buff}) and shifting (σ_{buff}) coefficients [25] for the optical Cs D1 and Rb D1 transition in Ne and Ar buffer gas cells:

Transition	Cs D1 [28]		^{87}Rb D1 [27]	
	Ar	Ne	Ar	Ne
Buffer gas	Ar	Ne	Ar	Ne
Broadening γ_{buff} (MHz/Torr)	19.73	10.12	9.8	3.91
Shift σ_{buff} (MHz/Torr)	-8.69	-2.88	-7.65	-0.41

Table 1-3: Broadening and shift coefficients for the optical Cs D1 and Rb D1 transition in Ne and Ar buffer gas cell [30, 31].

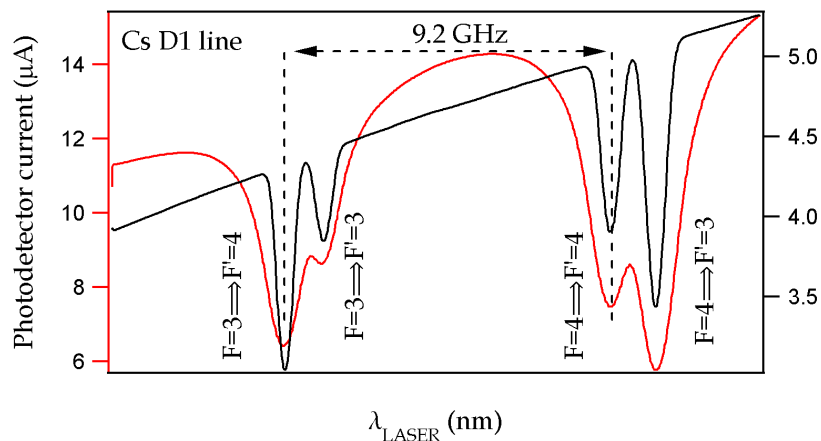


Figure 1-14: The red line represents the linear absorption spectrum obtained with the light field scanned over the Cs D1 line showing the absorption in the 19 mm long and 10 mm diameter glass-blown buffer gas cell with Ar and Ne (total pressure 40 Torr) heated to $T_c=338$ K. The black line shows the linear absorption spectrum obtained with the light field scanned over the Cs D1 line showing an absorption in the 25 mm long and 26 mm diameter glass-blown evacuated cell at room temperature.

Figure 1-14 shows the linear absorption spectrum obtained from the two different Cs vapor cells: evacuated Cs cell at room temperature and Cs cell containing the mixture of the buffer gases Ne and Ar at $T_c=338$ K. The Gaussian fit of the absorption peak representing the $F=4 \rightarrow F'=3$ transition, obtained from the evacuated cell without buffer gas, and the Voigt fit [3] of the same absorption peak obtained from the buffer gas cell allow estimation of the broadening and the shift of the absorption peaks due to the buffer gases: (464 ± 50) MHz and (-155.2 ± 2.2) MHz. Knowing the coefficient for Ne and Ar shifts and broadening of the Cs D1 line [31], it can be estimated that the buffer gas cell contains 8 Torr of Ar and 32 Torr of Ne, giving the Ar-Ne ratio of 1:4.

1.4 Systematic shifts in gas-cell atomic clocks

Gas-cell atomic clocks frequency shifts may be due to various operation parameters, i.e. the buffer gas pressure in the vapor cell, the temperature of the clock cell, the external magnetic field, light shift, etc. Residual variations of these parameters mentioned above contribute to the clock frequency instability. It is therefore critical to carefully stabilize all these parameters and to find a clock operational scheme that minimizes the sensitivity of the clock frequency towards them. The main sources of the gas-cell clock frequency shift are discussed below.

1.4.1 Buffer-gas pressure and temperature shift

With buffer gases in the vapor cell the clock resonance may be shifted by several hundred Hz per Torr, depending on the buffer gas. This pressure shift is the combined effect of several physical interactions. The hyperfine splitting of alkali-metal atoms is modified by the alteration of the valence electron density at the nucleus, when the collision with buffer gas atom occurs [32]. This is a result of the two forces: attractive long-range Van der Waals interactions and repulsive short-range Pauli exclusion forces. Van der Waals interactions decrease the electronic density at the nucleus and therefore reduce the hyperfine splitting. Pauli exclusion forces act in the opposite direction: they increase the electronic density at the nucleus and enhance the splitting. The resulting frequency shift depends on the nature of the gas, its density, and temperature and can be expressed as [33]:

$$\Delta\nu = \nu - \nu_0 = P_0(\beta + \delta(T - T_0) + \gamma(T - T_0)^2), \quad (1.7)$$

where P_0 is the pressure at the reference temperature T_0 ($T_0=(298-431\text{ K})$ [35]), β is the pressure shift coefficient and δ and γ are first- and second-order temperature shift coefficients.

It has been shown that for Cesium atoms the frequency shift is positive with light gases (He, Ne, N₂), where the Pauli exclusion forces are dominant. In the case of the heavy gases (Ar, Kr, Xe) the frequency shift of Cs atoms is negative, mainly due to the Van der Waals interactions [34].

This thesis presents studies on temperature shift of the atomic clock frequency due to buffer gas in the vapor cell. Other related phenomena such as buffer gas variation due to adsorption, permeation [35], reaction with impurities, leakages [36], etc., depend on the cell production processes and they are not studied here.

If the vapor buffer gas cell is placed in atmospheric pressure (no pressure-controlled environment, which is sometimes the case for atomic clocks), buffer gas pressure variations will occur whenever the ambient temperature changes. This effect is known as the barometric effect [37]. Studies given in ref [37] showed that a cm-scale glass-cell clock has a sensitivity of $1.3 \times 10^{-13}/\text{Torr}$ of external pressure. In ref [37] the barometric effect is scaled with respect to cell window dimensions. Therefore it can be estimated that in the case of the microfabricated cell (see section 3.2), the barometric effect is $1.3 \times 10^{-16}/\text{Torr}$.

Absolute shift of the atomic clock frequency due to the buffer gas pressure variation is negligible compared to the total buffer-gas shift, for example (see section 1.4.4, Table 1-4).

1.4.2 Magnetic field shift

A static magnetic field is applied to the atoms to provide the quantization axis and gives rise to the further splitting of the hyperfine atomic levels into Zeeman sublevels, characterized by the quantum number m_F . The Hamiltonian describing the atomic hyperfine structure interaction in the presence of an external magnetic field with flux density \vec{B} is:

$$H_{\text{hfs}} = \frac{h\nu_{\text{hfs}}}{2(I + \frac{1}{2})} \vec{I}\vec{J} + \frac{g'_j \mu_B}{h} \vec{J}\vec{B} + \frac{g'_i \mu_B}{h} \vec{I}\vec{B} \quad (1.8)$$

In the case of total electronic angular momentum quantum number $J = \frac{1}{2}$ the energy splitting of the ground-state magnetic sublevels is given by the Breit-Rabi formula:

$$\nu_{m_F} = -\frac{\nu_{\text{hfs}}}{2(2I + 1)} + \frac{g'_i m_F \mu_B}{h} B \pm \frac{\nu_{\text{hfs}}}{2} \sqrt{1 + \left(\frac{4m_F}{2I + 1} x\right) + x^2}, \quad (1.9)$$

where $x = (\mu_B/h\nu_{\text{hfs}})B(g'_j - g'_i)$, B magnetic flux density, ν_{hfs} is the hyperfine ground-state splitting frequency, g'_j and g'_i fine structure Landé and nuclear g' -factors and μ_B Bohr magneton. The $m_F=0$ sublevels are shifted only quadratically causing a shift of the hyperfine frequency according to the equation [22]:

$$\Delta\nu = K_0 B_0^2, \quad (1.10)$$

where B_0 is the magnetic induction in Tesla and $K_0=427.45 \times 10^8 \text{ HzT}^{-2}$ for Cs and $K_0=575.14 \times 10^8 \text{ HzT}^{-2}$ for ^{87}Rb .

1.4.3 Light shift (AC-Stark shift)

Besides pressure, temperature and magnetic shift, the light shift (LS) is one of the biggest contributors to the atomic-clock instability. The LS is the shift of atomic energy levels due to the interaction of the induced atomic dipole moment with the oscillating electric field of the light and can be approximated by a dispersive Lorentzian as function of a light field detuning and light field intensity [38].

$$\delta\nu_i(\nu_L, I) = \frac{1}{4} |g_R|^2 \frac{\nu_L - \nu_0}{(\nu_L - \nu_0)^2 + \Gamma^2/4} \quad (1.11)$$

It depends on the laser intensity $I \sim |g_R|^2$, where g_R is optical Rabi frequency, ν_L is the laser frequency, ν_0 is the resonant frequency and Γ is the width of the optical transition to the excited state. A more detailed analysis of the LS will be given in Chapter 2.

1.4.4 Summary of typical shifts in gas-cell atomic clocks

Typical absolute shifts of buffer gas vapor-cell clock frequency due to different clock parameter variations, e.g., light field, magnetic field, vapor cell temperature are listed in Table 1-4:

Physical effect	Coefficient	Typical value	Absolute shift
Buffer gas pressure	$\sim 10^2\text{-}10^3$ Hz/Torr	30-100 Torr	$\sim 10^3\text{-}10^4$ Hz
Magnetic field	$\sim 500 \times 10^8$ Hz/T ²	1-5 μ T	< 1 Hz
Intensity LS	$\sim 10^{-12}$ cm ² / μ W	10-90 μ W/ cm ²	< 0.1 Hz
Frequency LS	$\sim 10^2$ mHz/MHz	100 kHz	< 0.1 Hz
Buffer gas cell temperature	~ 0.5 Hz/Torr*K	30-100 Torr	$\sim 15\text{-}50$ Hz/K

Table 1-4: Typical absolute shifts of the gas-cell clock frequency, estimated for the typical clock operating conditions.

The light field, the vapor cells temperature, etc., will not only shift the clock frequency. The small fluctuation of these parameters will also influence the clock frequency stability. The typical stabilized laser intensity and frequency variations are \sim few 10^{-4} and \sim few 10^{-10} for $\tau=10$ 000s, respectively, which contribute to the clock frequency stability on the level of $\sim 10^{-11}\text{-}10^{-12}$. The typical buffer gas mixture cell temperature variation is \sim tens mK for $\tau=10$ 000s which influences the clock frequency stability on the $\sim 10^{-12}\text{-}10^{-13}$ level. The typical buffer gas pressure variation due to barometric effect is $\sim 1.3 \times 10^{-13}$ and $\sim 1.3 \times 10^{-16}$, for the cm-scale glass cell and the microfabricated cell, respectively (see section 1.4.1). The barometric effect is negligible in the atomic clock short-term frequency stability. In the case of the atomic clock long-term stability the influence of the buffer gas pressure variation due to barometric effect (for a typical one-month atmospheric pressure variation of 50 Torr) is $\sim 6.5 \times 10^{-13}$ and $\sim 6.5 \times 10^{-16}$, for the cm-scale glass cell and the microfabricated cell, respectively. Buffer gas variations due to alkali atom permeation through the walls of glass-blown alkali vapor cells and due to the leak are typically 1.5×10^{-13} mbar 1/s [35] and 2×10^{-9} mbar 1/s [36], respectively.

The studies performed in this thesis focused on:

- Evaluation of the intensity and frequency LS and temperature shift in a vapor-cell atomic clock (Chapter 4) and proposition of mechanisms which will minimize these shifts.

- Evaluation of the laser intensity, laser frequency and vapor cell temperature variations and their impacts to the clock frequency instabilities (Chapter 5)

1.5 Atomic clock frequency stability

The Allan variance $\sigma_y^2(\tau)$ is a measure of clock frequency stability. An example of the signal used for the Allan variance calculation is shown in Figure 1-15:

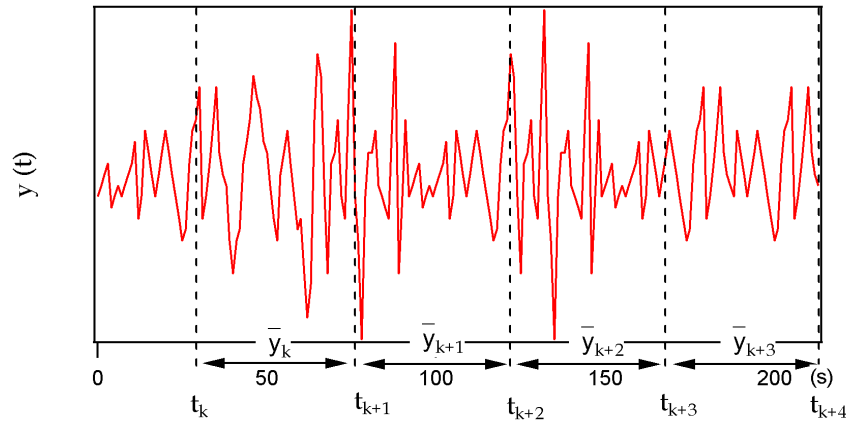


Figure 1-15: Example of a signal used for the calculation of the Allan variance. $y(t)$ is signal measured value, the x-axis represents the measurement time.

The \bar{y}_k represents the average signal $y(t)$ value in the time interval $[t_k, t_{k+1}]$, where the average time for each average is $\tau = t_{k+1} - t_k$:

$$\bar{y}_k = \frac{1}{\tau} \int_{t_k}^{t_{k+1}} y(t) dt \quad (1.12)$$

The Allan variance is defined as one half of the square of the time average of the difference between successive readings of \bar{y}_k (deviation of $y(t)$ averaged over the sampling period):

$$\sigma_y^2(\tau) = \frac{1}{2} \langle (\bar{y}_{k+1,\tau} - \bar{y}_{k,\tau})^2 \rangle = \frac{1}{2} \lim_{n \rightarrow \infty} \left\{ \frac{1}{n} \sum_{k=1}^n (\bar{y}_{k+1,\tau} - \bar{y}_{k,\tau})^2 \right\} \quad (1.13)$$

The Allan variance can also be expressed through the power spectral density $S_y(f)$ of $y(t)$ [39]:

$$\sigma_y^2(\tau) = \int_0^{\infty} S_y(f) |H(f)|^2 df, \quad (1.14)$$

where $H(f)$ is the transfer function of the detector detecting the clock signal. The noise spectrum $S_y(f)$ can be expressed as a sum of different type of noises with a frequency dependence f^α :

$$S_y(f) = \sum_{\alpha=-2}^2 h_\alpha f^\alpha \quad (1.15)$$

The coefficient α determines the type of the noise dominating in the measurements, e.g. $\alpha=0$ correspond to the white frequency noise. The experimentally measured value is the Allan deviation $\sigma_y(\tau)$, which is a square root of Allan variance.

Table 1-5 reviews the values of different coefficients, their impact as function of sampling time and indicates the name of the various processes [40].

α	$\sigma_y(\tau)$	Type of noise
2	$\sim \tau^{-1}$	White PM
1	$\sim \tau^{-1}$	Flicker PM
0	$\sim \tau^{-1/2}$	White FM
-1	$\sim \tau^0$	Flicker FM
-2	$\sim \tau^{1/2}$	Frequency random walk
-2	$\sim \tau^1$	Frequency drift

Table 1-5: α values for different types of noise: evaluation of the influence to the Allan variance for each value of alpha. FM corresponds to the Frequency Modulation and PM to the Phase Modulation.

An example of the typical Allan deviation as function of sampling time τ is given in Figure 1-16, including typical types of the noise dominating for specific regions of τ . The

graph shows that the white frequency noise typically dominates clock short-term frequency stability and that is limited by, so called, Flicker phase modulation noise. The clock frequency drift due to various clock intrinsic parameters usually determines long-term clock frequency stability.

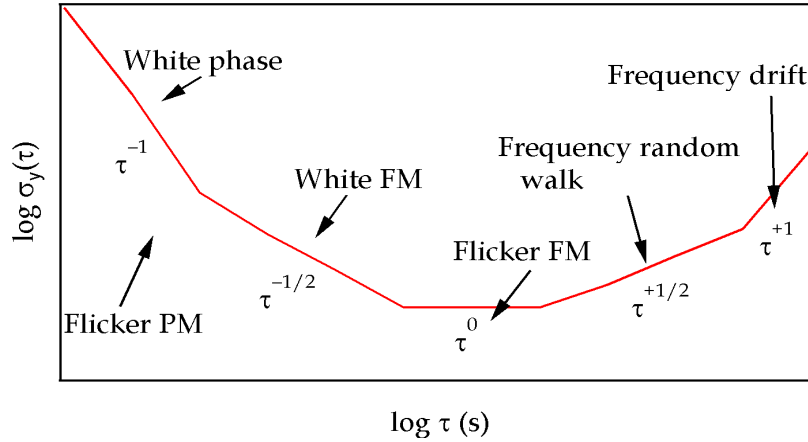


Figure 1-16: Example of the Allan deviation graph in double-logarithmic scale.

The Allan deviation can also be estimated as function of $\tau^{-1/2}$ (only in the case of white FM noise) [40]:

$$\sigma_y(\tau) = \frac{1}{v_0} \frac{N_{\text{PSD}}}{\sqrt{2D}} \sqrt{\frac{1}{\tau}}, \quad (1.16)$$

where N_{PSD} [V/Hz^{1/2}] is the measured noise of the atomic transition detection during one cycle, v_0 [Hz] is the resonant atomic frequency, and D [V/Hz] is the experimental discriminator slope (see Chapter 3) which depends on the signal amplitude A and signal linewidth FWHM: $D \approx A/\text{FWHM}$ (see Chapter 3). By measuring the clock detection noise, knowing the resonant atomic frequency and evaluating the signal discriminator slope it is possible to calculate the expected clock short-term frequency stability. This formula is used in the further text for the prediction of the clock frequency stability.

Main processes studied in this thesis are white noise ($\sigma \sim \tau^{-1/2}$) influencing the clock short-term stability, and clock frequency random walk and drift ($\sigma \sim \tau^1$) influencing the clock medium- and long-term stability. In particular, the focus will be on the evaluation of the LS and temperature shift-effects contributions to the clock short-, medium and long-term frequency stability (Chapter 5).

1.6 Summary and conclusions

The DR and the CPT methods in the standard three level model of alkali atom are described in this chapter. Clock schemes using these methods are depicted. A short summary on Cs and Rb atoms is given, including the equation for the atomic density calculation (1.1), important for the calculation of the DR and CPT signals. This chapter also discusses linear and saturated absorption in a Cs and Rb vapor-cell. Shifts and broadenings of the optical transitions in a buffer gas vapor-cell are explained by comparing the absorption signals obtained from two different cells: the Cs glass-blown vapor cell containing the mixture of the buffer gases Ne and Ar, heated up to $T_c=338$ K and the Cs glass-blown evacuated cell at room temperature. The typical contributions to shifts in gas-cell atomic clocks (pressure, temperature, magnetic and LS) have been evaluated (Table 1-4). The light field, the vapor cell temperature, etc. will not only shift the clock frequency but the small fluctuation of these parameters will also influence the clock frequency stability. The typical stabilized laser intensity and frequency variations are few 10^{-4} and few 10^{-10} for $\tau=10\ 000$ s, respectively, which contributes to the clock frequency stability on the level of 10^{-11} - 10^{-12} . The typical buffer gas mixture cell temperature variation is some of tens mK for $\tau=10\ 000$ s, which influences the clock frequency stability on the $\sim 10^{-12}$ - 10^{-13} level. The introduction of the Allan deviation, a measure of the clock frequency stability, concludes the chapter (important for Chapter 5 where the influence of the light shift and temperature coefficient to the clock frequency stability is evaluated).

REFERENCES:

- [1] J. BROSSEL and A. KASTLER, *La détection de la résonance magnétique des niveaux excités - l'effet de depolarization des radiations de résonance optique et de fluorescence*, Compt. Rend. Hebd. Acad. Sci. 229 (1949), pp. 1213-1215.
- [2] F. BITTER, *The optical detection of radiofrequency resonance*, Phys. Rev. 76 (1949), pp. 833-835.
- [3] G. MILETI, *Etude du pompage optique par laser et par lampe spectrale dans les horloges a vapeur de rubidium*, PhD thesis, Université de Neuchâtel (1995).
- [4] www.spectratime.com; Passive Hydrogen Maser (PHM)

- [5] www.symmetricom.com/; Chip Scale Atomic Clock (CSAC)
- [6] J. A. KUSTERS and C. A. ADAMS, *Performance requirements of communication base station time standards*, RF Design, Vol. May (1999), pp. 28-38.
- [7] H. FRUEHAUF, *Fast "direct-P(Y)" GPS signal acquisition using a special portable clock*, 33rd Annual Precise Time and Time Interval (PTTI) Meeting, Long Beach, CA, USA, (2001), pp. 359-369.
- [8] J. MURPHY and T. SKIDMORE, *A low-cost atomic clock: impact on the national airspace and GNSS availability*, Proc. ION GPS-94; 7th Int. Meet. Satellite Division of the Institute of Navigation, Salt Lake City, UT, USA (1994), pp. 1329-1336.
- [9] P. WALLER, F. GONZALEZ, J. HAHN, S. BIND, R. PIRIZ, I. HIDALGO, G. TOBIAS, I. SESIA, P. TAVELLA and G. CERRETO, *In-orbit performance assessment of GIOVE clocks*, 40th Annual Precise and Time Interval (PTTI) Meeting, (2008), pp. 69-82.
- [10] G. ALZETTA, A. GOZZINI, M. MOI and G. ORRIOLS, *Experimental-method for observation of $r. f.$ transitions and laser beat resonances in oriented Na vapour*, Nuovo Cimento B 36 (1976), pp. 5-20.
- [11] O. SCHMIDT, R. WYNANDS, Z. HUSSEIN and D. MESCHEDÉ, *Steep dispersion and group velocity below $c/3000$ in coherent population trapping*, Phys. Rev. A 53 (1996), pp. 27-30.
- [12] P. R. HEMMER, S. EZEKIEL and C. C. LEIBY, *Stabilization of a microwave-oscillator using a resonance Raman transition in a sodium beam*, Opt. Lett. 8 (1983), pp. 440-442.
- [13] C. AFFOLDERBACH, A. NAGEL, S. KNAPPE, C. JUNG, D. WIEDENMANN and R. WYNANDS, *Nonlinear spectroscopy with a vertical cavity surface-emitting laser (VCSEL)*, Appl. Phys. B Lasers Opt. 70 (2000), pp. 407-413.
- [14] M. STAHLER, R. WYNANDS, S. KNAPPE, J. KITCHING, L. HOLLBERG, A. TAICHENACHEV and V. YUDIN, *Coherent population trapping resonances in thermal Rb-85 vapour: D-1 versus D-2 line excitation*, Opt. Lett. 27 (2002), pp. 1472-1474.
- [15] N. CYR, M. TETU and M. BRETON, *All-Optical Microwave Frequency Standard: A Proposal*, IEEE Trans. Instrum. Meas. 42 (1993), pp. 640-649.
- [16] M. MERIMAA, T. LINDVALL, I. TITTONEN and E. IKONEN, *All-optical atomic clock based on coherent population trapping in ^{85}Rb* , JOSA B 20 (2003), pp. 273-279.

- [17] N. CASTAGNA, R. BOUDOT, S. GUERANDEL, E. DE CLERCQ, N. DIMARCQ and A. CLAIRON, *Investigations on continuous and pulsed interrogation for a CPT atomic clock*, IEEE Trans Ultrason Ferroelectr Freq Control. 56(2) (2009), pp. 246-253.
- [18] R. BOUDOT, P. DZIUBAN, M. HASEGAWA, R. K. CHUTANI, S. GALLIOU, V. GIORDANO and C. GORECKI, *Coherent population trapping resonances in Cs-Ne vapor microcells for miniature clocks applications*, J. Appl. Phys. 109 (2011), pp. 014912-11.
- [19] V. GEORGINOV, S. KNAPPE, P. D. SCHWINDT, L. HOLLBERG and J. KITCHING, *Long-term frequency instability of atomic frequency references based on coherent population trapping and microfabricated vapor cells*, J. Opt. Soc. Am. B 23 (2006), pp. 593-597.
- [20] J. KITCHING, L. HOLLBERG, S. KNAPPE and R. WYNANDS, *Compact atomic clock based on coherent population trapping*, Electron. Lett. 37 (2001), pp. 1449-1451.
- [21] D. A. STECK, *Alkali D line data*, version 2.1.4, <http://steck.us/alkalidata/cesiumnumbers.pdf>, (2010).
- [22] T. UDEM, J. REICHERT, T. W. HANSCH and M. KOUROGI, *Absolute optical frequency measurement of the cesium D2 line*, Phys. Rev. A 62 (2000), pp. 031801-4.
- [23] C. B. ALCOCK, V. P. ITKIN and M. K. HORRIGAN, *Vapor Pressure Equations for the Metallic Elements: 298-2500 K*, Can. Metall. Quart. 23 (1984), pp. 309-313.
- [24] E. N. da C. ANDRADE, *Doppler and the Doppler Effect*, Endeavour Vol. XVIII No. 69 (1959).
- [25] J. VANIER and C. AUDOIN, *The Quantum Physics of Atomic Frequency Standards*, Adam Hilger, Bristol, UK, (1989).
- [26] J. L. HALL and C. BORDE, *Measurement of Methane Hyperfine Structure Using Laser Saturated Absorption*, Phys. Rev. Lett. 30 (1973), pp. 1101-1104.
- [27] T. W. HANSCH, M. D. LEVENSON and A. L. SCHAWLOW, *Complete hyperfine structure of a molecular iodine line*, Phys. Rev. Lett. 26 (1971), pp. 946-949.
- [28] K. M. EVENSON, J. S. WELLS, F. R. PETERSEN, B. L. DANIELSON, G. W. DAY, R. L. BARGER and J. L. HALL, *Speed of Light from Direct Frequency and Wavelength Measurements of the Methane-Stabilized Laser*, Phys. Rev. Lett. 29 (1972), pp. 1346-1349.

- [29] N. BEVERINI, P. MINGUZZI and F. STRUMIA, *Foreign gas induced caesium hyperfine relaxation*, Phys. Rev. A 4 (2) (1971), pp. 550-555.
- [30] N. ALLARD and J. KIELKOPF, *The effect of neutral nonresonant collisions on atomic spectral lines*, Rev. Mod. Phys. 54 (4) (1982), pp. 1103-1182.
- [31] E. BERNABEU and J. M. ALVAREZ, *Shift and broadening of hyperfine components of the first doublet for caesium perturbed by foreign gases*, Phys. Rev. A 22 (1980), pp. 2690-2695.
- [32] W. HAPPER, *Optical pumping*, Rev. Mod. Phys. 44 (2) (1972), pp. 169-249.
- [33] J. VANIER, R. KUNSKI, N. CYR, J. SAVARD and M. TETU, *On hyperfine frequency shifts caused by buffer gases: application to the optically pumped passive rubidium frequency standard*, J. Appl. Phys. 53 (8) (1982), pp. 5387-5391.
- [34] M. ARDITI and T. R. CARVER, *Pressure, Light, and Temperature Shifts in Optical Detection of 0-0 Hyperfine Resonance of Alkali Metals*, Phys. Rev. 124 (3) (1961), pp. 800-809.
- [35] J. CAMPARO, C. M. KLIMCAK, S. J. HERBULOCK, *Frequency equilibration in the vapor-cell atomic clock*, IEEE Trans. Instrum. Meas. 54 (5) (2005), pp. 1873-1880.
- [36] R. STRAESSLE, M. PELLATON, C. AFFOLDERBACH, Y. PETREMAND, D. BRIAND, G. MILETI and N. F. de ROOIJ, *Low-temperature indium-bonded alkali vapor cells for chip-scale atomic clocks*, J. Appl. Phys. 113 (2013), pp. 064501-8.
- [37] W. J. RILEY, *The physics of the environmental sensitivity of rubidium gas cell atomic frequency standards*, IEEE Trans. Ultrason. Ferroelectr. Freq. Control. 39(2) (1992), pp. 441-452.
- [38] J. DENG, *Light shift compensation in a Rb gas cell frequency standard with two-laser pumping*, IEEE Trans. Ultrason. Ferroelectr. Freq. Control 48 (2001), pp. 1657-1661.
- [39] D. W. ALLAN, *Time and Frequency (Time-Domain) Characterization, Estimation, and Prediction of Precision Clocks and Oscillators*, IEEE Trans. Ultrason., Ferroelectr., Freq. Control 34 (1987), pp. 647-654.
- [40] G. MILETI and P. THOMANN, *Study of the S/N performance of passive atomic clocks using a laser pumped vapour*, Proc. of the European Frequency and Time Forum, Besancon (France), (1995), pp. 271-276.

Chapter 2 Coherent Population Trapping theory

This chapter introduces the CPT theory through the simple model of a three-level atom. Equations for the calculation of the CPT signal linewidth and amplitude are given and the main contributors to the CPT signal linewidth are discussed. The theoretical description of the CPT LS for a simple three level model atom is given. The description starts with the simpler picture of LS in the case of monochromatic laser light. Subsequently taking into account the multi-frequency laser spectrum in order to obtain the CPT LS picture extends this description. Then, we introduce the theoretical description of the LS in a CPT gas-cell atomic clock for a four level model atom (Cs D1 and ^{87}Rb D1 lines). Finally, the theory of the temperature-shift effect in two different vapor cells (buffer gas and wall-coated cell) is discussed.

2.1 Three-level models for CPT in Λ systems

The relevant atom-light system for CPT with Λ configuration is depicted in Figure 2-1. In a Λ system, it is assumed that, in first approximation, every light field interacts with one atomic ground-state level, only. If the light field is applied to one transition, e.g. field ν_1 to the transition $|1\rangle \rightarrow |3\rangle$ the atomic population will be optically pumped into state $|2\rangle$ due to spontaneous emission from $|3\rangle$. Atoms in state $|2\rangle$ cannot be excited anymore with the light field and stay trapped in this state (in absence of a second light field ν_2 and in absence of relaxation). Experimentally, this effect will be observed as a reduction of fluorescence signal or an enhancement in the transmission. If a second light field ν_2 is applied, the atoms initially in state $|2\rangle$ will be re-pumped to the excited state $|3\rangle$ and fluorescence and absorption of light fields ν_1 and ν_2 are observed again. If the laser frequencies ν_1 and ν_2 correspond to the transition frequencies of the atom ground-state levels $|1\rangle$ and $|2\rangle$ to the excited state $|3\rangle$ and if the fields have a fixed phase relation (see 2.8), the CPT effect occurs, i.e. absorption reduction of both fields ν_1 and ν_2 is observed.

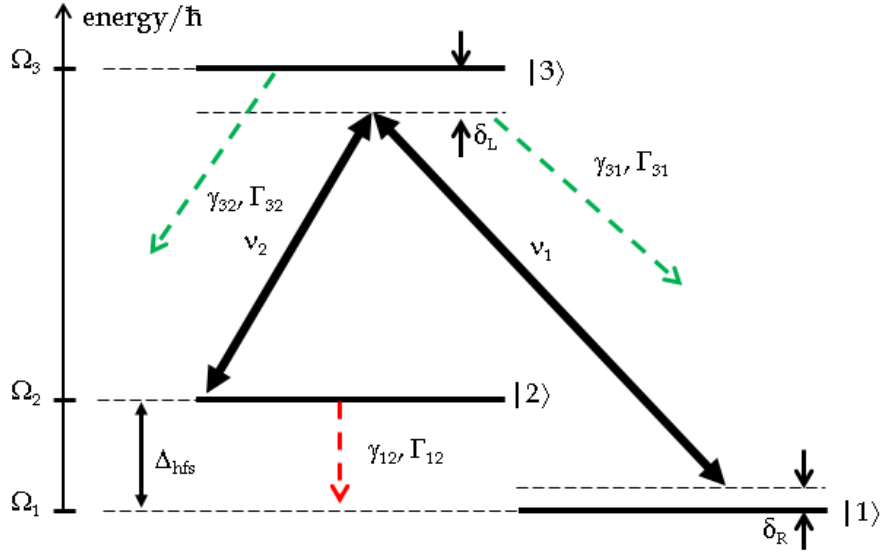


Figure 2-1: Level diagram of the ideal three-level Λ system. $\delta_L = \nu_1 - (\Omega_3 - \Omega_1)$ and $\delta_R = \nu_1 - \nu_2 - \Delta_{\text{hfs}}$ represent the optical and Raman detuning, respectively. $\Omega_{1,2,3}$ are energies of the atomic levels and ν_1 and ν_2 are the laser frequencies. Δ_{hfs} is the frequency of the ground-state hyperfine splitting in the atom. Γ_{31} and Γ_{32} are population decay rates from the excited state $|3\rangle$ to the ground-state levels $|1\rangle$ and $|2\rangle$, respectively. γ_{31} and γ_{32} are the spontaneous emission rates. γ_{12} and Γ_{12} are hyperfine ground-state coherence relaxation and population decay rate, respectively. $\Gamma_i = \gamma_i / \pi$. This notation will be kept throughout the thesis.

A more detailed semi-classical description of CPT is done by treating the light-fields classically and using quantum mechanics to describe the atomic levels shown in Figure 2-1. The light field is composed of two monochromatic light waves and can be expressed as:

$$E = E_1 \cos(\nu_1 t + \varphi_1) + E_2 \cos(\nu_2 t + \varphi_2) \quad (2.1)$$

The Hamiltonian \hat{H} describing the atom-field interaction is composed of two terms: an unperturbed atomic part \hat{H}_0 and a part describing the light-atom interaction in the electric dipole approximation ($\hat{H}_{\text{int}} = -\vec{d}\vec{E}$):

$$\begin{aligned} \hat{H} = \hat{H}_0 + \hat{H}_{\text{int}} = & \sum_i \hbar\Omega_i |i\rangle\langle i| + \frac{\hbar g_1}{2} e^{-i\nu_1 t - i\varphi_1} |3\rangle\langle 1| \\ & + \frac{\hbar g_2}{2} e^{-i\nu_2 t - i\varphi_2} |3\rangle\langle 2| + \text{h. c.}, \end{aligned} \quad (2.2)$$

where $\hbar\Omega_i$ for $i=1, 2$ are the energies of the energy levels and g_i are the Rabi frequencies used to express the interaction strengths; all are assumed to be real (all polarizations and vector properties of the electric dipole operator omitted):

$$g_i = -\frac{\langle 3|e\hat{r}|i\rangle}{\hbar} E_i, \quad i \in \{1,2\} \quad (2.3)$$

Instead of the ground-state levels $|1\rangle$ and $|2\rangle$ it is instructive to consider a new orthogonal basis for the ground-state consisting of the so-called “coupling” state $|C\rangle$ and “non-coupling” state $|NC\rangle$:

$$|C\rangle = \frac{1}{\sqrt{|g_1|^2 + |g_2|^2}} (g_1 e^{-i\Omega_1 t} |1\rangle + g_2 e^{-i\Omega_2 t + i(\varphi_2 - \varphi_1)} |2\rangle) \quad (2.4)$$

$$|NC\rangle = \frac{1}{\sqrt{|g_1|^2 + |g_2|^2}} (g_2 e^{-i\Omega_1 t} |1\rangle - g_1 e^{-i\Omega_2 t + i(\varphi_2 - \varphi_1)} |2\rangle) \quad (2.5)$$

The transition amplitude between the new states and the excited state $|3\rangle$ can be expressed as:

$$\langle 3|H_{\text{int}}|C\rangle = \frac{\hbar}{2\sqrt{|g_1|^2 + |g_2|^2}} e^{-i(\Omega_1 + \nu_1)t + i\varphi_1} (g_1^2 + g_2^2 e^{i\delta_R t + i(\varphi_2 - \varphi_1)}) \quad (2.6)$$

$$\langle 3|H_{\text{int}}|NC\rangle = \frac{\hbar g_1 g_2}{2\sqrt{|g_1|^2 + |g_2|^2}} e^{-i(\Omega_1 + \nu_1)t - i\varphi_1} (1 - e^{i\delta_R t - i(\varphi_2 - \varphi_1)}), \quad (2.7)$$

with the Raman detuning $\delta_R = \nu_1 - \nu_2 - \Delta_{\text{hfs}}$.

If the Raman detuning is zero, i.e., $\nu_1 - \nu_2 = \Omega_2 - \Omega_1$, $|NC\rangle$ is a solution of the Schrödinger equation: $i\hbar \frac{\partial}{\partial t} |\Psi\rangle = |\Psi\rangle$ and it is shown that for $\varphi_1 - \varphi_2 = n\pi$, $n \in \mathbb{Z}$:

$$\langle 3|H_{\text{int}}|NC\rangle = 0 \text{ and } \langle 3|H_{\text{int}}|C\rangle = \frac{\hbar\sqrt{|g_1|^2 + |g_2|^2}}{2} e^{-i(\Omega_1 + \nu_1)t - 2i\varphi_1} \quad (2.8)$$

From equation (2.8) it can be seen that the atom in the state $|NC\rangle$, called “dark state”, cannot be excited by the resonantly interacting light-fields. This is not true for the state $|C\rangle$ which can again be excited.

To obtain a more adequate approach towards the CPT effect, for the case of a three-level system a spontaneous emission channel must be included because it is the essential process for populating the coherent dark state $|NC\rangle$. This is done with the help of the density matrix formalism [1]. Solutions of the density matrix equations, using a perturbation approach, in the fully three-level symmetric system ($\Gamma_{31}=\Gamma_{32}=\Gamma$ and $\gamma_{31}=\gamma_{32}=\gamma$) and exactly on the optical resonance $\delta_L=0$, provide the (Lorentzian) signal absorption (Eq. 2.9) and signal dispersion (Eq. 2.10) of the dark line resonance, respectively [2]:

$$g\text{Im}(\rho_{32}) \approx \frac{1}{2} \left(\frac{g}{\Gamma}\right)^2 \left(\frac{2\Gamma_{12} + \frac{g^2}{\Gamma}}{\left(2\Gamma_{12} + \frac{g^2}{\Gamma}\right)^2 + \delta_R^2} \right) \quad (2.9)$$

$$g\text{Re}(\rho_{32}) \approx \frac{1}{2} \left(\frac{g}{\Gamma}\right)^2 \left(\frac{\delta_R}{\left(2\Gamma_{12} + \frac{g^2}{\Gamma}\right)^2 + \delta_R^2} \right), \quad (2.10)$$

where the broad background due to the optical transition is neglected (since the natural optical linewidth is typically five orders of magnitude broader than the dark line resonance) and it is assumed that hyperfine ground-state population and coherence decay rates are approximately the same, i.e. $\Gamma_{12} \sim \gamma_{12}$ is used. From these Lorentzians the CPT linewidth Γ_{CPT} and the amplitude A_{CPT} of the absorption signal are extracted, using the approximation that the ground-state coherence decay rate is much smaller than population decay rates from the excited state $\Gamma_{12} \ll \Gamma$:

$$\Delta\nu_{\text{CPT}} = \left(2\Gamma_{12} + \frac{g_1^2 + g_2^2}{2\Gamma}\right) = \left(2\Gamma_{12} + \frac{g^2}{\Gamma}\right) \quad (2.11)$$

$$A_{\text{CPT}} = \frac{\left(\frac{g_1^2 + g_2^2}{2\Gamma}\right)^2}{\left(2\Gamma_{12} + \frac{g_1^2 + g_2^2}{2\Gamma}\right)} = \frac{\left(\frac{g^2}{\Gamma}\right)^2}{\left(2\Gamma_{12} + \frac{g^2}{\Gamma}\right)} \quad (2.12)$$

where Γ_{12} is the hyperfine ground-state population decay rate, $g_1=g_2=g$ are the Rabi frequencies and $\Gamma=\Gamma_{31}=\Gamma_{32}$ for a symmetric Λ system. These formulas will be used to calculate signal linewidth and the amplitude for the case of the two laser fields of similar power and the small optical detuning ($< \text{MHz}$).

2.2 CPT signal amplitude and linewidth

An example of a transmission CPT signal, having a Lorentzian shape, is given in Figure 2-2 showing the signal linewidth and amplitude.

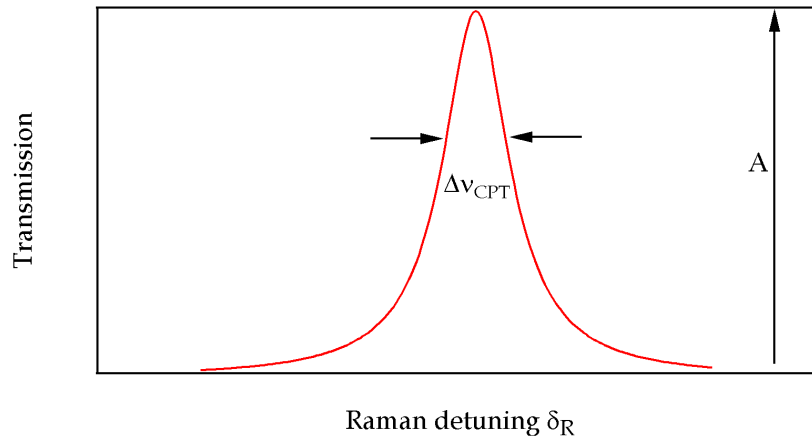


Figure 2-2: The transmission CPT signal as function of the Raman detuning. $\Delta\nu_{\text{CPT}}$ is the signal full width at the half maximum (FWHM) and A is the signal amplitude. Typical linewidth for a buffer gas cell is few kHz and typical signal amplitude is on the level of μA .

The amplitude A of the CPT signal in the case of a three-level system, with $g_1=g_2=g_R$ can be calculated with equation (2.12) [3]. The amplitude of the CPT signal is proportional to the density of the alkali atoms, which increases with the cell temperature. Hence, the CPT signal amplitude increases with the cell temperature. However, it is necessary to find the optimum cell temperature for which the signal amplitude is at maximum, since for very high temperatures the CPT signal vanishes due to the optical density of alkali

vapor such that no resonant light is transmitted [4]. The CPT transmission resonance signal has a Lorentzian shape in the case of a symmetric Λ system ($\Gamma_{31}=\Gamma_{32}=\Gamma$ and $g_1^2=g_2^2=g^2$) and the width of the resonance is given by the equation (2.11) [5]. Equation (2.11) clearly shows that the width of the CPT resonance depends linearly on the laser radiation intensity. At very low laser intensities the CPT linewidth is dominated by γ_{12} , i.e. by the buffer gas collisions (or time-of-flight broadening).

In the following, the main contributions to the CPT signal linewidth are discussed, e.g. time of flight, Doppler broadening and broadening due to different types of collisions: alkali atoms with alkali atoms, alkali atoms with the gas-cell walls and alkali atoms with buffer gas atoms. Each contribution to the CPT signal linewidth is evaluated through the two broadening rates (γ_{TOF} (rad/s) and γ_{DOPP} (rad/s)) and three ground state coherence rates (γ_{SE} (rad/s), γ_{diff} (rad/s), γ_{buff} (rad/s)), for the two Cs buffer gas cells of different sizes. The CPT signal linewidth is then calculated as $\Gamma_{12}=\gamma_{12}/\pi=(\gamma_{\text{SE}} + \gamma_{\text{diff}} + \gamma_{\text{buff}})/\pi$ (Hz).

2.2.1 Time of flight

In the case where the vapor cell only contains alkali atoms, the linewidth of the CPT signal is usually dominated by the limited interaction time between the atoms and laser light field (atoms move through the laser beam of limited diameter). As a result the signal resonance is narrower if the interaction time is longer (usually called “time-of-flight”, TOF):

$$\gamma_{\text{TOF}} = \frac{v_R}{d} = \frac{1}{d} \left(4 \ln 2 \sqrt{\frac{k_B T_C}{m}} \right), \quad (2.13)$$

v_R is the mean atom velocity, k_B is Boltzmann constant, m is the mass of the alkali atom, T_C is the vapor cell temperature, and d is the length of the atom’s path through the laser beam volume. At the cell temperature of $T_C=354$ K, the calculated mean velocity is $v_R \approx 413$ m/s. Using a $d=2$ mm beam (measured to be in our experiment) through a Cs vapor “time-of-flight” coherence rate is $\gamma_{\text{TOF}} \sim 206000$ rad/s. Any linewidth limitation from TOF is overcome by the presence of a buffer gas in the cell. The motion of alkali atoms becomes diffusive and essentially keeps the atoms longer time in the laser beam, reducing the TOF broadening (see section 2.2.5).

2.2.2 Spin-exchange

Another contributor to the overall signal resonance is the spin-exchange interaction between individual alkali atoms. In these collisions, the total angular momentum is conserved but a transfer between the hyperfine states is possible [6]. The spin exchange collision contribution to the overall ground-state coherence rate is [7]:

$$\gamma_{SE} = \left(\frac{6I + 1}{8I + 4} \bar{v}_S n_{AL} \sigma_{SE} \right), \quad (2.14)$$

where I is the total nuclear angular momentum, $\bar{v}_S = \sqrt{\frac{8k_B T}{\pi \mu}}$ is the mean relative velocity between the two colliding Cs atoms with reduced mass μ between them, n_{AL} is the density of alkali atoms and σ_{SE} is the cross-section of spin exchange collisions. In the case of Cs with nuclear spin quantum number $I=7/2$ the spin exchange cross-section is $\sigma_{SE}=(2.18 \pm 0.12) \times 10^{-14} \text{ cm}^2$ [8]. For the cell temperature $T_c=354 \text{ K}$ the density of Cs atoms is $3 \times 10^{12} \text{ atoms/cm}^3$ (see Chapter 1, Figure 1-7). Therefore, it can be calculated that the spin-exchange contribution to the signal linewidth, in these conditions is $\gamma_{SE}=1857 \text{ rad/s}$.

2.2.3 Doppler broadening

The Doppler broadening exists not only for the optical transitions but also for the microwave transitions, due to same reasons (see Chapter 1). It is given by:

$$\gamma_{DOPP} = v_{hfs} \sqrt{\frac{2 \ln 2 k_B T_c}{m c^2}}, \quad (2.15)$$

where m is alkali atom mass, k_B is the Boltzmann constant, $c=299,792,458 \text{ m/s}$ and T_c the vapor cell temperature. At the gas cell temperature $T_c=354 \text{ K}$, $\gamma_{DOPP} \approx 5400 \text{ rad/s}$. With buffer gas in the vapor cell the Doppler broadening is eliminated through the Dicke effect [9], when the mean free path between two collisions is smaller than the relevant wavelength scale, given by the ground-state hyperfine splitting. Doppler broadening can also be suppressed by coating the vapor cell walls with anti-relaxation coating material. With cells coated with anti-relaxation material at low laser intensity

such that the crossing time of atoms through the laser beam is faster than optical pumping, velocity averaging during multiple passes of the atoms through the beam also creates the signal narrowing.

2.2.4 Atom-cell walls collisions (diffusion equation)

As mentioned in Chapter 1 the vapor cells contain buffer gas in order to prevent collisions of alkali atoms with the cell walls and keep their state of polarization. With this technique the signal resonance becomes narrower [9], since the time that alkali atoms spend passing through the laser beam increases and time-of-flight broadening is suppressed. The motion of the alkali atoms through the neutral buffer gas atoms can be treated as diffusive motion with a small relaxation, since the collision frequency between alkali and buffer gas atoms is much higher than the collision frequency between alkali atoms and of alkali atoms with the cell walls [7]. Relaxation rates of the alkali atoms due to collisions with the cell walls are obtained as solution of the diffusion equation. For low cell temperatures and small light beam diameters ($d \ll R$) the ground-state coherence rate is given by the [7]:

$$\gamma_{\text{diff}} = \left(\left(\frac{2.405}{R} \right)^2 + \left(\frac{\pi}{L} \right)^2 \right) D_0 \frac{P_0}{P} \left(\frac{T_C}{T_0} \right)^{3/2}, \quad (2.16)$$

where R and L are cell radius and length of a cylindrical cell, respectively, D_0 is the diffusion constant of Cs in the buffer gas considered, P_0 and P are the reference and cell pressure, and T_0 and T_c are the reference and cell temperature, respectively. It is clear that γ_{diff} is inversely proportional to the buffer gas pressure. High buffer gas pressure seems desirable in order to reach minimal linewidth. For the Cs micro-fabricated cell studied here, the diffusional ground-state coherence decay rate can be expressed as function of the buffer gas pressure:

$$\gamma_{\text{diff}} = 1.8 \times 10^5 \text{ Torr} * \text{rad/s} * \frac{1}{P}, \quad (2.17)$$

calculated for the gas-cell dimensions of $R=1$ mm and $L=1.4$ mm, cell temperature $T_c=354$ K and diffusion constant of Cs in Ne (for $T=273$ K and $P_0=760$ Torr) $D_0=(0.15 \pm 0.014)$ cm²/s [10]. For 75 Torr of Ne cell, $\gamma_{\text{diff}}=2418$ rad/s.

2.2.5 Collisions with buffer gas atoms

The frequent collisions with the buffer gas atoms cause an additional contribution to the alkali hyperfine ground-state coherence rate:

$$\gamma_{\text{buff}} = L_0 \bar{v}_r \sigma_{\text{buff}} \frac{P}{P_0}, \quad (2.18)$$

where $L_0 \approx 2.69 \times 10^{25} \text{ m}^{-3}$ is the Loschmidt constant, $\bar{v}_{\text{rel}} = \sqrt{\frac{8k_B T}{\pi \mu_r}}$ is the mean relative velocity between the alkali and buffer gas atoms at the cell temperature (μ_r is reduced mass between Cs and buffer gas atoms), and σ_{buff} is the collisional cross-section between alkali and buffer gas atoms. γ_{buff} is directly proportional to the buffer gas pressure since the density of the atoms increases with the pressure. For the studied micro-fabricated cell here, the hyperfine ground-state coherence rate can be expressed as function of the buffer gas pressure:

$$\gamma_{\text{buff}} = 0.136 \frac{\text{Hz}}{\text{Torr}} * P, \quad (2.19)$$

for the cell temperature $T_c = 354 \text{ K}$ and the collisional cross section between Cs and Ne of $\sigma_{\text{buff}} = (9.27 \pm 0.90) \times 10^{-23} \text{ cm}^2$. For the 75 Torr of Ne, γ_{buff} is 10 rad/s.

Since Γ_{diff} is inversely proportional, and Γ_{buff} is directly proportional to the buffer gas pressure, for low buffer gas pressures the resonance linewidth strongly drops with increasing pressure caused by the diffusive effects, while for higher pressures the linewidth increases again due to collisional ground-state dephasing [11], as described in Eq. (2.18), see Figure 2-3.²

γ_{TOF} and γ_{DOPP} are only evaluated for evacuated Cs cells and their contribution to the linewidth is significantly suppressed by having a buffer gas in the cell. In the case of a vapor cell with buffer gas, the ground-state coherence rate can be calculated with (2.11), where γ_{12} is:

² Figure 2-3 reprinted with permission from: S. Brandt, A. Nagel, R. Wynands and D. Mechede, Phys. Rev. A 56, pp. R1063-R1066, 1997. Copyright (1997) by the American Physical Society. <http://link.aps.org/doi/10.1103/PhysRevA.56.R1063>.

$$\gamma_{12} = (\gamma_{SE} + \gamma_{diff} + \gamma_{buff}) \quad (2.20)$$

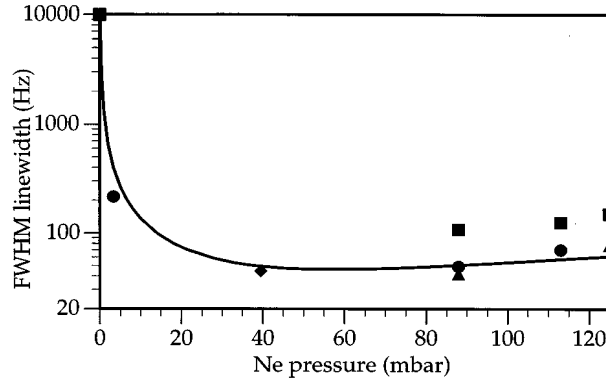


Figure 2-3: Measured coherent dark resonance linewidth vs. neon pressure for very low laser intensity (squares, $17 \mu\text{W}/\text{cm}^2$; triangles, $11 \mu\text{W}/\text{cm}^2$; circles, $6 \mu\text{W}/\text{cm}^2$; diamond, $1 \mu\text{W}/\text{cm}^2$). The solid line is calculated using values measured by direct excitation of RF transitions between cesium ground-state levels [10], and does not involve any adjustable parameters. This figure was taken from [11].

Table 2-1 summarizes the CPT signal linewidth contribution due to all mentioned effects above, for the two different Cs cells: for the MEMS cell with 75 Torr of buffer gas Ne total γ_{12} is $\gamma_{12}=4285 \text{ rad/s}$ and for the cm-scale cell with 90 Torr of Ne $\gamma_{12}=209 \text{ rad/s}$:

Vapor cell	micro-fabricated Cs	cm-scale Cs
Dimensions (mm)	R=1 and L=1.4	R=10 and L=10
Cell temperature (K)	354	323
Beam diameter (mm)	2	5
Ne buffer gas (Torr)	75	90
γ_{TOF} (rad/s)	206×10^3	39.5×10^3
γ_{DOPP} (rad/s)	5400	3575
γ_{SE} (rad/s)	1857	200
γ_{diff} (rad/s)	2418	23
γ_{buff} (rad/s)	10	18
Total $\gamma_{12}=\gamma_{\text{SE}}+\gamma_{\text{diff}}+\gamma_{\text{buff}}$ (rad/s)	4285	241
Total $\Gamma_{12}=\gamma_{12}/\pi$ (Hz)	1364.6	76.7

Table 2-1: Signal linewidth broadening contributions due to different effects, in the case of two different cells.

2.3 Light shift in CPT for a simple three-level model atom

In this section the theoretical description of the LS in a CPT gas-cell atomic clock is given. The explanation will start with the LS for a simplified three-level model atom, in the case of the monochromatic laser field, already briefly discussed in 1.4.3. Sum over all existing laser frequency components gives the total LS in the case of a multi-frequency laser spectrum, e.g. for CPT induced with a frequency-modulated laser. Previously published CPT LS reduction technique is discussed here in order to distinguish this technique from the one that will be proposed in this thesis (Chapter 4).

The LS is the shift of atomic energy levels due to the interaction of the induced atomic dipole moment with the oscillating electric field of the light [12, 13]. The LS δv_i of a single atomic level can be approximated by a dispersive Lorentzian (as function of a single laser frequency ν_L and intensity $I \sim |g_R|^2$) of width Γ_i centered at the optical atomic resonance ν_i , [14, 15]:

$$\delta v_i(\nu_L, I) = \frac{1}{4} |g_R|^2 \frac{(\nu_L - \nu_i)}{(\nu_L - \nu_i)^2 + \Gamma_i^2/4} \quad (2.21)$$

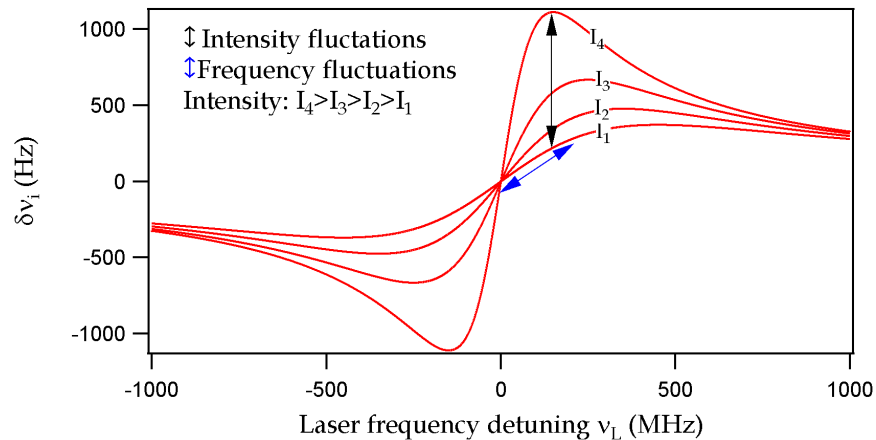


Figure 2-4: Diagram depicting the intensity and frequency light - shift effect. The x-scale shows the laser frequency detuning around the frequency of the specific transition in alkali atom, i.e., $F=3 \rightarrow F'=3$ in Cs D1 line, etc.

The total LS of the microwave atomic clock transition (in the case of the ideal three level symmetric model atom shown in Figure 2-1) is the difference of the two $m_F=0$ atomic level shifts involved:

$$\delta\nu_{00}(\nu_L, I) = \delta\nu_2(\nu_L, I) - \delta\nu_1(\nu_L, I), \quad (2.22)$$

which is depicted in Figure 2-5. The dashed blue line indicates the LS due to the interaction of a single laser frequency with one ground-state level only. The solid red line indicates the full LS due to both ground states.

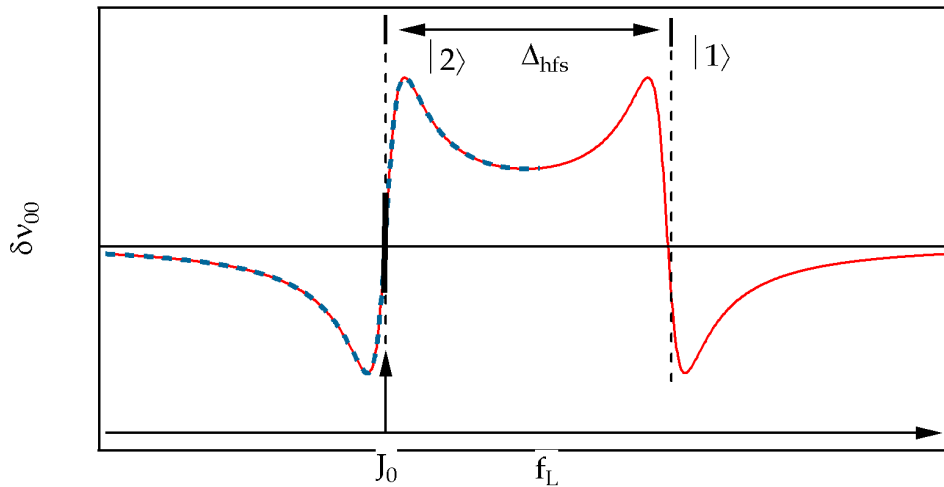


Figure 2-5: The total LS of the microwave atomic clock transition in the case of ideal three-level system and single laser frequency. Two ground-state levels are depicted above the LS curve. The dashed blue line indicates the frequency-dependent LS of the one atomic ground-state level ($|2\rangle$) in presence of one single light frequency ν_L . The red solid line gives the full LS including both ground-state levels (LS of the clock transition). Below the LS curve, the monochromatic laser spectrum (laser carrier J_0) is depicted. Solid black line represents the local slope used for β estimation (see below).

When the laser frequency is modulated in order to create sidebands for inducing CPT resonances, the intensities I_j of the carrier and the j -th sidebands are $I_j \approx |J_j(M)|^2$, depending on the phase-modulation index M through the Bessel functions J_j (if the amplitude modulation is small or negligible) [16] (see Chapter 3). While M can be optimized in order to obtain maximized light intensity in the two first-order sidebands creating the CPT resonances (one of the possibilities, see Figure 1-5), it is not possible to simultaneously have zero intensity in the laser carrier and the higher-order ($|j| \geq 2$) laser sidebands.

In the case of a multi-frequency laser spectrum the total LS is obtained as the sum over the contributions from all existing laser frequency components ν_j with their respective intensities I_j :

$$\delta v_{00}^{\text{CPT}}(v_L, I) = \sum_j [\delta v_2(v_j, I_j) - \delta v_1(v_j, I_j)], \quad (2.23)$$

where v_L is the laser carrier frequency ($j=0$) and $j \neq 0$ indicates the orders of the modulation sidebands.

In a CPT atomic clock application, the LS can be expressed locally (for a given laser frequency and laser intensity) by coefficients known as the intensity LS coefficient α and the frequency LS coefficient β , by taking the respective partial derivatives of (2.23):

$$\alpha(v_L, I) = \frac{dv_{00}^{\text{CPT}}}{dI} \quad (2.24)$$

$$\beta(v_L, I) = \frac{dv_{00}^{\text{CPT}}}{dv_L}$$

With α and β having in general non-zero values, it is evident that residual fluctuations in the laser intensity or laser frequency give rise to fluctuations in the atomic level energies and thus to instabilities of the atomic clock. Changes in the amplitude of the solid red line due to the laser intensity instabilities correspond to the intensity LS coefficient α in Figure 2-5. The local slopes of the solid red line give the frequency LS coefficient β in the same Figure. Usually, β is evaluated as a local slope around zero (black solid line in Figure 2-5). It is common practice to express the LS coefficients and clock frequency stability in fractional values, i.e., normalized to v_{00} .

There is already one method developed for LS reduction in CPT-based vapor-cell clocks [14, 17-20]. In this case the LS can be significantly reduced by optimizing the modulation index of the RF frequency-modulated laser field used to create the CPT signal [14, 17]. It is also possible to obtain modulation conditions where the frequency LS β is reduced to first-order, because the slopes of the LS curve at the $\pm 1^{\text{st}}$ -order sidebands are of opposite sign and can largely compensate each other for appropriate sideband intensities [17]. However, second-order effects due to the carrier and higher-order sidebands result in a non-negligible quadratic frequency LS, and the M values required for obtaining suppressed α or β are not necessarily the same [14]. In Chapter 4 of this thesis a novel technique of the LS reduction will be proposed – a technique based on optimizing the vapor cell temperature, not the modulation index M.

³ In order to be compatible with widespread literature convention, the two different coefficients are labeled with the same symbol β : Frequency LS coefficient β (mHz/MHz) and the pressure coefficient β (Hz/Torr) introduced in Eq (1.7).

2.4 Light shift in CPT for a four-level model atom

The LS for a four-level model atom is calculated by using Eq. (2.21) taking into account that Cs D1 line cannot be approximated by the simple three-level model since the influence from the off-resonant excited state must be considered (see Figure 1-8). Therefore the LS δv_i of a single atomic ground-state level is (Eq. (2.21) becomes):

$$\delta v_i(v_L, I) = \frac{1}{4} \sum_{k=3}^4 |g_{Rk}|^2 \frac{(v_L - v_{ik})}{(v_L - v_{ik})^2 + \Gamma_{ik}^2/4}, \quad (2.25)$$

where $i=3, 4$ and the LS from the off-resonant excited state is included. The difference of the involved ground-state level shifts is then calculated by using:

$$\delta v_{00}(v_L, I) = \delta v_4(v_L, I) - \delta v_3(v_L, I), \quad (2.26)$$

and shown schematically in Figure 2-7 (b), for a case of a single laser frequency.

Rabi frequencies g_{Rk} depend on the nature of the atom, the optical transition in the atom, the light intensity and light field polarization (see Appendix 3). In our case we deal with right hand (σ^+) polarization light field geometry inside the cell, shown in Figure 2-6:

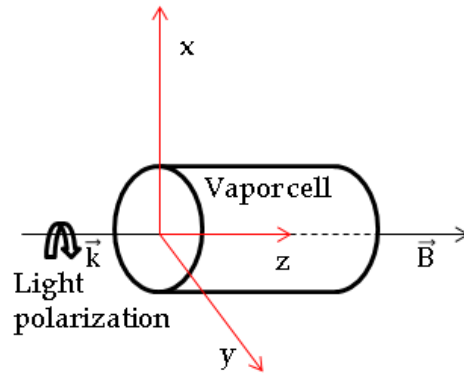


Figure 2-6: Scheme of the light and magnetic field vectors inside the vapor cell. The black solid arrow represents the circular σ^+ polarization.

Optical transition strengths are different for the different light polarizations and are dependent on the square of the dipole matrix elements, which are usually given in the literature [7]. Table 2-2 represents the optical transition probabilities for the $F=3 \rightarrow F'=4$ transition of Cs D1 line (for detailed Cs and Rb atom transition probabilities see Appendix 3):

		Transition probability							
		$m_F=-3$	$m_F=-2$	$m_F=-1$	$m_F=0$	$m_F=1$	$m_F=2$	$m_F=3$	
Optical transition in Cs	TP	Selection rule							
$F=3 \rightarrow F'=4$	π	$\Delta m_F=0$	7/48	1/4	5/16	1/3	5/16	1/4	7/48
$F=3 \rightarrow F'=4$	$\sigma+$	$\Delta m_F=+1$	1/48	1/16	1/8	5/24	5/16	7/16	7/12
$F=3 \rightarrow F'=4$	$\sigma-$	$\Delta m_F=-1$	7/12	7/16	5/6	5/24	1/8	1/6	1/48

Table 2-2: TP denotes transition polarization. Optical transition probabilities for the ground state $F=3$ of Cs atom for $\sigma+$, $\sigma-$ and π light polarization are taken from [21].

In our specific case we are interested only in the LS of the $F=3, m_F=0 \rightarrow F=4, m_F=0$ (clock transition) of Cs D1 transition. For $F (m_F=0) \rightarrow F' (m_F=+1)$ transitions in the case of $\sigma+$ laser polarization, the transition strengths for the four transitions are:

Optical transition in Cs D1 line	Transition probability
$F=3 \rightarrow F'=4$	5/24
$F=3 \rightarrow F'=3$	1/8
$F=4 \rightarrow F'=4$	5/24
$F=4 \rightarrow F'=3$	1/8

Table 2-3: Optical transition probabilities for the Cs D1 line in the case of right handed $\sigma+$ light polarization, taken from [21].

Figure 2-7 shows the schematic view of LS of the clock transition in the case of CPT on the Cs D1 line, in presence of one single light frequency only. The top curve in Figure 2-7 shows an example of an optical transmission spectrum for a thermal Cs vapor, while a typical example of a multi-frequency laser spectrum, for CPT excitation by the positive and negative first-order sidebands is depicted by the lowest curve. Clock transition LS on Cs D1 line, in presence of one single light frequency only, is calculated by using Eq. (2.26). Broadening due to the buffer gas is taken into account by approximate choice of Γ_{ik} in Eq. (2.25). Optical transition probabilities from Table 2-2 are implemented into Eq. (2.25) and Eq. (2.26) through the Rabi frequencies g_{Rk} .

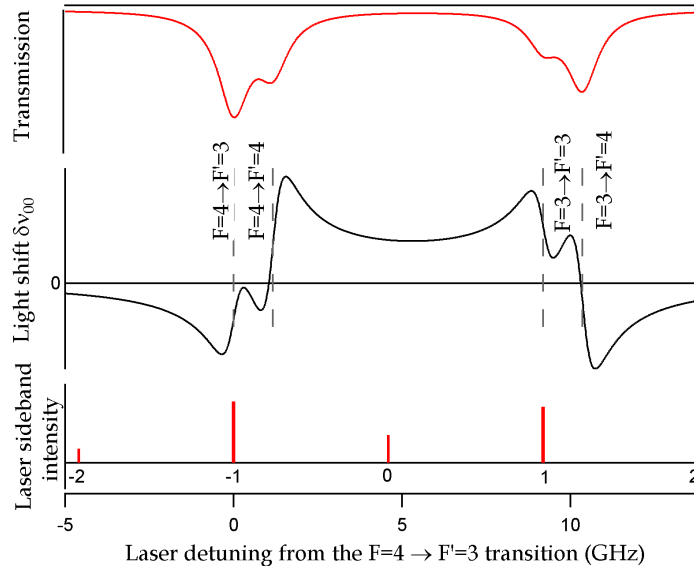


Figure 2-7: Schematic view of LS in the case of CPT on the Cs D1 line. Top curve: Example of an optical transmission spectrum for a thermal Cs vapor, showing line broadening by a buffer gas. Middle curve: Frequency-dependence of the LS of the clock transition in presence of one single light frequency only. The dashed vertical lines indicate the positions of the optical transitions. Lowest curve: Typical example of a multi-frequency laser spectrum, for CPT excitation by the positive and negative first-order sidebands.

In the case of a multi-frequency laser spectrum, the total CPT LS in the case of Cs D1 line can be calculated as the sum over the contributions from all existing laser frequency components ν_j with their respective intensities I_j (Eq. 2.23). Therefore, the total CPT LS of the Cs D1 line is calculated by using the formula (2.26), where the sum over all the contributions are taken into account:

$$d\nu_{00}^{\text{CPT}}(\nu_L, I) = \sum_j \left(\delta\nu_4(\nu_{Lj}, I_j) - \delta\nu_3(\nu_{Lj}, I_j) \right) \quad (2.27)$$

Using Eq. 2.27 and the transition rates for the Cs D1 line (see Table 2-2 and Annex 3) in the case of σ^+ polarization, i.e. using the g_{Rk} of Table 2-3, the total CPT LS for Cs D1 line (in a cold vapor cell, i.e. neglecting light absorption in the cell) can be calculated for a different values of the modulation index M , Figure 2-8. In this case, the positive and negative first-order sidebands of the laser are used to create CPT. Taking into account the light absorption in the cell, i.e. calculating LS or a high cell temperatures, was not investigated in this thesis.

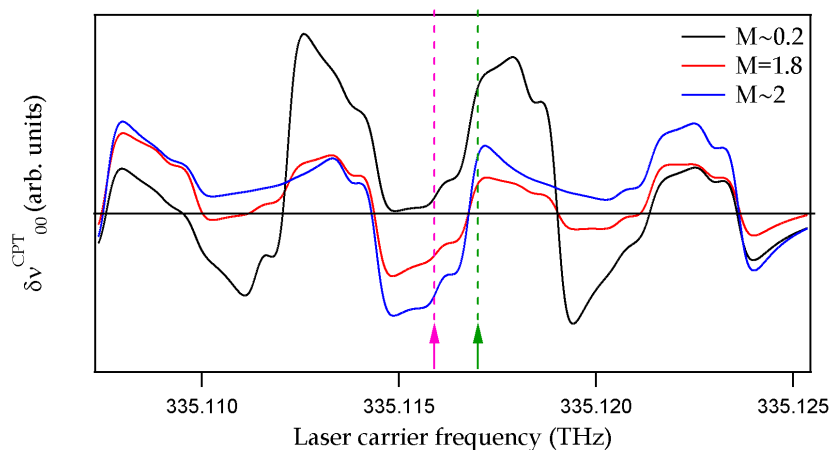


Figure 2-8: Frequency-dependence of the LS of the clock transition in presence of the multi-frequency laser spectrum (see Figure 2-7 (c)), for a various modulation indices M . The pink arrow indicates the laser carrier frequency when the CPT is created by coupling to the $F'=3$ state. The green arrow shows the laser carrier frequency when CPT is created by coupling to the $F'=4$ state. δv_{00}^{CPT} is in arbitrary units and additional work must be done in order to have it in Hertz.

The LS model (Figure 2-8) shows that in the case when two first-order sidebands create CPT by coupling to the $F'=3$ state (pink arrow), LS is negative for $M=1.8$ and $M=2$, and only for small $M < 0.4$ the LS becomes positive. This model also shows that in the case of CPT created by coupling to the $F'=4$ state (green arrow), the LS is always positive, independent on the modulation index M .

The theoretical treatments shown in Figures 2-7 and 2-8 are in agreement with the experimental measurements discussed in Chapter 4:

- Section 4.2.1 - Experimental results of the CPT intensity LS in Cs MEMS buffer gas cell, fit to the calculations shown in Figure 2-8. CPT created by coupling to the $F'=3$ state LS is negative and CPT created by coupling to the $F'=4$ state LS is positive (for $M=1.8$).
- Section 4.3.1 - Experimental results of the DR frequency LS shown in Figure 4-18 fit to the calculations introduced in Figure 2-7.

2.5 Temperature coefficient

Theoretical description of the temperature shift in a CPT gas-cell atomic clock is given in the following. This effect is considered for two different vapor cells: buffer gas and wall-coated cell. Temperature coefficient for both cells is evaluated.

2.5.1 Temperature coefficient in a buffer gas cell

In addition to the LS, the temperature coefficient (TC) of the clock cell is another main source of instability in atomic clocks. With each buffer gas species (typically Ar, Ne, N₂, etc.) is associated a shift of clock frequency which depends on the gas pressure and temperature (temperature coefficient) and thus links the clock frequency to the environmental conditions (see Chapter 1, (1.7)). To limit this effect, a mixture of two buffer gases with opposite temperature coefficients is generally used in order to obtain a suppressed linear TC at a specific inversion temperature $\left. \frac{d\nu}{dT} \right|_{T_{inv}} = 0$ (see 1.7) [22-24].

Table 2-4 represents the pressure and temperature coefficients according to Equation (1.7), for different buffer gases in Cs cell.

Buffer gas	N ₂ [23]	Ar [23]	He [24]
β (Hz/Torr)	921.8 ± 12.8	-183.4 ± 4.2	1185 ± 46
δ (Hz/(Torr*K))	0.826 ± 0.012	-1.088 ± 0.025	1.49 ± 0.150
γ (mHz/(Torr*K ²))	-2.6 ± 0.04	0.0 ± 0.3	-3.9 ± 0.06

Table 2-4: Linear and quadratic temperature coefficients for different buffer gases in a Cs cell, taken from [23, 24].

The total shift from the resonant frequency due to the pressure and temperature shifts can be calculated by using (1.7). In the case of Cs vapor cell with buffer gas mixture formula (1.7) becomes:

$$\Delta\nu = \nu - \nu_0 = P_0 \left(\frac{(\beta_1 + r\beta_2)}{1+r} + \frac{(\delta_1 + r\delta_2)}{1+r} (T - T_0) + \frac{(\gamma_1 + r\gamma_2)}{1+r} (T - T_0)^2 \right), \quad (2.28)$$

where β_i , δ_i and γ_i are pressure, linear and quadratic temperature coefficients for two buffer gases, respectively, P_0 is the total buffer gas pressure, and r is the buffer gas ratio $r=P_2/P_1$.

For 80 Torr of Ar-N₂ buffer gas pressure in Cs vapor cell, $T_0=354$ K and r (P_{Ar}/P_{N_2})=0.48 the inversion temperature can be calculated. In this case $T_{inv}=329.9(2)$ K. The result is shown in Figure 2-9.

TC for the single buffer gas N₂ ($P=57$ Torr) is $TC=d\nu/dT \approx 4.8 \times 10^{-9}$ (1/K) while for the buffer gas mixture Ar-N₂ ($P=80$ Torr and $r=0.48$) same coefficient is $TC \approx 1.2 \times 10^{-10}$ (1/K).

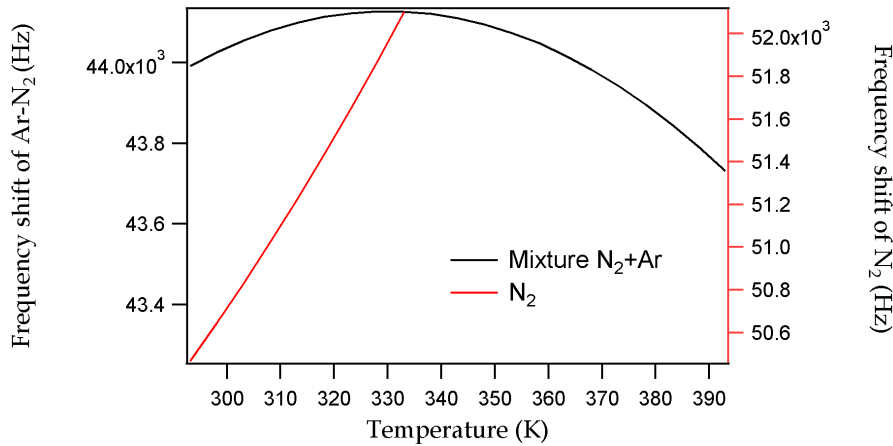


Figure 2-9: Black solid line represents the temperature shift in Cs vapor cell with buffer gas mixture Ar-N₂. Inversion temperature for 80 Torr of total pressure and $r=0.48$ is $T_{inv}=329.9(2)$ K. Red solid line represents the temperature shift in Cs vapor cell with 57 Torr of single buffer gas N₂.

2.5.2 Temperature coefficient in a wall-coated cell

Adding buffer gas to the resonance cell is not the only technique to reduce depolarizing collisions of the alkali atoms with the cell walls. Another possibility is the use of wall-coated cells where a thin layer of tetracontane or a silane on the cell walls reduces the sticking time of the alkali atoms on the walls, thus strongly reducing

ground-state depolarization. With the tetracontane coating material the atomic coherence can survive several thousand wall-collisions and the observed linewidths can be as narrow as only few Hertz [26]. Dicke narrowing is possible in this case too, when the mean free path between two collisions is smaller compared to the wavelength $\lambda_{\text{hfs}}=c/\Delta_{\text{hfs}}$ of the involved transition between the two ground states ($\lambda_{\text{hfs}}=3.2$ cm for Cs). For a spherical wall-coated vapor cell, in the case of the ideal coating, the relaxation rate is given by [7]:

$$\gamma = \frac{3 \bar{v}}{4 R}, \quad (2.29)$$

where R is the radius of the cell and \bar{v} is the average speed of the atom.

Table 2-5 lists obtained wall-shifts and signal linewidth for different coatings in different ^{87}Rb cell sizes.

Reference	[26]	[27]	[28]
Coating	Tetracontane	Paraffin	OTS
Cell diameter (cm)	3.6	2.3	4
Wall- shift (Hz)	-52	-107	-600
Linewidth (Hz)	10.6	260-346	870
TC	$\sim 2 \times 10^{-10}/\text{K}$	$\sim 3 \times 10^{-10}/\text{K}$	n.c.

Table 2-5: Measured wall-shifts, linewidths and TC in different wall-coated ^{87}Rb cell, with different dimensions. n.c. denotes not communicated.

The TC of a wall-coated cell is intrinsic property of the coating material itself [29]. The variations in the cell temperature will determine the physics of atoms interacting with the wall-coating and its impact on their polarization state. Temperature frequency shift behavior can be explained introducing the adsorption process of the alkali atom on the coated walls, assuming uniform adsorption energy E_a in the overall cell volume [30-32]:

$$\tau_a = \tau_0 e^{\frac{E_a}{k_B T}}, \quad (2.30)$$

where τ_a is adsorption time of an atom on the walls, τ_0 is the period of vibration of the adsorbed atom in the wall potential, k_B is the Boltzmann constant and T is the absolute temperature.

If we consider the formula for the clock frequency wall shift due to temperature [33]:

$$\Delta\nu = (\Delta\nu_a) \frac{\tau_a}{\tau_c}, \quad (2.31)$$

with $\Delta\nu_a$ is the difference between the resonant hyperfine frequency while the Rb is absorbed on the surface and in the free space and τ_c is the correlation time for atom-wall collisions (depends on cell radius R and mean velocity $\langle v \rangle$ of Rb atoms inside the spherical cell), the fractional change in adsorption time by the influence of the temperature can be written as [30]:

$$\frac{d\Delta\nu}{\Delta\nu} = - \frac{E_a}{k_B T} \frac{dT}{T} \quad (2.32)$$

TC measurements gives the information about adsorption energy E_a , using (2.32). Typical $TC=d\Delta\nu/dT$ for the cell coated with tetracontane is on the level of $\sim 10^{-10}/K$.

2.6 Summary and conclusions

In this chapter three-level models for CPT in Λ systems are discussed. This model includes spontaneous emission in CPT effect by using the density matrix formalism. CPT signal linewidth and amplitude equations are given and the main contributors to the CPT signal linewidth (TOF, spin-exchange, Doppler broadening, atom-cell walls collisions and collisions with buffer gas) are introduced. The theoretical description of the CPT LS for a simple three-level model atom and TC in a gas-cell atomic clock is discussed. It is shown that the total CPT intensity LS is given by the sum over all sideband contributions and can be minimized by adjusting M to balance the positive and negative contributions. Later, the theoretical description of the LS in a CPT gas-cell atomic clock for a four level model atom is introduced. Theory of TC in a buffer gas and wall-coated vapor cell is also discussed here. Typical TC for the single buffer gas is on the $10^{-9}/K$ level (for 57 Torr of N_2 $TC \approx 4.8 \times 10^{-9}$ 1/K) while for the buffer gas mixture same coefficient is on the $\sim 10^{-11}$ - $10^{-12}/K$ level (for N_2 -Ar mixture ($P=100$ Torr and $r=1.3$) $TC \approx 1.2 \times 10^{-10}$ 1/K). Typical TC for the wall-coated cell is on the level of $\sim 10^{-10}/K$. The

experimental measurements of the LS effect and TC in the Cs buffer gas and the Rb wall-coated cells are discussed in Chapter 4.

REFERENCES:

- [1] E. ARIMONDO, *Coherent population trapping in laser spectroscopy*, Prog. Optics 35 (1996), pp. 257-354.
- [2] A. NAGEL, S. KNAPPE, C. AFFOLDERBACH and R. WYNANDS, *Line shapes of coherent population trapping resonances*, AIP Conf. Proc. 559 (2000), pp. 257-259.
- [3] J. VANIER, A. GODONE and F. LEVI, *Coherent population trapping in cesium: Dark lines and coherent microwave emission*, Phys. Rev. A 58 (1998), pp. 2345-2358.
- [4] S. KNAPPE, J. KITCHING, L. HOLLBERG and R. WYNANDS, *Temperature dependence of coherent population trapping resonances*, Appl. Phys. B 74 (2002), pp. 217-222.
- [5] J. VANIER, *Atomic clocks based on coherent population trapping: a review*, Appl. Phys. B 81 (2005), pp. 421-442.
- [6] I. M. SAVUKOV and M. V. ROMALIS, *Effects of spin-exchange collisions in a high-density alkali-metal vapor in low magnetic fields*, Phys. Rev. A 71 (2005), pp. 023405-8.
- [7] J. VANIER and C. AUDOIN, *The Quantum Physics of Atomic Frequency Standards*, Adam Hilger, Bristol, UK, (1989).
- [8] T. G. WALKER and W. HAPPER, *Spin-exchange optical pumping of noble-gas nuclei*, Rev. Mod. Phys. 69 (1997), pp. 629-642.
- [9] R. H. DICKE, *The effect of collisions upon the Doppler width of spectral lines*, Phys. Rev. 76 (1953), pp. 472-473.
- [10] N. BEVERINI, P. MINGUZZI and F. STRUMIA, *Foreign-Gas-Induced Cesium Hyperfine Relaxation*, Phys. Rev. A 4 (1971), pp. 550-555.
- [11] S. BRANDT, A. NAGEL, R. WYNANDS and D. MECHEDE, *Buffer-gas-induced linewidth reduction of coherent dark resonances to below 50 Hz*, Phys. Rev. A 56 (1997), pp. R1063-R1066.
- [12] C. COHEN-TANNOUDJI and J. DUPONT-ROC, *Experimental study of Zeeman light shifts in weak magnetic fields*, Phys. Rev. A5 (1972), pp. 968-984.

- [13] J. BARRAT and C. COHEN-TANNOUDJI, *Etude du pompage optique dans le formalisme de la matrice densité*, J. Phys. Radium 22 (1961), pp. 329-336.
- [14] F. LEVI, A. GODONE and J. VANIER, *The light shift effect in the coherent population trapping cesium maser*, IEEE Trans. Ultrason. Ferroelectr. Freq. Control 47 (2000), pp. 466-470.
- [15] J. DENG, *Light shift compensation in a Rb gas cell frequency standard with two-laser pumping*, IEEE Trans. Ultrason. Ferroelectr. Freq. Control 48 (2001), pp. 1657-1661.
- [16] G. C. BJORKLUND, *Frequency-modulation spectroscopy: a new method for measuring weak absorptions and dispersions*, Opt. Lett. 5 (1980), pp. 15-17.
- [17] M. ZHU and L. S. CUTLER, *Theoretical and experimental study of light shift in a CPT based Rb vapour cell frequency standard*, Proceedings of the 32nd Precise Time and Time Interval Systems and Applications Meeting, ed. By L.A. Breakiron (US Naval Observatory, Washington, DC, 2000) (2000), pp. 311-324.
- [18] V. GEORGINOV, S. KNAPPE, P. D. SCHWINDT, L. HOLLBERG and J. KITCHING, *Long-term frequency instability of atomic frequency references based on coherent population trapping and microfabricated vapor cells*, J. Opt. Soc. Am. B 23 (2006), pp. 593-597.
- [19] E. E. MIKHAILOV, T. HORROM, N. BELCHER and I. NOVIKOVA, *Performance of a prototype atomic clock based on lin//lin coherent population trapping resonances in Rb atomic vapour*, J. Opt. Soc. Am. B 27 (2010), pp. 417-422.
- [20] R. BOUDOT, P. DZIUBAN, M. HASEGAWA, R. K. CHUTANI, S. GALLIOU, V. GIORDANO and C. GORECKI, *Coherent population trapping resonances in Cs-Ne vapor microcells for miniature clocks applications*, J. Appl. Phys. 109 (2011), pp. 014912-11.
- [21] D. A. STECK, Alkali D line data, version 2.1.4, (2010).
- [22] R. BOUDOT, D. MILETIC, P. DZIUBAN, C. AFFOLDERBACH, P. KNAPKIEWICZ, J. DZIUBAN, G. MILETI, V. GIORDANO and C. GORECKI, *First-order cancellation of the Cs clock frequency temperature-dependence in Ne-Ar buffer gas mixture*, Opt. Express 19 (2011), pp. 3106-3114.
- [23] K. DENG, X. CHEN and Z. WANG, *Minimization of the temperature coefficient of resonance frequency shift in the coherent population trapping clock*, Opt. Lett. 36 (2011), pp. 1740-1742.

- [24] O. KOZLOVA, S. GUERANDEL, E. DE CLERCQ, *Temperature and pressure shift of the Cs clock transition in the presence of buffer gases: Ne, N₂, Ar*, Phys. Rev. A 83 (2011), pp. 062714-9.
- [25] N. BEVERINI and F. STRUMIA, *Buffer-gas pressure shift in the $m_F=0$ - $m_F=0$ ground state hyperfine line in Cs*, Opt. Commun. 37 (1961), pp. 394-396.
- [26] H. G. ROBINSON and C. E. JOHNSON, *Narrow Rb hyperfine-structure resonances in an evacuated wall-coated cell*, Appl. Phys. Lett. 40 (1982), pp. 771-773.
- [27] A. RISLEY, S. JARVIS and J. VANIER, *The dependence of frequency upon microwave power of wall-coated and buffer-gas-filled gas cell ⁸⁷Rb frequency standards*, J. Appl. Phys. 51 (1980), pp. 4571-4576.
- [28] Y. W. YI, H. G. ROBINSON, S. KNAPPE, J. E. MACLENNAN, C. D. JONES, C. ZHU, N. A. CLARCK and J. KITCHING, *Method for characterizing self-assembled monolayers as antirelaxation wall coatings for alkali vapor cells*, J. Appl. Phys. 104 (2008), pp. 023534-7.
- [29] J. VANIER, R. KUNSKI, A. BRISSON and P. PAULIN, *Progress and prospects in rubidium frequency standards*, J. de Physique 12, (1981), pp. 139-150.
- [30] D. BUDKER, L. HOLLBERG, D. F. KIMBALL, J. KITCHING, S. PUSTELNY and V. V. YASCHCHUK, *Microwave transitions and nonlinear magneto-optical rotation in anti-relaxation-coated cells*, Phys. Rev. A 71 (2005), pp. 012903-9.
- [31] M. STEPHENS, R. RHODES and C. WIEMAN, *Study of Wall Coatings for Vapor-Cell Laser Traps*, J. Appl. Phys. 76 (1994), pp. 3479-3487.
- [32] H. M. GOLDENBERG, D. KLEPPNER and N. F. RAMSEY, *Atomic Beam Resonance Experiments with Stored Beams*, Phys. Rev. 123 (1961), pp. 530-537.
- [33] C. RAHMAN and H. G. ROBINSON, *Rb 0-0 hyperfine transition in evacuated wall-coated cell at melting temperature*, IEEE J. Quantum Electron. QE-23 (1987), pp. 452-454.

Chapter 3

Experimental methods

This chapter discusses the experimental methods used in this thesis. The laser source is described and its linewidth is estimated using two different experimental methods. The laser modulation technique is shown and modulation indices are evaluated for the modulation frequency $\nu = \nu_{\text{Cs}}/2 = 4.596$ GHz. Three different vapor cells used in the experiments are described, followed by the presentation of the two experimental setups used in this thesis. Finally, the two different CPT signals (obtained from the Cs MEMS single buffer gas cell and the ^{87}Rb wall-coated cell) are discussed. Signals linewidth and amplitudes are evaluated as functions of laser intensity and microwave power and compared to the theoretical values calculated in Chapter 2. The signal discriminator slope D is introduced and optimized in order to obtain the best clock short-term stability, discussed in Chapter 5.

3.1 Laser sources

It was already shown (see Chapter 2) that two light fields interacting with a three-level atomic system, in various configurations, can lead to CPT, where the Λ configuration is of special interest. These two light fields ω_1 and ω_2 can be produced by two phase-locked lasers [1] or by one frequency modulated laser, whose sidebands are used for creating the CPT signal. The number of sidebands and their amplitude depend on the laser modulation technique, e.g., single beam modulation techniques using Acousto-Optical Modulator (AOM), Electro-Optical Modulator (EOM), current modulation of the laser source, etc.

Two phase-locked diode laser excitations have been used in several CPT experiments since 1996 with Cs and Rb vapor cells [2-4] and atomic beam experiments [5]. Here, the beams from the two lasers (reference and slave laser) overlap on a photodiode. The phase difference between the two light fields is detected on the beat signal and compared with a stable reference phase. The error signal is used to make a correction to the tunable slave laser. The disadvantage of this method is that the setups to realize phase-locking are rather complex and more expensive.

Single beam modulation techniques, using an (AOM) [6], (EOM) [7] or current modulation of the laser source [8], are less complex allowing easier experimental realization. There are already reported CPT experiments using an EOM [9] and current modulation of the laser source [10, 11]. Today, one of the most common single beam modulation techniques is current modulation of the vertical-cavity surface-emitting laser diode (VCSEL). VCSELs are characterized by high modulation bandwidths (> 4 GHz range). This makes them very suitable for use in CPT experiments, where the splitting between sidebands corresponds usually to half or full hyperfine splitting frequencies of alkali atoms (Rb, Cs, etc.). VCSELs are intrinsically single-mode devices with a circularly shaped output beam. They have low threshold currents and require only few mA of drive current to operate. Typical single-mode VCSEL's linewidths are around 50 MHz (a VCSEL at 894.6 nm produced by Ulm Photonics has a linewidth of 20-25 MHz [12]). The laser linewidth plays a significant role in CPT contrast. Natural width of the optical transition in alkali atom is usually few MHz (6 MHz for Rb, 5.3 MHz for Cs, etc.). If the laser linewidth is larger than few MHz, only part of the laser power will drive the transitions and be involved in creating a CPT signal while all of the laser power contributes to the signal background. By adding a buffer gas to the metal vapor in the cell the optical transitions get homogeneously broadened and thus all power contained in the full VCSEL linewidth can contribute to the CPT signal.

The problem mentioned above can be also avoided by using a distributed feedback (DFB) lasers instead of VCSEL since typical DFBs have a linewidth of few MHz. Unfortunately the limited bandwidth of the DFB prohibits direct current modulation in the GHz range. Therefore a DFB laser carrier frequency is modulated by using other mechanisms for single beam modulation techniques: AOM or EOM. Using a DFB laser in a CPT atomic clock will limit the clock miniaturization possibilities due to the setup complexity, compared to the configurations using current modulated VCSELs.

At the beginning of this work (mid 2009) no commercial VCSELs emitting 894.6 nm (Cs D1 line) were available. Therefore, the CPT experimental clock utilized a DFB laser at 894.6 nm as a light source, modulated with an external EOM, see Figure 3-18. Also, the use of a DFB laser was a better option for characterizing the experimental clock parameters, providing a better control of the laser spectrum. Later, the further CPT clock miniaturization (since the goal of this work is devising the first European chip-scale atomic clock (CSAC)) was done by project partners in 2011-2012, by implementing the first VCSEL at 894.6 nm in the clock demonstrator [12].

3.1.1 DFB lasers

The DFB laser at 894.6 nm used in the experiment with Cs MEMS buffer gas cell is described below. The DFB laser at 795 nm (^{87}Rb D1 line) used in the experiment with ^{87}Rb wall-coated cell will be described in Annex A.

DFB laser diodes achieve intrinsic single-mode operation from the diode chip itself by a grating structure imprinted on the laser chip for mode selection. These lasers show low noise levels and narrow linewidths around 10 MHz [13] or less. The DFB laser diode wavelength used in the experiment is tuned for emission around 894.6 nm (Cs D1 line) [14]. The laser is packaged into 5.6 mm TO packages and placed into a home-made laser head. Figure 3-1 show the laser diode housing and control electronics.

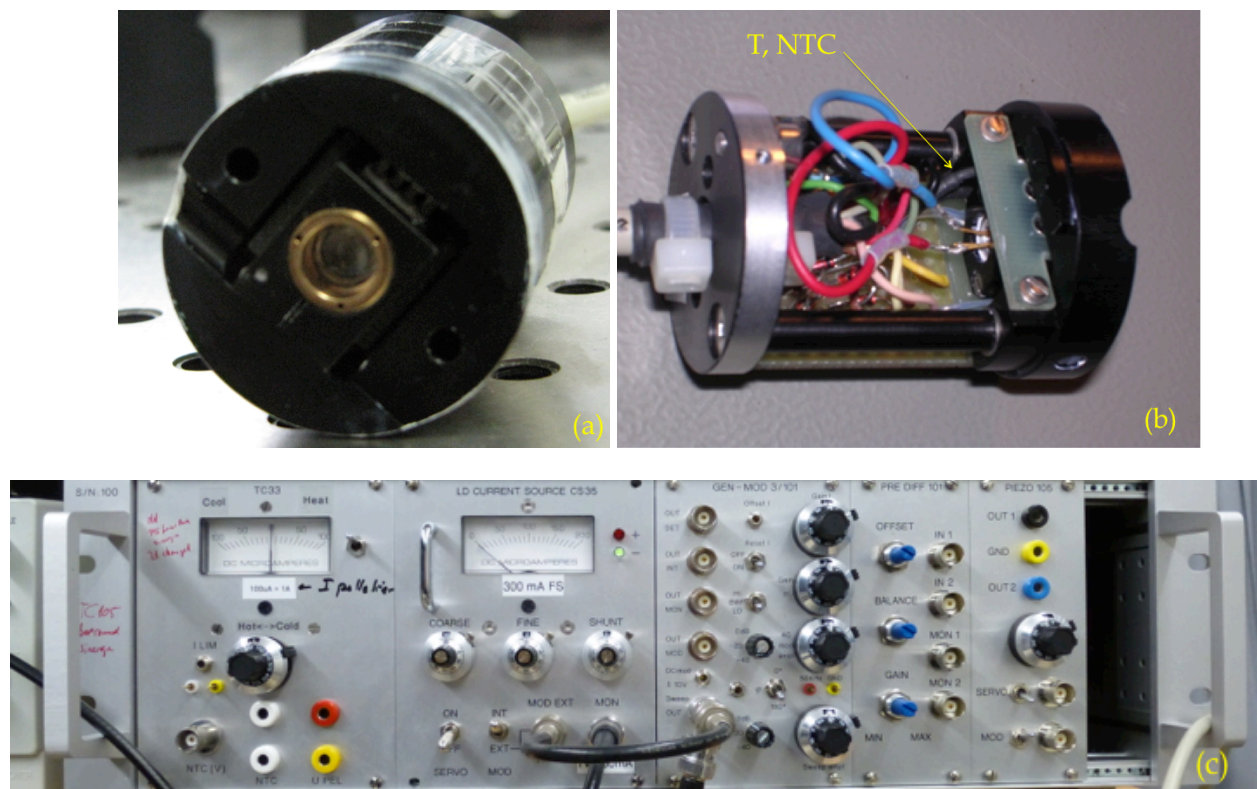


Figure 3-1: (a) DFB laser mounted in 35 mm diameter housing. The laser head is thermally isolated and then temperature stabilized with a Peltier-element and NTC. (b) View into the laser housing. Red and blue wires connect the chip with current and the ground sources, respectively. T and NTC indicate the laser temperature control. (c) Control electronics used to operate the DFB. Left: temperature control unit (283–333 K), Center: low-noise current unit (0–100mA). Right: lock-in detection unit. This unit modulates the DC current at 50 kHz for phase-sensitive detection and servo-locking of the laser frequency to maximum absorption in vapor cell.

The dynamic range of the current and temperature control are 0–100 mA and 283–333 K, respectively. The system operates with three servo-loops:

Current source unit: the voltage drop of the output current (across an internal resistor) is stabilized to a stable reference voltage in order to have low noise and stable laser frequency. External modulation inputs (modulation and servo) used in conjunction with the lock-in detector (GEN-MOD) allow laser locking. This module generates a 50 kHz signal used to modulate the laser current. The response signal is fed back to a synchronous detection stage, where finally a DC correction is applied to the laser current.

Lock-in detector (GEN-MOD): the lock-in unit is used to modulate/de-modulate the laser frequency at 50 kHz. This procedure generates a phase-sensitive error-signal that is zero when the laser frequency is locked (via the current) to maximum absorption in the cesium cell. The bandwidth of the lock-in detector is several kHz.

Temperature control unit: the resistance of an NTC (mounted next to the DFB) is compared with a stable reference resistance in order to have low noise and stable laser temperature (therefore, stable laser frequency). The NTC resistance is “locked” to the reference by heating/cooling the laser head (NTC + DFB) with a Peltier-element.

3.1.2 Laser linewidth measurements

The linewidth of the DFB laser was measured using two different principles. The first linewidth measurement is done by using a confocal Fabry-Perot cavity, formed by two, identical, spherical mirrors separated by their common radius of curvature, with a free spectral range (FSR) of 1 GHz. Laser light (10.58 mW) enters the Fabry-Perot cavity and undergoes multiple reflections between the mirrors so that the light wave can interfere with itself many times. The light will be transmitted only if the frequency of the incident light is such that constructive interference occurs within the Fabry-Perot cavity. Otherwise, destructive interference will not allow any light being transmitted through the Fabry-Perot interferometer [15]. Intrinsic linewidth of the used Fabry-Perot is < 5 MHz. In order to vary the transmitted wavelength a ramp voltage is applied to the piezoelectric spacers of the Fabry-Perot cavity. In this way, the mirror separation usually is scanned over several half wavelengths of the incident light resulting in a spectrum displaying a transmission peak every time the constructive interference equation is satisfied. The adjacent peaks of this repeating pattern are simply different orders of interference of the same incident wavelength. The laser linewidth, obtain by measuring the transmission of a Fabry-Perot cavity is 22(4) MHz, shown in Figure 3-2.

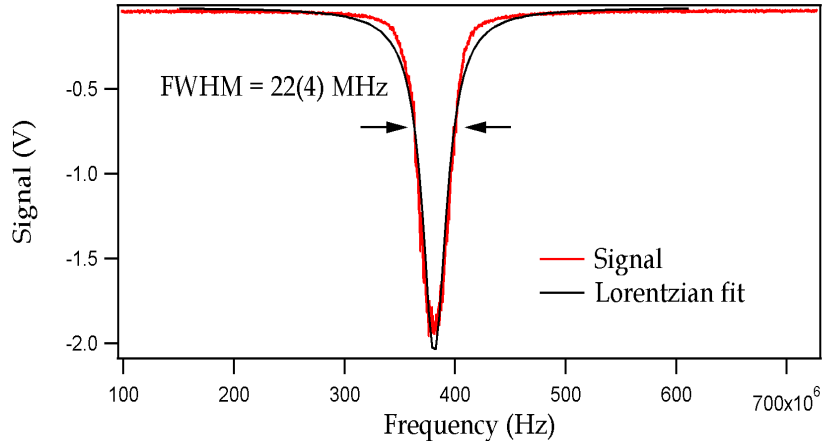


Figure 3-2: The laser spectrum obtained by measuring the transmission of a Fabry-Perot cavity with free spectral range FSR=1 GHz (red curve). Lorentzian fit of the transmission peak gives the laser linewidth (black curve).

By subtracting the intrinsic linewidth of the used Fabry-Perot from the measured laser linewidth we can conclude that the laser linewidth is $\sim 18(4)$ MHz.

Laser linewidth measurements are also done using the so-called, “beat measurement”. Heterodyne beat-note measurements are measurements between two independent lasers expected to be identical [15]. If we consider the beat note of the two light waves:

$$E_1 = E_{01} \cos(\nu_1 t - \varphi_1(t)) \text{ and } E_2 = E_{02} \cos(\nu_2 t - \varphi_2(t)) \quad (3.1)$$

The beat note between them can be expressed as:

$$E_{\text{beat}} = E_1 E_2 \cos(\Delta \nu t + \Delta \varphi(t)), \quad (3.2)$$

where $\Delta \nu = \nu_2 - \nu_1$ and $\Delta \varphi(t) = \varphi_2 - \varphi_1$.

The experimental setup used for the beat-note measurement between two DFBs at the same optical output power (18.8 mW) is given in Figure 3-3:

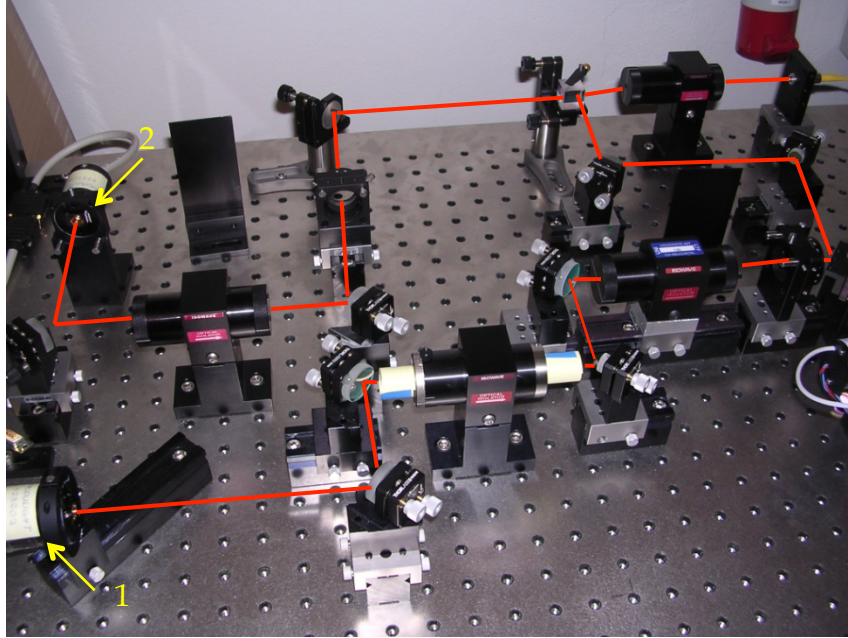


Figure 3-3: Experimental setup used for the beat-note measurements for the two DFB lasers (denoted as 1 and 2) expected to be identical. The red solid line represents the optical paths of the two DFB lasers, having the approximately same output power.

Figure 3-5 shows the result of a beat-note measurement obtained by using the experimental setup shown in Figure 3-3, giving a beat signal linewidth of 28.4(4) MHz. Assuming that the two DFBs are identical, the linewidth of each laser is half of this value, giving a result of $\sim 14.2(4)$ MHz.

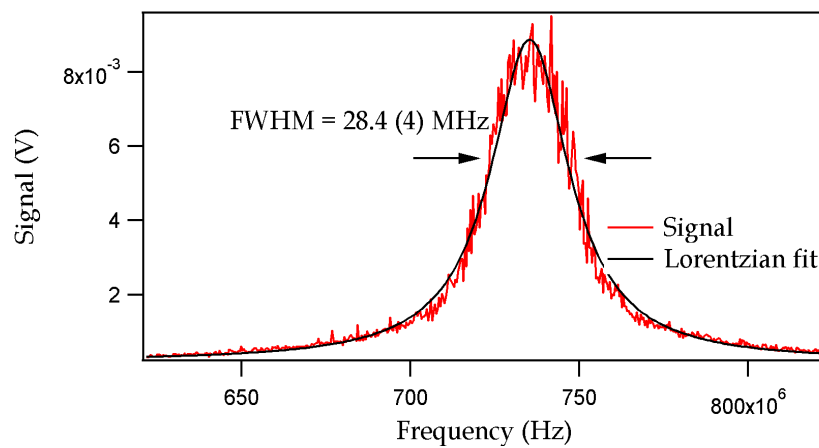


Figure 3-4: Beat note measurement obtained between two DFBs. The linewidth of each DFB corresponds to half of the beat-note linewidth. The black solid line represents the Lorentzian fit of the data.

The difference in the linewidth (18(4) MHz with FP measurements and 14.2(4) MHz with the beat note) can be explained by the different optical powers used in these two measurements, since the linewidth depends on the optical output power [16]. It is also

possible that the second laser in the beat-note measurement had significantly narrower linewidth, leaving the “measured” laser with the linewidth of 20 MHz or more. However, including the error of the measurements we can conclude that the laser linewidth is in the range of 14-18(4) MHz.

3.1.3 Laser noise

Relative intensity noise (RIN) can be one of the limitations of the clock short-term stability and therefore needs to be low. RIN was measured with a photodetector and a FFT spectrum analyser for different optical output powers of the DFB. For the case of the DFB laser emitting at 894.6 nm a $\text{RIN} \leq 10^{-11}$ /Hz is found at frequencies ≥ 100 Hz, see Figure 3-5:

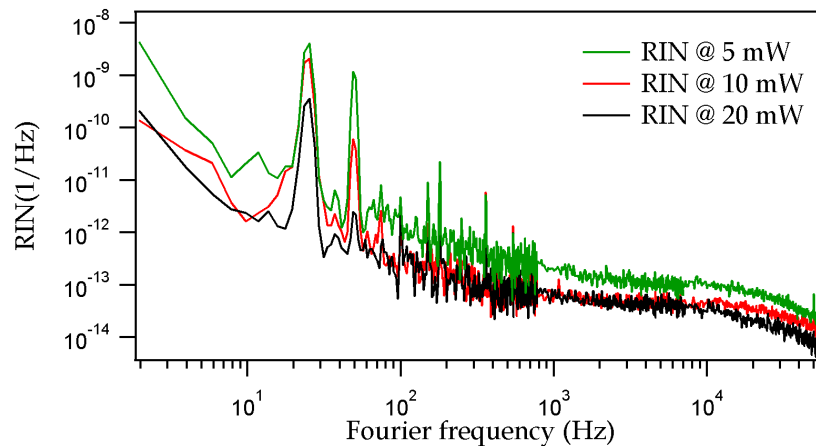


Figure 3-5: RIN for different output powers of a DFB emitting at 894.6nm.

The frequency noise (S) of the laser also adds to the noise budget of the atomic clock. The frequency noise was measured by translating it into intensity noise on the steep discriminator slope (C) at the side of the Cs atomic absorption signal, and subtracting the pure intensity noise measured with the laser tuned out of the atomic absorption (see Figure 3-6):

$$S^2 = \frac{U_{\text{Cs-locked}}^2 - U_{\text{laser}}^2}{C^2} \quad (3.3)$$

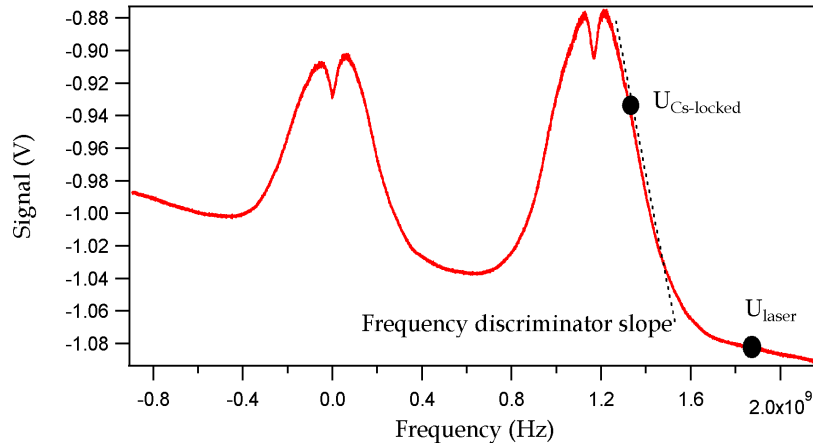


Figure 3-6: Saturated absorption signal used to measure the FM noise. Dashed black line indicates discriminator slope.

The frequency noise spectra were measured with a FFT spectrum analyser showing the $1 \times 10^8 \text{ Hz}^2/\text{Hz}$ at 300 Hz and $2 \times 10^7 \text{ Hz}^2/\text{Hz}$ at 50 kHz, Figure 3-7.

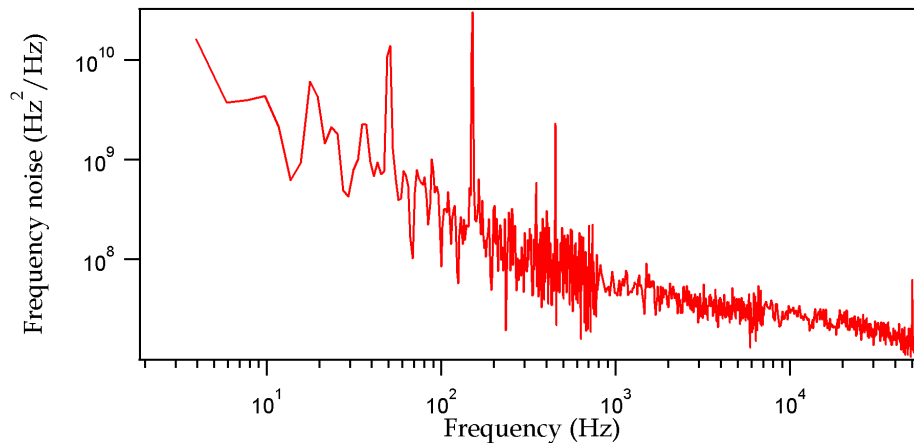


Figure 3-7: FM noise of a DFB laser emitting at 894.6 nm.

Using the PSD of the laser's frequency fluctuations $S(f)$ it is possible to calculate the laser linewidth using an approximated equation for the case when FM noise is sufficiently high so that one can neglect correcting for the β line [17]:

$$\text{FWHM} = \sqrt{8 \ln 2 A} \quad (3.4)$$

where A represents the integral over $S(f)$. In our case $A = 49(2) \text{ MHz}$ and the resulting laser linewidth is $\text{FWHM} = 16(1) \text{ MHz}$. This calculated linewidth shows a good agreement with the measured values given in section 3.1.2.

3.1.4 Laser modulation with Electro-Optical Modulator (EOM)

As mentioned at the beginning of this chapter, the DFB laser is modulated using an Electro-Optical Modulator (EOM). Direct current modulation of a DFB laser at 4.6 GHz shows a low efficiency since the DFB laser bandwidth is limited. The EOM principle is shown in Figure 3-8. A EOM consists of a crystal, usually lithium niobate (LiNbO_3) whose refractive index is a linear function of the local electric field strength (created by placing a parallel plate capacitor across the crystal). The simplest type of EOM is a phase modulator, where an electric field changes the phase delay of a laser beam sent through the crystal. When the crystal is exposed to an electric field the phase of the light leaving the crystal is directly proportional to the length of time it took the light to pass through it. Therefore, changing the electric field in the crystal can control the phase of the laser light exiting an EOM.

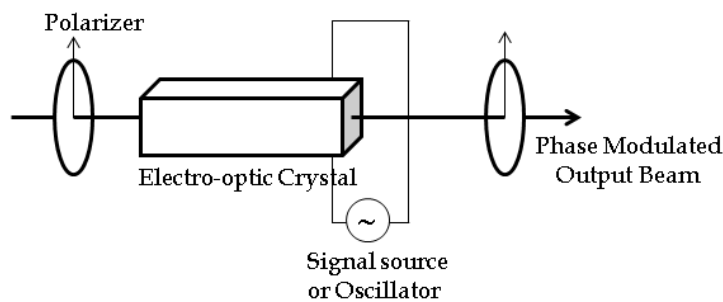


Figure 3-8: Electro-optic phase modulation of a laser beam. The electric field in a LiNiO_3 crystal is modulated to generate sidebands separated at chosen frequency.

The phase modulator combined with other optical elements, in particular with polarizers, represents an amplitude modulator - modifying the polarization state and a polarizer for subsequently converting this into a change in transmitted optical amplitude and power. The EOM used in the Cs CPT experiment with the MEMS buffer gas cell (section 3.3.1) shows the phase and the amplitude modulation of the laser frequency while the EOM used in experiment with the Rb wall-coated cell (discussed in section 3.3.2) shows only laser frequency phase modulation. This difference arises from the different modulation frequencies (in the case of Cs CPT the modulation frequency is $\nu = \nu_{\text{Cs}}/2 = 4.6$ GHz and in the case of Rb CPT $\nu = \nu_{\text{Rb}} = 6.8$ GHz).

If we apply a sinusoidal voltage with angular frequency ω_{RF} to the EOM crystal the modulation results in amplitude and phase modulation. The modulated laser field is given by [18]:

$$\begin{aligned}
E(t) &= \frac{E_0}{2} [1 + R \sin(v_{RF}t + \Psi)] e^{i(v_0 t + M \sin(v_{RF}t))} + c. c. \\
&= \frac{E_0}{2} \sum_{k=-\infty}^{+\infty} a_k e^{i(v_0 t + k v_{RF} t)} + c. c.,
\end{aligned} \tag{3.5}$$

where R is the amplitude modulation index, M the phase modulation index, Ψ the relative phase between frequency and amplitude modulation, and a_k are the coefficients of the Fourier expansion. These coefficients can be expressed in terms of Bessel functions J_k :

$$a_k = J_k(M) - i \frac{R}{2} J_{k-1}(M) e^{i\Psi} + i \frac{R}{2} J_{k+1}(M) e^{-i\Psi} \tag{3.6}$$

The optical power of the k th sideband is proportional to $|a_k|^2$. Formulas (3.5) and (3.6) show the modulated laser field: the laser emission is a multi-frequency field composed of the carrier ($k=0$) and sidebands ($k \neq 0$). The frequency spacing between two nearby components is equal to ω_{RF} . The fraction of the total power contained in the k th sideband, deduced from the coefficient a_k is:

$$S_k = \frac{J_k^2(M) \left(1 + 2k \frac{R}{M} \sin \psi + k^2 \left(\frac{R}{M} \right)^2 \right) - \frac{R^2}{2} J_{k-1}(M) J_{k+1}(M) (1 + \cos 2\psi)}{1 + \frac{R^2}{2}}, \tag{3.7}$$

with the normalization of $\sum_k S_k = 1$. If the amplitude modulation is negligible ($R \ll M$), then the $S_k = J_k^2(M)$.

In order to determine the phase modulation index M for the laser frequency modulation of 4.6 GHz, the laser spectrum was recorded using a Fabry-Perot cavity, for different values of microwave (P_{RF}) power.

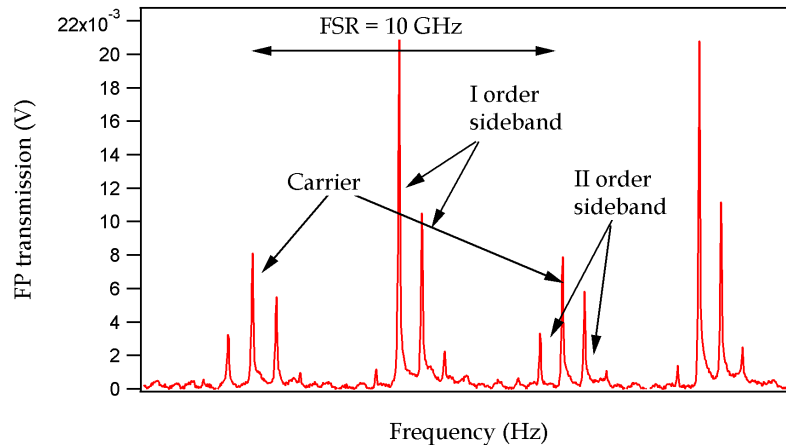


Figure 3-9: The spectrum of the DFB modulated at 4.6 GHz, sampled by a Fabry-Perot interferometer scanning. The spectrum was obtained by measuring the transmission of a Fabry-Perot cavity with free spectral range FSR=10 GHz. The x-scale represents the laser frequency.

An example of such a spectrum, for microwave power of $P_{RF}=3.5$ dBm is shown in Figure 3-9. The amplitude of the first-order sidebands shows that 35(2) % and 18(2)% of the optical power are transferred to the +1st and -1st first-order sidebands, respectively; 14(2) % is in the carrier, while the remaining power is distributed over higher-order sidebands. This corresponds to $M=1.8$, $R=0.6$ and $\Psi=\pi/7$. This evaluation has been done for different microwave powers and the normalized transmission of the carrier and the first-order sideband versus microwave power in dBm is displayed in Figure 3-10.

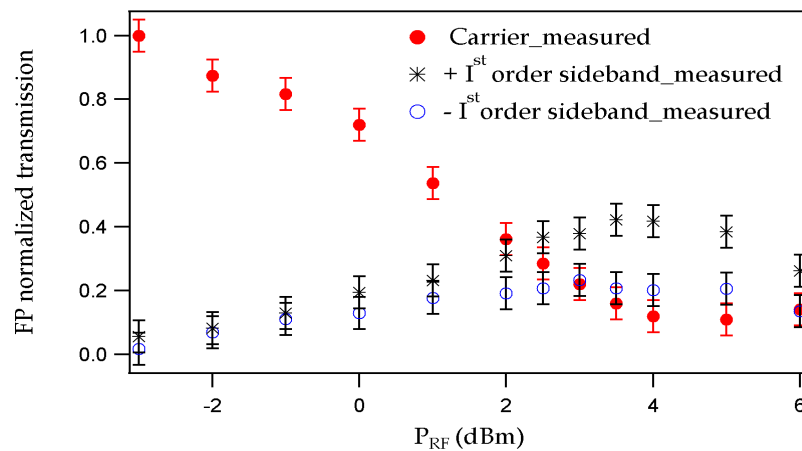


Figure 3-10: Normalized transmission of the carrier and the first-order sideband versus RF power in mW. Conversion between dBm and mW is P (mW) $=10^{P(\text{dBm})/10}$.

In the case of 4.6 GHz modulation, the two first-order sidebands are used to create CPT. Therefore, maximum optical power in two first-order sideband is needed. Figure 3-10 shows that this is the case when $P_{RF}=3.5$ dBm=2.23 mW.

Figure 3-11 shows the relative sideband power as function of M , where solid lines represent fits to equation (3.6) for the k^{th} -order sideband, with $k=0$ and $k=\pm 1$.

The amplitude modulation index R and the phase Ψ are chosen to be close to the experimental results observed in this experiment and fitted parameter is M . The experimental results show good agreement with the theory. The ratio between the carrier and the sideband amplitude is equal to the ratio between the corresponding functions S_k calculated from (3.7).

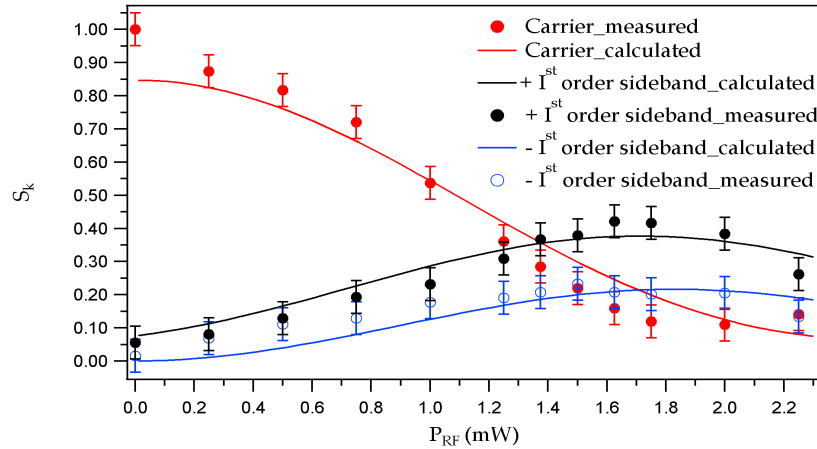


Figure 3-11: Sideband amplitudes as function of RF power. The red solid line represents the amplitudes of the carrier. Blue and black solid lines represent the negative and positive first-order sideband amplitudes, respectively. All solid lines represent the calculations using equation (3.7). The red marker represents the measured carrier amplitude. Blue circles and black stars are measured negative and positive first-order sideband amplitudes, respectively. The P_{RF} (mW) is linearly scaled with the fitted scaling factor of $\pi/9$ in order to have the results as function of M .

3.2 Micro-fabricated (MEMS) and glass-blown cells

As mentioned before, vapor cells, placed at the heart of a conventional gas-cell atomic clock, contain alkali atoms. They are usually made from fused quartz glass or borosilicate glass and of cylindrical, spherical or cubical shape. Beside alkali atoms, these cells contain either buffer gases or their inner walls are coated with an anti-relaxation material (see sections 2.2.4 and 2.2.5). Results discussed in this thesis are obtained from four different types of vapor cells. These cells are different in size, content and cell production technique:

Micro-fabricated Cs (MEMS) cells:

- 4x6 mm single buffer gas cell (FEMTO cell), section 3.2.1
- 4x6 mm single and mixture buffer gas cell (PWL cell), section 3.2.2
- 10x10 mm buffer gas mixture cell (SAMLAB-LTF cell), section 3.2.3

Glass-blown ^{87}Rb cell:

- 14x14 mm ^{87}Rb glass-blown wall-coated cell, section 3.2.4

3.2.1 The Cs MEMS single buffer gas cell (FEMTO cell)

The FEMTO cell (made by FEMTO-ST, France) consists of a glass/silicon (Si)/glass structure containing two cavities as described in [19] and shown in Figure 3-12. The dimensions of a single cell chip are (4x6) mm and 2.4 mm thick (inner dimensions are (3.7x4.7) mm and 1.4 mm thick). The first cavity contains a Cs metallic dispenser while the second cavity (2 mm diameter and 1.4 mm length) is devoted to be the volume where the CPT interaction takes place. Both cavities are connected through filtration channels.



Figure 3-12: The FEMTO cell photo. The microcell has two cavities: in one is a Cs dispenser and the second is CPT detection cavity.

In the first step of the cell production, a glass wafer is anodically bonded to the Si wafer in which both cavities are realized by deep reactive ion etching techniques. A Cs dispenser is then placed in the first cavity. In a second step the cell is completely sealed by anodically bonding a second glass wafer on the top surface of the Si wafer in a buffer gas atmosphere (Ne) at the desired pressure. After complete sealing of the cell, the Cs dispenser is heated by a high-power 808 nm laser source in order to generate Cs vapor that migrates into the second cavity. The activation time is typically 1-6 minutes for a laser power of 1.25 W. This technique is expected to allow keeping a stable atmosphere

inside the cell because Cs vapor activation is done after the anodic bonding process that requires high temperatures (623 K).

After fabrication, absorption measurements are performed to confirm the presence of Cs and buffer gas inside the micro-fabricated cell. For this purpose, the optical beam of an 894.6 nm DFB is split into two directions and sent through the microcell and a cm-scale pure Cs reference cell. The transmitted optical power at the output of each cell is then monitored by a low noise photodiode. Figure 3-13 shows the optical linear absorption spectrum of the Cs D1 transition obtained for a microcell filled with a nominal Ne pressure of 50 Torr for different temperatures compared to the spectrum obtained from the Cs evacuated reference cell at a temperature of $T_c=294$ K.

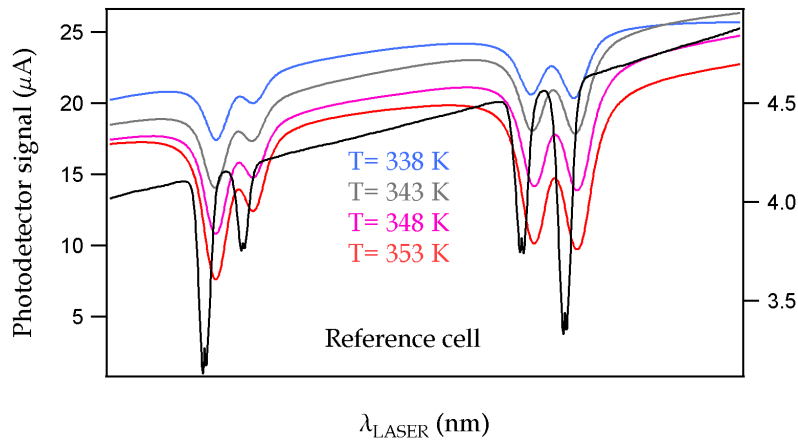


Figure 3-13: Optical absorption lines (Cs D1 line) obtained in a micro-fabricated cell filled with an expected Ne pressure of 50 Torr (estimated to be 46 Torr after sealing of the cell, calculated from the total buffer gas shift and broadening) at various temperatures compared to absorption lines obtained in a centimeter-scale pure Cs reference cell at $T_c=294$ K.

The broadening and red shift of the optical absorption lines demonstrate the presence of buffer gas in the microcell. In this example, employing data reported in reference [19], the actual buffer gas pressure in the microcell is measured to be about 46 Torr since optical broadening is ~ 500 MHz and optical shift ~ 135 MHz. Thermal aging behavior has been investigated to verify that the internal cell atmosphere remains constant over time. The lifetime of the cell is estimated by the so-called $Q_{10} = 2$ method, assuming that the rate of aging increases by a factor of 2 for every 10 K increase in temperature. Usually, 50-100 days-long thermal tests are performed at 373 K during which absorption lines are recorded periodically. These tests showed that the lifetime of these cells is expected to be at least 220 days at $T_c=353$ K [19].

3.2.2 The Cs MEMS single and mixture buffer gas cell (PWL cell)

PWL cells (produced by Politechnika Wroclawska, Poland) have the same dimensions and are fabricated in the same way as the FEMTO cells (discussed in section 3.2.1). The only difference between these cells and cells made by FEMTO is that they were filled with a buffer gas mixture also. More than five cells were characterized: filled with both, Ar and Ar-Ne mixtures. Absorption measurements are performed to confirm the presence of Cs and buffer gas inside the micro-fabricated cell.

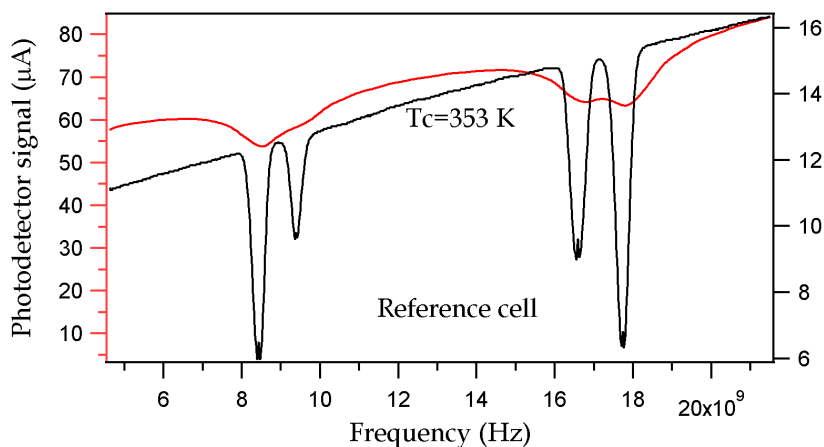


Figure 3-14: Optical absorption lines (Cs D1 line) obtained in a PWL micro-fabricated cell filled with an expected Ar-Ne pressure of 180 Torr (estimated to be 68 Torr after sealing of the cell, calculated from the total buffer gas shift and broadening) at cell temperature $T_c=353$ K (red curve), compared to absorption line obtained in a centimeter-scale pure Cs reference cell at $T_c=294$ K (black curve).

3.2.3 The Cs MEMS cell with buffer gas mixture (SAMLAB-LTF cell)

The SAMLAB-LTF cell, produced in collaboration of SAMLAB and LTF, Neuchatel (Switzerland) is shown in Figure 3-16. The outer dimensions of a single cell chip are (10x10) mm and 3 mm thickness, with an internal cell volume of 5 mm diameter by 2 mm height occupied by the Cs atomic vapor. This cell is made by using the anodic bonding technique. The difference between this cell and the cell described in 3.2.1 is in the cell dimensions and the number of the cell cavities (only one cavity) [21]. The cell holds the buffer gas mixture of Ar-N₂. Linear laser absorption studies are not performed on this cell. The temperature shift of the clock using this cell is discussed in Chapter 4 (see section 4.1.3).

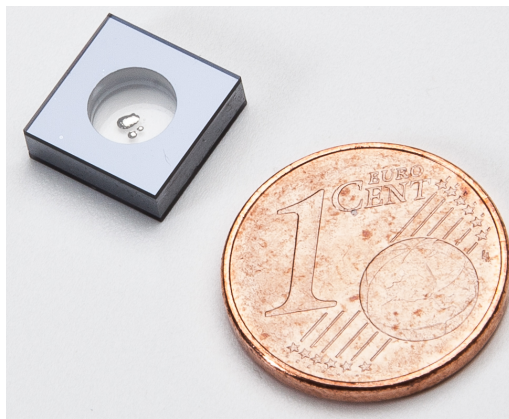


Figure 3-15: SAMLAB-LTF cell. The outer dimensions of a single cell chip are 10x10 mm and 3mm thickness, with an internal cell volume of 39 mm³ (5 mm diameter, 2 mm height).

3.2.4 The glass-blown ⁸⁷Rb cm-scale wall-coated cell

The ⁸⁷Rb glass-blown wall-coated cell is shown in Figure 3-17. The inner (outer) dimensions are diameter $d=12$ (14) mm and length $L=12$ (14) mm. Purified tetracontane (C₄₀H₈₂) is applied on the inner walls by vapor deposition. This cell was procured in an external collaboration.

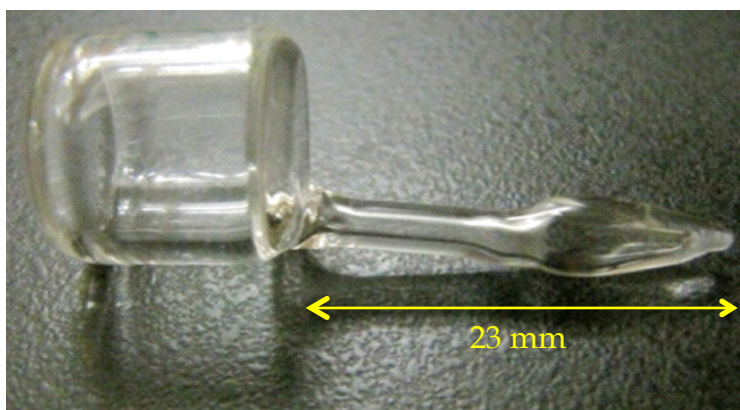


Figure 3-16: Tetracontane coated ⁸⁷Rb cell. This cylindrical cell is 14 mm long and has 14 mm diameter. The cell stem (reservoir), depicted with the yellow arrow is 23 mm long.

Purpose of the stem is to keep the metallic rubidium away from the coated surfaces. Since the coating material is sensitive to the temperature, the cell temperature must be carefully controlled and not go above $T_c=352$ K which is the melting temperature of tetracontane [22]. Also, the temperatures of cell volume (T_v) and cell stem (T_s) are maintained at a gradient to avoid formation of Rb droplets on the coated walls ($T_s < T_v$).

Absorption measurements are performed to confirm the presence of ^{87}Rb inside the wall-coated cell. The optical beam of a 795 nm is split into two directions and sent through the wall-coated cell and an uncoated ^{87}Rb reference cell. The transmitted optical power at the output of each cell is then monitored by a low noise photodiode. Figure 3-17 shows the optical linear absorption spectrum of the ^{87}Rb D1 transition obtained for a wall-coated ^{87}Rb cell at $T_v=329$ K and $T_s=321$ K, compared to the spectrum obtained from the ^{87}Rb evacuated reference cell at a temperature of $T_c=308$ K.

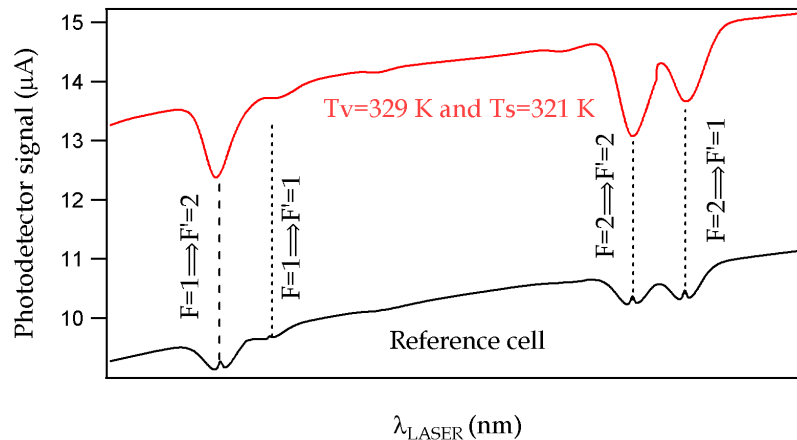


Figure 3-17: Optical absorption line (^{87}Rb D1 line) obtained in a cm-scale cell whose inner walls are coated with tetracontane. Cell volume temperature is $T_v=329$ K and cell stem temperature is $T_s=321$ K. This signal is compared to saturated absorption line obtained in a 10x19 mm pure ^{87}Rb reference cell at $T_c=308$ K.

The LS and TC of the clock using this wall-coated cell are discussed in Chapter 4 (section 4.3).

3.3 Clock experimental setup

There are two different experimental setups which are used for the clock LS and TC measurements given in Chapter 4: the experimental CPT clock using the MEMS Cs buffer gas cell and the experimental DR and/or CPT clock using the cm-scale Rb wall-coated cell. Both experimental setups are described in details in this section.

3.3.1 The CPT clock using the MEMS Cs buffer gas cell

The CPT resonance is prepared using a DFB laser emitting at 894.6 nm, i.e. resonant with the Cs D1-line. The block diagram of the experimental setup is given in Figure 3-18. Two phase-coherent electromagnetic fields, separated by $2\nu \approx \nu_{\text{Cs}} \approx 9.2$ GHz, are generated by modulating the laser frequency at $\nu = \nu_{\text{Cs}}/2 \approx 4.6$ GHz using a fiber-coupled EOM. The two first-order sidebands are used to create the CPT effect. In this experiment 3.5 dBm of RF power (P_{RF}) was applied, resulting in a phase modulation index of $M=1.8$. The 4.6 GHz frequency is generated by a commercial frequency synthesizer (HP 83620A [23]), referenced to a 10 MHz quartz local oscillator. The quartz is compared to a Hydrogen Maser, monitored against a Global Positioning System (GPS) receiver for improved accuracy and stability in our measurements. A beam splitter is placed directly after the EOM in order to split off one part of the optical beam and send it through a 25 mm long and 26 mm diameter glass-blown evacuated Cs reference cell. The resulting absorption signal can be used to stabilize the laser frequency using a standard lock-in scheme.

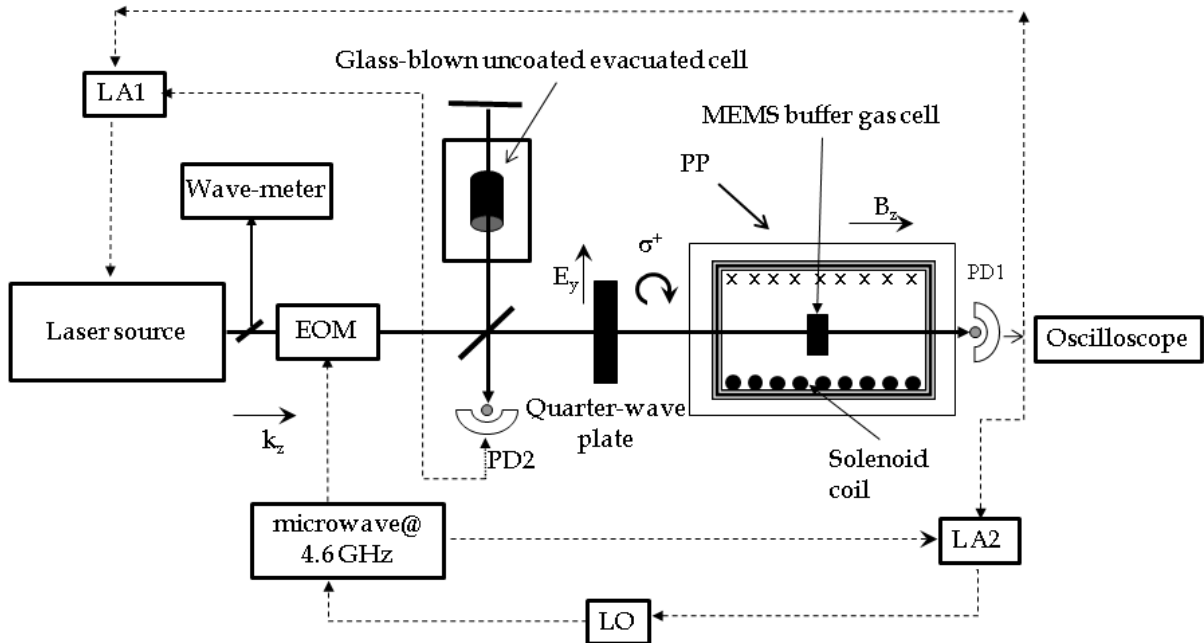


Figure 3-18: Block diagram of the experimental CPT clock using the MEMS Cs buffer gas cell setup. LA1 is a lock-in amplifier operating at 50 kHz, used for laser frequency stabilization. LA2 is a second lock-in amplifier operating at 660 Hz, used to increase signal-to-noise ratio of the clock signal. PD1: photodetector detecting a CPT (clock) signal, PD2: photodetector detecting the saturated-absorption signal from the evacuated cell and PP: physics package. The solid black arrows indicate the optical path and the dashed black arrows the electrical path.

The second part of the laser beam is circularly polarized by a quartz-plate before passing through a MEMS Cs buffer gas cell. This MEMS cell is filled with 75 Torr of Ne and placed in a clock physics package (PP), shown in Figure 3.19, where it is heated and temperature-controlled to a cell temperature T_c in the 318 K to 363 K range (temperature variation $\ll 0.1$ K). Beside the MEMS cell, the PP also contains a solenoid that generates a static magnetic field of $12 \mu\text{T}$ across the cell, oriented parallel to the light propagation vector to split the degeneracy of the Zeeman sublevels. Finally, two concentric μ -metal magnetic shields (thickness of 1.1 mm and 0.8 mm, length of 45 mm and 101 mm and width of 32 and 92 mm, respectively) to reduce perturbations from external magnetic fields complete the PP.

At the entrance to the MEMS cell the laser beam has a Gaussian profile with diameter 2.08 (2) mm, centered with respect to the cell diameter. A Si photodiode PD1 is placed directly after the physics package to detect the transmitted CPT signal. CAD design of the physic package is shown in Figure 3-19.

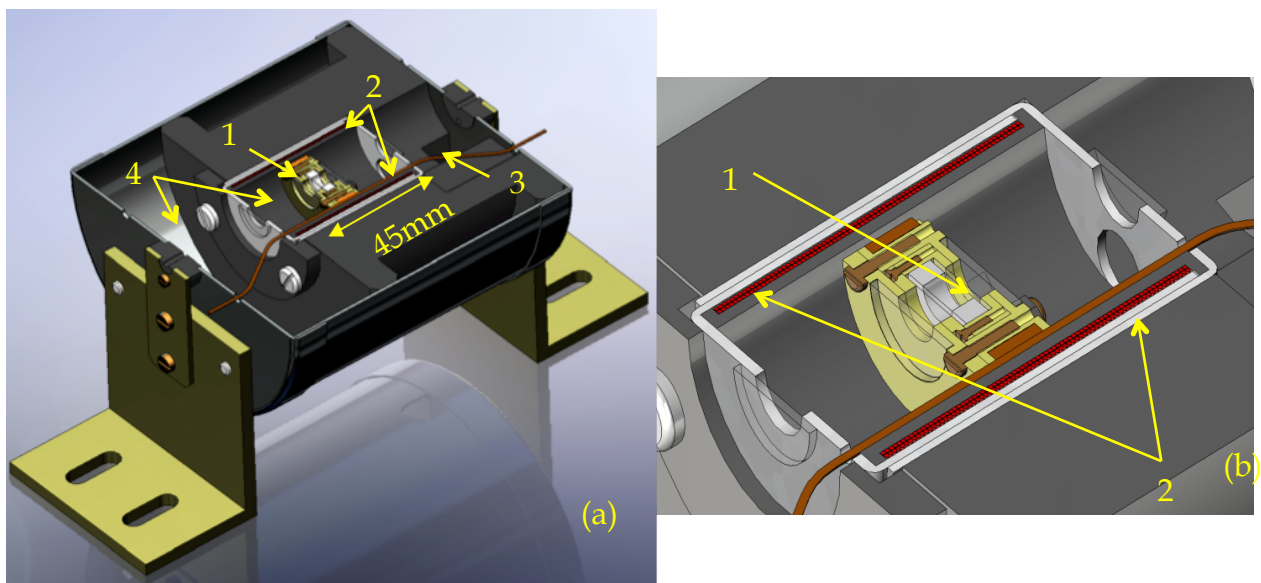


Figure 3-19: (a) CAD design view of Physic Package (PP). Number 1 labels the MEMS cell support with heater. Number 2 labels the C-field solenoid that generates a static magnetic field, number 3 denotes the demagnetization wire and number 4 shows two μ -metal magnetic shields. (b) CAD design view of Physic Package (PP), zoom on the cell holder. Number 1 labels the MEMS cell support. Number 2 labels the coils for producing the magnetic field.

A photo of the experimental setup is shown in Figure 3-20.

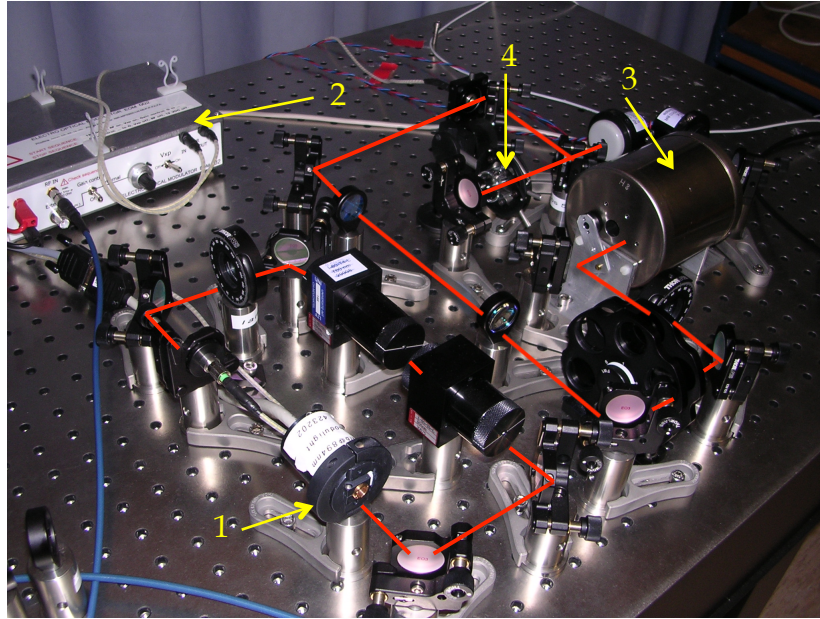


Figure 3-20: CPT experimental setup, using the MEMS Cs buffer gas cell. The red line indicates the laser beam path. 1 label DFB laser; 2 shows EOM driver; 3 denotes PP and 4 shows the reference cell.

3.3.2 The DR and/or CPT clock using the cm-scale Rb wall-coated cell

The experimental setup, shown in Figure 3-21 represents the clock scheme for the ^{87}Rb wall-coated cell, which can be operating in both regimes: DR and/or CPT. Previous studies of the influence on the laser source to the clock based on the $|\text{lin}| |\text{lin}|$ CPT and studies of light effects in the atomic-motion-induced Ramsey narrowing of CPT resonances in wall-coated cells, using the same identical laser source were published in [24-26]. Studies of the tetracontane wall-shift and temperature shift were reported in [27, 28] in DR clock regime, using the same physic package and wall-coated cell described here.

The light source is a compact laser head (see Appendix B) [29]. Its output frequency is stabilized to sub-Doppler saturated absorption lines of the ^{87}Rb D1 transition (at 795 nm) obtained from a separate Rb cell (see Figure 3-17), and passed through an Electro-Optical Modulator (EOM). At the entrance of the Rb cell, the laser beam is linearly polarized and has a diameter of 5 mm. DR is obtained by injecting the 6.835 GHz microwave signal from the local oscillator (courtesy of L'Istituto Nazionale di Ricerca Metrologica (INRIM), Torino, Italy) [30] into the magnetron cavity [31], whereas CPT is obtained by injecting the microwave into the EOM. The DR or CPT photodetector signal is used to stabilize the microwave frequency to the center of the clock transition using a

Proportional/Integrator (PI) feed-back loop. In the CPT case, the microwave modulation frequency is equal to the Rb hyperfine frequency $\nu_{\text{Rb}} = 6.835$ GHz.

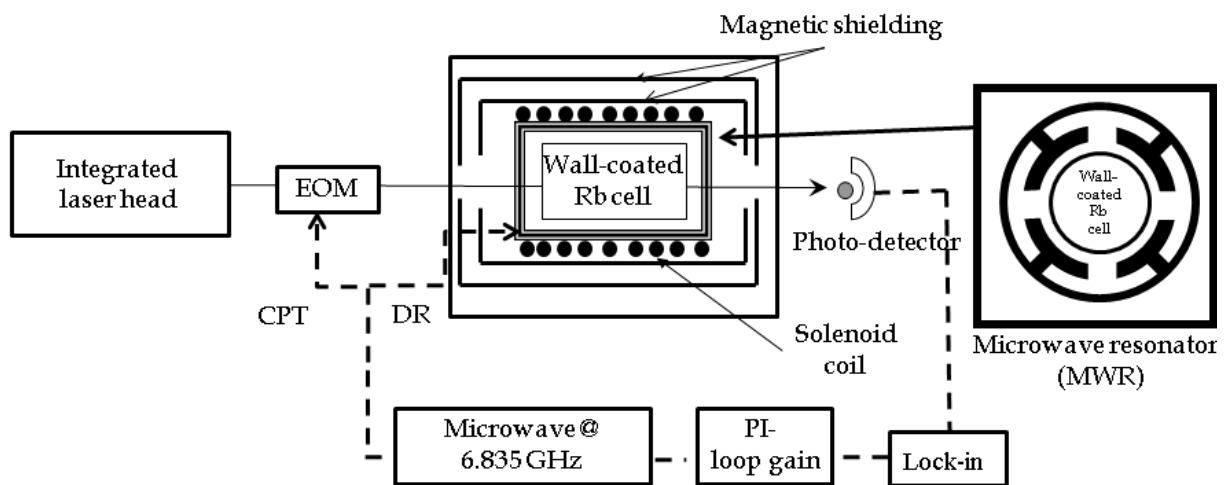


Figure 3-21: Block diagram representing the DR and/or CPT experimental setup using the Rb wall-coated cell setup.

The wall-coated cell is placed inside a magnetron-type microwave resonator (MWR) with TE₀₁₁-like field geometry [27], placed inside the physic package (PP) shown in Figure 3-22.

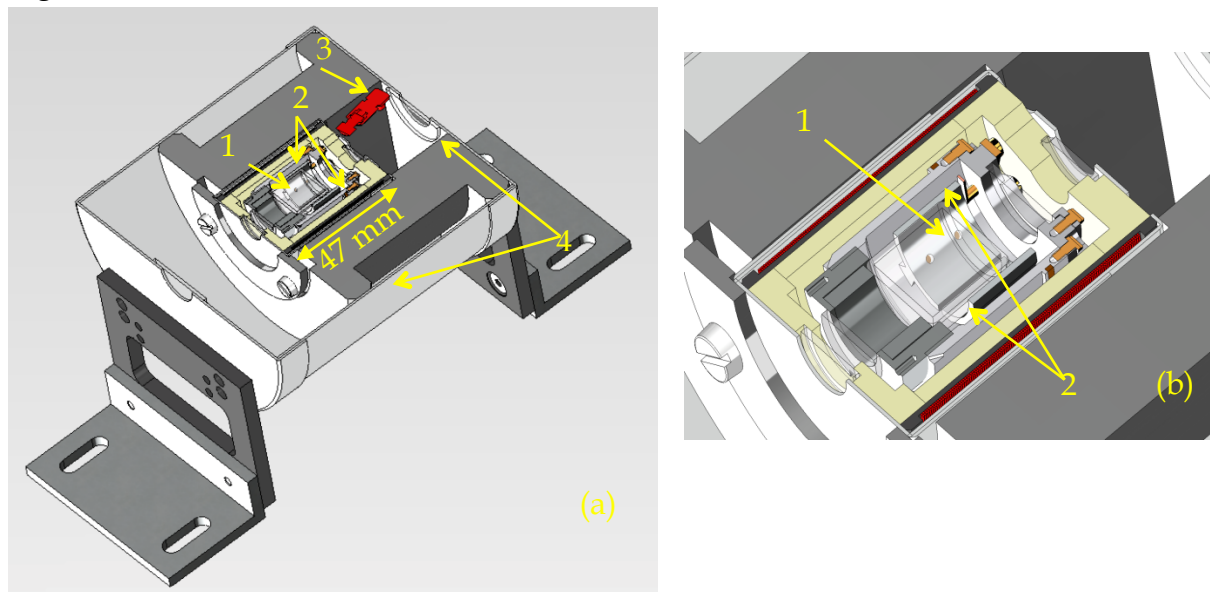


Figure 3-22: (a) CAD design of the Physic Package (PP). Number 1 labels the wall-coated Rb cell support with heater. Number 2 labels the MWR, number 3 denotes the connector for the injecting the 6.834 GHz in MWR and number 4 shows two μ -metal magnetic shields. (b) CAD design view of Physic Package (PP), zoom on the cell holder. (b) Number 1 labels the wall-coated Rb cell support with heater and number 2 labels the MWR.

A solenoid around the MWR generates a static magnetic field parallel to the light propagation vector in order to split the degeneracy of the Zeeman sublevels. Inside the PP the cell volume is heated and temperature-controlled to $T_v=329$ K and the cell stem to $T_s=321$ K (uncertainty $\ll 0.1$ K). The two μ -metal magnetic shields surround the whole ensemble.

The photo of the experimental setup is shown in Figure 3-23. CPT is created when the atoms from the two ground-state levels of the ^{87}Rb atom are coupled to a common excited state, using the laser carrier and one of the laser first-order sidebands. In order to have the highest signal contrast, the modulation index M must be optimized in order to have the maximum power in the carrier and the first-order sideband. The laser spectrum was recorded using a Fabry-Perot cavity, for different values of microwave (P_{RF}) powers (same principle as in Figures 3-10 and 3-11). Normalized transmission of the carrier and the first-order sideband versus RF power in mW is evaluated giving the P_{RF} value for which the carrier and the first-order sidebands have same intensity. For $P_{\text{RF}}=10$ dBm the carrier and the first-order sidebands have approximately the same intensity. The amplitude of the first-order sidebands shows that the 27(2) % and 28(2) % of the optical power are transferred to the +1st and - 1st first-order sidebands, respectively; 38(2) % is in the carrier, while the remaining power is distributed over higher-order sidebands. This correspond to the modulation index $M=1.5$ (amplitude modulation is negligible here, $R \ll M$).

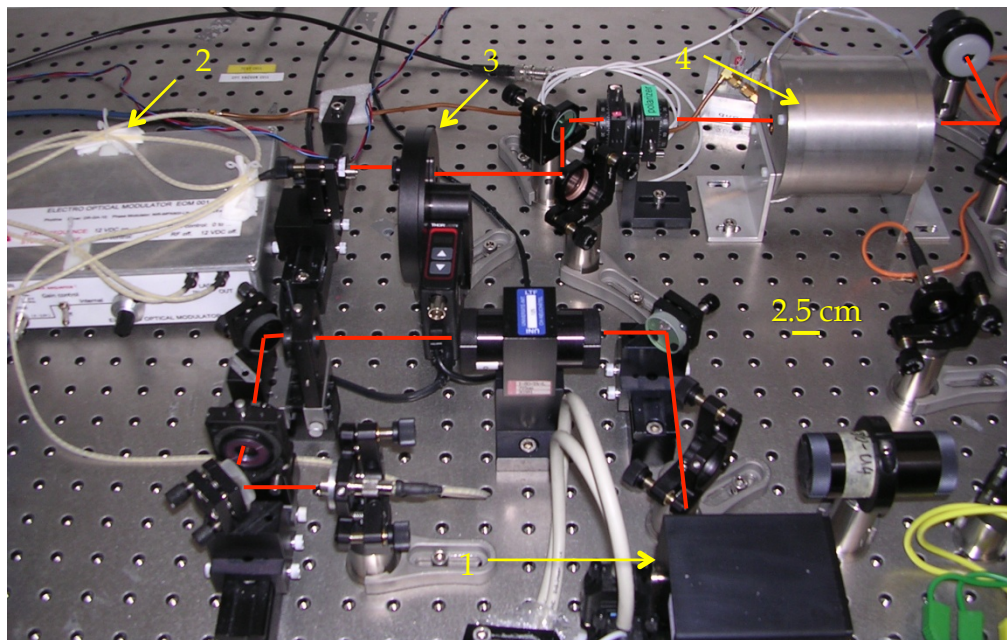


Figure 3-23 The CPT and/or DR experimental setup using the cm-scale Rb wall-coated cell. The red line indicates the laser beam path. 1 labels DFB laser head; 2 shows EOM, 3 denote the rotational holder of neutral density filters and 4 show the PP.

When the laser carrier frequency is stabilized to the $F=2 \rightarrow F'=1$ transition (see Figure 3-18), the carrier and one of the two first-order sidebands are exciting the atoms from the both ground states to a common excited state and CPT occurs; the CPT signal is detected with the photodetector in Figure 3-21.

3.4 DR and CPT signal: first characterization

In this section the two different CPT signals are discussed: the one obtained from the Cs MEMS single buffer gas cell (section 3.2.1), using the experimental setup described in section 3.3.1 and the other obtained from the ^{87}Rb wall-coated cell (section 3.2.3), using the experimental setup described in section 3.3.2. Signal linewidth and amplitudes are evaluated as function of the laser intensities and microwave powers in both cases. The signal discriminator slope D is introduced and optimized in order to have the best clock short-term stability (Chapter 5).

3.4.1 CPT signal obtained from the Cs MEMS cell

The laser frequency can be stabilized using the signal from the Cs reference evacuated cell or the Cs MEMS cell.

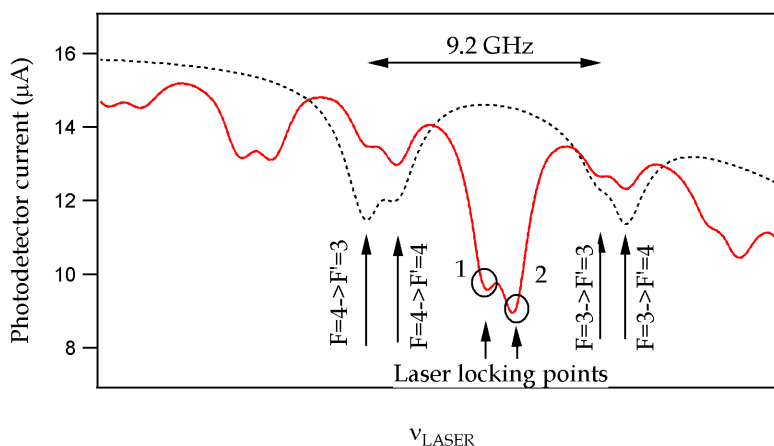


Figure 3-24: Dashed black line: Absorption spectrum obtained with a single, non-modulated light field scanned over the Cs D1 line showing an absorption in the MEMS cell heated to $T_c=353.0(1)$ K. Solid red line: Same spectrum obtained with the modulated light field. Laser locking point 1: coupling via $F'=3$ state. Laser locking point 2: coupling via $F'=4$ state.

In the second case, the laser frequency is stabilized to a broadened line (Voigt profile resulting from Doppler and homogeneous broadening due to the buffer gas inside the MEMS cell). All the results given in this thesis are obtained with the laser frequency stabilized to the MEMS cell (except for the results shown in Figure 4-13 where both cases are discussed).

When the laser frequency is stabilized to the point 1 or 2 in Figure 3-24, the two first-order sidebands are exciting the atoms from the two ground states to a common excited state and CPT occurs; the CPT signal is detected at the PD1 in Figure 3-18. Figure 3-25 shows the typical CPT signal observed for the laser modulation at $\nu=4.6$ GHz, in the case when the laser is stabilized to point 1 in Figure 3-24. The laser intensity is $I_L=1.78$ mW/cm² (all data in this thesis are presented with respect to $2\Delta=\Delta_{Cs}=9.192631770$ GHz). The CPT signal contrast C is the ratio between signal amplitude and signal background ($C=A/BCG$) and it is only few percent in this case - much smaller than the contrast of the typical DR signal [32]. Therefore, to improve signal-to-noise ratio frequency modulation (FM) [33] is performed: the frequency ν is frequency-modulated at 660 Hz and the phase-sensitive CPT signal is detected with a lock-in amplifier (LA2 in the Figure 3-18).

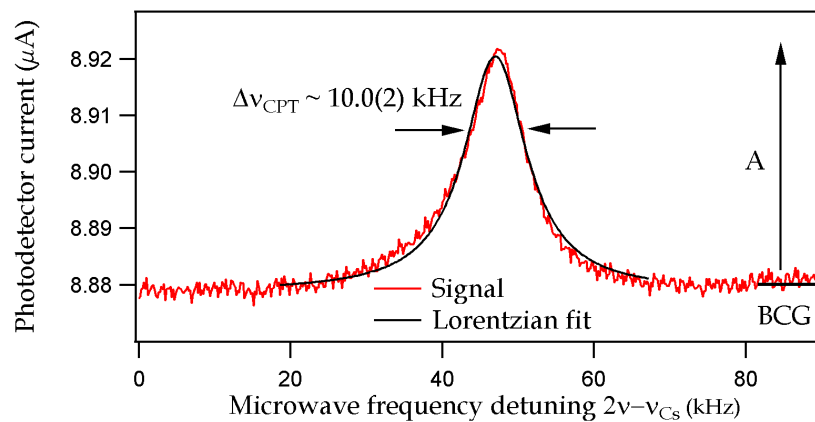


Figure 3-25: CPT signal observed on the Cs MEMS cell heated to $T_c=353.0$ K. The signal amplitude is $A=0.042(2)$ μ A, linewidth $\Delta\nu=10.1(1)$ kHz, and contrast $C=A/8.88$ μ A=0.5 %.

The LA2 extracts the signal in the desired bandwidth by mixing the overall photodiode signal with the applied modulation signal as a reference, giving the two signals: in-phase and quadrature lock-in signal. To retrieve the original line shape the FM spectra can be numerically inverted with the help of a purely analytical algorithm [34]. The obtained in-phase lock-in signal for the same experimental conditions as for Figure 3-25 is shown in Figure 3-26.

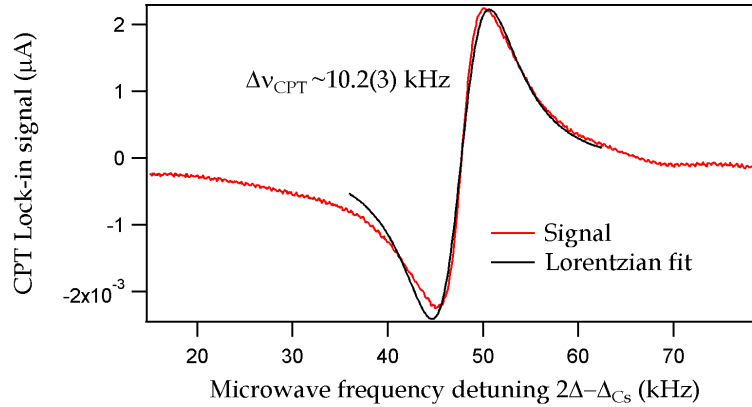


Figure 3-26: Lock-in CPT signal observed on the MEMS cell heated to $T_c=353.0$ K. The frequency $\Delta=4.6$ GHz is frequency-modulated at 660 Hz. The signal amplitude is $A=0.0043(5)$ and linewidth $\Delta\nu_{\text{CPT}}=10.2(3)$ kHz.

The equation for the CPT linewidth calculation (see Chapter 2, Eq. (2.11)), in the symmetric case, can be written as:

$$\Delta\nu_{\text{CPT}} = \frac{1}{\pi} \left(\gamma_{12} + \frac{G}{\Gamma} I \right), \quad (3.7)$$

where $G=g^2/I$ contains all intensity-independent parts of the square of the Rabi frequency. Eq. (3.7) written in this manner shows that the CPT linewidth depends linearly on the laser intensity, which is confirmed by the measurements shown in Figure 3-27 (a). The solid line is the fit of the Eq. (3.7) where γ_{12} and G/Γ are the free parameters. The zero-intensity width is limited by the hyperfine ground-state coherence relaxation rate γ_{12} , estimated from the fit to be $\gamma_{12}=10.6(4)$ rad/s. The broadening rate as function of the laser intensity is $G/\Gamma=12.7(2)$ kHz/(mW/cm²). The CPT linewidth, calculated for the total laser intensity $I_L=1.78$ mW/cm², is $\Delta\nu_{\text{CPT}}=10.6(6)$, which is confirmed by the measurements shown in Figures 3-25 and 3-26.

Comparison of these results with the theoretical calculations obtained in Chapter 2, Table 2-1 shows a difference by factor of 2.5.

Intrinsic linewidth (Hz)	Calculated	Measured
Γ_{12}	1364	3384.4(4)

Table 3-1: Comparison table of measured and calculated intrinsic linewidth Γ_{12} .

A possible difference between expected and sealed buffer gas pressure cannot be the reason for the observed discrepancy, since the total CPT shift is measured (Figure 3-25) and it corresponds to the expected buffer gas pressure of 75 Torr. However, this difference may be explained by the fact that the diffusive equation (2.17) (the biggest contributor to the calculated intrinsic linewidth) is based on the assumption that the

sampled atoms are in a laser beam that is narrow compared to the cell diameter, which cannot be applied in the experiment with the MEMS cell.

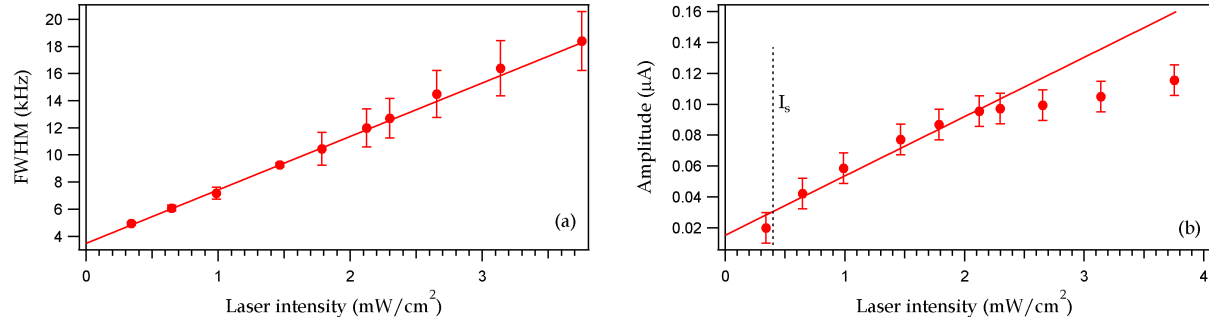


Figure 3-27: (a) CPT resonance linewidth (FWHM) as function of the laser intensity. (b) CPT resonance amplitude as function of the laser intensity. The laser frequency is stabilized to point 2 in Figure 3-20 and the MEMS cell temperature is $T_c=353$ K. Red solid lines represent the fit of the Eq. (3.7) and (3.8), respectively.

For the CPT amplitude based on the same symmetric three-level theory a similar behavior is expected, i.e. a quadratic increase for small laser intensities and a linear rise for larger ones. The equation for the CPT amplitude calculation (see Chapter 2, Eq. (2.12)), in the close symmetric case, can be written as:

$$A_{\text{CPT}} \approx \frac{G^2 I^2}{\Gamma^2} \frac{1}{2\Gamma_{12} + GI/\Gamma} \approx \frac{I^2}{I_s + I} \quad (3.8)$$

For low intensities, i.e., $I \ll I_s = \Gamma_{12}\Gamma/G$, the amplitude is expected to rise quadratically and to increase proportional to I at higher intensities. Using the parameters of the resonance width estimated fitting Eq. (3.7) to the data ($G/\Gamma=4.06(6)$ kHz/(mW/cm²) and $\gamma_{12}=10.7(7)$ Hz), it can be estimated that the CPT saturation intensity is $I_s=0.4(2)$ mW/cm². This result is in the agreement with the experiment shown in Figure 3-27 (b). The dots are the measured values while the solid line is a fit of Eq. (3.8) to the data below 2.3 mW/cm². The value of I_s is taken from the fit to the CPT resonance width and therefore the scaling factor of the amplitude remains the only fit parameter. The CPT resonance amplitude shows linear behavior for higher laser intensities $I > I_s$. The linear fit does not fit for the laser intensities > 2.4 mW/cm², due to the optical intensity saturation effect (for Cs is $I_L=2.5$ mW/cm² [34]). Quadratic behaviors as function of the laser intensity for $I \ll I_s$ is expected but not observed here, due to the limited number of measurement points for low laser intensities.

CPT signal amplitude and linewidth were measured as function of microwave power P_{RF} . The laser frequency is stabilized to point 2 in Figure 3-24 and the Cs MEMS cell temperature is $T_c=353$ K. The measurements are performed with $I_L=2.3$ mW/cm². It is expected that the CPT signal amplitude and signal linewidth show the same behavior as function of P_{RF} . Maximum of the signal amplitude is obtained for the microwave power of $P_{\text{RF}}=3.5$ dBm, for which the most optical power is contained in the two

resonant light fields. For the same P_{RF} the highest CPT width is obtained because maximum optical power is contained in the two resonant light fields and therefore the highest contribution due to the optical broadening is present. Solid lines represent the polynomial fit to the data to guide the eye.

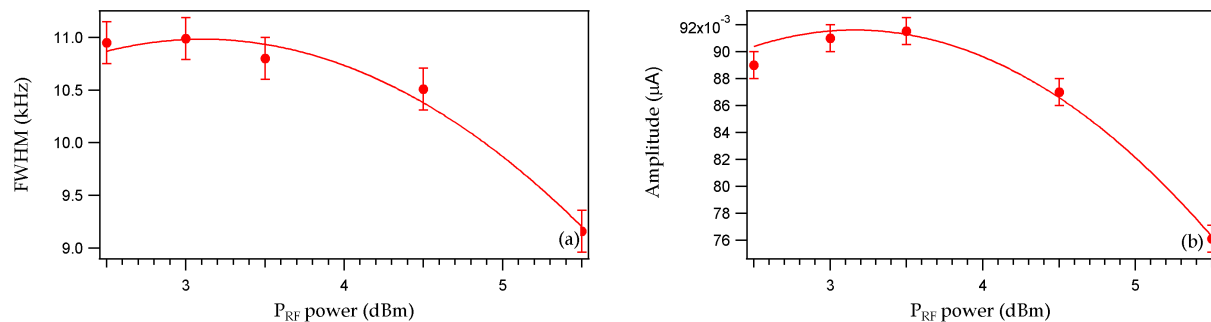


Figure 3-28: (a) CPT resonance linewidth (FWHM) as function of the microwave power P_{RF} . (b) CPT resonance amplitude as function of the microwave power P_{RF} . Solid lines represent the polynomial fit to the data to guide the eye.

The important information for a clock application is the so-called clock signal discriminator slope D . D can be estimated as the ratio between the signal amplitude and signal linewidth ($D \approx A/FWHM$). It has an important impact on the clock stability, see Chapter 1 Eq. (1.16). Therefore it is important to optimize the signal discriminator slope as function of laser intensity and of P_{RF} in order to reach the best possible clock stability. Figures 3-28 (a) and (b) and Figures 3-29 (a) and (b) show that D is optimized for a total laser power $I_L = 1.5 \text{ mW/cm}^2$ and $P_{RF} = 3.5 \text{ dBm}$. In order to clarify the role of the clock discriminator slope Figures 3-29 (a) and 3-29 (b) display the clock discriminator slope D as a functions of laser intensity and microwave power. Red solid lines represent the fit to the data calculated as deviation of two fit functions from Figures 3-27 (a) and (b) and Figures 3-28 (a) and (b), respectively. This information will be useful for the estimation of the clock short-term stability in Chapter 5.

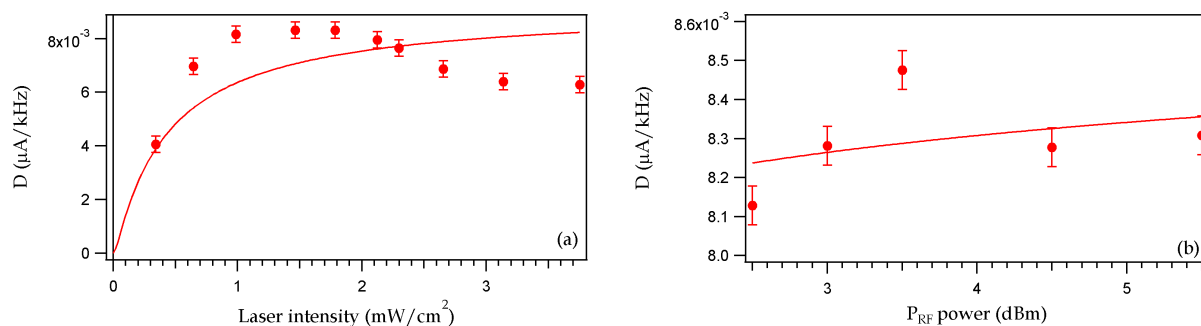


Figure 3-29: (a) CPT resonance discriminator slope D as function of the total laser intensity. (b) CPT discriminator slope D as function of the microwave power P_{RF} . Solid lines represent the polynomial fit to the data to guide the eye.

3.4.2 The DR and CPT signal obtained from the ^{87}Rb wall-coated cell

Figure 3-30 presents typical DR and CPT signals obtained from the ^{87}Rb wall-coated cell, using the experimental setup described in section 3.3.2. In this case the laser modulation is $\nu=6.835$ GHz and total laser intensity is $I_L=0.47$ mW/cm². The wall-coated cell volume and stem temperatures are $T_v=329$ K and $T_s=321$ K, respectively. The laser frequency is stabilized to the $F=2 \rightarrow F'=1$ transition. All the frequency data are given with respect to $\Delta_{\text{Rb}}=6.834682611$ GHz.

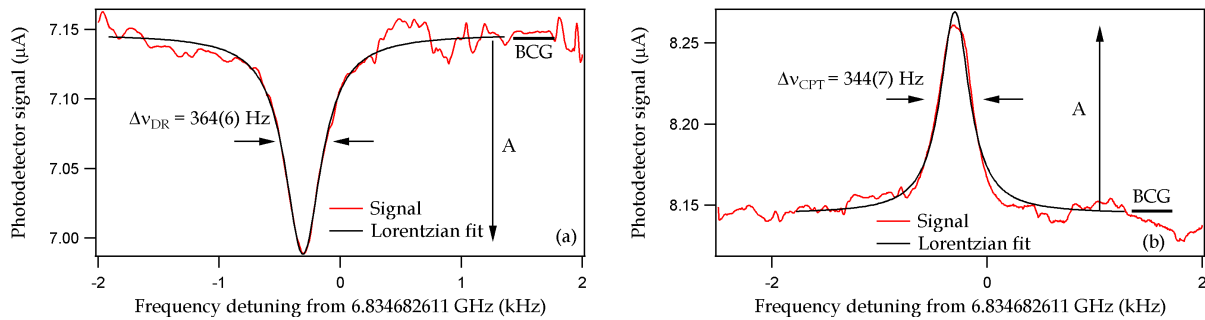


Figure 3-30: DR and CPT signals observed on the Rb wall-coated cell heated to $T_v=329$ K and $T_s=321$ K. DR signal amplitude is $A=0.155(2)$ μA , linewidth $\Delta\nu_{\text{DR}}=364(6)$ Hz, shift from the Δ_{Rb} is $-301(3)$ Hz and contrast $C=A/7.14$ $\mu\text{A}=2.17$ %. CPT signal amplitude is $A=0.126(2)$ μA , linewidth $\Delta\nu_{\text{CPT}}=344(7)$ Hz, shift from the ν_{Rb} is $-288(3)$ Hz and contrast $C=A/8.15$ $\mu\text{A}=1.55$ %.

Like in the previous section, the CPT signal amplitude and the linewidth are evaluated as function of the laser intensity and microwave power, Figures 3-31 (a) and 3-32 (b).

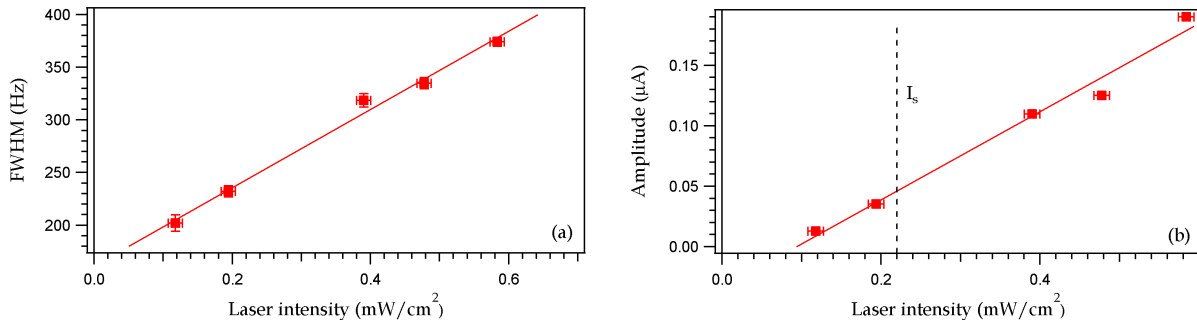


Figure 3-31: (a) CPT resonance linewidth (FWHM) as function of the total laser intensity. (b) CPT resonance amplitude as unction of the total laser intensity. Red solid lines represent the fit of the Eq. (3.7) and (3.8), respectively.

The DR signal linewidth and amplitude show the same behavior like the CPT signal linewidth and amplitude shown in Figure 3-31 (a) and Figure 3-31 (b) and therefore will not be presented in detail here. Equations (3.7) and (3.8) can be also applied in this case. The only difference from the buffer gas Cs MEMS cell is the hyperfine ground-state

coherence relaxation rate γ_{12} (calculated for the buffer gas cell, see Table 2-1). (3.7) predicts a linear increase of the CPT resonance width with intensity, which is well in agreement with the experimental data shown in the figure 3-31 (a). The solid line in Figure 3-31 (a) is a fit of the Eq. (3.7), with γ_{12} and G/Γ as free parameters. The zero-intensity width is limited by the hyperfine ground-state relaxation rate γ_{12} , estimated from the fit to be $\gamma_{12}=505.4(7)$ rad/s. The broadening rate as function of the laser intensity is $G/\Gamma=1166.5(6)$ Hz/(mW/cm²). γ_{12} is limited by the atom-wall coating collisions [35], the spin-exchange collisions (see Eq. 2.4) and the contribution from the atoms escaping through the Rb reservoir [36].

The contribution to the signal linewidth of the spin-exchange can be evaluated by using the equation:

$$\Gamma_{SE} = 2 \frac{5}{8\pi} n \sqrt{2} v_R \sigma_{SE} \approx 4 \text{ Hz} \quad (3.9)$$

v_R is the mean relative atom velocity defined in (2.14), n is the density of Rb atoms ($n_{\text{atom}}=1 \times 10^{11}$ atoms/cm³ for $T_s=329$ K, see Figure 1-7) and σ_{SE} is the cross-section of spin exchange collisions between ⁸⁷Rb atoms $\sigma_{SE}=(1.6 \pm 0.2) \times 10^{-14}$ cm² [37].

The linewidth contribution due to reservoir losses (hole contribution), in our case the channel from the reservoir to the cell cavity, is given by [38]:

$$\Gamma_{\text{hole}} = 2 \frac{a}{\pi V} v_s \approx 116 \text{ Hz}, \quad (3.10)$$

where V is the volume of the cell cavity, a is the area of the hole and v_s the mean atom velocity. For a $d_h=1.0(0.1)$ mm diameter hole, Γ_{hole} is at level of 116(7) Hz.

The contribution $\Gamma_{\text{wall-coll}}$ from the collisions between the Rb-atoms and the coating (which depends on the cell geometry) can be written as [39]:

$$\Gamma_{\text{wall-coll}} = 2 \frac{\Phi^2}{\pi} v_{\text{coll}} \approx 24 \text{ Hz} \quad (3.11)$$

for Rb phase shifts per collision in tetracontane of $\Phi=0.03$ rad [38] and $v_{\text{coll}}=v_s/l$ is the average collisional rate between atoms and walls of the cell. v_s is the mean atom velocity and l is the mean distance between two collisions and depends on the geometry of the cell.

The total intrinsic linewidth Γ_{12} is calculated to be $\Gamma_{12}=144(7)$ Hz. Comparison of these results with the theoretical calculations obtained in Chapter 2 shows a good agreement:

Linewidth (Hz)	Calculated	Measured
Γ_{SE}	4	
Γ_{hole}	116	
$\Gamma_{wall-coll}$	24	
$\Gamma_{12} = \Gamma_{SE} + \Gamma_{hole} + \Gamma_{wall-coated}$	144(7)	161.2(7)

Table 3-2: Comparison table of measured and calculated intrinsic linewidth Γ_{12} .

For the CPT amplitude the same symmetric three-level theory agrees similarly well with the experiment. Using the parameters of the resonance width $G/\Gamma=1166.5(6)$ kHz/(mW/cm²) and $\Gamma_{12}=161.2(7)$ it can be estimated that the CPT saturation intensity is $I_s=0.22(2)$ mW/cm². It cannot be concluded if this result is in agreement with the experiment shown in Figure 3-31 (b) due to the small number of measurement data. The dots are the measured values while the solid line is a fit of Eq. (3.8) to the data. The value of I_s is taken from the fit to the CPT resonance width and therefore the scaling factor of the amplitude remains the only fit parameter. The CPT resonance amplitude shows linear behavior for higher laser intensities $I>I_s$. Quadratic behaviors as function of the laser intensity for $I<I_s$ is expected but not observed here, due to the limited number of measurement points for low laser intensities.

In Figure 3-32 the CPT signal amplitude and linewidth is evaluated as function of microwave power P_{RF} .

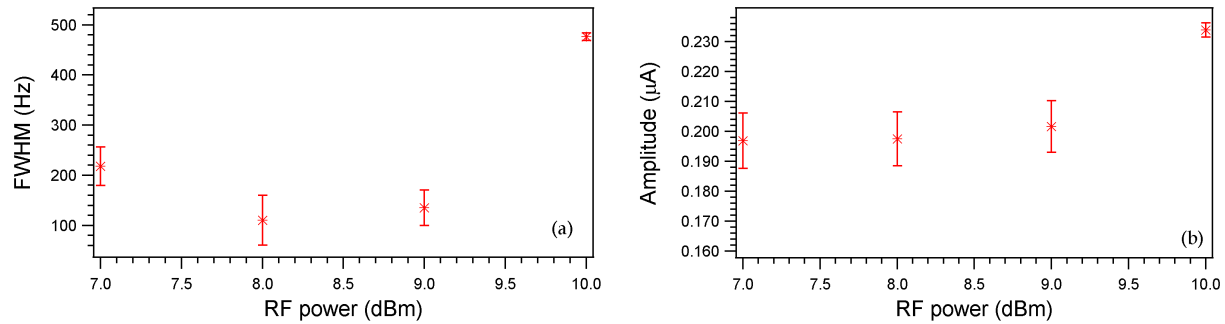


Figure 3-32: (a) CPT resonance linewidth (FWHM) as function of the P_{RF} . (b) CPT resonance amplitude as function of the P_{RF} .

The measurements are performed with $I_L=1.06$ mW/cm². The laser frequency is stabilized to the transition $F=2 \rightarrow F'=1$ and the wall-coated cell temperature is $T_v=329$ K and $T_s=321$ K. Maximum of the signal amplitude is obtained for the microwave power where most optical power is contained in the two resonant light fields, i.e. for $P_{RF}=10$ dBm. For the same P_{RF} the highest CPT width is obtained because maximum optical power is contained in the two resonant light fields and therefore the highest contribution due to the optical broadening is present.

It is expected that the CPT signal amplitude and signal linewidth show the same behavior as in the case of the MEMS cell (section 3.4.1). In Fig. 3.28 (a) and (b) signal amplitude and linewidth are decreasing with the microwave power, while in Fig. 3-32 (a) and (b), signal amplitude and linewidth are increasing with the microwave power. The explanation is following: in the case of the MEMS cell, laser frequency modulation is $\nu=4.6$ GHz and the two first order sidebands (+1st=35(2) % and -1st=18(2) %) are used for creating the CPT. For wall-coated cell laser frequency modulation is $\nu=6.8$ GHz and CPT is created by the carrier (38(2) %) and one of the first order sideband (~27(2) %). Since different laser sidebands are used in these two different experiments, their respective powers and thus the optical Rabi frequencies will vary differently when the microwave power P_{RF} drive power is changed.

The discriminator slope D is optimized as function of laser intensity and as function of P_{RF} in order to reach the best possible clock stability. Figure 3-33 (a), (b) shows that D is optimized for $I_L=0.58$ mW/cm² and $P_{RF}=10$ dBm, for the studied range of I and P_{RF} . This information will be used for the estimation of the clock short-term stability in Chapter 5. Figure 3-34 (a) and Figure 3-34 (b) present the clock discriminator slope D as functions of laser intensity and microwave power. Solid lines represent the polynomial fit to the data to guide the eye. This information will be useful for the estimation of the clock short-term stability in Chapter 5.

Similar explanation given by comparison of Fig.3-28 and 3-32 can be applied to the comparison of Fig. 3-33 (a) and Fig 3-29 (a) and comparison of Fig. 3-33 (b) and Fig. 3-29 (b).

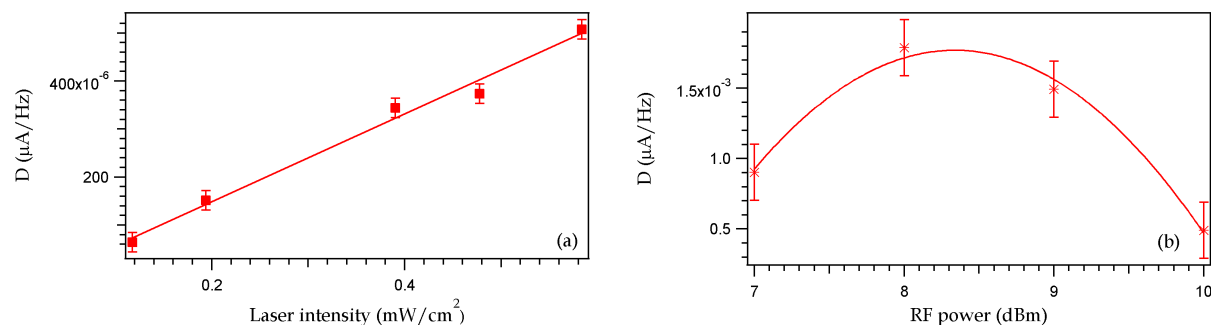


Figure 3-33: (a) CPT resonance discriminator slope D as function of the laser intensity. (b) CPT resonance discriminator slope D as function of the microwave power P_{RF} . Solid lines represent the polynomial fit to the data to guide the eye.

3.5 Summary and conclusions

Chapter 3 described the laser source used in the experiment with the MEMS Cs buffer gas cell (the laser used in the experiment with the ^{87}Rb wall-coated cell is described in Appendix B). The linewidth of this laser at 894.6 nm is determined with two different experimental methods: using the Fabry-Perot interferometer and with the beat-note measurement. With these two methods different linewidths are obtained: 18(4) MHz and 14.2(4) MHz, possibly due to the different optical power used in these measurements. The laser modulation technique was introduced and modulation indices are evaluated for the modulation frequency of $\nu=4.596$ GHz ($R=0.6$, $\varphi=\pi/7$ and $M=1.8$). The two experimental setups used in this thesis and the three different vapor cells used in the experiments are described. The two different CPT signals (obtained from the Cs MEMS single buffer gas cell and the one obtained from the ^{87}Rb wall-coated cell) are discussed. Signals linewidth and amplitude are measured as function of the laser intensity and the microwave power. These values are compared to the theoretical values calculated using the equations introduced in Chapter 2. In the case of Cs MEMS cell the intrinsic linewidth Γ_{12} is expected to be $\Gamma_{12}=1364$ Hz (the main contribution comes from the atom-cell walls collisions). The measured value is $\Gamma_{12}=3384.4(4)$ Hz. This difference may be explained by the fact that the diffusive equation (2.17) (the biggest contributor to the calculated intrinsic linewidth) is based on the assumption that the sampled atoms are in a laser beam that is narrow compared to the cell diameter, which is not fulfilled in the experiment with the MEMS cell. A good agreement between the theoretical and measured value of Γ_{12} is shown in the case of the Rb wall-coated cell - calculated $\Gamma_{12}=144(7)$ Hz and measured is $\Gamma_{12}=161.2(7)$. Here, Γ_{12} is limited by the atom-wall coating collisions, the spin-exchange collisions and the contribution from the atoms escaping through the Rb reservoir. In both cases, the broadening rates as function of the laser intensity and saturation intensities I_s were evaluated. The signal discriminator slope D is optimized in order to obtain the best clock short-term stability (see Chapter 5).

REFERENCES:

- [1] M. PREVEDELLI, T. FREEGARDE and T. W. HANSCH, *Phase locking of grating tuned diode lasers*, Appl. Phys. B 60 (1995), pp. 241-248.
- [2] O. SCHMIDT, R. WYNANDS, Z. HUSSEIN and D. MESCHÉDE, *Steep dispersion and group velocities below $c=3000$ in coherent population trapping*, Phys. Rev. A 53 (1996), pp. 27-30.

- [3] S. BRANDT, A. NAGEL, R. WYNANDS and D. MESCHÉDE, *Buffer-gas-induced linewidth reduction of coherent dark resonances to below 50 Hz*, Phys. Rev. A 56 (1997), pp. 1063-1066.
- [4] M. ERHARD, S. NUßMANN and H. HELM, *Power broadening and Doppler effects of coherent dark resonances in Rb*, Phys. Rev. A 62 (2000), pp. R061802-4.
- [5] M. MULLER, F. HOMANN, R.-H. RINKLEFF, A. WICHT and K. DANZMANN, *Heterodyne measurement of parametric dispersion in electromagnetically induced transparency*, Phys. Rev. Lett. 64 (2001), pp. 013803-8.
- [6] A. M. AKULSHIN, S. BARREIRO, and A. LEZAMA, *Electromagnetically induced absorption and transparency due to resonant two-field excitation of quasidegenerate levels in Rb vapour*, Phys. Rev. A 57 (1998), pp. 2996-3002.
- [7] E. A. KORSUNSKY, N. LEINFELLNER, A. HUSS, S. BALUSCHEV and L. WINDHOLTZ, *Phase-dependent electromagnetically induced transparency*, Phys. Rev. A 59 (1999), pp. 2302-2305.
- [8] C. AFFOLDERBACH, A. NAGEL, S. KNAPPE, C. JUNG, D. WIEDENMANN and R. WYNANDS, *Nonlinear spectroscopy with a vertical cavity surface-emitting laser (VCSEL)*, Appl. Phys. B Lasers Opt. 70 (2000), pp. 407-413.
- [9] R. BOUDOT, D. MILETIC, P. DZIUBAN, C. AFFOLDERBACH, P. KNAPKIEWICZ, J. DZIUBAN, G. MILETI, V. GIORDANO and C. GORECKI, *First-order cancellation of the Cs clock frequency temperature-dependence in Ne-Ar buffer gas mixture*, Opt. Express 19 (4) (2011), pp. 3106-3114.
- [10] J. KITCHING, L. HOLLBERG, S. KNAPPE and R. WYNANDS, *Compact atomic clock based on coherent population trapping*, Electron. Lett. 37 (2001), pp. 1449-1451.
- [11] A. NAGEL, S. KNAPPE, C. AFFOLDERBACH and R. WYNANDS, *Line shapes of coherent population trapping resonances*, AIP Conf. Proc. 559 (2000), pp. 257-259.
- [12] F. GRUET, E. KROEMER, L. BIMBOES, D. MILETIC, C. AFFOLDERBACH, A. AL-SAMANEH, D. WAHL, R. BOUDOT, G. MILETI and R. MICHALZIK, *Metrological characterization of custom-designed 894 nm VCSELs for miniature atomic clocks*, Opt. Express 21(5) (2013), pp. 5781-5792.
- [13] <http://www.eagleyard.com/>
- [14] F. GRUET, D. MILETIC, C. AFFOLDERBACH and G. MILETI, *Characterization of aged/non-aged 894 nm DFB for their application in Cs atomic clocks*, Proc. of the International Symposium On Reliability Of Optoelectronic For Space (ISROS), Cagliari (Italy), May 11-15 (2009), pp.1-14.
- [15] E. HECHT, *Optics*, Addison-Wesley, Boston, USA, (1990).

- [16] K. PETERMANN, *Laser diode modulation and noise*, Advances in Optoelectronics, Kluwer Academic Publishers, (1991).
- [17] G. DI DOMENICO, S. SCHILT, and P. THOMANN, Simple approach to the relation between laser frequency noise and laser line shape, *Appl. Opt.* 49 (2010), pp. 4801-4807.
- [18] A. YARIV, *Optical electronics*, Saunders College Publishing, 4th edition, Philadelphia, USA (1991).
- [19] A. DOUABI, L. NIERADKO, J. C. BEUGNOT, J. DZIUBAN, H. MAILLOTE, S. GUERANDEL, M. MORAJA, C. GORECKI and V. GIORDANO, *Vapour microcell for chip scale atomic frequency standard*, *Electron. Lett.* 43 (2007), pp.279-280.
- [20] N. ALLARD and J. KIELKOPF, *The effect of neutral nonresonant collisions on atomic spectral lines*, *Rev. Mod. Phys.* 54 (4) (1982), pp. 1103-1182.
- [21] M. PELLATON, C. AFFOLDERBACH, Y. PETREMAND, G. MILETI and N. F. DE ROOIJ, *Study of laser-pumped double-resonance clock signals using a microfabricated cell*, *Phys. Scr.* T149 (2012), pp. 1-5.
- [22] S. J. SELTZER, D. J. MICHALAK, M. H. DONALDSON, M. V. BALABAS, S. K. BARBER, S. L. BERNASEK, M.-A. BOUCHIAT, A. HEXEMER, A. M. HIBBERD, D. F. JACKSON KIMBALL, C. JAYE, T. KARAUANOV, F. A. NARDUCCI, S. A. RANGWALA, H. G. ROBINSON, A. K. SHMAKOV, D. L. VORONOV, V. V. YASHCHUK, A. PINES and D. BUDKER, *Investigation of antirelaxation coatings for alkali-metal vapor cells using surface science techniques*, *J. Chem. Phys.* 133 (2010), pp. 144703-11.
- [23] www.home.agilent.com/ HP 83620A
- [24] E. BRESCHI, G. KAZAKOV, R. LAMMEGGER, B. MATISOV, L. WINDHOLZ and G. MILETI, *Influence of laser sources with different spectral properties on the performance of vapor cell atomic clocks based on $|\downarrow\rangle|\uparrow\rangle$ CPT*, *IEEE Trans. Ultrason. Ferroelectr. Freq. Control.* 56(5) (2009), pp. 926-930.
- [25] E. BRESCHI, G. KAZAKOV, R. LAMMEGGER, G. MILETI, B. MATISOV and L. WINDHOLZ, *Quantitative study of the destructive quantum-interference effect on coherent population trapping*, *Phys. Rev. A* 79 (2009), pp. 063837-10.
- [26] E. BRESCHI, G. KAZAKOV, C. SCHORI, G. DI DOMENICO, G. MILETI, A. LITVINOV and B. MATISOV, *Light effects in the atomic-motion-induced Ramsey narrowing of dark resonances in wall-coated cells*, *Phys. Rev. A* 82 (2010), pp. 063810-7.
- [27] T. BANDI, C. AFFOLDERBACH and G. MILETI, *Study of Rb 0-0 hyperfine double-resonance transition in a wall-coated cell*, *Proc. of the European Frequency and Time Forum (EFTF)*, Noordwijk (Netherlands), 13-16 April (2010), pp.1-8.

- [28] T. BANDI, C. AFFOLDERBACH and G. MILETI, *Laser-Pumped Paraffin-Coated Cell Rubidium Frequency Standard*, Journal of Applied Physics 111 (2012), pp. 124906-8.
- [29] C. AFFOLDERBACH and G. MILETI, *A compact laser head with high-frequency stability for Rb atomic clocks and optical instrumentation*, Rev. Sci. Instrum. 76 (2005), pp. 073108-5.
- [30] C. E. CALOSSO, F. LEVI, E. K. BERTACCO, A. GODONE and S. MICALIZIO, *Low-noise electronic design for the ^{87}Rb coherent population trapping maser*, IEEE Trans. UFFC, 52 (11) (2005), pp. 1923-1930.
- [31] G. MILETI, I. RUEDI and H. SCHWEDA, *Line inhomogeneity effects and power shift in miniaturized rubidium frequency standards*, Proc. of 6th European Frequency and Time Forum (1992), p. 515.
- [32] D. MILETIC, T. BANDI, C. AFFOLDERBACH, and G. MILETI, *AC Stark-shift in Double Resonance and Coherent Population Trapping in Wall-Coated Cells for Compact Rb Atomic Clocks*, Phys. Scr. T149 (2012), pp. 1-3.
- [33] M. GEHRTZ and G. C. BJORKLUND, *Quantum-limited laser frequency-modulation spectroscopy*, J. Opt. Soc. Am. B 2 (1985), pp. 1510-1525.
- [34] R. WYNANDS and A. NAGEL, *Inversion of frequency modulation (FM) spectroscopy line shapes*, J. Opt. Soc. Am. B 16 (1999), pp. 1617-1622.
- [35] J. VANIER and C. AUDOIN, *The Quantum Physics of Atomic Frequency Standards*, Adam Hilger, Bristol, UK, (1989).
- [36] N. CASTAGNA, G. BISON, G. Di DOMENICO, A. HOFER, P. KNOWLES, C. MACCHIONE, H. SAUDAN and A. WEIS, *A large sample study of spin relaxation and magnetometric sensitivity of paraffin-coated Cs vapor cells*, Appl. Phys. B 96 (2009), pp. 763-772.
- [37] S. MICALIZIO, A. GODONE, F. LEVI and J. VANIER, *Spin-exchange frequency shift in alkali-metal-vapor cell frequency standard*, Phys. Rev. A 73 (2006), pp. 033414-5.
- [38] H. G. ROBINSON, *Evacuated, Wall-coated, Sealed, Alkali Atom Cell for an Atomic Frequency Standard*, U.S. Pat. 4596962, June (1986).
- [39] D. BUDKER, L. HOLLBERG, D. F. KIMBALL, J. KITCHING, S. PUSTELNY and V. V. YASHCHUK, *Microwave transitions and nonlinear magneto-optical rotation in anti-relaxation-coated cell*, Phys. Rev. A 71 (2005), pp. 012903-9.

Chapter 4 Light shift and temperature shift in CPT atomic clocks

After the theoretical introduction in Chapter 2, we here present experimental studies on the light shift (LS) effect and temperature coefficient (TC) in CPT vapor-cell standards. These measurements are performed in two different experimental cases: 1.) the Cs D1 line using the MEMS buffer gas cell (section 4.2) and 2.) the Rb D1 line, using the cm-scale cell coated with tetracontane (section 4.3).

The case of the Cs MEMS buffer gas cell is considered first, starting with the intensity LS measurements as function of the two different parameters: modulation index M and MEMS cell temperature. The description of the LS suppression as function of the cell temperature is proposed. The frequency LS for different MEMS cell temperatures is measured and the laser frequency is found for which the frequency LS coefficient β is minimized. Finally, the temperature shift of a Cs cell is measured and the inversion temperature is evaluated, for different buffer gases.

The measurements of the LS and temperature shift are also performed in the case of a ^{87}Rb cm-scale wall-coated cell. The frequency LS is measured and compared to the theoretical calculations by using the equations introduced in Chapter 2. Intensity LS measurements as function of various parameters, e.g., microwave power, laser frequency detuning, the cell volume and cell stem temperatures are performed. The TC for the tetracontane wall-coated cell is evaluated.

Finally, in order to compare the experimental results of the LS coefficients α and β and temperature coefficients in two different experimental conditions a summarizing table of the measured coefficients concludes the chapter.

4.1 Light shift and temperature shift in the Cs MEMS cell with buffer gas

4.1.1 Intensity light shift in the Cs MEMS cell with buffer gas

It was shown that the light shift of the clock resonance frequency is a linear function of light intensity [1]. For low light intensities ($I \ll 2.5 \text{ mW/cm}^2$ for Cs) LS shows linear dependence while saturation of the LS has been experimentally verified and explained in terms of the optical pumping inhomogeneity [2, 3, 4].

Figures 4-1 (a) and (b) report the intensity LS of the clock transition, measured in the experimental setup described in section 3.3.1 as function of the total laser intensity, for four different RF powers driving the EOM (i.e. different modulation index M , see Chapter 3). CPT coupling is via the $F'=3$ excited state (laser carrier frequency stabilized to point 1 in Figure 3-24). The lock-in signal is recorded for several RF powers and laser intensities (see Figure 3-27). A Lorentzian fit function of the lock-in signal provides the shift of the clock transition frequency.

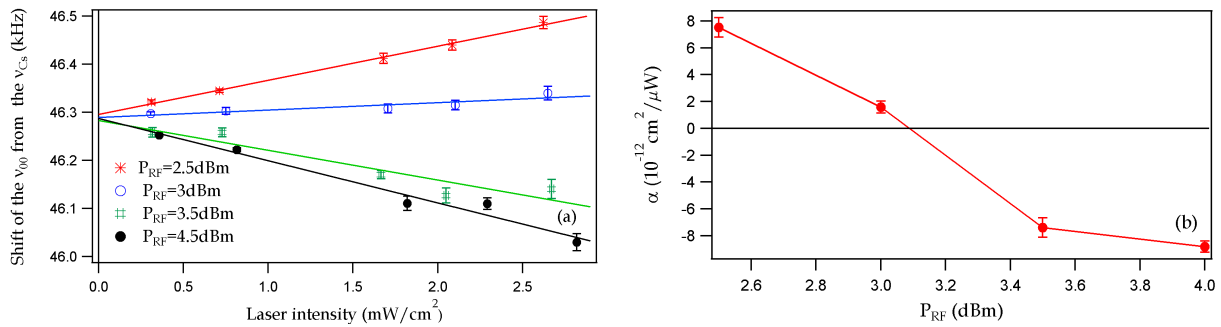


Figure 4-1 (a): Shift of the CPT clock transition as function of total light intensity, for several RF powers P_{RF} . The MEMS Cs buffer gas cell temperature is $T_c=353 \text{ K}$. Solid lines are linear fits to the data representing the intensity coefficient α . **(b)** Intensity coefficient α as function of the P_{RF} .

Figures 4-1 (a) and (b) show that the intensity LS coefficient α (slope of the data in Figure 4-1 (a)) can be minimized by a proper choice of the modulation index M (via the RF modulation power P_{RF} here). Such behavior was already reported in [5] using a current-modulated extended-cavity diode laser (ECDL) and current-modulated vertical-cavity surface-emitted lasers (VCSEL) [6-9]. For $P_{RF}=3 \text{ dBm}$, α is minimized to $\alpha = 1.6 \times 10^{-12} \text{ cm}^2/\mu\text{W}$ while for $P_{RF}=2.5 \text{ dBm}$ and 3.5 dBm α is increased by factors of +4.5

and -4.5, respectively. From Figure 4-1 (a) it can be seen that the resonance frequency shift for zero laser intensity, i.e. the total buffer gas pressure shift is (46.29 ± 0.01) kHz, which corresponds to the total Ne pressure of 72(4) Torr.

If we compare these data with the theoretical calculation of the CPT LS on Cs D1 line (see 2.4, Fig. 2-8), the observed effect shows the behavior expected from Fig. 2-8: By increasing the P_{RF} the modulation index M is taking higher values. Figure 2-8 (pink arrow) shows that the total CPT LS in the Cs cell varies from positive to negative values by increasing the M , with the laser frequency stabilized to the transition $F \rightarrow F' = 3$. The same behavior is confirmed by the measurements shown in Figure 4-1 (b): by increasing the P_{RF} the modulation index M increases accordingly and the intensity LS coefficient changes from positive to negative values, with the laser frequency being stabilized to the $F \rightarrow F' = 3$ transition. In further experiments we chose to apply RF modulation power of $P_{RF} = 3.5$ dBm in order to obtain the highest CPT contrast (see section 3.4.1), although that it is not the best condition for the intensity LS.

The intensity LS has been measured for different MEMS Cs buffer gas cell temperatures, at microwave power of $P_{RF} = 3.5$ dBm. The shift of the clock transition frequency is estimated from the Lorentzian fit function of the lock-in signal, for various cell temperatures and two laser carrier frequency stabilization points (1 and 2, see Figure 3-24) and shown in Figure 4-2 and Figure 4-4.

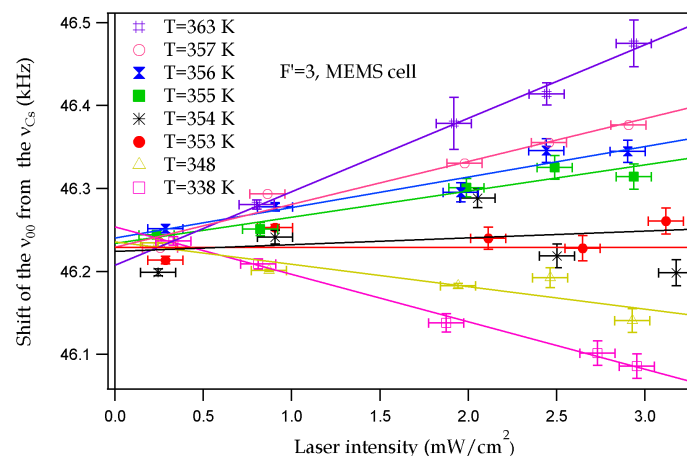


Figure 4-2: Shift of the CPT clock transition measured on the MEMS Cs buffer gas cell, as function of laser intensity for different cell temperatures, results for the laser frequency tuned for coupling via the $F' = 3$ excited state. Solid lines are linear fits to the data.⁴

⁴ Intensity LS measured for $P_{RF} = 3.5$ dBm and $T_c = 353$ K is shown in Figure 4-1 (green hash) and Figure 4-2 (red dots), and these results may appear different. The y-scale (shift of the ν_{00} from the ν_{Cs}) on both graphs is different, and therefore give the impression that the results are not the identical. Plotting these data on the same graph shows that these two measurements give the same result.

When CPT is created by coupling via the $F'=3$ excited state, the intensity LS coefficient α (given by the slope of the lines) can be adjusted over a wide range around zero value by changing the cell temperature: α is strongly suppressed at $T_c=354$ K, while for lower temperatures α is negative and for higher temperatures α is positive. Figure 4-2 also gives the information about clock resonance frequency for zero laser intensity of (46.24 ± 0.06) kHz, which is in good agreement with the value obtained from the measurement given in Figure 4-1 (a).

The data of Figure 4-2 are shown differently in Figure 4-3 where intensity LS coefficient α is presented as function of the cell temperature. Figure 4-3 clearly demonstrates that for $T=354$ K α is strongly suppressed when the laser carrier frequency is stabilized to the $F'=3$ transition.

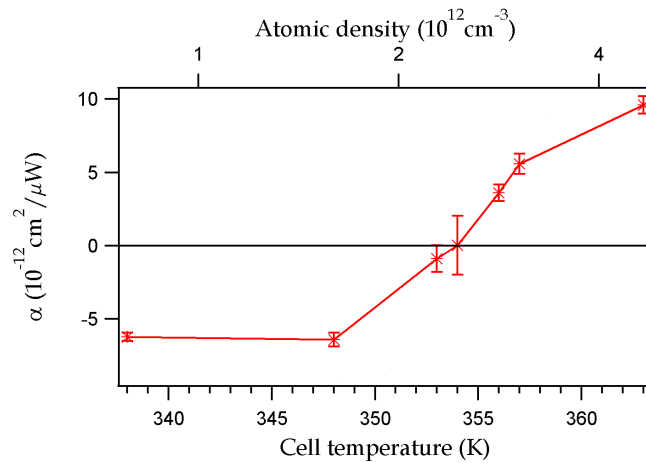


Figure 4-3: Intensity LS coefficient α as function of the cell temperature. α crosses the zero-value level for a cell temperature of 354 K. Coupling is via the $F'=3$ excited state.

In the case of CPT created by coupling via $F'=4$ (Figure 4-4), α is always positive for any cell temperature used and we do not find a cell temperature with similarly strong suppression of α as for coupling via $F'=3$ (Figure 4-2). The data of Figure 4-4 are given differently in Figure 4-5 where the intensity LS coefficient α is presented as function of the cell temperature, similar as in Fig. 4-3. Figure 4-5 clearly shows that the condition with α strongly suppressed is not reached when the laser carrier frequency is stabilized to the $F'=4$ transition. Comparing the Figure 4-3 and 4-5 we can conclude that α is one order of magnitude higher in the case when the laser carrier frequency is stabilized to the $F'=4$ transition.

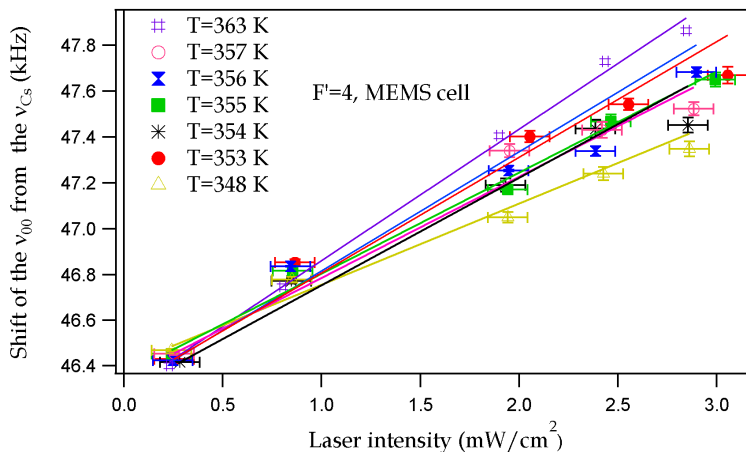


Figure 4-4: Shift of the CPT clock transition measured with the MEMS Cs buffer gas cell, as function of laser intensity for different cell temperatures, results for the laser frequency tuned for coupling via the $F'=4$ excited state. Solid lines are linear fits to the data.

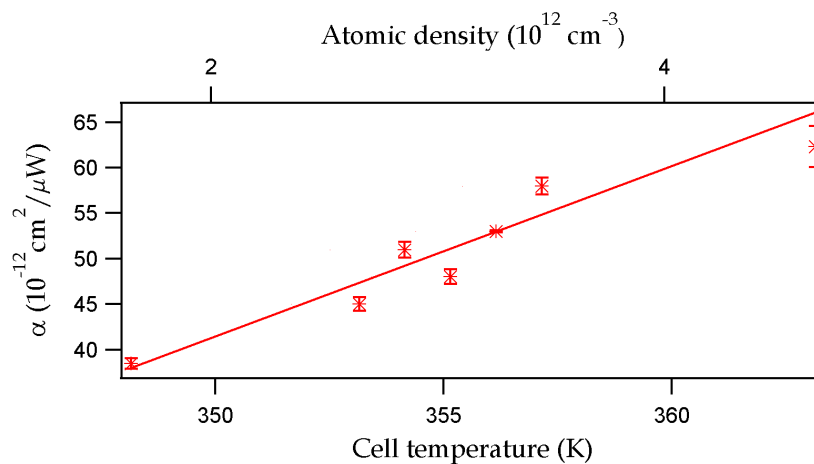


Figure 4-5: Intensity LS coefficient α as function of the cell temperature. Laser frequency is tuned for coupling via the $F'=4$ excited state.

The LS measurements shown in Figure 4-2 and Figure 4-4 confirm the theoretical calculations given on Figure 2-8 (section 2.4), where the LS is calculated for a multi-frequency laser field varied around the Cs D1 transition. In Figure 2-8 the pink and green arrows indicate the laser frequencies used for the laser carrier stabilization (pink represents the transition $F \rightarrow F'=3$, green the $F \rightarrow F'=4$ transition). From this graph it can be seen that in the case of the laser frequency stabilized to the transition $F \rightarrow F'=3$ the LS is negative (confirmed by the measurements shown in Figure 4-1, for a low cell temperatures). In the case when the laser frequency is stabilized to the transition $F \rightarrow F'=4$ (green arrow in Figure 2-8) the LS is always positive, which is confirmed by the measurements shown in Figure 4-4). A explanation for such LS behaviour is found in overall contributions from all the sidebands and including the influence from the off-

resonant excited state to the LS. We start the explanation with Figure 2-7 which presents the calculated LS for a single frequency laser field varied around the Cs D1 transition. Figure 2-7 shows that for coupling via the $F'=3$ excited state, the carrier and +1st-order sideband contribute a positive LS, while the contribution of all other sidebands is negative. With increasing the cell temperature, the atomic density in the cell increases and hence the resonant light (first-order sidebands) is absorbed more strongly in the cell. As a result, the overall intensity LS from all laser sidebands changes from negative to positive, as it is shown here.

To confirm this statement, the absorption of the resonant laser light was measured as function of the cell temperature (Figure 4-6). A Fabry-Perot interferometer was placed after the MEMS Cs buffer gas cell and for each cell temperature the transmitted laser spectrum was recorded (see Figure 3-9). The laser frequency is stabilized to the $F'=3$ transition.

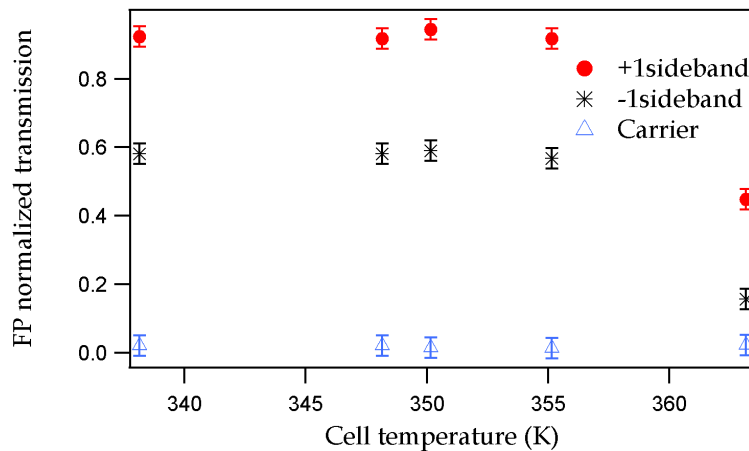


Figure 4-6: Fabry Perot transmission of the laser carrier and the two first-order sidebands (normalized to the +1st order sideband) as function of the MEMS Cs buffer gas cell temperature.

It is shown that for all cell temperatures, the carrier is transmitted essentially non-attenuated through the cell (such behavior is expected for the higher-order sidebands also). The -1st-order sideband is absorbed more strongly than the +1st-order sideband. This means that the temperature-induced increase in optical absorption of the $F=4 \rightarrow F'=3$ transition will reduce the negative LS contribution from the -1st-order sideband more strongly than the smaller increase of optical absorption of the $F=3 \rightarrow F'=3$ transition reduces the positive LS contribution from the +1st-order sideband. Therefore in the case of the Cs D1 line when the two first-order sidebands used for creating CPT, the LS will change with the vapor cell temperature increase, going from negative to positive values. In the case of a laser stabilized to the transition coupling to the $F'=4$ state, the reasoning why only positive LS is observed is the same: the temperature-

induced increase in optical absorption of the $F=3 \rightarrow F'=4$ transition will reduce the negative LS contribution from the +1st-order sideband more strongly than the smaller increase of optical absorption on the $F=4 \rightarrow F'=4$ transition reduces the positive LS contribution from the -1st-order sideband. Since the contribution from the carrier is also positive and the negative LS contribution is reduced, the LS is always positive for the case of the laser stabilized to the transition coupling to the $F'=4$ state.

By changing the cell temperature it is possible to obtain the suppressed intensity LS only for coupling via the $F'=3$ state, since in this case the initial (low-temperature) value of α is one order magnitude smaller than in the case of coupling via the $F'=4$ state. α is strongly positive for the case of coupling via $F'=4$ state. Here the initial absolute value of α is too large and positive compared to the adjustment range of $\delta\alpha \approx 1.5 \times 10^{-11} \text{ cm}^2/\mu\text{W}$ achievable by changing the cell temperature (see Figure 4-4), which is on the same order for both couplings via $F'=3$ and $F'=4$. This prevents obtaining a suppressed α value when coupling via $F'=4$ in the same range of cell temperatures, so that in this case we observe always a positive α .

The light- shift effect was studied and reported for the case of an optically-pumped double-resonance ^{87}Rb clock in [11] but not studied as function of the vapor cell temperature. There, the intensity LS coefficient α is significantly smaller for coupling to the higher-lying excited state ($F'=2$), but was not measured for CPT clocks or Cs.

4.1.2 Frequency light-shift in the Cs MEMS cell with buffer gas

Before discussing the frequency LS it is useful to list the transition frequencies of the Cs D1 line in the MEMS cell with 75 Torr of Ne and in the Cs evacuated cm-scale cell, Table 4-1. Transition frequencies for the evacuated cell are taken from [10], while for the MEMS buffer gas cell they are calculated by adding the -216 MHz of buffer gas shift [12]. Transition frequencies of the $F \rightarrow F'=3$ and $F \rightarrow F'=4$ in Cs MEMS and evacuated cell (points 1 and 2 of Figure 3-24) are measured directly, using the wavemeter. The wavemeter resolution is on the MHz level. It is not possible here to identify exactly the -216 MHz of the buffer gas shift in the case of CPT locking to the $F \rightarrow F'=3$ and $F \rightarrow F'=4$ transitions (points 1 and 2 in Fig. 3-24) due to a problem of locking precision to the line, but it is visible that this shift is negative and on the < GHz level.

Cs vapor cell	Buffer-gas MEMS	Evacuated cm-scale
F=3 → F'=3 (THz)	335.120 3464 842	335.120 562 842
F=3 → F'=4 (THz)	335.121 514 522	335.121 730 522
F=4 → F'=3 (THz)	335.111 154 211	335.111 370 211
F=4 → F'=4 (THz)	335.112 321 891	335.112 537 891
CPT: F→F'=3 (THz) (point 1 Figure 3-15)	335.1159 (3)	335.1160 (3)
CPT: F→F'=4 (THz) (point 2 Figure 3-15)	335.1170 (3)	335.1172 (3)

Table 4-1: Transition frequencies of the Cs D1 line in the MEMS buffer gas cell and the cm-scale evacuated cell. Transition frequencies for the evacuated cell are taken from [10], frequencies for the MEMS buffer gas cell are calculated by adding the -216 MHz buffer gas shift [12]. Transition frequencies of the F→F'=3 and F→F'=4 (points 1 and 2 of Figure 3-24) are measured directly, using a wavemeter.

The shift of the clock transition as function of the laser frequency is measured and shown in Figure 4-7, for different laser intensities and the Cs MEMS cell temperature of $T_c=338$ K. These data are recorded for the laser frequency varied slightly around 335.1160(3) THz, i.e. for coupling via the F'=3 excited state. For the chosen frequency, precisely measured by the wavemeter, the CPT signal was recorded. Lorentzian fit of the CPT signal gives the ν_{Cs} plus the total shift of the CPT clock transition ν_{00} (see Fig. 3-25). The frequency LS coefficient β is given by the slopes of the line fits in Figure 4-7 e.g. $\beta=-644$ mHz/MHz for a total laser intensity of 4.04 mW/cm². The intersection of the three lines fits (for different light intensities) gives the laser frequency for which a zero α -coefficient is obtained. This intersection point depends on the cell temperature and for $T_c=338$ K this point is at 335.11603(3) THz, which is closer the transition F→F'=3 than to the transition F→F'=4 in the Cs MEMS cell (see Table 2-2).

We choose to use the intersection point of the black and the red curve and not the black and the green curve since the data presented with the green dots are more scattered and therefore a linear fit is less precise. This result confirms the previous conclusions on the intensity LS (Figure 4-2 and Figure 4-4) where it is stated that suppressed α can be obtained when the laser frequency is stabilized to the F→F'=3 transition.

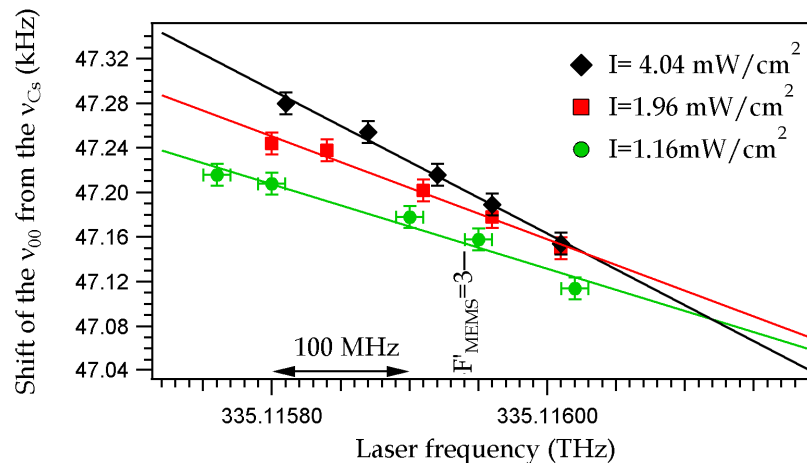


Figure 4-7: Shift of the clock resonance line as function of laser frequency, measured for different total laser intensities (I_L). The LS coefficient α is given by the slopes of the line fits. The Cs MEMS cell temperature is $T_c = 338 \text{ K}$.

The shift of the clock transition as function of the laser frequency was also measured for the MEMS cell temperature of $T_c = 363 \text{ K}$, Figure 4-8. For this temperature the intersection point of the three lines (and intensity LS coefficient α is zero) is $335.11641(3) \text{ THz}$. This frequency is $\sim 500 \text{ MHz}$ different from the frequency $F \rightarrow F' = 3$ in the buffer gas cell (see Table 4-1).

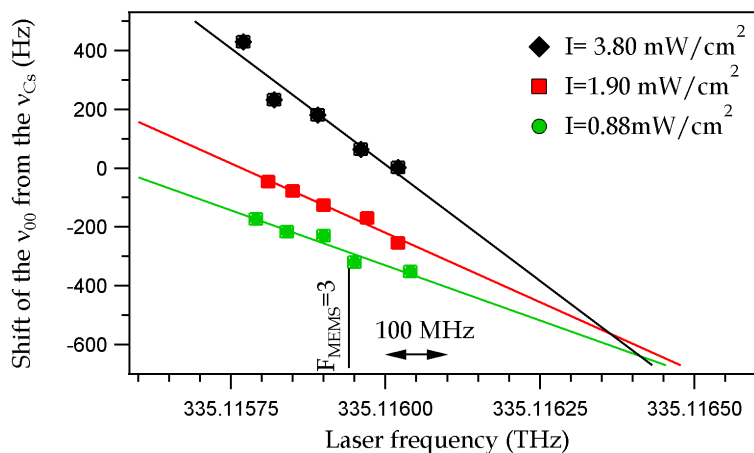


Figure 4-8: Shift of the clock resonance line as function of laser frequency, measured for three total laser intensities (I_L). The LS coefficient α is given by the slopes of the line fits. The MEMS cell temperature is $T_c = 363 \text{ K}$.

These measurements were performed before the discovery that $T_c = 354 \text{ K}$ is the MEMS cell temperature for which α is suppressed. Therefore, there is no measurement of the frequency LS for the cell temperature of $T_c = 354 \text{ K}$, but the intersection point frequency for this temperature can be extrapolated from the two measurements shown above, for $T_c = 338 \text{ K}$ and $T_c = 363 \text{ K}$, see Figure 4-9. With this method the intersection point for

$T_c=354$ K was linearly extrapolated to be at 335.11627(3) THz. This means the intensity LS coefficient α is zero for 335.11627(3) THz, in the case when $T_c=354$ K. This frequency is close to the frequency of $F \rightarrow F'=3$ transition (see Fig. 4-9). Therefore if the laser is stabilized to $F \rightarrow F'=3$ transition, the intensity LS will be low (much lower than in the case of laser frequency being stabilized to the $F \rightarrow F'=4$ transition).

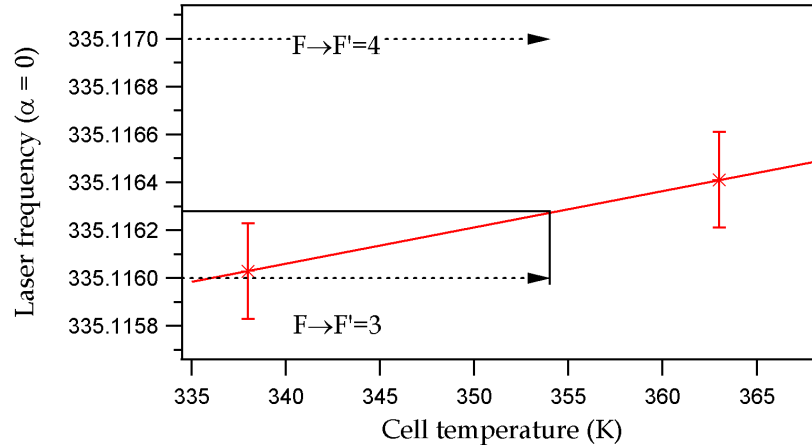


Figure 4-9: Laser frequency for which the intensity LS coefficient is zero, as function of the cell temperature. Dashed black arrows indicate the laser frequencies of the transitions $F \rightarrow F'=3$ and $F \rightarrow F'=4$. The red solid curve is a linear fit of the data estimated from Figure 4-7 and Figure 4-8. The solid black line indicates the estimated laser frequency (for $\alpha=0$) for the cell temperature of $T_c=354$ K.

The frequency LS measurements are repeated for the case of the laser carrier frequency stabilized to the two transitions (via $F'=3$ and $F'=4$ state), but in the separate evacuated reference Cs cell. Figure 4-10 displays the intensity LS coefficient α for the laser frequency stabilized to the 4 possible laser lock points, namely for coupling via the $F'=3$ or $F'=4$ excited states in either the MEMS cell or the evacuated cell. The smallest intensity LS (lowest value of $|\alpha|$) is found with the laser stabilized to the $F \rightarrow F'=3$ transitions in the MEMS or evacuated cell, close to 335.1160(3) THz. This means that the best possible solution is to stabilize the laser carrier frequency to the transition to $F'=3$ state (in MEMS or evacuated cell), for which the frequency LS is the smallest.

Figure 4-10 shows a good agreement (except for the case of $F'_{EVAC}=4$) with the theoretical calculations shown in Figure 2-8 (for the case of $M=1.8$, using transition rates from Table 2-2 and where free parameter is the amplitude of the δv_{00}^{CPT}). These theoretical calculations are done for the case of the 75 Torr Ne MEMS cell (see section 3.2.1), including the buffer gas shift of -216 MHz.

Figure 4-10 also confirms the measurements shown in Figure 4-2 and Figure 4-4: in the case of coupling via $F'=3$ state, $\alpha=1.5(6) \times 10^{-12}$ and it is one order magnitude smaller than

in the case of coupling via $F'=4$ state where $\alpha=2.6(3)\times 10^{-11}$, comparing for the $T=355\text{K}$ (α is strongly positive for the case of coupling via $F'=4$ state). Therefore by changing the cell temperature it is possible to obtain the suppressed intensity LS.

These measurements supply an important information for an atomic clock, namely the laser frequency for which the intensity LS is smallest. For the cell temperature of $T_c=354\text{ K}$ this frequency is $335.1160(3)\text{ THz}$ (closest to the $F \rightarrow F'=3$ transition) and therefore this transition should be used in evacuated or MEMS cell for the laser frequency stabilization in order to minimize the intensity LS.

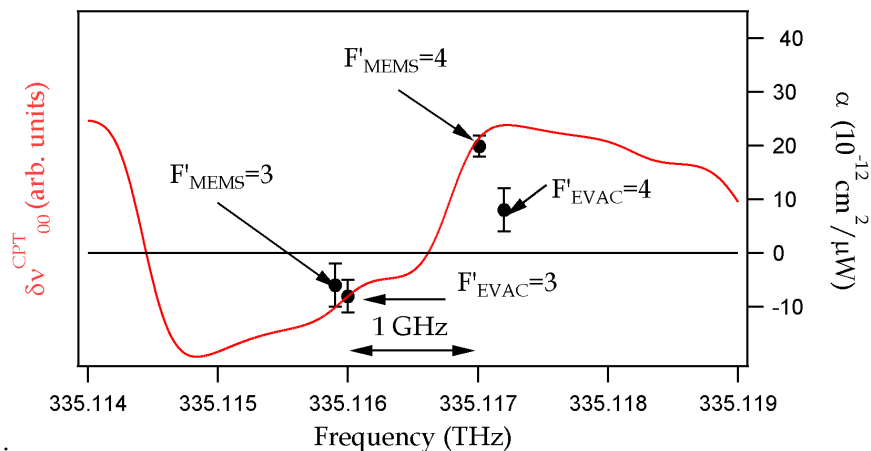


Figure 4-10: The red solid curve indicate the CPT LS in Cs MEMS cell (shown in Figure 2-7) zoomed around $F \rightarrow F'=3$ and $F \rightarrow F'=4$ transitions, for $M=1.8$. Black dots indicate the intensity LS coefficients α for laser frequencies stabilized to the $F \rightarrow F'=3$ or $F \rightarrow F'=4$ transitions in either the MEMS cell or the evacuated cell. The MEMS cell temperature is $T_c=338\text{ K}$. The solid black line indicate the zero LS level.

4.1.3 Comparison of the light-shift coefficients α and β

Comparisons between already published values for α and β with the results discussed in this thesis are shown in Table 4-2. Our reported data are for the case of laser stabilization to the $F \rightarrow F'=3$ transitions in the Cs MEMS cell. In particular we find that our result for β has the same sign, but is a factor of 2 smaller than the value reported in [14], when rescaled to the resonant laser intensity used in [14]. This difference can be attributed to the different intensities of the first-order sidebands in both works, resulting in a different degree of β compensation between these sidebands. In [14] a current-modulated VCSEL is used and amplitude modulation causes a

stronger sideband asymmetry than the EOM-modulated technique used in this work (the Ne pressures used in these works differ by 3% only).

Reference	[13]	[14]	[15]	[16]	This work
Transition	Cs D ₂	Cs D ₂	Cs D ₂	Cs D ₂	Cs D ₁
Buffer-gas	Ne	Ne	N ₂ /Ar	Ne	Ne
Laser	TWO PHASE- LOCKED LASERS	VCSEL	VCSEL	VCSEL	DFB + EOM
I ₋₁ / I ₀ / I ₊₁ (%)	60/0/40	19/8/47	no data	14/14/33	32/16/35
α (($\mu\text{W}/\text{cm}^2$) ⁻¹)	8.7x10 ⁻¹⁰	1.08x10 ⁻¹⁰	1.6x10 ⁻¹⁰	-3.2x10 ⁻¹²	-1.7 x10 ⁻¹³
β (mHz/MHz)	no data	-20	no data	no data	-11

Table 4-2: Comparison of the different intensity LS coefficients α and frequency LS coefficients β reported in the literature and in this work. The values for β are normalized to the resonant laser intensity of $I=45 \mu\text{W}/\text{cm}^2$ used in [14]. The line labeled “I₋₁ / I₀ / I₊₁” gives the percentage of total light intensity contained in the -1st-order sideband, the carrier, and the +1st-order sideband in the respective studies (CPT is induced using the two first-order sidebands in all cases).

4.1.4 Temperature shift in the Cs MEMS cell with buffer gas

Temperature shift was introduced in Chapter 2. To obtain a suppressed linear TC at a specific inversion temperature, a mixture of two buffer gases with opposite temperature coefficients is generally used [16-18]. The perfect buffer gas mixture ratio can be calculated by measuring vapor cells containing only one buffer gas and estimate from these measurements the pressure and first-order temperature shift coefficients β and δ (see Eq. (1.7)). To estimate the second-order temperature shift coefficient usually vapor cells with different mixtures of gases are used.

The barometric effect or the other buffer-gas related aging processes discussed in sections 1.4.1 and 1.4.4 will not significantly change the turnover temperature because the relative pressure change is negligible.

In this thesis, the LS measurements (Figure 4-2 and Figure 4-4) are used to isolate the TC of the MEMS Cs cell with buffer gas content. This is done by extrapolating the CPT clock frequency to zero light intensity, for each Cs MEMS cell temperature. The example of TC measurement in a single buffer gas cell is shown in Figure 4-11, for the Cs FEMTO MEMS cell with 28 Torr of Ar:

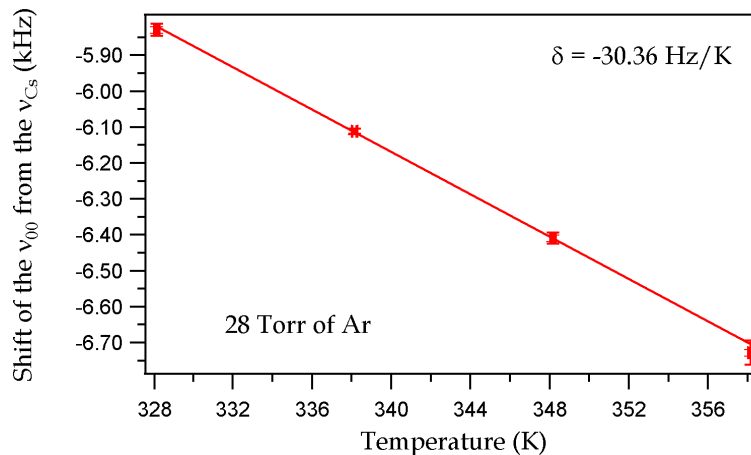


Figure 4-11: Resonance frequency shift extrapolated at zero laser power as function of the cell temperature (temperature shift). The MEMS cell contains 28 Torr of Ar. The solid line indicate the fit of the Eq. (1.7).

The solid line indicates the fit of the Eq. (1.7) estimating the linear TC of $\delta = -3.3 \times 10^{-9}$ 1/K = -30.36 Hz/K. Estimation of the linear TC δ for the 28 Torr Ar cell from the literature value (Table 2-4), gives the same result (within 0.1 Hz/K of error) $\delta = -30.46$ Hz/K.

In the case of buffer gas mixture the same measurements are performed for the Cs SAMLAB-LTF cell with the mixture of two buffer gases Ar and N₂, with the ratio of $r = \frac{P_{Ar}}{P_{N_2}} = 0.37$ and 10 Torr of total pressure (Figure 4-12).

In this case, it is possible to evaluate the linear and quadratic temperature coefficients δ and γ of the buffer gas mixture by fitting the Eq. (2.28) to the data (given with the red stars) where the fixed parameters are buffer gas ratio r , total buffer gas pressure and T_0 . The linear TC in this case is evaluated to be $\delta = 2.6(5)$ Hz/K and the quadratic TC is $\gamma = 0.03(1)$ Hz/K² for $T_0 = 333$ K. These coefficients are in agreement with the one listed in Table 2-4: using the coefficients from the Table 2-4, for the 10 Torr of buffer gas mixture Ar-N₂ with ratio $r = 0.37$, the estimated linear TC is $\delta = 3.1$ Hz/K and the quadratic TC is $\gamma = 0.018$ Hz/K². The inversion temperature (for the buffer gas mixture Ar-N₂ with ratio of $r = 0.37$) of $T_{inv} = 348.4(3)$ K is calculated by using the Eq. (2.28).

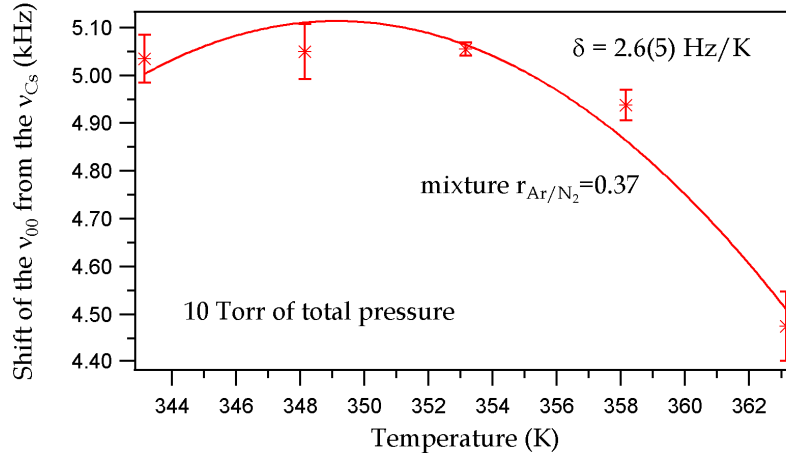


Figure 4-12: Resonance frequency shift extrapolated at zero laser power as function of the cell temperature (temperature shift). The SAMLAB-LTF MEMS cell contains 10 Torr of buffer gas mixture Ar-N₂ in the ratio of $r=P_{Ar}/P_{N_2}=0.37$. The solid line represents the fit of the Eq. (2.28).

The measurements of the TC for the buffer gas mixture are also performed in Rb cm-scale cell (experimental setup using the cm-scale Rb cell is described in Appendix A). The buffer gas mixture is Ar and N₂ with the ratio of 60-40 and the obtained inversion temperature is $T_{inv}=338.0(1) \text{ K}$, Figure 4-13.

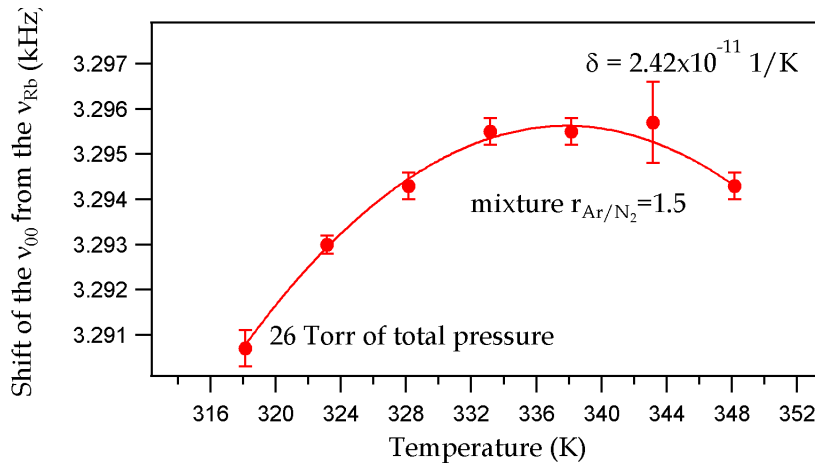


Figure 4-13: Resonance frequency shift extrapolated at zero laser power as function of the cell temperature (temperature shift). The cm-scale Rb cell contains 26 torr of Ar/N₂ mixture. Solid line represents the fit of the Eq. (2.27).

The linear TC in this case is evaluated to be $\delta=0.16 \text{ Hz/K}$ and the quadratic TC is $\gamma=4.8 \times 10^{-4} \text{ Hz/K}^2$ for $T_0=333 \text{ K}$. These coefficients are in agreement with those shown in [19]. Using the coefficients from [19] for the 26 Torr of buffer gas mixture Ar-N₂ with ratio $r=1.5$, estimated linear TC is $\delta=0.15 \text{ Hz/K}$ and quadratic TC is $\gamma=7.5 \times 10^{-4} \text{ Hz/K}^2$.

From the Figure 4-12 and Figure 4-13 it can be seen that the choice of the buffer gas mixture and the ratio between used buffer gases will determine the inversion temperature, for which the clock temperature shift is suppressed [16].

We discover that performing the temperature shift measurements on the single buffer gas Ne cell shows that the inversion temperature of $T_c=354$ K can be reached [20]. The temperature shift of the 75 torr Ne Cs MEMS cell is measured and shown in Figure 4-14.

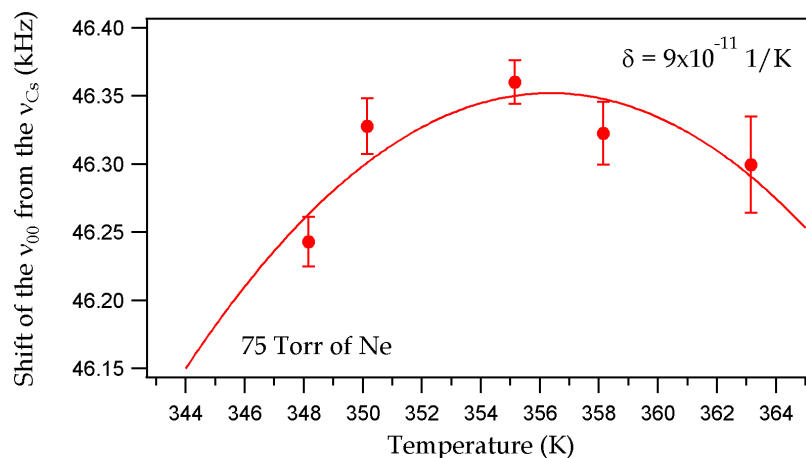


Figure 4-14: Resonance frequency shift extrapolated at zero laser power as function of the cell temperature (temperature shift). The MEMS cell contains 75 torr of Ne. Solid line represents the fit of the Eq. (1.7).

The fit of Eq. (1.7) represented by the solid red curve in Figure 4-14 gives the linear coefficient of $\delta=0.83$ Hz/K and quadratic coefficient $\gamma=-1.8 \times 10^{-5}$ Hz/K² for a pure Ne Cs cell [20]. This result shows that the mixture of two buffer gases is not necessary in order to obtain a low temperature coefficient. The low TC can be reached by using single buffer gas cell containing Ne at $T_c=354$ K cell temperature. This result was later confirmed by Kozlova, SYRTE institute, Paris giving the linear temperature coefficient of $\delta=-0.264$ Hz/Torr*K and the quadratic coefficient $\gamma=-1.70$ mHz/Torr*K² [18], for a $T_0=273$ K.

Fig. 4-14 shows that no mixture of buffer gases is needed to obtain turnover temperature because such behavior can be obtained by using a single Ne buffer gas cell. The advantage of a low TC with Ne buffer gas cell lies in the fact that the Cs metal in dispenser inside the MEMS cell will not chemically react with Ne (it was shown that the Cs dispenser has a chemical reaction with N_2 , for example) [21].

4.1.5 Summary and conclusions

The intensity LS measurements on the Cs D1 line in MEMS cell with 75 Torr of Ne are discussed here. The LS suppression as function of the modulation index M , already reported before was confirmed. The LS was also measured as function of the MEMS Cs cell temperature. The conditions were found for which α is suppressed, if the laser frequency is stabilized to the transition coupling ground states to a common $F'=3$ excited state on Cs D1 line. A qualitative explanation of this effect is proposed. The LS measurements shown here are the first LS measurements for a CPT clock on the Cs D1 line. Previously published results were obtained on the Cs D2 line. These results show that conditions exist where the intensity LS coefficient α can be minimized by choosing an appropriate cell temperature, even in the case of non-optimized phase-modulation index M . This allows working with a higher CPT signal amplitude for improved clock stability (as is the case for our data obtained with $P_{RF}=3.5$ dBm) compared to the LS compensation scheme using adjustment of M only, or to adjust M for minimized intensity LS α .

The frequency LS was also measured for the laser frequencies around coupling via the $F'=3$ excited state and for different MEMS cell temperatures. The frequency LS coefficient β is evaluated for each light intensity and found to be two times smaller than the one already reported on the Cs D2 line (see Table 4-2). These results confirm the previous measurements on the intensity LS (section 4.1.1). Most favorable for a low LS is to stabilize the laser to transitions which couples the ground states to a $F'=3$ excited state.

The temperature shift in the single buffer gas Cs MEMS cell was evaluated. It was found that the low TC can be obtained by using the 75 Torr Ne cell at $T_c=354$ K. This temperature of $T_c=354$ K coincides with the cell temperature for suppressed intensity LS for coupling ground states to a common $F'=3$ excited state on Cs D1 line.

The results obtained here are the first results on the full LS picture, intensity and frequency LS coefficient α and β , published for the Cs D1 line. The MEMS cell temperature is defined for which the clock will operate at best possible conditions: low intensity LS and low TC. The application of these results will significantly improve medium and long-term frequency stability of the atomic clocks (see Chapter 5).

4.2 Light shift and temperature shift in the ^{87}Rb wall-coated cm-scale cells

The measurements of the LS and temperature shift are also performed for ^{87}Rb tetracontane coated cm-scale cell. These measurements are done, using the same cell, in both clock regimes: DR and CPT and it will allow drawing comparisons between the frequency shifts of the two different CPT clocks: using the Cs micro-fabricated buffer gas cell (section 4.1) or the Rb cm-scale wall-coated cell. Also, it is possible to compare the frequency shift measurements in CPT and DR cases, and thus obtain an overall picture of the observed effects.

The intensity LS is measured as function of different parameters, e.g., microwave power, laser frequency detuning, the cell volume and cell stem temperatures. The frequency LS is measured and compared to the theoretical values calculated using the equation given in Chapter 2. The TC for the tetracontane wall-coated cell is evaluated. Finally, in order to compare the experimental results of the LS and TC in the two different experimental conditions with the two different vapor cells, a summarizing table of the measured coefficients is given.

The measurements are done in both clock regimes: DR and CPT. If the final results are the same in both clock regimes, only results for CPT case will be shown followed by the statement that the results for DR case are the same. Only if the results in DR are different from the ones obtained in the CPT regime, both data sets will be reported here.

4.2.1 Frequency light shift in the ^{87}Rb wall-coated cell

Frequency LS, for the DR-scheme clock on the ^{87}Rb D1 line has been measured and is shown in Figure 4-15. This measurement is performed with the experimental setup shown in Chapter 3, section 3.3.2, operated as DR clock. The laser frequency is not stabilized to the reference transitions, but is set to different detunings and is measured with a high-resolution wavemeter (see section 3.3.2). For each chosen frequency, the DR or CPT signals were recorded and from the signal Lorentzian fit the total shifts of the ν_{00} from the ν_{Rb} were extracted. Figure 4-15 shows the result obtained for DR case. The LS coefficient β is given by the local slopes of the data and depends on both the laser detuning and the laser intensity. The solid black horizontal line corresponds to the level of zero intensity LS (see Figure 4-21). Figure 4-15 also gives information about intensity

LS coefficient α : α is positive when the laser frequency is stabilized to the transitions $F=1 \rightarrow F'=1$ and $F=2 \rightarrow F'=2$ or negative for the laser frequency stabilized to the transitions $F=1 \rightarrow F'=2$ and $F=2 \rightarrow F'=1$.

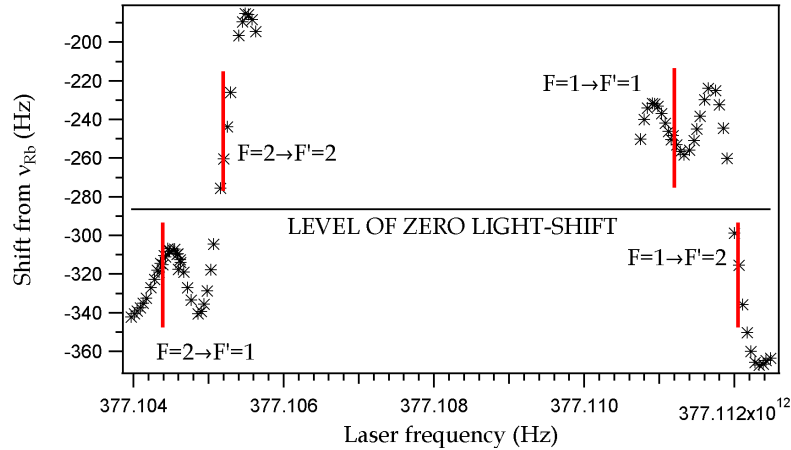


Figure 4-15: LS of the clock transition in the DR scheme, as function of the laser frequency. Total laser intensity is 0.2 mW/cm^2 . Short red vertical lines indicate four possible frequencies used for the laser stabilization. The solid black line represents the zero LS level.

For comparison of the measured frequency LS in the case of ^{87}Rb D1 line with the theoretical calculations of this effect, we started with the calculations following a similar approach as proposed in [22]. The procedure for theoretical calculations of the frequency LS were already shown in Chapter 2 (see Eq. (2.26) and Figure 2-7), for the Cs D1 line. In the case of the Rb D1 line the theoretical approach is the same; there are two excited states and the contribution from the off-resonant state must be included (section 2.4). The linewidth of the optical resonance is Doppler broadened $\Gamma=525 \text{ MHz}$ (see section 2.2.3). The difference of the involved ground-state level shifts is then calculated by using Eq. (2.27) and the transition probabilities listed in Table 4-3 and using the $m_F=0$ ground state sublevels only (see p. 50-51).

We use the Rb D1 transition rates for the σ^+ and σ components of the linearly polarized light field shown in Table 4-3, published in [10, 23]. The calculated frequency LS (solid blue line) and the measured frequency LS (black stars) are shown in Figure 4-16. The amplitude of the calculated frequency LS curve is the only fitted parameter while the optical transition frequency and the level of zero LS are fixed at the known values. A good agreement between calculated and measured frequency LS shown in Figure 4-16 also validates the model for the LS calculations in the case of the Cs D1 line (Eq. (2.26) and Figure 2-7).

Optical transition in ^{87}Rb D1 line	Transition probability
$F=1 \rightarrow F'=2$	1/2
$F=1 \rightarrow F'=1$	1/6
$F=2 \rightarrow F'=2$	1/2
$F=2 \rightarrow F'=1$	1/6

Table 4-3: Optical transition probabilities for the ^{87}Rb D1 line in the case of the linear π light polarization, taken from [10].

From the Figure 4-16 we can conclude that there are two possible laser frequencies for which the total LS is zero: -70 (5) MHz shifted from the transitions $F=2 \rightarrow F'=2$ and 44 (5) MHz from $F=1 \rightarrow F'=2$.

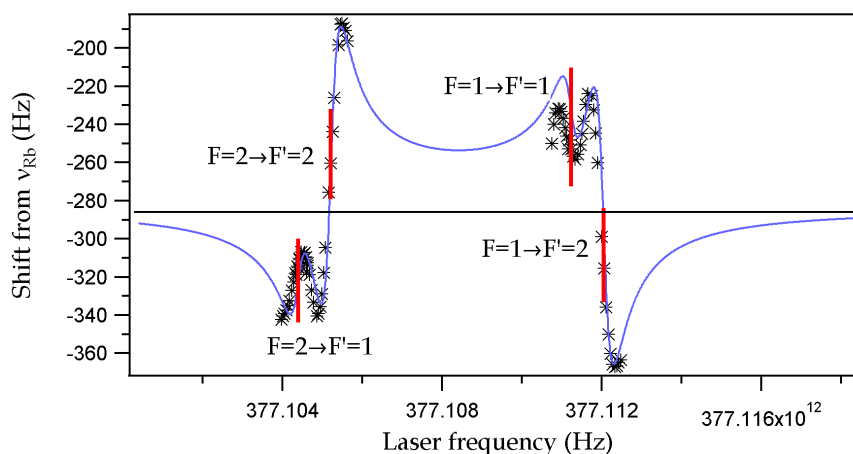


Figure 4-16: LS of the clock transition in the DR scheme, as function of the laser frequency. Black stars represent the experimental measurements and the blue solid line calculated values. Total laser intensity is 0.2 mW/cm². Short red vertical lines indicate four possible frequencies used for the laser stabilization. Hyperfine dipole transition strengths are taken from [23]. The solid black line represents the zero LS level.

The frequency LS curve shown in Figure 4-16 is different from the one published in [22], mainly by the number of the laser frequencies for which the total LS is zero (here there are two such laser frequencies for which the total LS is zero while in the case of [22] there are four such frequencies). The LS curve published in [22] is shown in Fig. 4-17.⁵

⁵ Figure 4-17 reprinted with permission from: B. S. Mathur, H. Tang and W. Happer, Phys. Rev. 171, pp. 11-19, 1968. Copyright (1997) by the American Physical Society.
<http://link.aps.org/doi/10.1103/PhysRev.171.11>

This difference comes from different Rb D1 transition rates used in the LS equation (2.25). Similar measurements of the frequency LS have been reported in [11] for the DR case in a buffer gas ^{87}Rb cell, but not over such a large laser frequency range showing the two laser frequencies for which the total LS is zero: the frequency are close to the $F=1 \rightarrow F'=2$ and $F=2 \rightarrow F'=2$ transitions.

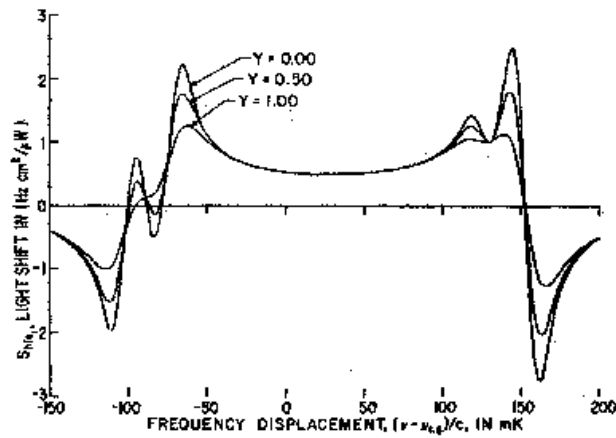


Figure 4-17: The LS of the clock transition in the DR scheme, as function of the laser frequency for a different normalized broadening parameters γ , published in [22].

The measurements of the frequency LS have also been performed for the CPT case and results are shown in Figure 4-18.

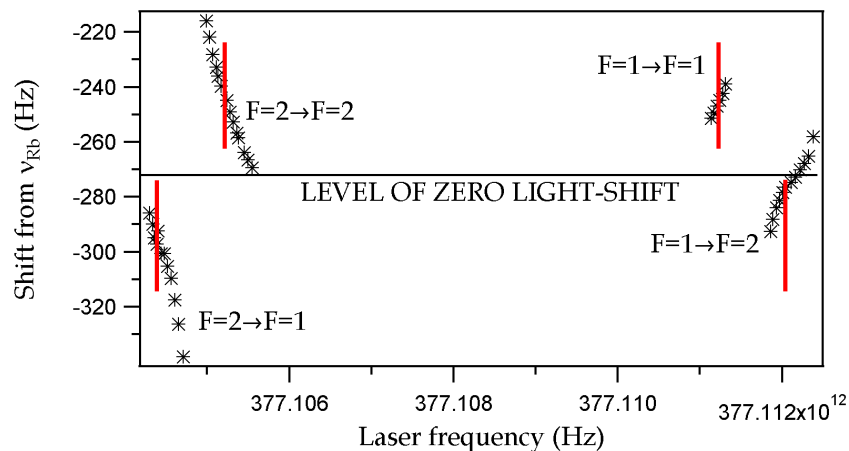


Figure 4-18: LS of the clock transition in the CPT scheme, as function of the laser frequency. Total laser intensity is 0.2 mW/cm^2 . Short red vertical lines indicate four possible frequencies used for the laser stabilization. Solid black line represents the zero LS level.⁶

⁶ Note that zero LS level is not the same for DR and CPT, Fig. 4-18 and Fig. 4-20. In the case of DR zero LS level is -287 Hz and in the CPT case -272 Hz . This difference comes from the error bars in the measurements, which can be seen from Fig. 4-24 and 4-25.

In this case there are less experimental points than in the DR case (Figure 4-15), since no CPT is created using the carrier and first-order sideband, for the laser frequencies between the indicate four possible frequencies used for the laser stabilization.

Concerning the theoretical calculations of the frequency LS in the case of CPT, we assume that the theoretical approach is similar to case of Figure 4-16. Only here, the contributions from all the sidebands and their relative intensities must be included in the calculations (see section 2.4, Equation 2.27). The Doppler width of the optical resonance is $\Gamma=525$ MHz (see section 2.2.3). For relative sideband intensities see Chapter 3, section 3.3.2.

Using Eq. 2.27 with $\Gamma=525$ MHz and correct transition strengths, the calculated and measured CPT frequency LS show serious discrepancies. Therefore we can conclude that the present model used for the calculation of the CPT LS is too simple and that processes like the light absorption in the cell must be taken into account. Further development of the theoretical model must be done in order to detect the present reasons for the differences between the measurements and theoretical calculations.

4.2.2 Intensity light shift in the ^{87}Rb wall-coated cell

4.2.2.1 Intensity light shift as function of total laser intensity

Figure 4-19 reports the CPT intensity LS measured in this experimental setup with a wall-coated cell as function of the total laser intensity, for five different RF powers driving the EOM (i.e. different modulation index M). The laser carrier frequency is stabilized to the transition $F=2 \rightarrow F'=1$ in wall-coated ^{87}Rb cell and for each RF power the shift of the clock transition frequency from the ν_{Rb} is measured.

A different presentation of these data is given in Figure 4-20 where the intensity LS coefficient α is presented as function of the microwave power P_{RF} . Changes in α with the RF power are visible, but unlike for the case of the experimental setup with MEMS cell where the suppressed LS was obtained for $P_{\text{RF}}=3$ dBm (Figure 4-1), here we did not find the same condition for the measured range of microwave powers.

One of the reasons why the suppressed LS is not obtained can be explained by the modulation performances of used the EOM (the EOM is not the same used in the experiment with the MEMS cell (4.1.1) and in this case the modulation frequency is

higher than in the case of 4.1.1). The used range of P_{RF} is narrow; it is conceivable that for higher P_{RF} values the sum of the all involved atomic level shifts and the sum over the contributions from all existing laser frequency components would nullify (see Figure 4-1).

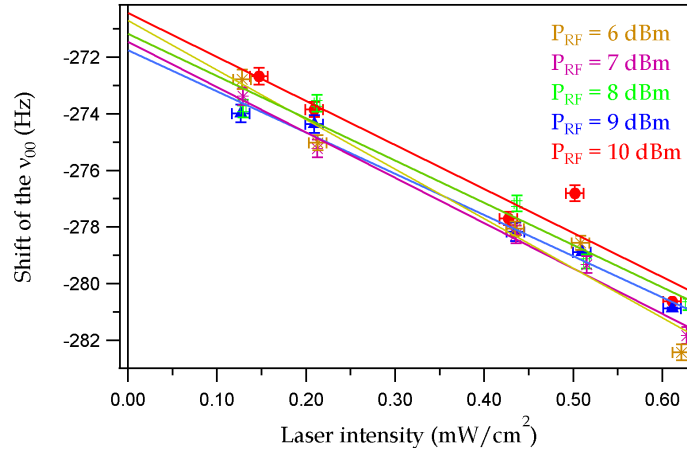


Figure 4-19: Shift of the CPT clock transition as function of total light intensity, for different RF powers. The lines are linear fits to the data.

Also, in the experiment with the MEMS cell CPT is created by using first order sidebands, where laser carrier is not totally suppressed acting halfway between the two ground-state levels in Cs (see 3.3.1). In this experiment with the ^{87}Rb wall-coated cell, CPT is created by using laser carrier and one of the first order sidebands and therefore there is no influence of the laser component acting between two ground-states in ^{87}Rb atom. This difference of different modulation frequencies used in two experiments can be one more reason why the suppressed LS is not obtained in Fig. 4-19.

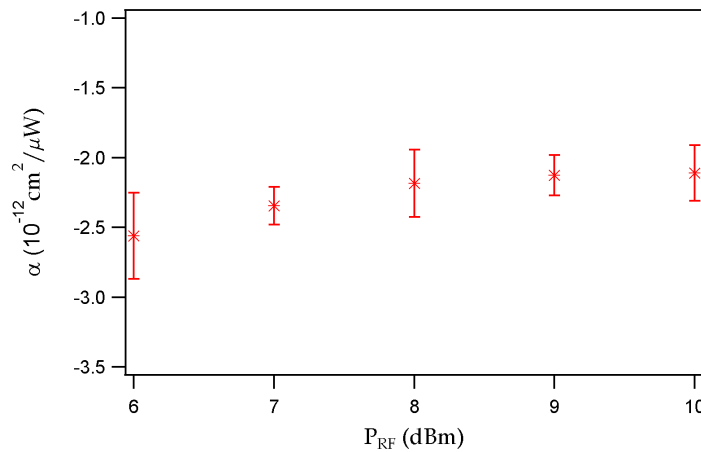


Figure 4-20: Intensity LS coefficient α as function of the microwave power P_{RF} . The laser carrier frequency is stabilized to the transition $F=2 \rightarrow F'=1$.

The tendency of the α increasing with P_{RF} is visible on the Figure 4-20. This behavior can be explained by looking at Figure 4-18. The laser carrier is stabilized to the $F=2 \rightarrow F'=1$ (α is negative) transition and 1st order sideband is on the $F=1 \rightarrow F'=1$ transition (α is positive). By increasing the modulation power P_{RF} (and modulation index M) the 1st order sideband relative intensity is increasing, while the relative intensity of the carrier is decreasing. Therefore, by the increasing the M it is expected that α will have a tendency to go from negative to positive values, which is shown in Figure 4-20.

It could not be measured for which P_{RF} α becomes zero, since $P_{RF}=10$ dBm is the maximum microwave power that can be used to drive the EOM. It can be concluded that in this experimental setup with the cm-scale ^{87}Rb wall-coated cell, a condition with suppressed α is not obtained due to the limited performance of the EOM, for the laser modulation of 6.834 GHz.

The CPT intensity LS was measured for several laser carrier stabilization frequencies (the four possible transitions in the Rb D1 line), for the chosen microwave power of $P_{RF}=10$ dBm and shown in Figure 4-21.

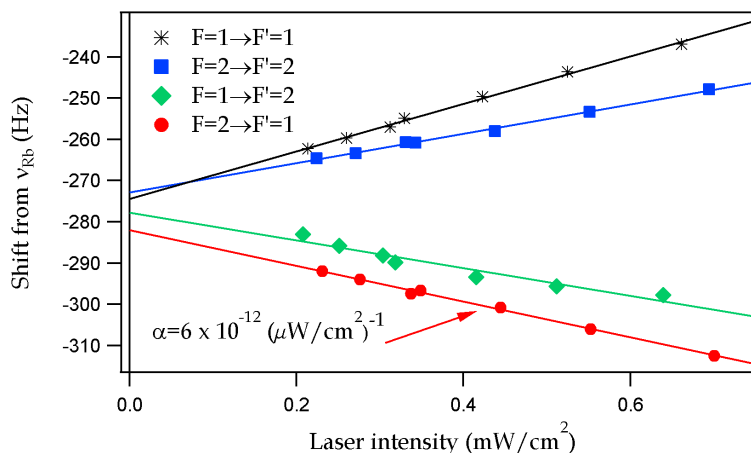


Figure 4-21: LS of the clock transition in the CPT scheme, as function of the laser intensity. The laser frequency is stabilized to the four transitions in Rb D1 line. Shifts are given relative to the unperturbed Rb clock transition frequency $\nu_{\text{Rb}}=6.834682611$ GHz.

When the laser carrier frequency is stabilized to the transitions $F=2 \rightarrow F'=1$ and $F=1 \rightarrow F'=2$ the intensity LS coefficient α (given by the slope of the lines) is negative: $\alpha=-6(1) \times 10^{-12} \text{ cm}^2/\mu\text{W}$. For the two other cases of laser carrier frequency stabilization ($F=2 \rightarrow F'=2$ and $F=1 \rightarrow F'=1$) the LS coefficient α has approximately the same value, but is positive. The wall-coated cell temperatures are $T_v=329$ K and $T_s=321$ K, the same as in DR case. Extrapolating the intensity LS to zero laser intensity gives the result about the

wall-shift. It confirms the wall-shift value measured in the Chapter 3 (Figure 3-30), 278(10) Hz. The CPT intensity LS results presented in Figure 4-21 confirm the data on the CPT frequency LS, presented in the Figure 4-18. From Figure 4-21 we can conclude that the sign of α is different, depending on the laser frequency detuning: positive when the laser frequency is stabilized to the transitions $F=1 \rightarrow F'=1$ and $F=2 \rightarrow F'=2$ or negative for the laser frequency stabilized to the transitions $F=1 \rightarrow F'=2$ and $F=2 \rightarrow F'=1$. Such behavior was already shown in Figure 4-17, for a much larger frequency scale.

The same measurements of the clock transition LS as function of the laser intensity is performed for the DR case and shown in Figure 4-22. The DR intensity LS results shown in Figure 4-22 confirm the data on the DR frequency LS, given in Figure 4-15. From Figure 4-22 the same conclusions can be given: the sign of α is different, depending on the laser frequency detuning: positive when the laser frequency is stabilized to the transitions $F=1 \rightarrow F'=1$ and $F=2 \rightarrow F'=2$ or negative for the laser frequency stabilized to the transitions $F=1 \rightarrow F'=2$ and $F=2 \rightarrow F'=1$. Such behavior is in agreement with the data of Figure 4-15, for a much larger frequency scale.

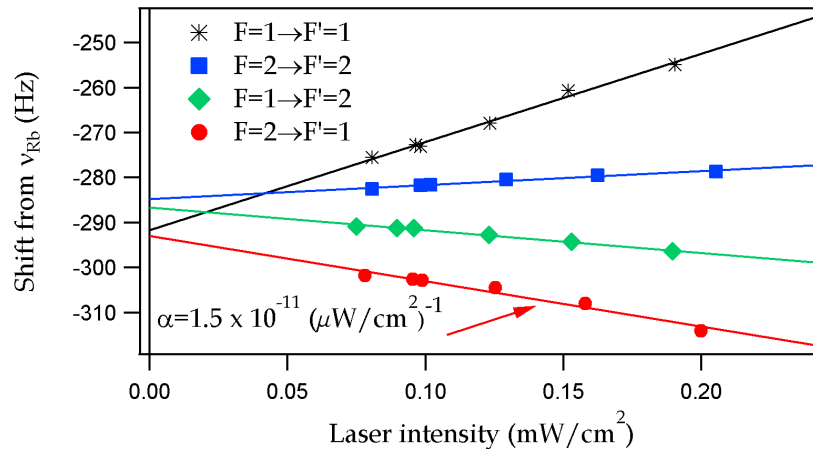


Figure 4-22: LS of the clock transition in DR scheme, as function of the laser intensity. The laser frequency is stabilized to the four transitions in Rb D1 line. Shifts are given relative to the unperturbed Rb clock transition frequency $\nu_{\text{Rb}}=6.834682611$ GHz.

4.2.2.2 Intensity light shift as function of the cell temperature

In order to investigate the intensity LS suppression as function of the cell temperature like in the case of the Cs buffer gas MEMS cell (section 4.1.1), the CPT intensity LS was measured at several wall-coated volume cell temperatures, when the laser carrier frequency is stabilized to the $F=2 \rightarrow F'=1$ transition, Figure 4-23.

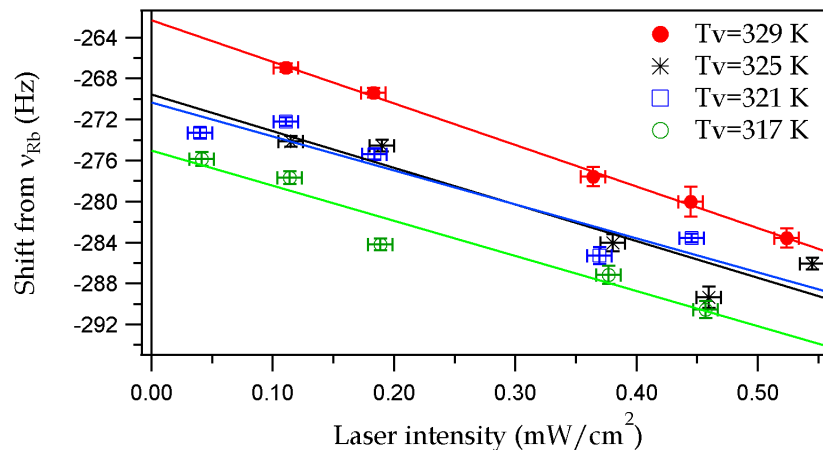


Figure 4-23: Shift of the CPT clock transition measured on the wall-coated cell, as function of laser intensity for different cell volume temperatures, while temperature of the cell stem is fixed to $T_s=313$ K. The solid lines are linear fits to the data.

When comparing these results with the same measurements obtained with the MEMS cell (Figure 4-2 and Figure 4-4) it is visible that in the case of the wall-coated cell there are no changes in α as function of the temperature. A different presentation of data from Figure 4-23 is given in Figure 4-24, where intensity LS coefficient α is evaluated as function of the cell volume temperature:

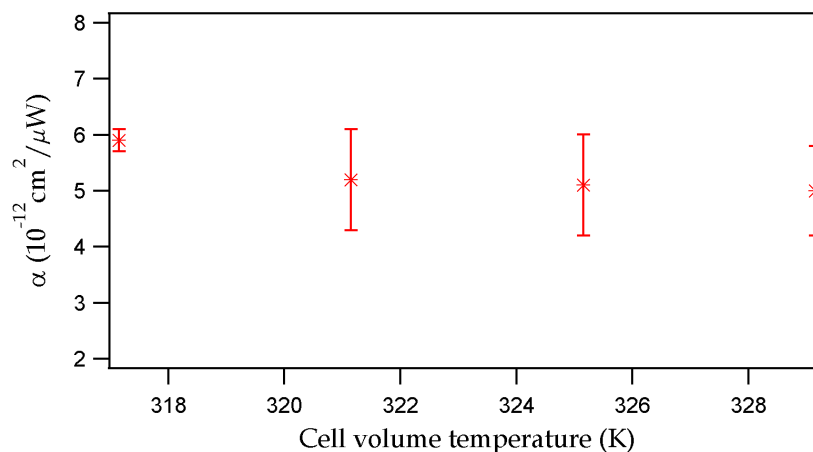


Figure 4-24: Intensity LS coefficient α as function of the cell volume temperature. The laser carrier frequency is stabilized to the transition $F=2 \rightarrow F'=1$.

The explanation is following: the clock frequency shifts with the temperature, but not α . In the case of the MEMS cell, α depends on the cell temperature due to the atomic density in the cell. Here, by changing the wall-coated cell volume temperature the atomic density does not change significantly (the atomic density change can be achieved only by changing the temperature of the cell stem that contains the liquid Rb

reservoir) therefore the α dependence on the cell volume temperature is not expected. The result of the intensity LS coefficient α being constant as function of the wall-coated cell volume temperature is confirmed by the same measurement in DR clock regime (data not shown).

The wall-coated cell stem acts as reservoir of Rb atoms and any temperature change of the cell reservoir will directly influence the density of the atoms in the cell. Following the explanation in this chapter about α depends on the cell temperature due to the atomic density in the cell (section 4.1.1), such behavior should only be obtained for the wall-coated cell in the case when the stem temperature varies (and not as function of the cell volume temperature). The LS intensity as function of different wall-coated cell stem temperatures is measured in both clock regimes: DR and CPT. In the case of DR, α dependence on the wall-coated cell stem temperature is visible. In CPT clock regime such behavior is not obtained, as will be shown in the following.

Figure 4-25 reports on the LS intensity as function of different wall-coated stem cell temperatures, for the laser carrier frequency stabilized to the $F=2 \rightarrow F'=1$ transition, in DR regime. From Figure 4-25 it can be concluded that, as expected, α depends on the wall-coated cell stem temperature. If we compare this result with the one obtained on the MEMS buffer gas cell (Figure 4-2) the LS behavior as function of the temperature shows the same tendency, going from negative to positive values, when the cell temperature is increasing.

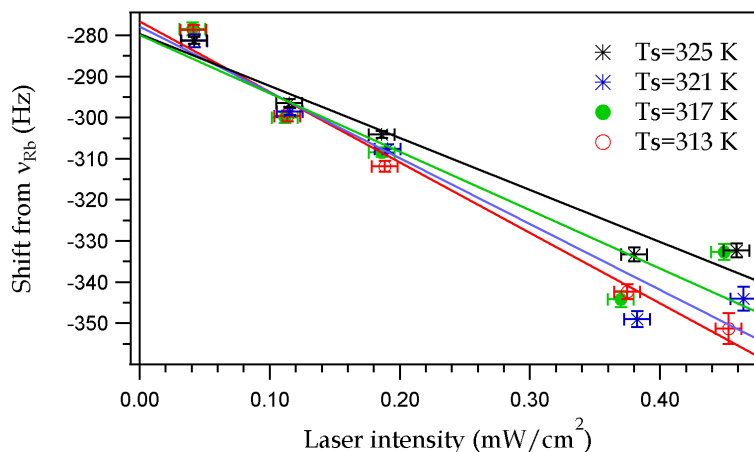


Figure 4-25: Shift of the DR clock transition measured on the wall-coated cell, as function of laser intensity for different cell stem temperatures, while the temperature of the cell volume is fixed $T_v=329$ K. The solid lines are linear fits to the data.

A different presentation of these data is given in Figure 4-26 where the DR intensity LS coefficient is presented as function of wall-coated stem temperatures:

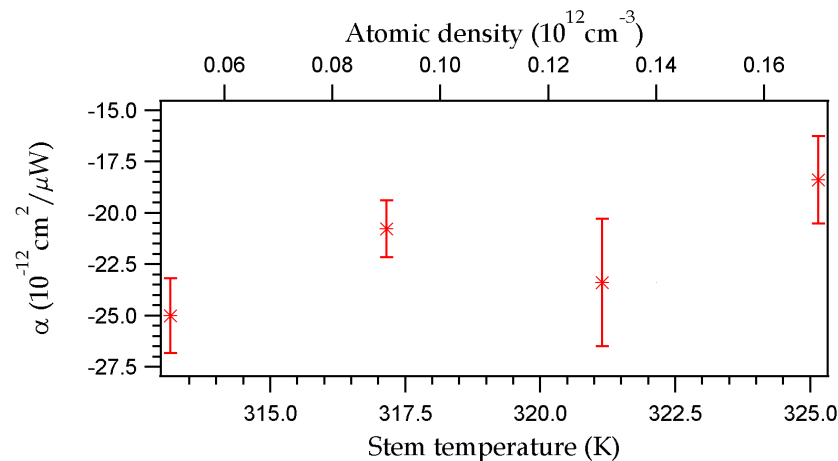


Figure 4-26: DR intensity LS coefficient α as function of the wall-coated stem temperature. The laser carrier frequency is stabilized to the transition $F=2 \rightarrow F'=1$ and the cell volume temperature is $T_v=329$ K.

The stem temperature of $T_s=325$ K is the maximum temperature used in this experimental setup, since the tetracontane coating melting temperature limits the use of higher stem temperatures. The atomic density is one order magnitude smaller here than in the case of the MEMS buffer gas cell, Figure 4-2. Here, the absolute value of the offset of α is much further away from zero than in the case of the MEMS buffer gas cell, Figure 4-2. Therefore, the tendency of α increasing with the cell stem temperature is visible and confirmed, but a condition for positive LS cannot be reached even for high stem temperatures ($T_s=373$ K).

The measurement displayed in Figure 4-25 for the case of DR is repeated for the CPT case. Figure 4-27 reports on the CPT intensity LS as function of different wall-coated stem cell temperatures, for the laser carrier frequency stabilized to the $F=2 \rightarrow F'=1$ transition. These measurements are precise within ± 4 Hz, which does not allow us to have strong conclusions about the behavior of α as function of the cell stem temperature in the case of CPT. It is expected that the LS goes from being negative to the positive, when the cell temperature is increasing (the same behavior like in DR case shown in Fig. 4-25). Data given in Fig 4-27 with its given error bars is equally compatible with α being constant, slightly increasing or decreasing with cell stem temperature.

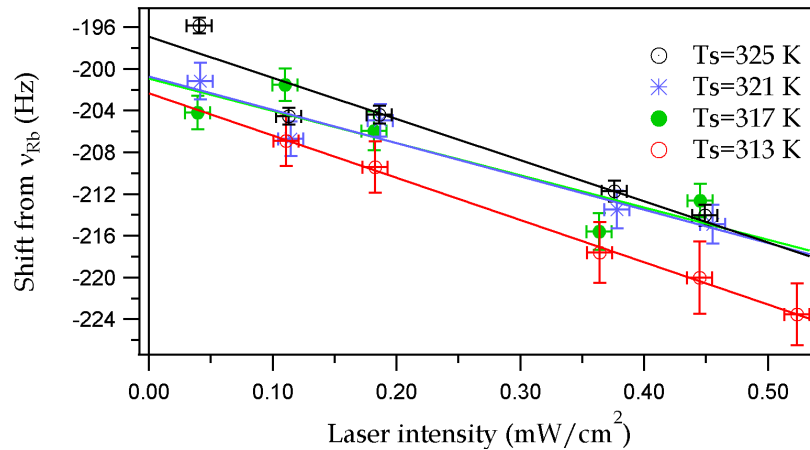


Figure 4-27: Shift of the CPT clock transition measured on the wall-coated cell, as function of laser intensity for different cell stem temperatures, while temperature of the cell volume is fixed $T_v=329$ K. Solid lines are linear fits to the data.

A different presentation of the data from the Figure 4-27 is given in Figure 4-28 where the CPT intensity LS coefficient α is presented as function of wall-coated stem temperatures. For the same range of the cell temperatures, the CPT signal contrast is much smaller than in the case of DR. This can be one of the possible explanations why the measurement resolution is not good enough to extract a strong conclusion in the case of CPT, since same behavior is expected in both clock regimes. No similar effect of the CPT LS dependence on the wall-coated cell temperature was observed and reported in the literature that would allow us comparison and further conclusions why in the case of CPT the same effect is not observed.

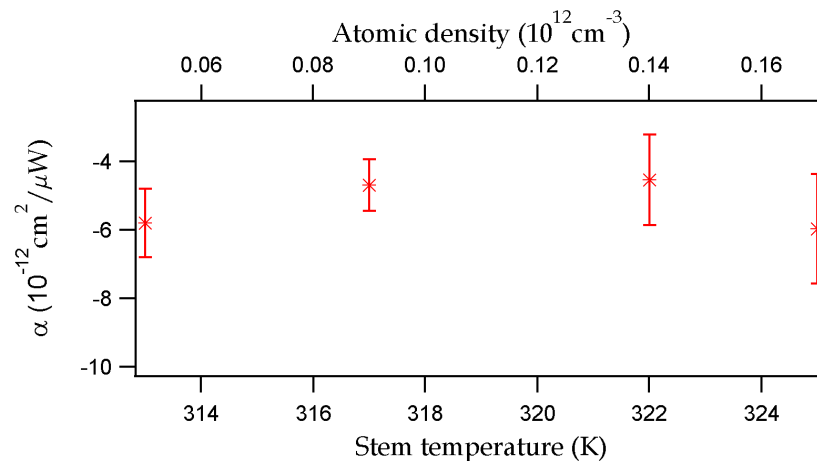


Figure 4-28: Intensity LS coefficient α as function of the wall-coated stem temperature, CPT experiment. The laser carrier frequency is stabilized to the transition $F=2 \rightarrow F'=1$ and the cell volume temperature is $T_v=329$ K.

4.2.3 Temperature shift in the ^{87}Rb wall-coated cell

The temperature shift of a wall-coated cell is an intrinsic property of the coating material itself [24] (see section 2.5.2). The physics of atoms interacting with the wall-coating will depend on variations in the cell temperature. The TC is calculated using the measurements of the intensity LS as function of cell volume and cell stem temperature, i.e. using both DR and CPT data (Figure 4-23 and Figure 4-25). For each temperature the shift as function of the laser intensity was measured. The linear fits of the data will give values for α and the resonance frequency shift extrapolated to zero laser power is the temperature shift (and in the case of DR interaction scheme microwave power shift). Cell volume temperature was varied in the range of [317-329 K]. Figure 4-29 shows the temperature shift due to the cell volume temperature in cell coated with tetracontane.

The temperature shift of the cell volume is determined by the atom-wall collisions [24]. Figure 4-29 gives the information about $\text{TC}=1.43(3)\times 10^{-10}$ 1/K in DR scheme, which can be used in calculation of the average Rb activation energy on the coating E_a (see 2.31). From (2.31) it can be found that $E_a=-(d(\Delta\nu)/dT)*k_B T/dv$. Measured $\text{TC}=1.43(3)\times 10^{-10}$ 1/K=0.977 Hz/K (Fig. 4-29) gives the energy of activation $E_a=0.031(4)$ eV. The TC has been measured in CPT regime and verified by the measurements in DR regime. The result is in agreement with the one published using the exact same wall-coated cell, by Bandi et al [25], see Table 4-4.

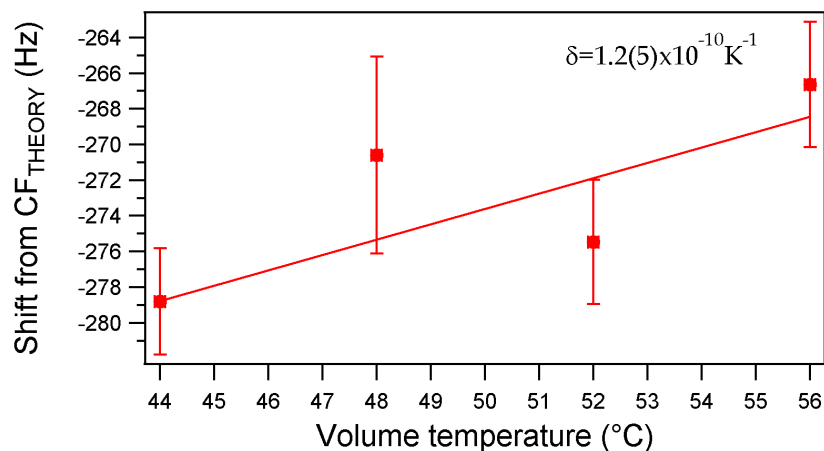


Figure 4-29: DR resonance frequency shift extrapolated at zero laser power as function of the cell volume temperature (temperature shift). The temperature of the cell stem is fixed $T_s=313$ K. The black solid curve represents the linear fit of the (Eq. 2.13) which gives the activation energy of $E_a=0.031(4)$ eV.

The stem of the wall-coated cell acts as reservoir of Rb atoms and any temperature change of the cell reservoir will directly influence the density of the atoms in the cell.

Therefore, the temperature shift due to the stem temperature change is mainly determined by the spin-exchange effect, see Eq. (2.16) [26]. The cell stem temperature was varied in the range of [313-325 K]. For each temperature the DR shift as function of the laser intensity was measured, see Figure 4-23. The DR resonance frequency shift extrapolated at zero laser power gives the TC of the cell stem temperature, Figure 4-30:

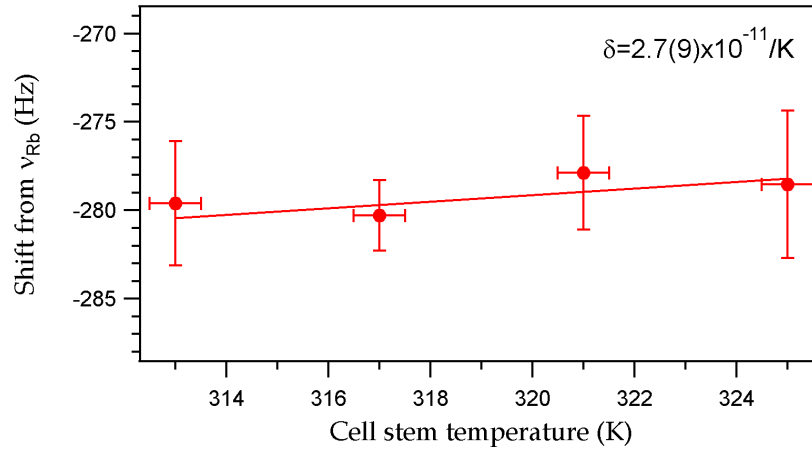


Figure 4-30: DR resonance frequency shift extrapolated at zero laser power as function of the cell stem temperature (temperature shift). The temperature of the cell volume is fixed $T_s=329$ K.

Table 4-4 lists the measured TC of volume and stem of the tetracontane coated cell in DR and CPT clock regime and compares these results with the those using the same physic package, already published in [25]. The measurements discussed in this thesis are consistent with the measurements published earlier in [25] using the same wall-coated cell. The stem TC is 2.5 times smaller than the TC of the cell volume in DR and CPT case. These measurements show that the shift of the clock frequency will be more influenced by the atom-wall collisions (change of the cell volume temperature) than by the spin-exchange (cell stem temperature), by a factor of 2.5. The influence of the TC and the LS on the clock frequency stability will be studied in detail in the next chapter.

	TC_{VOLUME}	TC_{STEM}
In DR (1/K)	$1.2(5) \times 10^{-10}$	$2.7(9) \times 10^{-11}$
In CPT (1/K)	$1.4(3) \times 10^{-10}$	$4(2) \times 10^{-11}$
In DR (1/K) [25]	$2.03(7) \times 10^{-10}$	$3.22(4) \times 10^{-11}$

Table 4-4: Measured cell volume and cell temperature coefficients, compared with the already published values in [25].

4.2.4 Summary and conclusions

The frequency LS measurements on the ^{87}Rb D1 line in cm-scale cell coated with tetracontane are discussed here. A full picture of the frequency LS is given in the both experimental setups: DR and CPT.

- DR: Preliminary theoretical calculations of the clock transition LS as function of laser frequency are done and show good qualitative understanding of the obtained measurements. Two possible laser frequencies are found for which the intensity LS is zero, a result different from the results published in [22], due to the different optical transition probabilities (which reflects different geometry and polarization in the experiments) in Rb atom used in the theoretical evaluations.
- CPT: The calculations of the CPT frequency LS show serious discrepancies compared to the measured LS. Further development of the theoretical model must be done in order to detect the reasons for the present differences between the measurements and theoretical calculations.
- The intensity LS is measured as function of the total laser intensity, for five different RF powers driving the EOM, in CPT studies. The LS suppression as function of the modulation index M (like it is shown in section 2.4) is not obtained due to the limited EOM efficiency at $\nu=6.8$ GHz used here, but the tendency of the α increasing with increasing the P_{RF} is shown.

The intensity LS is measured as function of the wall-coated cell temperature in both experimental schemes: DR and CPT.

- DR: The intensity LS as function of the cell volume temperature measurements show that there are no changes in α as function of the temperature. Such behavior is expected since the atomic density in the cell is not changed by changing the cell volume temperature and therefore α should remain the same for each cell volume temperature. In the case when cell stem temperature is changing, the LS behavior shows the same tendency as in the case of the MEMS Cs buffer gas cell (section 4.1.1), going from being negative towards zero, when the cell temperature is increasing. The usable temperature range in this case is smaller than in the case of the MEMS Cs buffer gas cell due to melting temperature limit of the coating (the maximum temperature stem temperature is $T_{\text{S}}=325$ K). Therefore the positive LS condition was not reached in this case, but it is expected at higher temperatures.

- CPT: The behavior that α does not change with the cell volume temperature, as already demonstrated in DR case, is confirmed for the CPT interaction scheme. However, the expected change of α with the cell stem temperature, already shown in DR case, could not be confirmed working in the CPT scheme. This might be possibly due to a limited measurement resolution.

The temperature shift of a tetracontane-coated cell is measured and evaluated for the cell volume and the cell stem temperature. It is evaluated that the shift of the clock frequency is more strongly influenced by the change of the cell volume temperature than by the cell stem temperature, by factor of 2.5, indicating that the atom-wall collisions influence the temperature shift of the clock frequency much more than the spin-exchange effect. Such behavior is obtained for both: the DR and CPT case. The average Rb adsorption energy on the coating E_a is calculated. These results showed a good agreement with the already reported ones, using the same wall-coated cell [25]. The influence of TC of the coating on the clock frequency will be evaluated in the next chapter and may be expected to have an important impact on the clock stability.

4.3 Comparison and discussions of the results

The possibility to measure and evaluate the LS and TC coefficients in different clock schemes, using different vapor cells, gives the opportunity to learn more about their dependence on used atoms, chosen experimental conditions or different cells.

The theoretical model for the frequency LS calculation for a four level model atom was proposed in section 2.4. Experimental measurements of the same effect for the two different experimental setups: using the Cs buffer gas MEMS cell in CPT and using the ^{87}Rb wall-coated cm-scale cell and in both CPT and DR are shown in section 4.1 and 4.2. These measurements are then compared to the theoretical calculations:

- DR in ^{87}Rb wall-coated cell: The theoretical model for the frequency LS calculation shows a good agreement with the measured frequency LS, for a single laser frequency (section 4.2.1).
- CPT in ^{87}Rb wall-coated cell: The same theoretical model can be applied in CPT case; only here the contributions from all sidebands and their relative intensities must be included in the calculations. But unlike in the DR case, the calculated and measured frequency LS show serious discrepancies. The present model is too simple to be used in the CPT case and further development of this model

must be done (e.g. including the processes like the light absorption in the cell) to obtain the full LS picture in CPT case.

- CPT in Cs buffer gas cell: Similar conclusion can be given for the CPT frequency LS model in the case of Cs buffer gas cell: there is a qualitative agreement between the calculated and measured LS (being positive in the case when CPT is created by coupling to $F'=3$ excited state or negative for coupling to $F'=4$ excited state), but the theoretical model must include the light absorption in the cell, etc. in order to obtain the full picture of the CPT frequency LS in buffer gas Cs cells.

Table 4-5 summarizes the results on the intensity LS coefficient α , frequency LS coefficient β and TC, including the results obtained with the cm-scale glass-blown ^{87}Rb cell with buffer gas mixture Ar- N_2 (experimental setup described in Appendix A).

Experiment	Section 4.1	APPENDIX A	Section 4.2	
Cell	Cs MEMS + Ne (75 Torr)	Rb cm-scale cell +Ar- N_2 (20 Torr)	Rb cm-scale wall-coated	
Interaction scheme	CPT	DR	DR	CPT
Optical transition	D1 line	D2 line	D1 line	D1 line
Tc (K)	354	343	$T_v=329$ and $T_s=321$	$T_v=329$ and $T_s=321$
Transition used for laser stabilization	Coupling to $F'=3$	CO 21 \rightarrow 23	$F=2\rightarrow F'=1$	$F=2\rightarrow F'=1$
α ($\text{cm}^2/\mu\text{W}$) $\times 10^{-12}$	0.17(1)	1.3(1)	-15.0(1)	-6.1(8)
β (mHz/MHz) ($I_L=0.2$ mW/cm 2)	-32(2) (Tc=338 K)	460(34)	80(5)	-93(5)
TC (1/K) $\times 10^{-10}$	0.10(2) $T_{\text{inv}}=354$ K	0.18(7) $T_{\text{inv}}=338$ K	1.2(2) _{volume}	1.4(3) _{volume}
			0.27(4) _{stem}	0.6(2) _{stem}

Table 4-5: Summarization of the intensity LS coefficient α , frequency LS coefficient β and TC for three different experimental setups.

The measured frequency LS in the case of the wall-coated ^{87}Rb cm-scale cell is three times higher than in the case of buffer gas Cs MEMS cell and 5-6 times smaller than in the case of ^{87}Rb cm-scale cell with buffer gas mixture. This difference can be attributed to:

- The width of the optical transitions is not the same and therefore this difference will contribute to the different frequency LS (see Eq. (2.21)). In the case of Cs, the width of the optical transition, due to the presence of Ne buffer gas atoms is $\Gamma=1510$ MHz while for the ^{87}Rb wall coated cell $\Gamma=525$ MHz. It is expected that this difference in Γ contribute to a lower LS in case of Cs cell.
- Different transition rates for Cs and Rb atoms will also contribute to the different LS (see Eq. (2.21)). In both experiments the D1 line is used: for Cs D1 line transition rates see Table 2-3 and for Rb D1 line transition rates see Table 4-3.
- The laser sidebands used in the two CPT experiments (section 3.3) have different intensities resulting in a different degree of β compensation between these sidebands. In experiments with the Cs MEMS cell, the two first-order laser sidebands are used and here the amplitude modulation causes a stronger sideband asymmetry while in the second experiment with the Rb wall-coated cell, the carrier and one of the first-order sidebands which have almost equal intensity are used to create CPT. This can lead to smaller LS in the experiment with the ^{87}Rb wall-coated cell. This is not the case for our results given in Table 4-5. The LS is bigger for the case of the experiment using the Cs MEMS cell compared to the case using the Rb wall-coated cell, which means that contributions from different transition rates and different optical widths are compensating the a stronger sideband asymmetry in the experiment with the Cs MEMS cell.

In both experimental setups (4.1 and 4.2) the laser frequency is determined for which the intensity LS is suppressed. It has been previously demonstrated that the intensity LS α and frequency LS β are inversely proportional to the buffer gas pressure, essentially due to the broadening of the optical resonance [13], so further reduction of the LS coefficients in the case of buffer gas cell may be expected when using higher buffer gas pressures [26].

The TC in the case of buffer gas mixtures can be suppressed at a selected temperature by choosing an optimized buffer gas ratio. This thesis shows that having a pure Ne buffer gas cell and choosing the proper temperature, the same effect can be obtained. Because of these findings, it is expected that TC will be significantly larger in the case of

the wall-coated cell than in the case of buffer gas cell. These expectations are confirmed by our measurements (see Table 4-5).

The experimental results discussed in this chapter are of importance for understanding the short- medium- and long-term stability limits of atomic clocks using buffer gas or wall-coated cells. The use of the MEMS buffer gas cells in atomic clocks is of high interest since the need for compact and low power instruments is constantly growing. The use of wall-coatings in atomic clocks is also of high interest since very narrow signal linewidths can be achieved from both, cm-scale and small dimension cells. These very narrow linewidths significantly improve the clock frequency stability (see Chapter 5). Evaluation of the possible frequency shifts of an atomic clock using the wall-coated or buffer gas cells is one step further towards the new generations of atomic clocks which will be used for satellite navigation and positioning systems (GPS, GALILEO), telecommunication, etc.

REFERENCES:

- [1] J. VANIER, R. KUNSKI, A. BRISSON and P. PAULIN, *Progress and prospects in Rubidium frequency standards*, Journal de Physique 42 (1981), pp. 139-150.
- [2] M. OHTSU, M. HASHIMOTO and H. OZAWA, *A Highly Stabilized Semiconductor Laser and Its Application to Optically Pumped Rb Atomic Clock*, Proc. of the 39th Annual Symposium on Frequency Control (FCS) (1985), pp. 43-53.
- [3] J. C. CAMPARO, R. P. FRUEHOLTZ and C. H. VOLK, *Inhomogeneous light shift in alkali-metal atoms*, Phys. Rev. A 27 (1983), pp. 1914-1924.
- [4] M. ARDITI and J. L. PICQUE, *Precision measurements of the light shifts induced by a narrow-band GaAs laser in the 0-0 ¹³³Cs hyperfine transition*, J. Phys. B: Atom. Molec. Phys. 82 (1975), pp. 331-335.
- [5] F. LEVI, A. GODONE and J. VANIER, *The light shift effect in the coherent population trapping cesium maser*, IEEE Trans. Ultrason. Ferroelectr. Freq. Control 47 (2000), pp. 466-470.
- [6] R. BOUDOT, P. DZIUBAN, M. HASEGAWA, R. K. CHUTANI, S. GALLIOU, V. GIORDANO and C. GORECKI, *Coherent population trapping resonances in Cs-Ne vapor microcells for miniature clocks applications*, J. Appl. Phys. 109 (2011), pp. 014912-11.

- [7] V. GEORGINOV, S. KNAPPE, P. D. SCHWINDT, L. HOLLBERG and J. KITCHING, *Long-term frequency instability of atomic frequency references based on coherent population trapping and microfabricated vapor cells*, J. Opt. Soc. Am. B 23 (2006), pp. 593-597.
- [8] E. E. MIKHAILOV, T. HORROM, N. BELCHER and I. NOVIKOVA, *Performance of a prototype atomic clock based on lin//lin coherent population trapping resonances in Rb atomic vapor*, J. Opt. Soc. Am. B 27 (2010), pp. 417-422.
- [9] V. SHAH, V. GEORGINOV, P. D. D. SCHWINDT, S. KNAPPE, L. HOLLBERG and J. KITCHING, *Continuous light-shift correction in modulated coherent population trapping clocks*, Appl. Phys. Lett. 89 (2006), pp. 151124- 3.
- [10] D. A. STECK, Alkali D line data, version 2.1.4, (2010).
- [11] J. Q. DENG, G. MILETI, J. M. LOPEZ-ROMERO, D. A. JENNINGS, F. L. WALLS and R. E. DRULLINGER, *Study of the frequency stability of laser-pumped rubidium gas-cell frequency standards*, Proceedings of the 11th European Frequency and Time Forum (EFTF) (1997), pp. 211- 215.
- [12] N. ALLARD and J. KIELKOPF, *The effect of neutral nonresonant collisions on atomic spectral lines*, Rev. Mod. Phys. 54 (4) (1982), pp. 1103-1182.
- [13] A. NAGEL, S. BRANDT, D. MESCHÉDE and R. WYNANDS, *Light shift of coherent population trapping resonances*, Europhys. Lett. 48 (1999), pp. 385-389.
- [14] S. KNAPPE, R. WYNANDS, J. KITCHING, H. G. ROBINSON and L. HOLLBERG, *Characterization of coherent population-trapping resonances as atomic frequency references*, J. Opt. Soc. Am. B 18 (2001), pp. 1545-1553.
- [15] R. LUTWAK, D. EMMONS, W. RILEY and R. M. GARVEY, *The Chip-Scale Atomic Clock – Coherent Population Trapping vs. Conventional Interrogation*, Proceedings of the 34nd Precise Time and Time Interval Systems and Applications Meeting (2002), pp. 1-12.
- [16] R. BOUDOT, D. MILETIC, P. DZIUBAN, C. AFFOLDERBACH, P. KNAPKIEWICZ, J. DZIUBAN, G. MILETI, V. GIORDANO and C. GORECKI, *First-order cancellation of the Cs clock frequency temperature-dependence in Ne-Ar buffer gas mixture*, Opt. Express 19 (2011), pp. 3106-3114.
- [17] K. DENG, X. CHEN and Z. WANG, *Minimization of the temperature coefficient of resonance frequency shift in the coherent population trapping clock*, Opt. Lett. 36 (2011), pp. 1740-1742.

- [18] O. KOZLOVA, S. GUERANDEL, E. DE CLERCQ, *Temperature and pressure shift of the Cs clock transition in the presence of buffer gases: Ne, N₂, Ar*, Phys. Rev. A 83 (2011), pp. 062714-9.
- [19] J. VANIER and C. AUDOIN, *The Quantum Physics of Atomic Frequency Standards*, Adam Hilger, Bristol, UK, (1989).
- [20] D. MILETIC, P. DZIUBAN, R. BOUDOT, M. HASEGAWA, R. K. CHUTANI, G. MILETI, V. GIORDANO and C. GORECKI, *Quadratic Dependence on Temperature of the Cs 0-0 Hyperfine Resonance Frequency in a Single Ne Buffer Gas Microfabricated Vapor Cell*, Electron. Lett. 46 (2010), pp. 1069-1070.
- [21] J. DZIUBAN, C. GORECKI, V. GIORDANO, L. NIERADKO, H. MAILLOTE and M. MORAJA, Procédé de fabrication d'une cellule à gaz active pour l'horloge atomique à gaz ainsi obtenue, French Patent No. 06/09089 (2006).
- [22] B. S. MATHUR, H. TANG and W. HAPPER, *Light shifts in the alkali atoms*, Phys. Rev. 171 (1968), pp. 11-99.
- [23] R. WYNANDS, A. NAGEL, S. BRANDT, D. MESCHEDE and A. WEIS, *Selection rules and line strengths of Zeeman-split dark resonances*, Phys. Rev. A 58 (1998) , pp. 196-203.
- [24] J. VANIER, R. KUNSKI, A. BRISSON and P. PAULIN, *Progress and prospects in rubidium frequency standards*, J. de Physique 12, (1981), pp. 139-150.
- [25] T. BANDI, C. AFFOLDERBACH and G. MILETI, *Laser-Pumped Paraffin-Coated Cell Rubidium Frequency Standard*, Journal of Applied Physics 111 (2012), pp. 124906-8.
- [26] D. BUDKER, L. HOLLBERG, D. F. KIMBALL, J. KITCHING, S. PUSTELNY and V. V. YASCHUK, *Investigation of microwave transitions and nonlinear magneto-optical rotation in anti-relaxation-coated cells*, Phys. Rev. A 71, 012903 (2005).
- [27] J. CAMPARO, J. COFFER and J. TOWNSEND, *Laser-pumped atomic clock exploiting pressure-broadened optical transitions*, J. Opt. Soc. Am. B 22 (2005), pp. 521-528.

Chapter 5

Clock frequency stability

This chapter reports investigations on short-, medium- and long-term stabilities of the two clocks, used for the studies in this thesis, based on the MEMS Cs buffer gas cell and the ^{87}Rb cm-scale wall-coated cell, respectively. The influence of the intensity LS, frequency LS and TC, experimentally measured and discussed in Chapter 4, on the clock short-, medium- and long-term frequency stability is evaluated.

5.1 CPT atomic clock using the MEMS Cs buffer gas cell

5.1.1 Short-term frequency stability

As shown in section 1.5 (Eq. 1.16), the atomic clock short-term frequency stability depends on the signal discriminator slope and the clock detection noise. The clock signal is preliminary optimized as function of the laser intensity and the MEMS cell temperature. First, the signal amplitude and the signal linewidth as function of the laser intensity were measured to optimize the signal discriminator slope D (see Figure 3-27 (a) and Figure 3-27 (b)) to obtain the best possible clock frequency stability (1.16)). The signal amplitude and signal linewidth were also measured as function of the MEMS cell temperature. The discriminator slope D is optimized for the laser intensity of $I_L=1.9$ mW/cm² and the cell temperature of $T_c=353$ K (Figures 3-29 (a) and 3-29 (b)), resulting in $D=8.4 \times 10^{-7}$ V/Hz.

The shot-noise limit, as ultimately achievable clock stability, is evaluated. Shot-noise represents the average statistical noise due to the statistical nature of photons arrival at the detector and the corresponding voltage noise density can be evaluated by using the formula:

$$n_{\text{shot}} = R * I_{\text{shot}} = R * \sqrt{(2eI_{\text{DC}}\text{BW})} = \sqrt{2eRV_{\text{DC}}\text{BW}} \left[\frac{\text{V}}{\sqrt{\text{Hz}}} \right], \quad (5.1)$$

where $R=100 \text{ k}\Omega$ is photodetector resistance, I_{shot} the shot-noise current for the DC signal current I_{DC} [$\text{A}/\text{Hz}^{1/2}$] recorded on the photodetector, e the elementary charge, V_{DC} the signal voltage recorded on the photodetector and BW the measurement bandwidth.

With this evaluation it is possible to predict the short-term stability for the case where the shot-noise limit is reached, using Eq. (1.16):

$$\begin{aligned} \sigma_y(\tau)_{\text{shot-noise}} &= \frac{1}{v_{\text{Cs}}} \frac{n_{\text{shot}}}{\sqrt{2D}} \sqrt{\frac{1}{\tau}} = \frac{1}{4.596 * 10^9 \text{ Hz}} \frac{5 * 10^{-8} \frac{\text{V}}{\sqrt{\text{Hz}}}}{\sqrt{2} * 8.4 * 10^{-7} \frac{\text{V}}{\text{Hz}}} \\ &= 1 * 10^{-11} \sqrt{\frac{1}{\tau}} \end{aligned} \quad (5.2)$$

In the atomic clock operating conditions it is often difficult to reach the shot-noise limit due to the additional noise contributions from different clock elements, e.g., local oscillator, laser intensity noise, laser FM-to-AM noise conversion in atomic vapor, EOM technical noise, etc. Therefore, the clock short-term stability is usually higher than the shot-noise limit.

The expected preliminary clock short-term stability can be evaluated by measuring the clock detection noise. The clock detection noise is measured as the PSD of the clock's photodetector output voltage by using a Fast Fourier Transform (FFT) spectrum analyzer as shown in Figure 5-1.

The clock short-term stability is estimated by using (5.2), but in this case n_{shot} is replaced by the measured detection noise shown in Figure 5-3. Taking into account that the noise measurements are preliminary and therefore noise spectrum spurious, n_{exp} is estimated as average value of spurious for 660 Hz, which is the FM frequency of the microwave frequency used in experiment here (see 3.3.1):

$$\begin{aligned}\sigma_y(\tau)_{\text{short-term}} &= \frac{1}{v_{Cs}} \frac{n_{\text{exp}}}{\sqrt{2D}} \sqrt{\frac{1}{\tau}} = \frac{1}{4.596 * 10^9} \frac{2 * 10^{-6} \frac{V}{\sqrt{\text{Hz}}}}{\sqrt{2} * 8.4 * 10^{-7} \frac{V}{\text{Hz}}} \\ &= 3.1 * 10^{-10} \sqrt{\frac{1}{\tau}}\end{aligned}\quad (5.3)$$

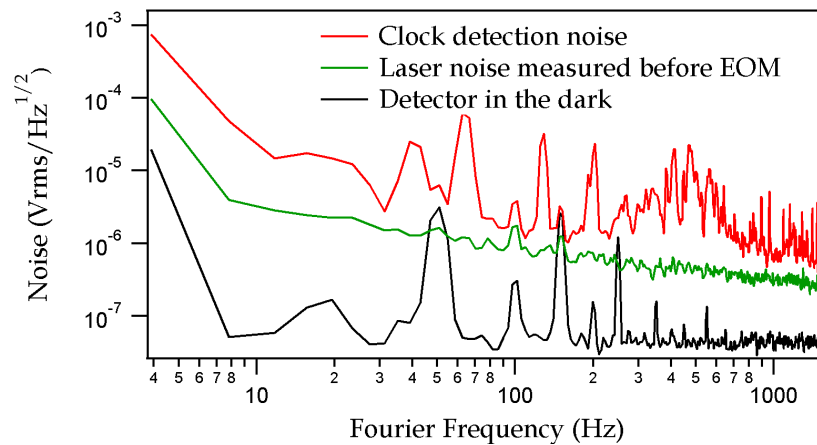


Figure 5-1: Clock detection noise measurement (measured on the clock photodetector) for the CPT resonance obtained by coupling via $F'=3$ state and cell temperature of $T_c=353$ K. The black line represents the measured noise of the detector in the dark. The green line is the measured laser noise on the photodetector placed before EOM (laser RIN noise) and the red line represents the noise on the photodetector placed after EOM and after the cell.

For the frequency stability measurements, the CPT atomic clock (using the MEMS Cs cell with buffer gas) frequency was compared to the 10 MHz output of a Hydrogen maser and measured with the Picotime frequency comparator device with phase time resolution of < 2 ps rms [1]. The laser carrier frequency was stabilized to the transition $F \rightarrow F'=3$. Figure 5-2 displays two results: red squares show the measured Allan deviation of the clock, for the MEMS cell temperature of $T_c=353$ K and laser intensity of $I_L=1.9$ mW/cm² and black circles represent the clock frequency stability after the LS and TC optimization (see 4.1.1 and 4.1.4).

The black solid line represents the predicted short-term stability (signal-to-noise limit) with optimized signal and measured detection noise, while the blue solid line represents the shot-noise limit. The clock shows a short-term stability of 5.6×10^{-10} at $\tau=1$ s (red squares in Fig. 5-2). For $\tau=100$ s to $\tau=1000$ s (onset of medium-term) it levels between 3×10^{-10} to 6×10^{-10} .

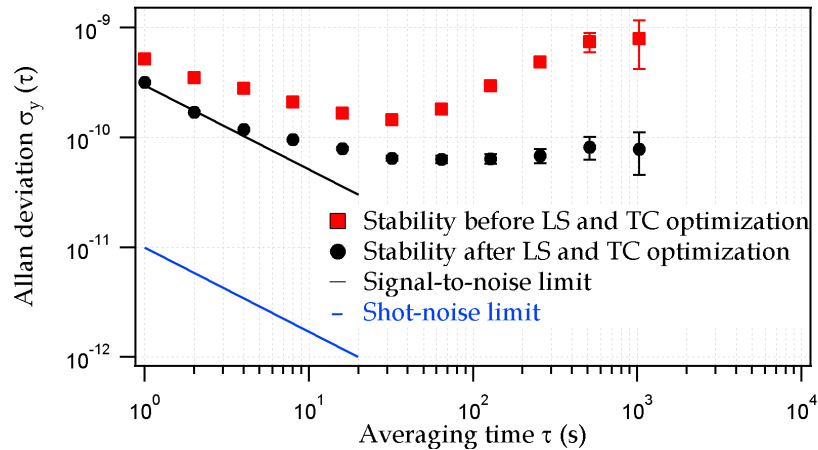


Figure 5-2: Short-term clock frequency stability measurement of the CPT atomic clock with buffer gas Cs MEMS cell, measured before (red squares) and after (black circles) optimizing the clock parameters for suppressed LS and TC. The black solid line represents the signal-to noise ratio calculated with (5.3) and the blue solid line represents the shot-noise limit, calculated with (5.2).

The measurements discussed in section 4.1 (Figure 4-2) showed that the intensity LS is suppressed for the MEMS cell temperature of $T_c=354$ K. Also, for the same MEMS cell temperature of $T_c=354$ K, the inversion temperature is reached, indicating that the TC is optimized (Figure 4-14). To see the impact of the LS and TC optimization on the clock frequency stability, the MEMS cell temperature was changed to $T_c=354$ K and the clock frequency stability re-measured (all the other clock parameters remained the same as in the measurement shown in red squares in Figure 5-2). The clock frequency stability data, with optimized LS and TC are shown in Figure 5-2 in black circles. The clock with optimized LS and TC displays a short-term stability of $3 \times 10^{-10} \tau^{-1/2}$ up to $\tau=30$ seconds, which is in a good agreement with the predicted value of $3.1 \times 10^{-10} \tau^{-1/2}$. The observed difference in the short-term (up to $\tau=30$ s) arises from the decreased detection noise of the system after optimizing the laser frequency stabilization parameters. Comparison between data in medium-term clock frequency stability indicates an improvement of one order magnitude in the clock frequency stability due to the optimization of the LS and TC.

Table 5-1 represents the summary of the instability contributions to the clock short-term frequency stability. The table includes measured short-term laser frequency stability and typical laser intensity variation in short-term, which are used in the equations for the calculation of the intensity and frequency LS contribution at $\tau=1-100$ sec. From the Table 5-1 it can be concluded that the total contribution of the LS to the clock frequency stability is on the level of 9.4×10^{-12} , for $\tau=1-100$ s. Intensity LS has negligible influence to the clock short-term and limitation on the 10^{-12} level comes from

the frequency LS. The intensity and frequency LS do not limit the present clock short-term stability since the measured clock short-term stability is on the 10^{-10} level.

From the Table 5-1 it can be concluded that the main contributor to the short-term frequency stability is the signal-to-noise ratio (mainly LO noise and small contrast of the CPT signal). Further improvement in short-term clock frequency stability can be obtained by detailed signal optimization (in the case above, the signal was preliminary optimized) and by decreasing the detection noise on the experimental setup originating from the various experimental setup elements, e.g., LO, laser (intensity noise and FM-to AM noise conversion in the cell), EOM, etc.

Physical effect	Experiment	Variation at 1 s	Equation	Instability ($\tau^{-1/2}$)
Shot-noise limit	/	$n_{\text{shot}}=5 \times 10^{-8}$ V/Hz ^{1/2}	Eq. (5.2)	1×10^{-11}
S/N limit	$D=8.4 \times 10^{-7}$ (V/Hz)	$n_{S/N}=2 \times 10^{-6}$ V/Hz ^{1/2}	Eq. (5.3)	3.1×10^{-10}
Intensity LS ($ \alpha $)	1.16(2) (mHz*cm ² /μW)	$\sigma_{I\text{-laser}} < 6 \times 10^{-4}$ [2]	$\frac{\alpha * I_L * \sigma_{I\text{-laser}}}{\nu_{Cs}}$	$< 1.4 \times 10^{-13}$
Frequency LS ($ \beta $)	644(2) (mHz/Hz)	$\sigma_{f\text{-laser}} < 4 \times 10^{-10}$	$\frac{\beta * \nu_L * \sigma_{f\text{-laser}}}{\nu_{Cs}}$	$< 9.4 \times 10^{-12}$
LO	not measured			unknown
Total instability contribution between 1-100 s				$\sim 3.1 \times 10^{-10}$

Table 5-1: Summary of the instability contributions to the clock short-term frequency stability ($\tau=1-100$ s). Intensity and frequency LS coefficients α and β are evaluated for the $F \rightarrow F'=3$ transition. σ_I is measured in the case of the DFB laser head and estimated to be 2 times worse here [2]. Instability due to intensity LS is evaluated for $I_L=3$ mW/cm².

After the preliminary short-term frequency measurements discussed above, Dr. Luc Schneller continued to work on the same experimental setup, optimizing the discriminator slope and replacing the commercial synthesizer providing the 4.6 GHz (see 3.3.1) with the Caesium Frequency synthesizer CS-1 OPT2 [8]. Due to the new frequency synthesizer and laser intensity optimization a one order-of-magnitude better short-term frequency stability is obtained, Figure 5-3.

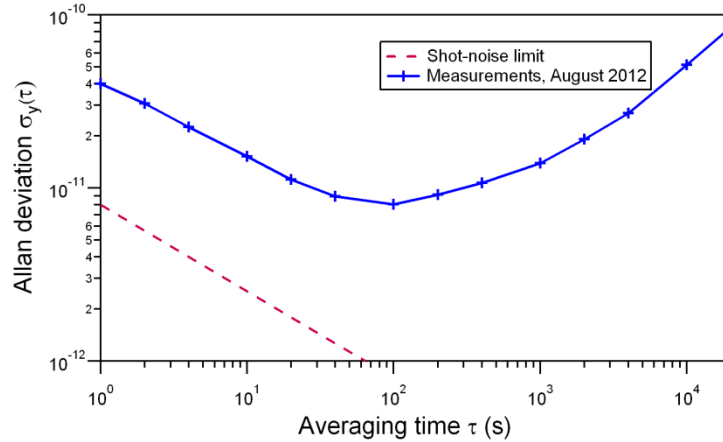


Figure 5-3: Short-term clock frequency stability measurement of the CPT atomic clock with buffer gas Cs MEMS cell, measured in August 2012, after replacing the LO and optimizing the clock parameters. Red dashed line represents the shot-noise limit and blue solid line connects the measured data. Dr. Luc Schneller performed this measurement [7].

5.1.2 Medium-term frequency stability

Here we discuss the medium-term clock frequency stability for the clock settings which short-term frequency stability is shown in Fig. 5-2. Instability contributions of physical perturbations on the clock transition in medium-term time scales may originate from the LS, TC and possible variations of the buffer gas pressure inside the vapor cell. By estimating the typical parameter variations, e.g. laser intensity and frequency stability and cell temperature stability, at 10 000 s, it is possible to estimate the influence of the intensity and frequency LS and TC to the medium-term clock frequency stability (using the same equations given in Table 5-1), shown in Table 5-2. Table 5-2 shows that the frequency LS contributes to the clock frequency stability on the level of 1.2×10^{-10} around $\tau = 10\,000$ s. Intensity LS contribution is negligible in the clock medium-term stability, being estimated as 6.7×10^{-13} at 10 000s. The buffer gas pressure variation contributes on the to the clock frequency instability on the level of 1.3×10^{-16} .

Comparing Table 5-2 results with the measured data shown in Figure 5-2 suggests the conclusion that the present clock medium-term frequency stability is limited by the frequency LS. The repeated clock frequency stability measurement performed by Dr. Luc Schneller (Figure 5-3) shows the clock frequency stability is 5×10^{-11} at 10 000 s (with optimized signal and four times less laser intensity than in the case shown in Figure 5-2). In this case the frequency LS coefficient β is four times smaller than the one shown in Table 5-2 due to the four times smaller laser intensity and this is expected to limit the

clock frequency stability on the 5×10^{-11} level. Therefore, the dominating contributor to the clock medium-term stability in both cases (Figure 5-2 and Figure 5-3) is the frequency LS.

The further improvements in the medium-term stability can be obtained by two methods: improving the laser frequency stability or suppressing the frequency LS by optimizing the microwave power P_{RF} [3].

Physical effect	Coefficient (See Chapter 4)	Variation at 10 000 s	Instability
Intensity LS ($ \alpha $)	1.16(2) (mHz*cm ² /μW)	< 5.3 μW/cm ² [4]*	< 6.7x10 ⁻¹³
Frequency LS ($ \beta $)	644(2) (mHz/MHz)	< 5x10 ⁻⁹ [5]**	< 1.2x10 ⁻¹⁰
TC	1x10 ⁻¹¹ (1/K)	10x10 ⁻³ K [4]	1x10 ⁻¹³
Barometric effect	~1.3x10 ⁻¹⁶ /Torr [6]***		< 1.3x10 ⁻¹⁶
Other buffer-gas related effects****	not measured		unknown
Total instability at 10 000 s			< 1.2x10⁻¹⁰

Table 5-2: Estimations of the LS, TC and buffer gas variation influence on the clock medium-term stability ($\tau=10\ 000$ s). Typical variation of the laser intensity and the cell temperature are measured and reported in [4]. Intensity and frequency LS coefficients α and β are evaluated for the $F \rightarrow F'=3$ transition. *Laser intensity variation is estimated to be ten times worse than in the case of measured intensity variation of the laser head (since in this case the experimental setup is consisted of the DFB and the EOM). **Laser frequency variation is expected to be 1000 times worse than in the case of the compact laser head, since in our case the laser frequency is stabilized to a Doppler broadened line obtained from the buffer gas cell, not from the separated evacuated cell like in [5]. ***The buffer gas pressure variation is taken from [6] where cm-scale cell is considered and estimated (with respect to the cell window dimensions) as to be 1000 less sensitive for the case of microfabricated cell. Instability contribution is then calculated taking the 1 Torr for atmospheric pressure variation at 10 000 s. **** These effects depend on the cell production processes (see section 1.4.1).

The laser frequency stability can be improved by improving the thermal control of laser itself and by thermal control of the MEMS cell, which is used for the laser frequency stabilization. Note, that variations in the reference cell temperature can have a strong impact on the laser frequency due to changes in the background Doppler profile and light absorption in the cell varying with the Cs atomic density. Table 5-2 shows that the influence of the intensity LS is negligible. It also shows that the microwave power can be optimized to suppress the frequency LS coefficient β without significantly increasing the influence of the intensity LS coefficient α on the clock stability. Further experimental

steps also include measurements of the buffer gas pressure variation in the MEMS cell in order to estimate its exact influence on the clock medium-term frequency stability.

5.1.3 Long-term frequency stability

Typical laser intensity, laser frequency and cell temperature drifts estimated at one month time scale are listed in Table 5-3.

Physical effect	Coefficient	Typical drift after 1 month	Drift after 1 month
Intensity LS ($ \alpha $)	1.16(2) (mHz*cm ² /μW)	Estimated >10.6μW/cm ² [4]	>1.8x10 ⁻¹²
Frequency LS ($ \beta $)	644(2) (mHz/MHz)	~ Estimated 5x10 ⁻⁸ [5]	~1.2x10 ⁻⁹
TC	1x10 ⁻¹¹ (1/K)	Estimated >20x10 ⁻³ K [4]	>2x10 ⁻¹³
Barometric effect	~1.3x10 ⁻¹⁶ /Torr [6]		~6.5x10 ⁻¹⁵
Other buffer-gas related effects*	not measured		unknown

Table 5-3: Estimations of the LS, TC and buffer gas variation influence on the clock drift. Intensity and frequency LS coefficients α and β are evaluated for the $F \rightarrow F' = 3$ transition. Temperature drift is estimated to be 2 times worse compared to the medium term measurements reported in [4]. Intensity LS and buffer gas variation are estimated to be ten and two times worse compared to the variations at 10 000 s, respectively. Laser frequency variation is expected to be 10 times worse compare to the variations at 10 000 s. The buffer gas pressure variation is taken from [6] where cm-scale cell is considered and estimated (with respect to the cell window dimensions) as to be 1000 less sensitive for the case of microfabricated cell. Instability contribution is then calculated taking the 50 Torr for atmospheric pressure variation at one month. *These effects depend on the cell production processes (see section 1.4.1).

Using these data the LS, TC and buffer gas variation influence to the clock drift after one month of operation is evaluated. Since the clock long-term frequency stability was

not measured, it is not known if the LS or the TC limits the present clock frequency stability. It can be expected that typical laser intensity drift after one month is two times worse compared to measured laser intensity variation at 10 000 s, due to expected laser aging and daily temperature cycles. This estimation leads to the assumption that intensity LS will influence clock drift on the 1.8×10^{-12} level. A similar estimation can be done for the TC. Typical temperature drifts after one month can be expected to be two times worse than the measured temperature variation at 10 000 s. Therefore, the TC will influence clock drift on the 2×10^{-13} level, however the clock frequency stability after one month should not be limited by the TC.

Table 5-3 shows that the limitation due to frequency LS for $\tau=1$ month is on the level of 1.2×10^{-9} . The expected limitation of the buffer gas pressure variation is on the level of 6.5×10^{-15} . Therefore, the clock frequency stability at 1 month can be expected to level on 1.2×10^{-9} , and to be limited by the frequency LS. The impact of the TC to the clock frequency stability is negligible compared to frequency LS effect in this case.

It is crucial to measure the long-term laser intensity and frequency stability as well as the temperature stability of the cell. Also, it is important to measure the buffer gas pressure variation over the one month, since the typical drift for one month taken from the reference [6] and it is not measured for the cell used in experiment here. In this way, it will be possible to know (not only assume) the limitation of the clock frequency stability in the long-term due to these effects.

5.1.4 Summary and conclusions

The measured frequency stability of the CPT clock (using the Cs MEMS cell with 75 Torr of Ne) corresponds to the predicted stability with optimized signal and measured detection noise. The main contributor to the short-term frequency stability is the signal-to-noise ratio (mainly laser detection noise and small CPT signal contrast). Further improvement in short-term clock frequency stability can be obtained by detailed signal optimization and by decreasing the detection noise on the experimental setup coming from the different experimental setup elements, e.g., laser, EOM, LO, etc.

Significant improvement of the clock medium-term frequency stability thanks to the TC and LS optimization was obtained (Figure 5-2). In this case the intensity LS and TC contribution to clock frequency instability is negligible (since both of these effects are suppressed, see section 4.1). Present clock frequency stability is limited by the frequency LS in medium-term. Further improvements in the clock frequency stability can be

reached by improvements in the laser frequency stability (improving the thermal control of the laser itself and by thermal control of the MEMS cell used for the laser frequency stabilization). The present frequency LS limitation in medium-term can also be overcome by optimizing the microwave power P_{RF} in an effort to suppress frequency LS coefficient β without significantly increasing the influence of the intensity LS coefficient α on the clock stability.

The clock long-term frequency stability is expected to level at 1.2×10^{-9} after one month. Limitation of the clock long-term frequency due to frequency LS is on the level of 1.2×10^{-9} , estimated using the measured laser frequency drift for one month. Contribution to the clock frequency instability from intensity LS and TC are assumed to be (estimating laser intensity variation and temperature variation at one month, as ten and two times worse as compared to their variation at 10 000 s, respectively) 1.8×10^{-12} and 2×10^{-13} , respectively. In order to estimate and not only assume the clock frequency drift due to LS and TC, it will be important to measure the long-term laser intensity and frequency stability and the temperature stability of the cell. Likewise, it is crucial to measure the barometric effect and buffer gas pressure variation due to adsorption, permeation, reaction with impurities, leakage, etc., over days in order to estimate the limitation to the clock frequency stability due to these effects. Also, dedicated studies on cell aging processes would be useful.

5.2 CPT and DR atomic clock using the cm-scale ^{87}Rb wall-coated cell

5.2.1 Short-term frequency stability

Clock frequency stability was studied for clocks based on DR and CPT, using the cm-scale ^{87}Rb tetracontane coated cell. Like in the case of CPT clocks with MEMS cell (section 5.1.1), the clock signal discriminator slope D was evaluated as function of laser intensity and cell stem and volume temperatures, in order to optimize the clock signal and measure the frequency stability of the atomic clock. The discriminator slope was optimized for the wall-coated cell volume temperature of $T_v=329$ K, cell stem temperature $T_s=321$ K and the laser intensity of $I_L=0.23$ mW/cm² (see Figures 3-33 (a) and 3-33 (b)). The laser frequency is tuned to the transition $F=2 \rightarrow F'=1$. Local oscillator

(LO) quartz delivers a 10 MHz frequency, which is converted to the 6.835 GHz frequency of the atomic transition by a multiplication chain.

To measure clock stability the LO output is compared to the signal delivered by a Hydrogen maser by using a Picotime frequency comparator. The clock frequency stability was measured in both clock operational schemes, DR and CPT. Using Eq. (5.1) the first estimation of the shot-noise limit and the predicted short-term stability is evaluated. Figure 5-4 compares the short-term clock frequency stability in DR (red circles) and CPT operation (black circles), including the DR and CPT shot-noise limit (dashed red and black lines, respectively) and DR and CPT predicted S/N short-term stability limits (solid red and black lines, respectively).

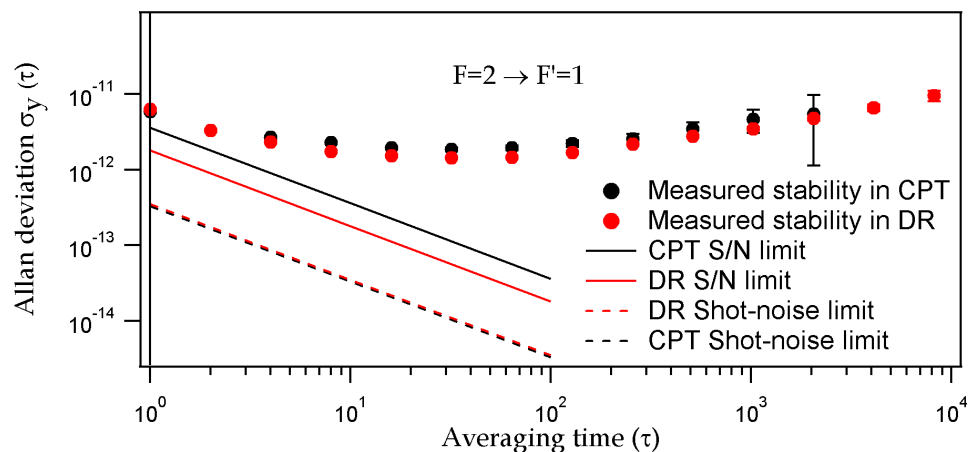


Figure 5-4: Short-term clock frequency stability measurement. Black squares represent the CPT clock frequency stability. Red dots represent the DR clock frequency stability. Solid red and black lines correspond to the predicted DR and CPT S/N stability limits, respectively. Dashed red and black lines correspond to the DR and CPT shot-noise limit.

Both clock operation (DR and CPT) display a short-term stability of $5\text{-}6 \times 10^{-12}$ at $\tau=1$ s up to $\tau=30$ s, which is in a reasonable agreement with the predicted value of $3.8 \times 10^{-12} \tau^{-1/2}$ or $4.6 \times 10^{-12} \tau^{-1/2}$ in DR and CPT case, respectively. Also, both of the measured clock frequency stabilities show similar behavior over measured time.

Table 5-4 represents the summary of the instability contributions to the clock short-term frequency stability. The table includes measured short-term laser frequency stability and typical laser intensity variation in short-term, which are used in the equations for the calculation of the intensity and frequency LS contribution at $\tau=1\text{-}100$ sec.

Physical effect	Experiment		Variation at 1 s	Formula	Instability ($\tau^{-1/2}$)
Shot-noise limit	DR		$n_{\text{shot}}=7 \times 10^{-8}$ $\text{V}/\text{Hz}^{1/2}$	Eq. (5.2)	3.5×10^{-13}
	CPT			Eq. (5.2)	3.3×10^{-13}
S/N limit	DR	$D=2.2 \times 10^{-5}$ (V/Hz)	$n_{\text{S/N}}=5 \times 10^{-7}$ $\text{V}/\text{Hz}^{1/2}$	Eq. (5.2)	1.8×10^{-12}
	CPT	$D=1.5 \times 10^{-5}$ (V/Hz)		$n_{\text{S/N}}=9 \times 10^{-7}$ $\text{V}/\text{Hz}^{1/2}$	Eq. (5.2)
Intensity LS ($ \alpha $)	DR	0.1(1) (Hz*cm ² /μW)	$\sigma_{I\text{-laser}} < 3 \times 10^{-5}$ [2]	$\frac{\alpha * I_L * \sigma_{I\text{-laser}}}{\nu_{\text{Rb}}}$	$< 1.2 \times 10^{-13}$
	CPT	0.05(8) (Hz*cm ² /μW)			$< 4.2 \times 10^{-14}$
Frequency LS ($ \beta $)	DR	80(5) (mHz/MHz)	$\sigma_{f\text{-laser}}: < 4 \times 10^{-12}$ [4]	$\frac{\beta * \nu_L * \sigma_{f\text{-laser}}}{\nu_{\text{Rb}}}$	$< 1.8 \times 10^{-14}$
	CPT	93(5) (mHz/MHz)			$< 2 \times 10^{-14}$
LO	-102 dBrad ² /Hz [4]				$\sim 6 \times 10^{-13}$
Total instability contribution between 1-100 s				DR	$< 1.9 \times 10^{-12}$
				CPT	$< 3.6 \times 10^{-12}$

Table 5-4: Summary of the instability contributions to the DR and CPT clock short-term frequency stability ($\tau=1-100$ s). σ_I is taken from [2]. σ_f is taken from [4]. Intensity and frequency LS coefficients α and β are evaluated for the $F=2 \rightarrow F'=1$ transition.

From the Table 5-4 it can be concluded that the main contributor to the short-term frequency stability is the signal-to-noise ratio (mainly FM-to-AM noise conversion in the cell) and intensity LS in the DR case. The total contribution of the intensity LS to the

clock frequency stability is on the level of 1.2×10^{-13} in DR and 4.2×10^{-14} in CPT, indicating that the intensity LS is higher in the DR case.

Further improvement in clock short-term frequency stability must be sought in optimizing the intensity LS, improvements of the resonance signal and noise contributions from the different elements of the experimental setup: LO, laser, etc.

5.2.2 Medium-term frequency stability

Measurements of the clock medium- and long-term frequency stability were performed only for the clock working in DR regime (shown in Figure 5-5). The operational parameters were identical to those in the short-term measurements, i.e. at the wall-coated cell volume temperature $T_v = 329$ K, cell stem temperature $T_s = 321$ K and laser intensity of $I_L = 0.23$ mW/cm². The laser frequency was tuned to the transition $F=2 \rightarrow F'=1$ excited state.

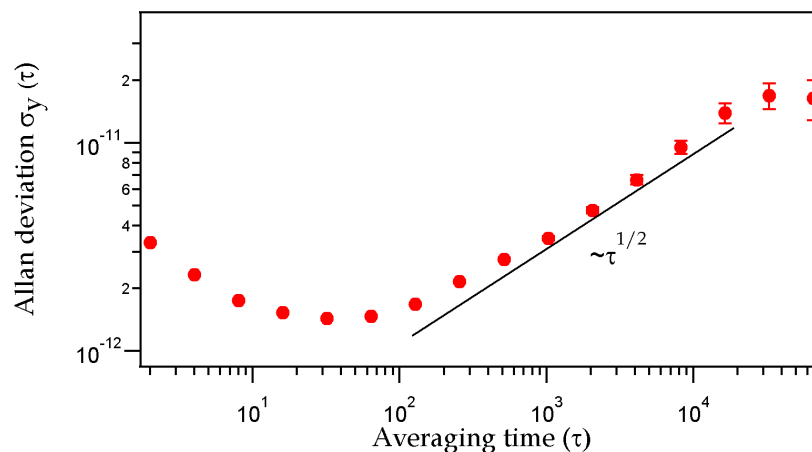


Figure 5-5: Medium-term clock frequency stability measurement in the case of DR.

After $\tau = 100$ s the clock frequency instability increases following a positive $\tau^{1/2}$ slope, which is typical for random walk processes, not for clock drift (see section 1.6). By estimation of the typical variation of the physical parameters at 10 000 s, we estimate the influence of the intensity and frequency LS and TC to the medium-term clock frequency stability, shown in Table 5-5. Frequency LS is negligible in this case, being estimated on the 10^{-14} level. From Table 5-5 we can conclude that the intensity LS, TC and wall-coating aging are limiting the medium-term clock frequency stability since the total contribution from these effects is on the level of $< 8.9 \times 10^{-12}$ and measured clock stability levels is 9×10^{-12} for $\tau = 10\,000$ s.

There are mechanisms to solve the problems of the clock frequency limitation due to the intensity LS. One of them is the suppression of the intensity LS by using the detuning method [9], for example. But the clock frequency stability limitation due to the cell TC in the case of the wall-coating stays the issue that requires detailed theoretical and experimental studies. Further experimental steps should include the measurements of the laser intensity, frequency variation, cell temperature variation and measurements of the DR microwave power shift, since the typical parameter variation used in Table 5-5 are taken from different references and thus only give an approximate description of the situation.

Physical effect	Coefficient (Chapter 4)	Variation at 10 000 s	Instability
Intensity LS ($ \alpha $)	0.1(1) (Hz*cm ² /μW)	<5.3 μW/cm ² [4]	<7.7x10 ⁻¹²
Frequency LS ($ \beta $)	80(5) (mHz/MHz)	5x10 ⁻¹² [4]	< 2.2x10 ⁻¹⁴
TC _{cell} at T _v = 331 K	1.43x10 ⁻¹⁰ (1/K)	10x10 ⁻³ K [4]	1.43x10 ⁻¹²
TC _{stem}	6x10 ⁻¹¹ (1/K)	10x10 ⁻³ K [4]	6x10 ⁻¹³
DR Microwave power shift	7.8(4) (Hz/μW) [3]	1x10 ⁻⁴ μW [4]	1.1x10 ⁻¹³
Wall-coating aging			2.7x10 ⁻¹² *
Total instability at 10 000 s			<8.9x10⁻¹²

Table 5-5: Estimations of the LS, TC and microwave power shift influence on the clock medium-term stability ($\tau=10^4$ s). Microwave power shift, laser intensity and frequency stability and cell temperature variations are taken from [4]. Intensity and frequency LS coefficients α and β are evaluated for the F=2→F'=1 transition. * Wall-coating aging is discussed in section 5.2.3.

5.2.3 Long-term frequency stability

In order to extract the clock frequency drift the relative clock frequency was monitored over 1 month, as shown in Figure 5-6. The observed drift of the relative clock frequency (linear fit of the data) is $-2.4 \times 10^{-11}/\text{day} = 7.2 \times 10^{-10}/\text{month}$. Figure 5-6 shows

not only the linear drift of the clock frequency, but also day-scale variations, due to the daily temperature oscillations in the laboratory.

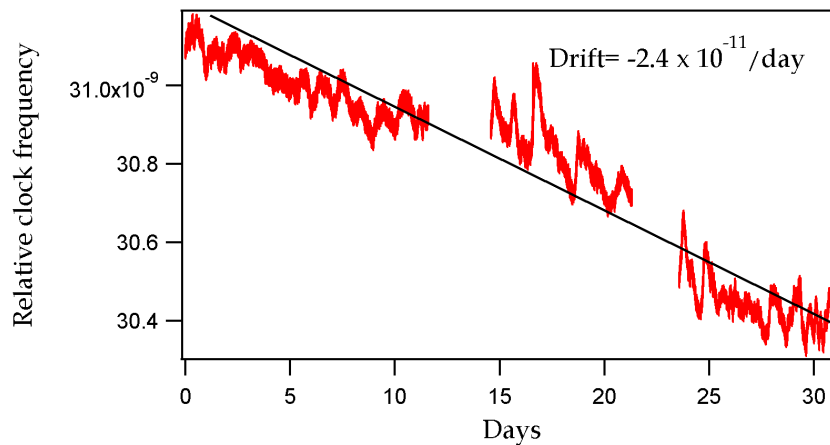


Figure 5-6: Measured relative clock frequency in DR. The laser frequency is tuned to the transition $F=2 \rightarrow F'=1$ excited state. Wall-coated cell volume temperature is $T_v = 329$ K and stem temperature is $T_s = 321$ K. Black solid line is the linear fit of the data.

The evaluation of the intensity and frequency LS and TC influence (measured and discussed in Chapter 4) on the clock drift is estimated and listed in Table 5-6.

The estimated total drift from the frequency LS is on the level of 10^{-13} /month, i.e., which is a far too small to explain the measured drift. Long term measurements of the laser intensity stability and cell temperature variations are not measured in this thesis. Expected laser intensity and cell temperature variations are assumed to be two times worse compared to their variations at 10 000 s, due to expected laser aging and daily temperature cycles. Using this assumption it can be evaluated that total drift from the intensity LS and TC is on the 1.5×10^{-11} and 10^{-13} /month level, respectively. Drifts originating from these effects cannot explain the measured drift in Figure 5-6 (Intensity LS is $> 1.5 \times 10^{-11}$ /months but for sure $< 1 \times 10^{-10}$ /month). Therefore this is a strong indication that recorded drift does not originate from physical effects like LS, TC or microwave power shift (in the case of DR). Buffer gas variations need not to be estimated here (like in Table 5-1) since there is no buffer gas. We suspect that the observed drift may arise from an aging effect of the wall shift due to the tetracontane coating in the cell.

Further experimental steps including studies of the long-term laser intensity stability and temperature stability of the cell will help to reveal the influence of the intensity LS influence and TC to the clock long-term stability. In addition, the detailed study of the wall shift due to the different coatings in the cell is crucial for the clock long-term frequency stability, since this effect seems to be that an origin of the recorded drift. The

barometric effect discussed in section 1.4.1 will be negligible here, but Rb outgassing or leak are expected and impact of these effects to the clock medium- and long-term must be studied in details.

Physical effect	Coefficient	Typical drift at 1 month	Drift at 1 month
Intensity LS ($ \alpha $)	0.1(1) (Hz*cm ² /μW)	Estimated >10.6μW/cm ² [4]	>1.5x10 ⁻¹¹
Frequency LS ($ \beta $)	80(5) (mHz/MHz)	~ 5x10 ⁻¹¹ [4]	~5.9x10 ⁻¹³
TC _{cell} at Tv = 331 K	1.16x10 ⁻¹⁰ (1/K)	20x10 ⁻³ K [4]	2.3x10 ⁻¹³
TC _{stem} (1/K)	2.6x10 ⁻¹¹	20x10 ⁻³ K [4]	5.2x10 ⁻¹³
DR Microwave power shift	7.8(4) [3] (Hz/μW)	2x10 ⁻³ μW [4]	2.3x10 ⁻¹²

Table 5-6: Estimations of the LS, TC and DR microwave power shift influence on the clock drift, measured for 31 days. Laser frequency variation is expected to be 10 times worse compare to the variations at 10 000 s while typical temperature drift is estimated to be 2 times worse than the measured one in medium term for the same physic package [4]. Laser intensity stability is estimated from [4] as 2 times worse compare to the measured one in medium term. Typical microwave power drift per one month is measured, taken from [4]. Intensity and frequency LS coefficients α and β are evaluated for the F=2→F'=1 transition.

5.2.4 Summary and conclusions

The study on the DR and CPT clock frequency stability, using the ⁸⁷Rb cm-scale cell coated with tetracontane was discussed. The measured short-term stability corresponds to the predicted stability with optimized signal and measured detection noise (Figure 5-4). The DR clock short-term frequency stability is limited by the intensity LS and the signal-to-noise ratio (mainly laser FM-to-AM noise conversion in the cell), while in the CPT case only the signal-to-noise ratio (laser FM-to-AM noise conversion in the cell and small CPT signal contrast) is the limiting factor. Frequency LS and TC are negligible. Further improvements of the DR clock short-term stability must be sought in reducing the intensity LS, by decreasing the laser RIN noise. In the case of CPT, further improvement is expected in optimizing the signal-to-noise ratio by

reducing FM-to-AM noise conversion in the cell. Signal contrast of few percent is typical for CPT case and cannot be improved much further with a simple excitation scheme as used here.

The measurements of the clock medium- and long-term frequency stability were performed only for the clock working in DR regime. The clock medium-term frequency stability is limited by the combined effects of the intensity LS and TC. The intensity LS can be reduced by using the detuning method [9], for example. But the clock frequency stability limitation due to the cell TC in the case of the wall-coating stays the issue that requires detailed theoretical and experimental studies

The measured drift of the relative clock frequency is $-2.4 \times 10^{-11}/\text{day} = 7.2 \times 10^{-10}/\text{month}$. We show that recorded drift doesn't originate from the LS, TC and microwave power shift, since the estimated total drift from these effects is on the level of $1.7 \times 10^{-11}/\text{month}$, i.e. one order magnitude smaller than measured drift. A possible reason for this drift can come from the wall shift due to the tetracontane coating in the cell and this assumption requires detailed experimental studies in the future. Further work should also include the Rb outgassing and leak studies so the influence of these effects to the clock medium- and long-term can be evaluated and possibly suppressed through the cell production process.

5.3 Conclusions and future prospects on the clock stability measurements

This chapter discussed the clock frequency stability measurements of the two different vapor-cell atomic clocks: using the Cs buffer gas MEMS cell and using the ^{87}Rb cm-scale cell coated with tetracontane. We considered the influences of the parameters related to the vapor cell, i.e., intensity LS, frequency LS and TC (discussed in Chapter 4) on the clock stability. Other parameters, e.g., noise contributions from different elements of the setup (laser, local oscillator, EOM, etc.), magnetic properties, light polarization, etc., are not studied here.

In the case of the CPT clock with Cs buffer gas MEMS cell, the influence of the intensity LS and TC is negligible to the clock stability. Frequency LS limits the clock frequency stability at $\tau = 10\,000$ s. Further improvements in the clock medium-term frequency

stability can be obtained by decreasing the frequency LS coefficient β . This can be done by improving the stabilization of the laser frequency (by improving thermal control of laser itself and of the MEMS cell used for the laser frequency stabilization) or by optimizing the microwave power P_{RF} . It is also important to measure the barometric effect and related phenomena of the buffer gas pressure variation over days (see sections 1.4.1 and 1.4.4) in order to estimate the limitation to the clock frequency stability due to these effects (and possibly improve the long-term effects of the buffer-gas through the cell production process). Beside their scientific interest, the given results on CPT atomic clock using the Cs MEMS buffer gas cell (sections 4.1 and 5.1.2) are important for improving the performances of the existing atomic clocks and for devising the new prototypes. The experimental results shown here form the basis in devising the first European integrated portable and low power atomic frequency reference [10]. These clocks (resonators based on CSAC (chip-scale atomic clocks) technology) may be an alternative to the conventional local oscillators used in e.g. 3G/4G wireless synchronization.

In the case of the DR or CPT clock using the ^{87}Rb cm-scale cell coated with tetracontane, the frequency LS influence on the clock frequency stability is negligible in short-, medium- or long-term. The clock short-term stability is limited by the signal-to-noise ratio (mainly FM-to-AM noise conversion in the cell) and intensity LS, while the medium-term stability is limited by the combined effects of intensity LS and TC. Further improvement in the clock short- and medium-term frequency stability can be obtained by FM-to-AM noise conversion reduction and intensity LS reduction, using the frequency detuning method [9]. The clock medium-term frequency stability limitation due to the cell TC stays an issue that requires detailed theoretical and experimental studies. The observed clock drift does not originate from LS or TC. A possible cause for the clock frequency drift may originate from the wall shift due to the tetracontane coating in the cell. Further experimental steps would include detailed studies of the wall shift in clocks with tetracontane coated cell and the influence of the Rb outgassing and leak from the wall-coated cells to the clock medium- and long-term frequency stability. For such studies, all the results obtained on DR and CPT atomic clock using the ^{87}Rb cm-scale cell coated with tetracontane provide the basic scientific research on the use of the wall-coated cells. In this way they are important for understanding the physics behind the studied processes.

REFERENCES:

- [1] www.spectratime.com, Picotime frequency comparator.
- [2] Dr. C. AFFOLDERBACH, *Allan deviation of the laser intensity stability at 1 s measurements*, private communication, Technical report LTF-01427-TN-0008, Laboratoire Temps-Fréquence (LTF) (2008).
- [3] M. ZHU and L. S. CUTLER, *Theoretical and experimental study of light shift in a CPT based Rb vapour cell frequency standard*, Proceedings of the 32nd Precise Time and Time Interval Systems and Applications Meeting, ed. By L.A. Breakiron (US Naval Observatory, Washington, DC, 2000) (2000), pp. 311-324.
- [4] T. BANDI, C. AFFOLDERBACH and G. MILETI, *Laser-Pumped Paraffin-Coated Cell Rubidium Frequency Standard*, J. App. Phys. 111 (2012), pp. 124906-8.
- [5] F. GRUET, M. PELLATON, C. AFFOLDERBACH, T. BANDI, R. MATTHEY and G. MILETI, *Compact and frequency stabilized laser heads for rubidium atomic clocks*, Proc. of International conference on Space Optics, (2012), pp.1-5.
- [6] W. J. RILEY, *The physics of the environmental sensitivity of rubidium gas cell atomic frequency standards*, IEEE Trans. Ultrason. Ferroelectr. Freq. Control. 39(2) (1992), pp. 441-452.
- [7] Dr. Luc Schneller, *Short-term clock frequency stability measurement of the CPT atomic clock using the MEMS Cs cell*, private communication
- [8] www.spectradynamics.com, Caesium Frequency synthesizer CS-1 OPT2.
- [9] C. AFFOLDERBACH, F. DROZ and G. MILETI, *Experimental demonstration of a compact and high-performance laser-pumped Rubidium gas-cell atomic frequency standard*, IEEE Trans. Instru. and Meas. 55 (2006), pp. 429-435.
- [10] www.mac-tfc.eu

Conclusions and prospects

This thesis discussed the studies on the two atomic clocks: the atomic clock based on CPT, using the Cs MEMS cell with 75 Torr of Ne and the atomic clock based on DR and/or CPT, using the ^{87}Rb cm-scale wall-coated cell.

- The atomic clock based on CPT, using the Cs MEMS cell with 75 Torr of Ne

A novel technique for the suppression of the intensity light shift and temperature coefficient in atomic clocks based on CPT was proposed and demonstrated experimentally (Chapter 4). It was shown here that, in the case of the CPT atomic clock using the Cs MEMS cell with 75 Torr of Ne, the intensity light shift coefficient α is suppressed as function of the cell temperature, on Cs D1 line (for the cell temperature is $T_c=354$ K and when the laser carrier frequency is stabilized to the transition $F \rightarrow F'=3$ state). It was also shown that at the same cell temperature of $T_c=354$ K the temperature coefficient is suppressed even when using a pure Ne buffer gas cell only (the mixture of two buffer gases is not necessary in order to obtain low TC). Therefore, the clock can operate at low intensity light shift and low temperature coefficient simultaneously, for a $T_c=354$ K.

The theoretical model of the frequency light shift effect in the case of four level model of atom is proposed (section 2.4). This model is used for the calculations of the light shift effect in the case of CPT in buffer gas cell, on Cs D1 line. The theoretical calculations and measurements on the light shift effect were compared and some qualitative understanding of LS effect was obtained, but for a quantitative understanding an additional development of the theoretical model must be done.

The clock frequency stability was measured and significant improvement of the clock medium-term frequency stability thanks to the temperature coefficient and intensity light shift optimization was obtained (section 5.1). Presently, the clock frequency stability in medium-term is limited by the frequency light shift. Therefore, next steps are finding the experimental conditions in which the frequency light shift is suppressed. This can be reached by improving in the laser frequency stability (by better thermal control of laser and of the vapor cell used for the laser frequency stabilization) or by optimizing the microwave power P_{RF} (see Chapter 5).

The results on the atomic clock based on CPT, using the Cs MEMS cell with 75 Torr of Ne are used in devising the first European chip-scale atomic clock (CSAC). This clock

will be useful in wireless synchronization where the goal is to replace the conventional local oscillators by resonators based on CSAC technology. Also, future studies of magnetic properties and their influence on the clock frequency stability will be helpful in improving the chip-scale magnetometers (CSAM) performances. One further potential and important application is in smart power grids, where a clock is essential for the precise electronic control, metering, and monitoring in order to avoid black-outs.

For a future work, the DFB light source should be replaced with the VCSEL. Once when the clock is operating using the VCSEL, it is necessary to repeat all the measurements discussed in this thesis. Signal optimization is important in order to obtain good clock short-term frequency stability (since it was shown here that in the case when DFB laser is used, the limitation factor in the short-term is the small CPT signal contrast). It is also very important to measure intensity and frequency LS since these effects will be different from the LS given in this thesis, due to different laser frequency spectrums (the DFB laser frequency is modulated using EOM, while VCSEL's frequency is modulated by direct current modulation) and evaluate the intensity and frequency LS impacts to the clock frequency stability. Also, aging of the MEMS cell must be studied, not only from the cell quality point of view (does the Cs number of atoms decrease over the time?) but also to discover the Cs dispenser behavior over the time (does it slowly-react with Cs atoms and therefore additionally decrease their number?). The barometric effect and related phenomena of the buffer gas pressure variation over days must be quantified in order to estimate the limitation to the clock frequency stability due to these effects (and possibly improve the long-term effects of the buffer-gas through the cell production process). Finally, when the miniature clock is devised it will be important to measure the clock frequency stability, detect what limits this frequency stability and possibly find the tools to suppress these limitations.

- The atomic clock based on DR and/or CPT, using the ^{87}Rb cm-scale wall-coated cell.

This thesis also discussed studies of light shift and temperature coefficient, performed on ^{87}Rb atomic clock using a cm-scale wall-coated cell based on both clock schemes: DR and CPT. A theoretical model of the light shift effect (section 2.3 and 2.4) was developed for both clock schemes: DR and CPT.

The intensity light shift as function of the wall-coated cell volume temperature measurements showed that there are no changes in α as function of the temperature. Such behavior is expected since the atomic density in the cell is not dependent on the

wall-coated cell volume temperature (only on the cell stem temperature) and therefore α should remain the same for each cell volume temperature. In the case when the wall-coated cell stem temperature is changing, the light shift behavior shows the same tendency as it is in the case of the MEMS Cs buffer gas cell (section 4.2.1), going from being negative towards zero, when the cell temperature is increasing. Such behavior is confirmed in both: DR and CPT regime.

The theoretical model of the frequency light shift effect used here have been applied in both clock schemes, DR and CPT. In DR these light shift calculations provide good qualitative understanding of the obtained measurements. In CPT, theoretical model of the light shift show serious discrepancies compared to the measured LS. Further development of the theoretical model must be done in order to find the present reasons for the differences between measurements and theoretical calculations.

Temperature shifts of a tetracontane coated cell were measured and evaluated as functions of cell volume and cell stem temperature. It was found that the shift of the clock frequency is more affected by the change of the cell volume temperature than by the cell stem temperature, by factor of about 2.5. It was concluded that the atom-wall collisions have a stronger influence on the temperature shift of the clock frequency than the spin-exchange effect. Such behavior is obtained for both, the DR and CPT configuration.

This work reports for the first time long-term frequency stability measurements on a wall-coated clock. The results show that the frequency light shift does limit the clock short-, medium- or long-term frequency stability. The clock short-term stability is limited by the intensity light shift, while medium term stability is limited by the combined effects of intensity light shift and temperature coefficient. The observed clock drift may originate from the wall shift due to the property of tetracontane coating in the cell. Future work should aim towards the reduction of the intensity light shift by implementing the frequency detuning technique and detailed study of the wall shift due to tetracontane coating in the cell. Recent work discovered new cell coatings (like OTS) that can sustain temperatures up to 443 K. It would be interesting to study the interaction of alkali atoms with different types of the cell coatings and confirm the result discussed in this thesis, especially since most of the measurements given here were limited by the cell temperature. The influence of the temperature coefficient of the coating on the clock transition appears to be the most important effect to be studied, since it is expected to have a significant impact on the clock frequency stability.

The experimental results on the wall-coating in vapor-cell atomic clocks are important for an understanding of the physics behind the studied processes. The use of wall-coatings in atomic clocks is not only of high interest to achieve narrow clock signal linewidths (therefore to improve the clock frequency stability) but it is also crucial for developments towards further clock miniaturization. Further experimental steps would be detailed studies of the wall shift in the case of the clock with tetracontane coated cell. The influence of the Rb outgassing and leak from the wall-coated cells to the clock medium- and long-term frequency stability must be studied and quantified. Also, the detailed study of the wall shift due to the different coatings in the cell is crucial for the clock long-term frequency stability, since we assumed here (section 5.2) that it is an origin of the recorded drift. Adding a small amount of buffer gas in wall-coated cell [2] will reduce the cell temperature dependence and therefore improve the performances of the clock using this cell. It has been shown that the DR light shift can be suppressed if the frequency of the pumped laser is modulated (similar like in CPT only here modulation frequencies are much lower) [1]. This method was demonstrated on the ^{87}Rb buffer-gas cell and it would be interesting to apply this method on the wall-coated cell, where the effects of the buffer gas broadening are not present.

REFERENCES:

- [1] C. AFFOLDERBACH, C. ANDREEVA, S. CARTALEVA, T. KARAUANOV, G. MILETI and D. SLAVOV, *Light-shift suppression in laser optically pumped vapour-cell atomic frequency standards*, Appl. Phys. B 80 (2005), pp. 841-848.
- [2] T. BANDI, C. AFFOLDERBACH and G. MILETI, *Laser-Pumped Paraffin-Coated Cell Rubidium Frequency Standard*, J. App. Phys. 111 (2012), pp. 124906-8.

Publications and Conferences

The results discussed in this thesis are published in five peer-reviewed journals, one special issue and presented at twelve different conferences:

Peer-reviewed articles:

1. D. MILETIC, P. DZIUBAN, R. BOUDOT, M. HASEGAWA, R. K. CHUTANI, G. MILETI, V. GIORDANO and C. GORECKI, *Quadratic Dependence on Temperature of the Cs 0-0 Hyperfine Resonance Frequency in a Single Ne Buffer Gas Microfabricated Vapor Cell*, *Electron. Lett.* 46 (2010), pp. 1069-1070.
2. R. BOUDOT, D. MILETIC, P. DZIUBAN, C. AFFOLDERBACH, P. KNAPKIEWICZ, J. DZIUBAN, G. MILETI, V. GIORDANO and C. GORECKI, *First-order cancellation of the Cs clock frequency temperature-dependence in Ne-Ar buffer gas mixture*, *Opt. Express* 19 (4) (2011), pp. 3106-3114.
3. D. MILETIC, T. BANDI, C. AFFOLDERBACH, and G. MILETI, *AC Stark-shift in Double Resonance and Coherent Population Trapping in Wall-Coated Cells for Compact Rb Atomic Clocks*, *Phys. Scr.* T149 (2012), pp. 1-3.
4. D. MILETIC, C. AFFOLDERBACH, M. HASEGAWA, C. GORECKI, R. BOUDOT and G. MILETI, *AC Stark shift in CPT-based Cs miniature atomic clocks*, *Appl. Phys. B* 109 (1) (2012), pp. 89-97.
5. F. GRUET, A. AL-SAMANEH, E. KROEMER, L. BIMBOES, D. MILETIC, C. AFFOLDERBACH, D. WAHL, R. BOUDOT, G. MILETI and R. MICHALZIK, *Metrological characterization of custom-designed 894 nm VCSELs for miniature atomic Clocks*, *Opt. Express* 21(5) (2013), pp. 5781-5792.

Special issue:

1. D. MILETIC, C. AFFOLDERBACH, G. MILETI, M. HASEGAWA and C. GORECKI, *Spectroscopy of micro-fabricated Cs vapor cells for miniature atomic clocks*, *Proc. SPIE of ISQE 7747* (2011), pp. 77470F-77470F-9.

Conference presentations with proceedings:

1. F. GRUET, D. MILETIC, C. AFFOLDERBACH and G. MILETI, *Characterization of aged/non-aged 894 nm DFB for their application in Cs atomic clocks*, *Proc. of the*

International Symposium On Reliability Of Optoelectronic For Space (ISROS), Cagliari (Italy), May 11-15 (2009), pp.1-14.

2. D. MILETIC, C. AFFOLDERBACH, E. BRESCHI, C. SCHORI, G. MILETI, M. HASEGAWA, R. CHUTANI, P. DZIUBAN, R. BOUDOT, V. GIORDANO and C. GORECKI, *Fabrication and spectroscopy of Cs vapour cells with buffer gas for miniature atomic clock*, Proc. of the European Frequency and Time Forum (EFTF), Noordwijk (Netherlands), 13-16 April (2010), pp.1-6.
3. D. MILETIC, C. AFFOLDERBACH, G. MILETI, M. HASEGAWA and C. GORECKI, *Light Shift in CPT Based Cs Miniature Atomic Clocks*, Proc. of the Joint Meeting of the European Frequency and Time Forum (EFTF) and the IEEE International Frequency Control Symposium (FCS), San Francisco (USA), May 2-5 (2011), pp. 200-202.
4. D. MILETIC, T. BANDI, C. AFFOLDERBACH and G. MILETI, *Light shift of double resonance and coherent population trapping in wall-coated cells for compact Rb clocks*, Proc. of the Joint Meeting of the European Frequency and Time Forum (EFTF) and the IEEE International Frequency Control Symposium (FCS), San Francisco (USA), May 2-5 (2011), pp. 203-205.
5. F. GRUET, L. BIMBOES, D. MILETIC, C. AFFOLDERBACH, G. MILETI, A. ALSAMANEH, D. WAHL and R. MICHALZIK, *Spectral characterization of VCSELs emitting at 894.6 nm for CPT-based miniature atomic clocks*, Proc. of the European Conference on Lasers and Electro-Optics and the XIIth European Quantum Electronics Conference (CLEO/Europe-EQEC), Munich (Germany), 22-26 May (2011), pp. 1-1.
6. T. BANDI, M. PELLATON, D. MILETIC, C. AFFOLDERBACH, F. GRUET, R. MATTHEY and G. MILETI, *Double-resonance in alkali vapor cells for high performance and miniature atomic clocks*, Proc. of the IEEE International Frequency Control Symposium (IFCS), Baltimore (USA), May 21-24 (2012).

Conference presentations without proceedings:

1. C. AFFOLDERBACH, F. GRUET, D. MILETIC and G. MILETI, *Optimizing a High-Stability CW Laser Pumped Rubidium Gas-Cell Frequency Standard*, Poster at the 7th Symposium on Frequency Standards and Metrology, Pacific Grove (USA), October 05-11 (2008).
2. D. MILETIC, C. AFFOLDERBACH, F. GRUET, M. DURRENBERGER and G. MILETI, *Progress on the optimization of a compact laser-pumped Rubidium frequency*

- standard*, Poster at European Frequency and Time Forum & International Frequency Control Symposium (EFTF-IFCS), Besançon (France), April 20 - 24 (2009).
3. D. MILETIC, M. PELLATON, C. AFFOLDERBACH, E. BRESCHI, Y. PETREMAND, C. SCHORI, N.F. DE ROOIJ and G. MILETIC, *CPT spectroscopy on miniature rubidium vapor cells*, Poster at the Annual Meeting of the Austrian Physical Society, Poster at Swiss Physical Society and Austrian Society of Astronomy and Astrophysics (SPS), Innsbruck (Austria) September 2-4 (2009).
 4. D. MILETIC, C. AFFOLDERBACH and G. MILETI, *AC Stark shift and temperature shift in laser pumped Rubidium frequency standard*, Poster at the Annual Meeting of the Austrian Physical Society, Swiss Physical Society and Austrian Society of Astronomy and Astrophysics (SPS), Innsbruck (Austria) September 2-4 (2009).
 5. D. MILETIC, C. AFFOLDERBACH and G. MILETI, *Spectroscopy of micro-fabricated Cs vapour cells for a miniature atomic clock*, Poster at Sixteenth International School on Quantum Electronics (ISQE), Nesebar (Bulgaria), September 20-24 (2010), Best poster award.
 6. D. MILETIC, T. BANDI, C. AFFOLDERBACH and G. MILETI, *Double-resonance (DR) and Coherent Population Trapping (CPT) in wall-coated cells for compact Rb atomic clocks*, Poster at III International Schools and Conference on Photonics, Belgrade (Serbia), August 29-September 2 (2011).
 7. R. BOUDOT, D. MILETIC, P. DZIUBAN, M. HASEGAWA, P. KNAPKIEWICZ, J. DZIUBAN, C. AFFOLDERBACH, G. MILETI, V. GIORDANO and C. GORECKI, *Cs collisional frequency shift measurements in microcells filled with a Ne-Ar buffer gas mixture*, Poster at the Joint Meeting of the European Frequency and Time Forum (EFTF) and the IEEE International Frequency Control Symposium (FCS), San Francisco (USA), May 2-5 (2011).
 8. D. MILETIC, T. BANDI, C. AFFOLDERBACH and G. MILETI, *Double-resonance (DR) and Coherent Population Trapping (CPT) in wall-coated cells for compact Rb atomic clocks*, Poster at the 43rd Congress of the European Group on Atomic Systems (EGAS), Fribourg (Switzerland), June 28-July 2 (2011).

Curriculum Vitae

Danijela Miletic Djoric

Rue des Lattes 15, 1217 Meyrin, Geneve

E-mail: danijelamiletic@yahoo.com

PERSONAL INFORMATION

Date of birth: 19.10.1980.

Gender: Female

Nationality: Serbian

Marital status: Married

EDUCATION

2008-2013 Ph.D. in Physic (candidate), University of Neuchâtel, Switzerland

1999-2007 M.Sc. in Physics Faculty, University of Belgrade, Serbia

1999-2007 B.Sc. in Physics Faculty of physics, University of Belgrade, Serbia

1995-1999 Gymnasium "Veljko Petrovic", Sombor, Serbia

1989-1999 State musical school, Piano, Serbia

TEACHING

2008-2013 Teaching assistant in laboratory class, General physics laboratory for undergraduates in the Faculty of Medicine, Biology and Pharmacy, University of Neuchâtel

- 2008-2011 Teaching assistant in laboratory class Physics laboratory I-II, 2nd and 3rd year in the Faculty of Physics and Micro-nanotechnology, University of Neuchâtel
- 2002-2004 Part time work as an editor of physics lecture notes at the Faculty of Physics, University of Belgrade
- 2003-2005 Teaching first and second year university students of physics and mathematics subjects, Serbia

LANGUAGES

Serbian: Mother tongue

French: Novice

German: Novice

Russian: Basic knowledge

English: Excellent written and spoken

COMPUTER SKILLS:

Fully PC literate, MS Windows XP, MS Office (Word, Access, Excel, PowerPoint), Pascal, Origin, IGOR

APPENDIX A DR atomic clock using the cm-scale glass-blown ^{87}Rb cell with buffer gas mixture

This appendix describes the experimental setup of a DR atomic clock using the cm-scale glass-blown ^{87}Rb cell with buffer gas mixture Ar-N₂. The result shown in section 4.2.3 (Figure 4-16) is obtained by using the experimental setup depicted here.

Experimental clock scheme is based on continuous-wave laser-microwave double-resonance spectroscopy of the ground state “clock” transition of ^{87}Rb atoms held in a vapor cell containing the buffer gas mixture Ar-N₂ [1]. The clock concept is shown in Figure A1-1.

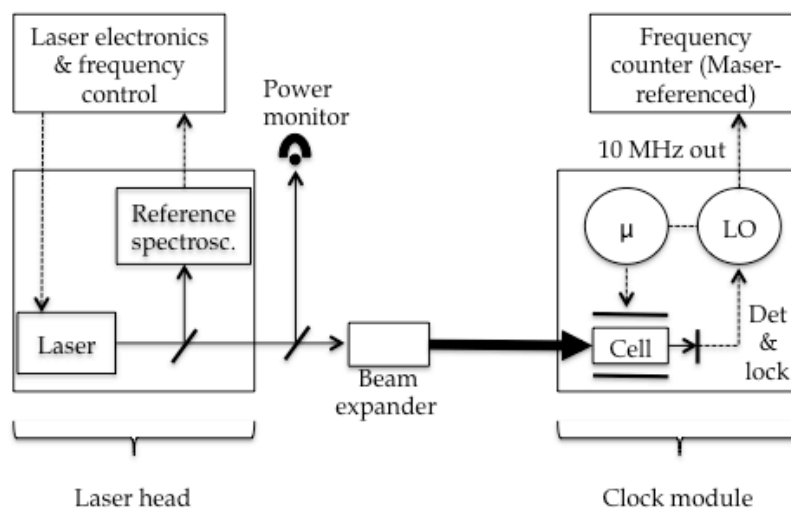


Figure A- 1: The experimental realization of the DR clock using the ^{87}Rb vapor cell containing the buffer gas mixture of Ar-N₂.

The pump light from a single-mode laser diode at 780 nm (Rb D2-line) is provided from a compact laser head (see Appendix B) [2]. In order to reduce frequency fluctuations of the pump light, the laser module includes frequency-stabilization to saturated-absorption lines from an internal reference cell. The pump light (beam diameter is

expanded to 9mm) is directed to a physics package that houses the Rb vapor cell (volume $\approx 2 \text{ cm}^3$) containing a buffer gas mixture Ar-N₂ for line narrowing and suppression of the temperature coefficient. Microwave radiation (equal to the Rb hyperfine frequency $\nu_{\text{Rb}}=6.835 \text{ GHz}$) from a low-noise synthesizer [3] is applied via a magnetron-type TE011 resonator cavity [4] placed around the cell. A solenoid around the resonator cavity generates a static magnetic field parallel to the light propagation vector to split the degeneracy of the Zeeman sublevels. Inside the physics package the cell is heated and temperature-controlled. Two μ -metal magnetic shields surround the whole ensemble. The clock transition is detected in the light transmission through the cell. This signal is used to stabilize the microwave frequency to the center of the clock transition using a Proportional/Integrator (PI) feedback loop. The picture of the experimental setup is shown at Figure A-2:

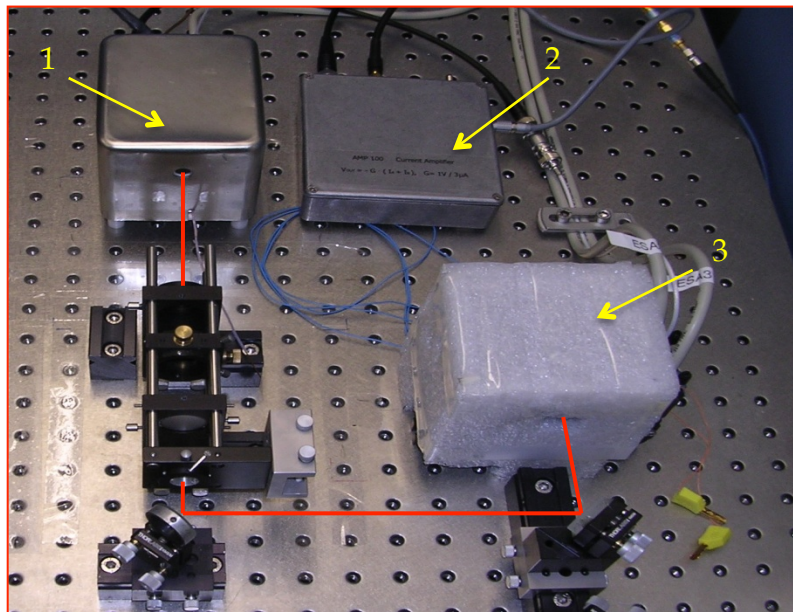


Figure A- 2: Picture of the experimental setup using the cm-scale ^{87}Rb buffer gas mixture cell. The red line indicates the laser beam path. 1 label the physic package, 2 shows the amplifier and 3 the laser head.

REFERENCES:

- [1] C. AFFOLDERBACH, F. DROZ, and G. MILETI, Experimental demonstration of a compact and high-performance laser-pumped rubidium gas cell atomic frequency standard, *IEEE Trans. Instrum. Meas.*55 (2006), pp. 429-35.

- [2] C. AFFOLDERBACH and G. MILETI, *A compact laser head with high-frequency stability for Rb atomic clocks and optical instrumentation*, Rev. Sci. Instrum. 76 (2005), pp. 073108-5.
- [3] C. E. CALOSSO, F. LEVI, E. K. BERTACCO, A. GODONE and S. MICALIZIO, *Low-noise electronic design for the ^{87}Rb coherent population trapping maser*, IEEE Trans. UFFC, 52 (11) (2005), pp. 1923-1930.
- [4] T. BANDI, C. AFFOLDERBACH and G. MILETI, *Study of Rb 0-0 hyperfine double-resonance transition in a wall-coated cell*, Proc. of the European Frequency and Time Forum (EFTF), Noordwijk (Netherland), 13-16 April (2010), pp. 1-8.

APPENDIX B Compact laser head

This appendix describes the compact laser head used in experimental setup depicted in section 3.3.2. The results shown in section 4.3 are obtained using the compact laser head as a light source.

The design of the laser heads is inspired by a previous design using Extended-Cavity Diode Lasers (ECDL) [1]. The laser head consist of a distributed-feedback laser (DFB) and frequency stabilization to Rb absorption lines from a small (10 x 19 mm) reference cell. All optical components are mounted on a thermally controlled baseplate. The laser part is composed of the DFB laser that emits at 795 nm, a collimation lens and a miniature optical isolator essential in order to avoid any retro-reflected beam that would perturb the laser emission. The frequency reference units consist of a small-saturated absorption spectroscopy setup, which delivers a narrow (FWHM \approx 20 MHz) Doppler-free resonance. The reference cell is evacuated cell containing Rb vapor. In order to increase the atomic density inside the cell, the cell is heated to around 311 K and temperature-stabilized within a precision on the mK level. The Rb cell is surrounded by a two μ -metal shielding in order to reduce stray magnetic fields originating from the environmental sources like isolator, etc. At the vapor cell the light polarization is linear and parallel for the pump and the probe beam (lin||lin configuration). The complete cell setup has a volume of 3 cm³ and a mass of 0.6 kg.

The DFB has a threshold current of about 38 mA (when operated around ambient temperature) and reaches an optical output power of about 65-70 mW at 120 mA [2]. Side-Mode Suppression Ratio (SMSR) is > 40 dB. Table B-1 lists the measured noise at two frequencies: 50 kHz used for the laser frequency stabilization and 300 Hz which is of interest for the atomic clock application.

A laser linewidth of < 4 MHz was measured using the beat-note method. Stabilization of the laser frequency to the reference absorption lines is achieved by frequency modulation of the laser frequency at 50 kHz, via injection current and lock-in demodulation of the signal. The error signals obtained in this way are applied to the laser diode current and piezovoltage, respectively, in order to correct frequency deviations. A picture of the compact laser head is shown in Figure B-1

Fourier frequency	300 Hz	50 kHz
FM noise ($\text{kHz} \cdot \text{Hz}^{1/2}$)	3	1.4
AM RIN (Hz^{-1})	2×10^{-14}	8×10^{-15}

Table B- 1: Measured noise for the compact laser head. Data are taken from [1].

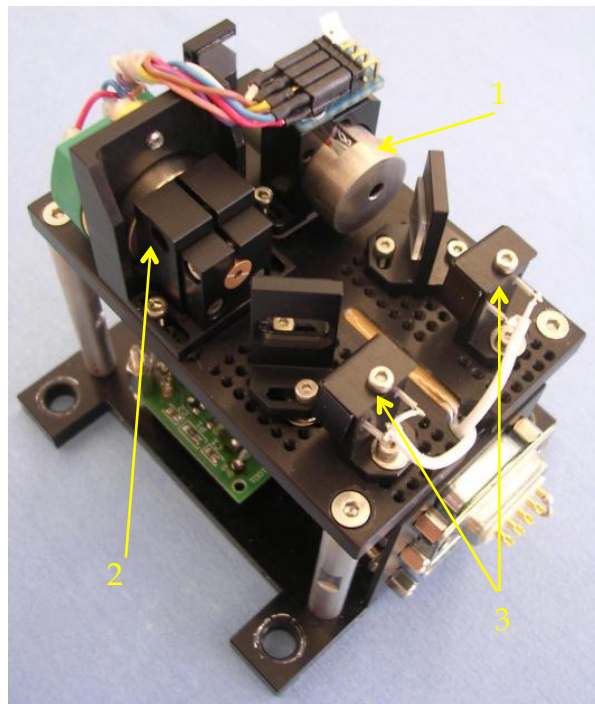


Figure B- 1: Photo of the laser head. 1 labels the Rb cell, 2 shows laser module and 3 shows the photodetectors for monitoring dc optical power and sub-Doppler absorption signal.

REFERENCES:

- [1] C. AFFOLDERBACH and G. MILETI, *A compact laser head with high-frequency stability for Rb atomic clocks and optical instrumentation*, Rev. Sci. Instrum. 76 (2005), pp. 073108-5.
- [2] F. GRUET, M. PELLATON, C. AFFOLDERBACH, T. BANDI, R. MATTHEY and G. MILETI, *Compact and frequency stabilized laser head for Rubidium atomic clocks*, Proc. Of Inter. Conf. on Space Opt. - ICSO (2012), pp. 1-5.

APPENDIX C Relative optical transition strengths of the D1 line in Cs and ^{87}Rb atoms

This appendix gives the relative line strengths of the optical transitions between hyperfine-Zeeman states $|n S_{1/2}, F, m_g \rangle \rightarrow |n S_{1/2}, F', m_e \rangle$ of the D1 line in Cs and ^{87}Rb atoms.

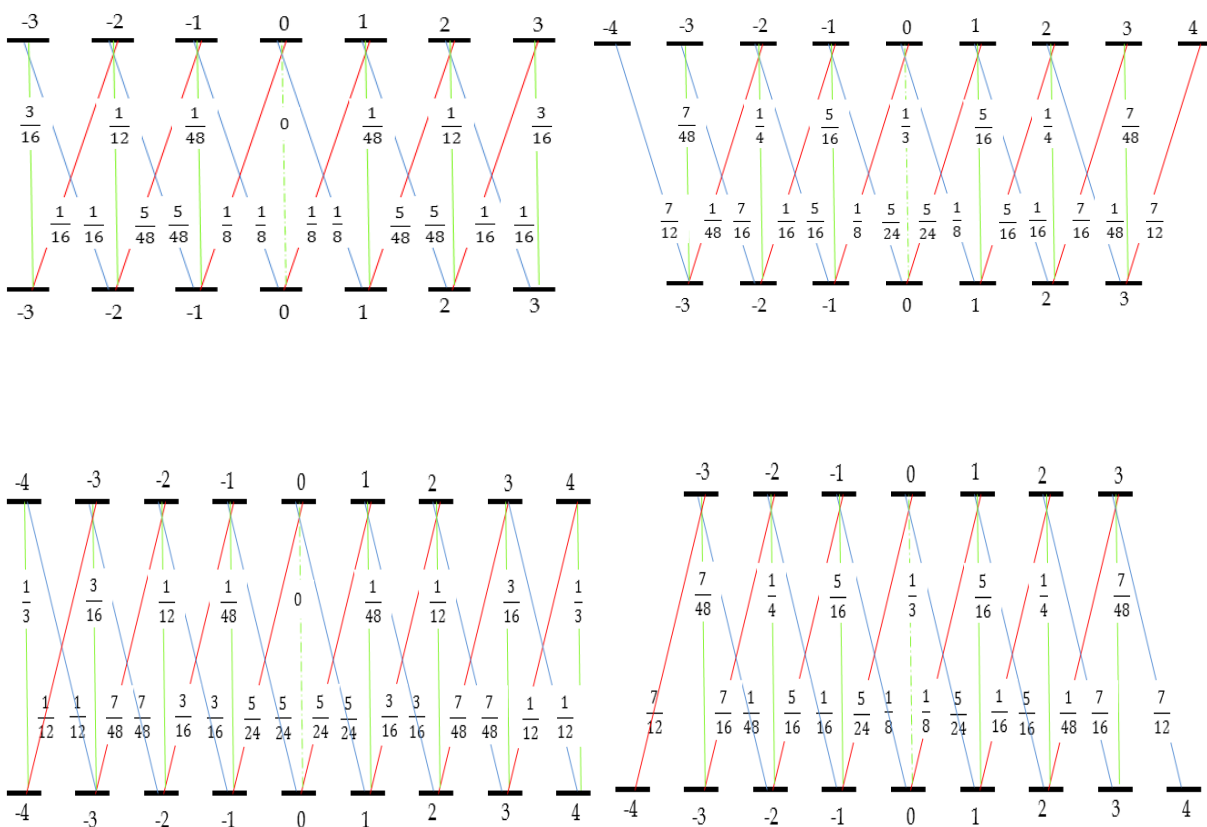


Figure C-1: Transition strengths for the D1 line of Cs atom [1].

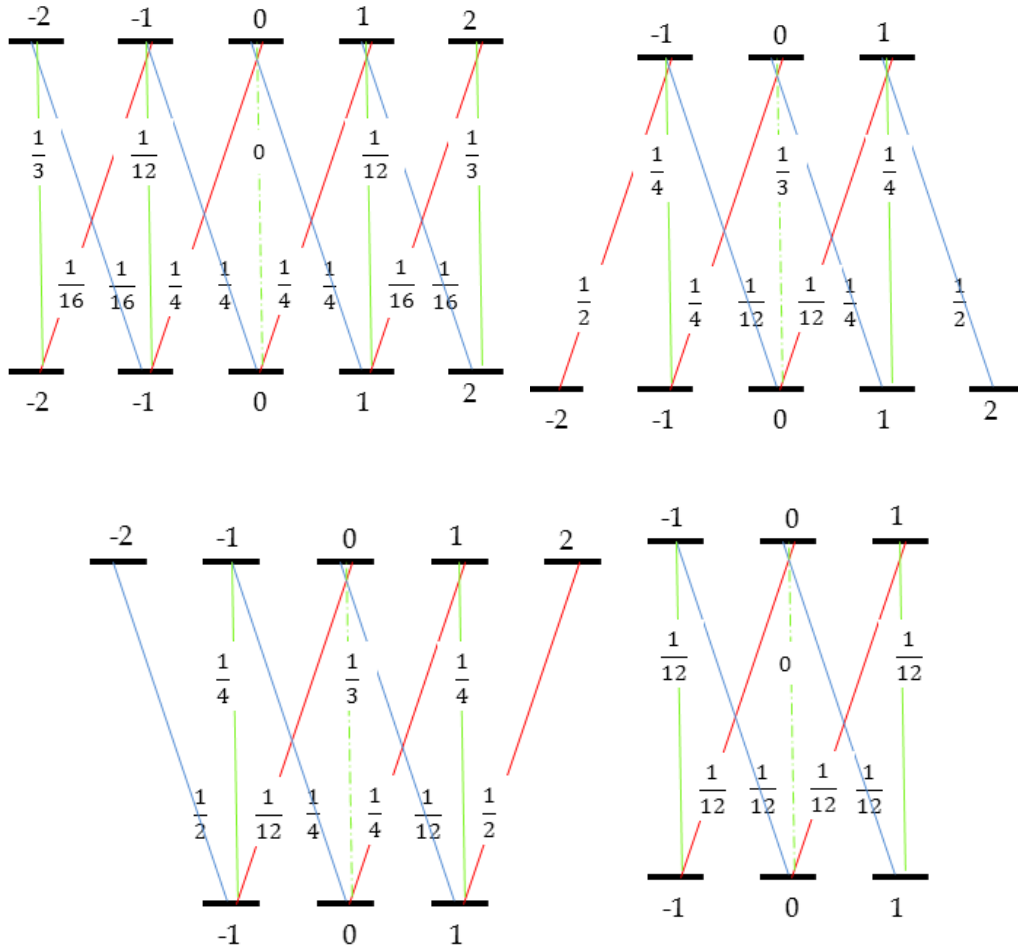


Figure C- 2: Transition strengths of the D1 line in ^{87}Rb atom [1].

REFERENCES:

- [1] J. VANIER and C. AUDOIN, *The Quantum Physics of Atomic Frequency Standards*, Adam Hilger, Bristol, UK, (1989).